Development of Novel Wearable Sensor Technology for Walking Training Toward Functional Restoration of Stroke Patients

By

Milad Nazarahari

A thesis submitted in partial fulfillment of the requirements for the degree of

Doctor of Philosophy

Department of Mechanical Engineering

University of Alberta

Abstract

Independent walking is a significant challenge for stroke patients, and improving mobility is of crucial importance for them. Supervised walking training is the standard rehabilitative program for this population; however, it can often be performed for only a few hours a week due to limited resources. Beyond these short periods, patients have to perform training independently, which can affect the training quality. The biofeedback-based therapeutic training has been shown to expedite the re-learning process for walking training. However, this approach requires dedicated laboratory equipment, which is rarely available at hospitals. As such, there is a lack of a practical motion capture system for walking training post-stroke.

To address this issue, this thesis aimed to develop a novel wearable technology using inertial measurement units (IMUs) to measure walking patterns during therapeutic training sessions. Then, the measured walking patterns can be compared to normal walking patterns, and the differences can be translated into auditory/visual biofeedback for the patient and therapist.

First, we proposed two simple, yet effective, sensor-to-segment calibration procedures, including (1) quiet standing and (at least) ten hip flexion/extension and (2) quiet standing and straight walking for (at least) eight steps. Using these calibration procedures, we transformed the measured quantities such as joint angles from the IMU sensor frame to the segment anatomical frame with high accuracy and repeatability to obtain clinically meaningful parameters.

Second, we performed a comprehensive survey of sensor fusion algorithms (SFAs) for body segment orientation tracking using IMUs. Using SFAs, we can combine the recordings of

the accelerometer, gyroscope, and magnetometer embedded in an IMU to obtain an accurate and robust estimate of body segment orientation. This survey identified efficient SFAs in the literature and techniques for obtaining robust performance under various motion patterns and intensities.

Third, we developed a framework for adaptive gain regulation of SFAs. We showed that the performance of SFAs depended highly on their chosen gains, and poor initialization of the gains would degrade their performance. Our experimental study showed that an optimized gain regulation scheme based on switching gains between two/three levels obtained sufficient accuracy.

Fourth, we proposed a novel linear Kalman filter and a novel robust extended Kalman filter for orientation tracking with IMUs. We included error sources in the raw IMU readouts in the state vector of our proposed Kalman filters so that the raw IMU readouts could be corrected before orientation estimation. Our experimental study showed that our proposed Kalman filters obtained more accurate and robust estimation in long-duration dynamic tasks. Also, in a benchmarking study, we compared the accuracy and robustness of our proposed SFAs to those of more than 30 SFAs in the literature and identified the most efficient choices for different applications.

Fifth, using the estimated foot orientation in the sagittal plane obtained with our proposed SFA, we proposed a novel real-time algorithm for gait event detection. Foot orientation provides physiologically meaningful features corresponding to our observational recognition of the foot's initial and terminal contacts with the ground. Our experimental study showed that using our proposed biomechanically meaningful rules and constraints resulted in (1) sensitivity and precision of 100% and (2) a temporal accuracy higher than or comparable with the literature.

Finally, using a single chest-mounted IMU, we developed a novel method for the detection and classification of a wide range of physical activities, including standing, sitting, lying, level walking, and walking upstairs and downstairs. The trunk inclination angle and variation of the

gravitational component of the accelerometer readout were used for the detection and classification of postural transitions and walking modalities. Our experimental study showed that the proposed method had higher accuracy, sensitivity, and specificity in detecting postural transitions and walking modalities than other methods in the literature.

Our research outcomes based on the steps above enable us to develop wearable sensor technology for gait training. In the future, a biofeedback control system should be designed to report the measured gait kinematics and the difference between the pathological movement patterns and the targeted normal ones to the patient and therapist. Also, our proposed daily activity recognition technology can reveal the efficacy of the training by assessing the users' activity in their natural living environment.

Preface

This thesis is an original work by Milad Nazarahari. This thesis received research ethics approval from the Health Research Ethics Board of the University of Alberta, Project Name "accuracy assessment of wearable technologies for objective clinical outcome evaluation," study ID Pro00065804.

Chapter 2 of this thesis has been published as: M. Nazarahari, H. Rouhani, "40 years of sensor fusion for orientation tracking via magnetic and inertial measurement units: Methods, lessons learned, and future challenges," Information Fusion, Vol. 68, pp. 67-84, 2021. I was responsible for conceptualization, methodology, investigation, writing the original draft, and visualization. H. Rouhani was the supervisory author and was involved with conceptualization and study design, structuring the review study and reviewing and editing the manuscript.

Chapter 3 of this thesis has been published as: M. Nazarahari, H. Rouhani, "Semi-automatic sensor-to-body calibration of inertial sensors on lower limb using gait recording," IEEE Sensors Journal, Vol. 19(24), pp. 12465 - 12474, 2019; and M. Nazarahari, A. Noamani, N. Ahmadian, H. Rouhani, "Sensor-to-body calibration procedure for clinical motion analysis of lower limb using magnetic and inertial measurement units," Journal of Biomechanics, Vol. 85, pp. 224-229, 2019. I was responsible for conceptualization, methodology, data collection, software development, investigation, writing the original draft, and visualization. A. Noamani and N. Ahmadian assisted with the data collection and contributed to manuscript edits. H. Rouhani was the supervisory author and was involved with conceptualization and study design, methodology, interpretation of the results, and reviewing and editing the manuscript.

Chapter 4 of this thesis has been published as: M. Nazarahari, H. Rouhani, "Adaptive Gain Regulation of Sensor Fusion Algorithms for Orientation Estimation with Magnetic and Inertial Measurement Units," IEEE Transactions on Instrumentation and Measurement, Vol. 70, 2020. I was responsible for conceptualization, methodology, data collection, software development, investigation, writing the original draft, and visualization. H. Rouhani was the supervisory author

and was involved with conceptualization and study design, methodology, interpretation of the results, and reviewing and editing the manuscript

Chapter 5 of this thesis has been published as: M. Nazarahari, H. Rouhani, "Sensor Fusion Algorithms for Orientation Tracking via Magnetic and Inertial Measurement Units: An Experimental Comparison Survey," Information Fusion, Vol. 76, pp. 8-23, 2021; and M. Nazarahari, H. Rouhani, "A Full-State Robust Extended Kalman Filter for Orientation Tracking During Long-duration Dynamic Tasks Using Magnetic and Inertial Measurement Units," Submitted to IEEE Transactions on Neural Systems and Rehabilitation Engineering, In-press, 2021. I was responsible for conceptualization, methodology, data collection, software development, investigation, writing the original draft, and visualization. H. Rouhani was the supervisory author and was involved with conceptualization and study design, methodology, interpretation of the results, and reviewing and editing the manuscript.

Chapter 6 of this thesis has been submitted as an original article: M. Nazarahari, A. Khandan, H. Rouhani, "Foot Kinematic Features Measured with Inertial Measurement Units: An Inherently Robust Approach to Real-time Gait Event Detection," Submitted, 2021. I was responsible for conceptualization, methodology, data collection, software development, investigation, writing the original draft, and visualization. A. Khandan assisted with the data collection and contributed to manuscript edits. H. Rouhani was the supervisory author and was involved with conceptualization and study design, methodology, interpretation of the results, and reviewing and editing the manuscript

Chapter 7 of this thesis has been published as: M. Nazarahari, H. Rouhani, "Detection of Daily Postures and Walking Modalities Using a Single Chest-mounted Tri-axial Accelerometer," Medical engineering & physics, Vol. 57, pp. 75-81, 2018. I was responsible for conceptualization, methodology, data collection, software development, investigation, writing the original draft, and visualization. H. Rouhani was the supervisory author and was involved with conceptualization and study design, data collection, methodology, interpretation of the results, and reviewing and editing the manuscript.

Dedicated to my lifelong mentor and beloved uncle

Yousef Asgariyan

whom without

I was not the person I am today!

Acknowledgements

I would like to express my sincere gratitude to my supervisor, Dr. Hossein Rouhani, for his guidance and support on every single step of my Ph.D. studies. I would also like to thank him for helping me go beyond what was required of me and explore, experience, and grow as a researcher and a teacher.

I would like to thank Drs. Jason Carey and Albert Vette for their invaluable insights as members of my supervisory committee. Also, I would like to thank Dr. Albert Vette for his support during all stages of my Ph.D. journey. Moreover, I would like to thank Drs. Edmond Lou and Bijan Najafi for serving on my Ph.D. thesis exam committee, and Dr. Ehsan Hashemi as my thesis exam chair.

The generous financial support of the Vanier Canada Graduate Scholarship, Alberta Innovates Graduate Student Scholarship, Izaak Walton Killam Memorial Scholarship, and other awards provided by the University of Alberta made my Ph.D. an enjoyable journey. Also, I had the privilege of collaborating with researchers at the Neuromuscular Control & Biomechanics Laboratory at the University of Alberta, including Alireza Noamani, Aminreza Khandan, and Niloufar Ahmadian, among many others.

In the end, I would like to thank my loving wife and family for their care, support, encouragement, and patience. Without any doubt, this journey would not be possible without them.

Table of Contents

List of Tables

List of Figures

List of Algorithms

Nomenclature

3D	:	Three-dimensional
AA	:	Abduction/adduction
AF	:	Anatomical frame
CF	:	Complementary filter
CKF	:	Complementary Kalman filter
EKF	:	Extended Kalman filter
FE	:	Flexion/extension
FOG	:	Fixed optimal gain
FQA	:	Factored quaternion algorithm
GDA	:	Gradient descent algorithm
GNA	:	Gauss-Newton algorithm
IC	:	Initial contact
IMU	:	Inertial measurement units
ISB	:	International society of biomechanics
KF	:	Kalman filters
LySi	:	Lie-to-sit transition
MCS	:	Motion capture system
PC5/8	:	Proposed calibration (straight walking for 5/8 steps)
PF	:	Plate frame
PT	:	Postural transition
QUEST	:	Quaternion estimator
RMS	:	Root-mean-square
RMSE	:	Root-mean-square-error
SF	:	Sensor frame
SFA	:	Sensor fusion algorithm
SiSt	:	Sit-to-stand transition
SiLy	:	Sit-to-lie transition
SRUKF	:	Square-root unscented KF
SRCKF	:	Square-root cubature KF
StSi	:	Stand-to-sit transition
SVM	:	Signal vector magnitude
TC	:	Terminal contact
TRIAD	:	TRi-axial attitude determination
VST	:	Vector selection technique

Chapter 1

Introduction

Chapter 1 presents the motivation and objectives of this research as well as the outline of the thesis.

1.1 Gait Rehabilitation Training

In 2013, it was estimated that over 400,000 Canadians were dealing with the consequences of stroke, and this number could grow to more than half a million in 2021 [1]. Independent walking is a major challenge for more than 85% of stroke survivors [2], and improving mobility is one of their priorities [3]. To help this population achieve a walking pattern close to normal, the standard rehabilitative procedure includes performing guided practice steps under therapist supervision to facilitate the re-learning process [4]. For efficient re-learning, the practice steps need to be completed with a proper technique in all training sessions. However, as the therapists are available for only a few hours a day, patients usually have to perform walking training independently. This can lead to reinforcement of an abnormal walking pattern that oftentimes leads to secondary health complications.

It has been shown that real-time movement feedback, including visual or auditory biofeedback, can help patients modify their abnormal walking patterns and accelerate the re-learning process [5], [6]. However, this approach requires an expensive camera motion-capture system (MCS), which is rarely available in small clinics. Moreover, laboratory space usually limits the length of the walking training platform and affects the natural walking pattern of the patient

[7]–[9]. Therefore, there is a lack of viable motion measurement technology for the instrumented biofeedback-based walking training of stroke survivors.

Wearable inertial measurement units (IMUs) have been widely used to assess human motion for movement disorder diagnosis [10]–[16], emergency conditions, such as fall detection [17], [18], and in-home rehabilitation [19], [20]. However, there is still a lack of wearable sensor technology for biofeedback-based walking training. As a result, this research aims to develop a wearable sensor technology that can provide quantitative and clinically relevant biofeedback on the walking pattern of stroke survivors and thus facilitate rehabilitative programs in small clinics and homes.

1.2 Thesis Objectives

This research aims to develop innovative wearable technology to measure the lower limb motion during walking in real-time. The primary application of this technology will be providing real-time biofeedback on the walking pattern of stroke patients during therapeutic training sessions, as shown in Figure 1. The two phases of this research project are to:

1. Develop a wearable sensor technology to accurately monitor the lower limb's three-dimensional (3D) motions, including joint angles and temporal gait events, in real-time during walking training.
2. Validate the accuracy of the gait kinematics measured by the developed wearable technology against those measured by MCS as a gold-standard reference.

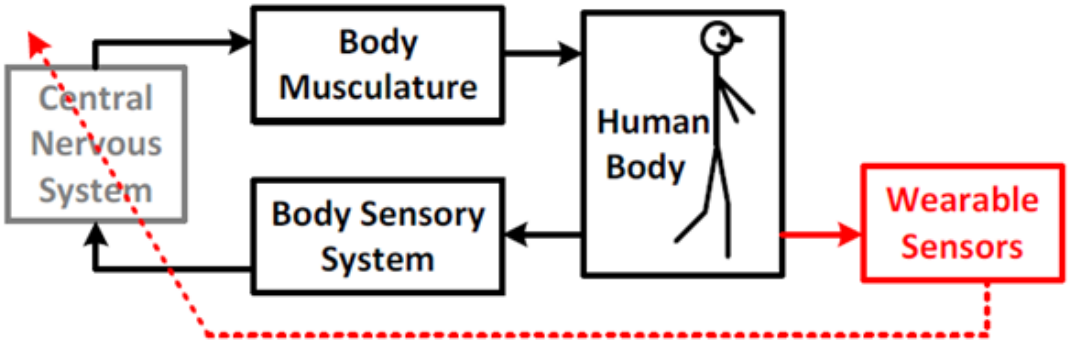

Figure 1 Development of a wearable system for biofeedback-based over-ground gait training of stroke patients. The grey box shows the impaired function of the central nervous system. The developed technology is shown in red. The dashed line shows the learning process in the central nervous system using biofeedback from wearable sensors.

1.3 Thesis Significance

Canada's healthcare system is facing new challenges in increasing healthcare costs due to a rapidly aging population. The direct financial burden of stroke is estimated to be $2.8B annually for the Canadian healthcare system [21]. Therefore, millions of dollars can be saved by introducing technological advancements in rehabilitative care. Although efforts have been made to develop technologies for rehabilitative care with a focus on walking training, the literature survey shows that:

1. Most of these technologies are based upon MCS, with the limitations mentioned in the previous sections.
2. Previously introduced wearable sensors were developed for motion monitoring of a single body joint or segment.

Therefore, for the first time, we propose wearable sensor technology for walking training by monitoring the motion of the whole lower limb toward providing real-time personalized biofeedback to the therapist and patient. The outcome of this research will provide the opportunity to:

1. Expedite the mobility function restoration of stroke survivors, thus enhancing the quality of life for these patients by providing personalized training and reducing recuperation time.
2. Decrease the financial burden of stroke for the Canadian healthcare system by reducing patients' hospitalization and minimizing the strain placed on therapists.

1.4 Thesis Outline

The remainder of this thesis is organized as follows and describes different steps toward the development of wearable sensor technology for walking training (Figure 2):

- Chapter 2 provides a background on gait rehabilitation training and a literature survey on how sensor fusion algorithms (SFA) have been used for orientation estimation using wearable IMUs. This chapter is partially based on publication [22].
- SFAs estimate the IMU's orientation in the sensor frame. Chapter 3 describes two innovative sensor-to-segment calibration procedures for transforming the measured quantities from the

IMU sensor frame to the body segment anatomical frame. This chapter is partially based on publications [23], [24].

- Following a sensor-to-segment calibration and to obtain accurate and robust estimations of the IMU sensor frame orientation, Chapter 4 details a novel technique for adaptive gain regulation of SFAs. This chapter is partially based on publication [25].
- The adaptive gain regulation of SFAs can typically ensure high accuracy and robustness for short-duration tasks. Chapter 5 describes the formulation of a linear Kalman filter (LKF) and a robust extended Kalman filter (EKF) for orientation tracking with IMUs during long-duration dynamic tasks. This chapter is partially based on publications [26], [27].
- After computing the lower limb joint angles using the methods proposed in Chapters 3, 4, and 5, Chapter 6 presents an accurate and reliable technique for temporal gait parameter detection with IMUs. This chapter is partially based on a submitted journal publication.
- Chapter 7 provides a method for daily activity monitoring using IMUs toward evaluating the efficacy of the gait rehabilitation training post-stroke. This chapter is partially based on publication [28].
- Chapter 8 presents the procedure for integrating the developed techniques toward creating wearable sensor technology for real-time measurement of lower limb joint angles and detection of gait events.
- Chapter 9 provides the conclusions and future directions.

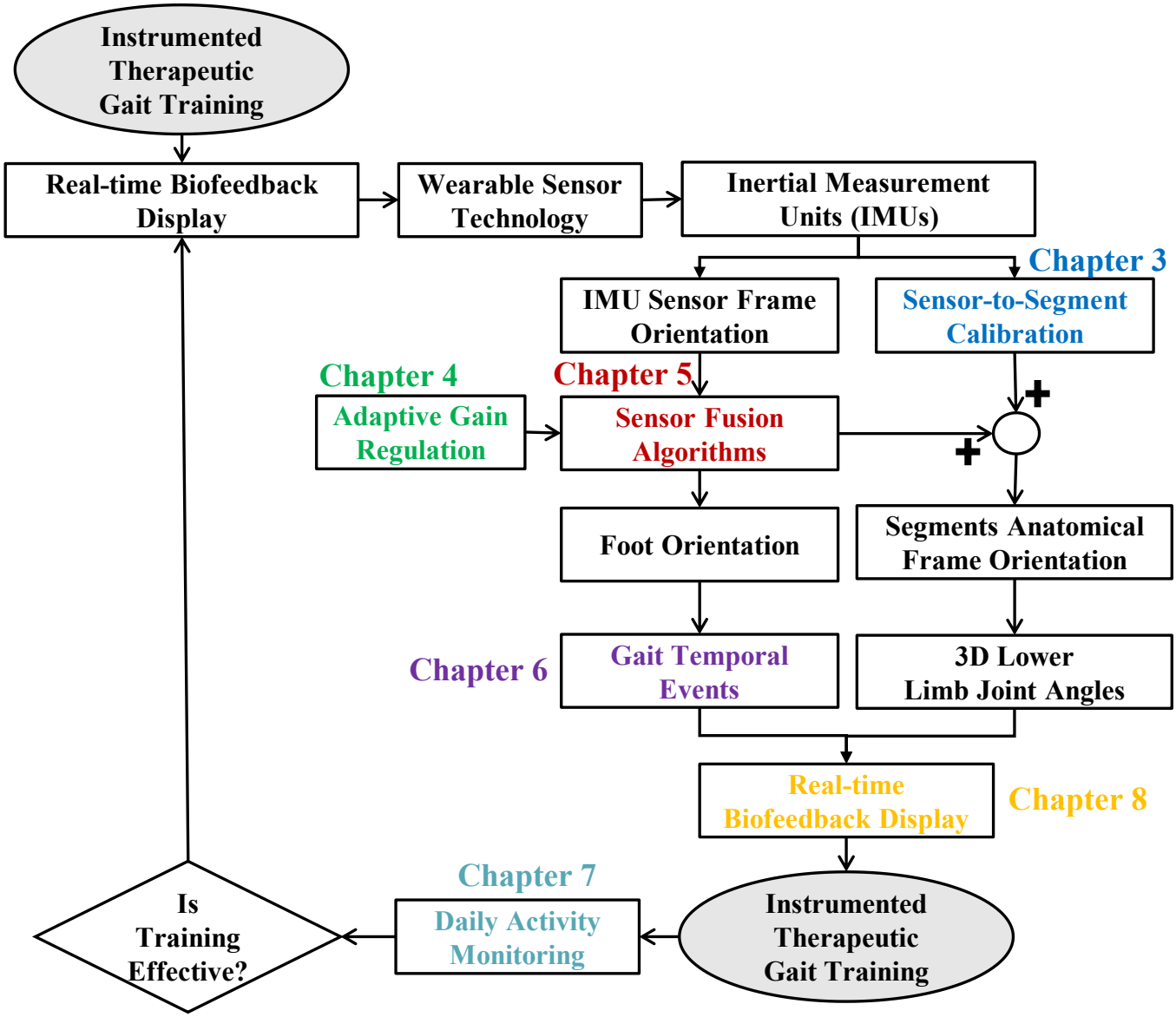

Figure 2 Elements of the proposed wearable sensor technology and their relation.

Chapter 2

Background and Literature Survey

This chapter provides an overview of the gait rehabilitation training and survey of SFAs proposed for orientation tracking with IMUs. Portions of this chapter have been adopted and/or edited from:

M. Nazarahari, H. Rouhani, "40 years of sensor fusion for orientation tracking via magnetic and inertial measurement units: Methods, lessons learned, and future challenges," Information Fusion, Vol. 68, pp. 67-84, 2021.

2.1 Gait Rehabilitation Training

Sensory and/or motor impairments may limit the walking abilities of patients who suffer from stroke. Restrictions in intrinsic biofeedback to the central nervous system caused by injury can lead to an altered gait and severely affect motor control [29]. Therefore, these patients are susceptible to unstable gait patterns, often accompanied by falls [30], [31].

If intrinsic biofeedback is impaired, external biofeedback provided by therapists or intelligent systems may compensate for the impaired sensory function. It has been shown that real-time movement biofeedback, including visual or auditory display, can help patients modify their abnormal walking pattern and accelerate the re-learning process [5], [6]. For example, a biofeedback system that demonstrated the deviations of the gait pattern from normal walking for patients with cerebral palsy helped them normalize their pathological gait pattern [32]. Also, the gait pattern of patients with spinal cord injury improved in short and medium terms by visualizing the mean knee angle from a speed-matched reference during walking training [5]. More recently,

it has been shown that real-time computer-generated verbalized biofeedback can normalize gait in individuals with spinal cord injury and stroke [33].

Traditionally, instrumented biofeedback-based gait training was performed by analyzing lower limb motion using a stationary camera-based MCS [34]–[36]. However, this method has limited clinical application for the following reasons:

1. Requiring a complex gait lab that is rarely available to clinicians/patients in most rehabilitation hospitals and clinics [8], [9].
2. A stationary MCS is usually limited to the confined space of a laboratory that may affect the gait pattern of the patient [8], [9], [37].
3. A stationary MCS was designed and developed originally for offline motion analysis; thus, it requires long preparation and post-processing time under the supervision of an experienced operator. The most recent MCSs can obtain only a few motion parameters in real-time rather than a continuous display of lower limb motion.
4. A common problem encountered in a camera-based MCS is information loss, i.e., some marker positions are often missed due to occlusions or ambiguities.

Therefore, there is a lack of reliable and practical technology for real-time motion measurement toward implementing an instrumented biofeedback-based walking training of stroke patients.

2.2 Wearable Inertial Measurement Units (IMUs)

Affordable wearable IMUs with lightweight, long battery life and large memory capacity have become increasingly popular for ambulatory human motion analysis [38], [39]. IMUs are comprised of a tri-axial accelerometer, gyroscope, magnetometer, as well as other aiding sensors such as barometer, and can measure acceleration, angular velocity, and the Earth's magnetic field. By measuring the acceleration and angular velocity of a rigid body, e.g., body segment, as well as the surrounding Earth's magnetic field, 3D orientation and position of the rigid body can be tracked. Because of their lightweight, small size, and long battery life [40], [41], IMUs have been used extensively as an ideal tool in aerospace, unmanned vehicle navigation, robotics, and human motion tracking. However, in almost all applications, whether the 3D joint angle measurement in an ambulatory human motion tracking system [42] or displacement estimation in a dead-reckoning system [43], the IMU orientation must be first calculated using an SFA.

2.3 Body Segment Orientation Tracking with IMUs

Raw IMU data can be used to estimate the sensor's orientation under specific conditions. In particular, the IMU's accelerometer measures the gravitational acceleration and can be used to compute the attitude. Also, in a magnetically neutral environment, the magnetometer measures the geomagnetic field, which can be used to estimate the yaw angle. Furthermore, the gyroscope measures the angular velocity (rate of change of orientation), which can be used to calculate the change in orientation using numerical strap-down integration.

However, using the accelerometer, gyroscope, and magnetometer alone may yield poor estimations in terms of accuracy or robustness due to various sources of error [44]. For example, accelerometers are not suitable for orientation estimation during dynamic tasks as they measure the external non-gravitational acceleration (due to motion) in addition to the gravitational acceleration. Also, the geomagnetic field could be distorted by ferrous materials, specifically during indoor motion tracking, which makes magnetometer-based estimations inaccurate. Moreover, because the cumulative error of the strap-down integration increases unboundedly over time, gyroscopes are not suitable for orientation estimation during long-duration tasks. Thus, various SFAs have been proposed in the literature to achieve an accurate and reliable estimation.

2.3.1 Orientation Parametrization

Rigid body orientation can be expressed via one of the following parametrizations: (1) Euler angles, i.e., roll and pitch (also known as the attitude) and yaw (also known as the heading); (2) quaternions; or (3) direction cosine matrix [45], [46]. Euler angles can be used when an intuitive physical meaning of the estimated orientation is needed. For example, controlling an unmanned vehicle [47], measuring human joint angles, or tracking in an augmented reality device [48]. However, under certain configurations, there are singularities associated with this parametrization that make Euler angles unsuitable for most control or tracking applications.

Quaternion or direction cosine matrix parametrization could be used to express/calculate the orientation without singularity in a computationally efficient manner [49], [50]. However, the unconstrained estimation of these parametrizations would lead to an ambiguous and meaningless representation. In particular, a *quaternion parametrization of orientation* is an element of the quaternion group, i.e., homeomorphic to rotation group $SO(3)$, with S^3 as its domain [51]. Therefore, to reduce its degrees of freedom from four to three, consistent with the dimension of

the $SO(3)$, a constrained quaternion estimation is required, such as enforcing the unit norm constraint after estimation. See more on constrained estimation in [51], [52]. A similar hard constraint must be used when using direction cosine matrix parametrization [53], [54].

2.3.1.1 Previous Surveys on Sensor Fusion Algorithms

Previous surveys have reviewed the literature related to IMUs with a focus on applications [55]–[60], technical developments [43], [56], [61], [62], and/or experimental comparison. However, in line with the aim of the present paper, in this section, we review the previous surveys of SFAs for IMU orientation estimation only. Table 1 summarizes the surveys with a focus on the experimental comparison. Table 1 identifies the filter with the best performance in each survey and provides the details of the SFAs tested, parameter tuning strategies, and experimental validations.

Cavallo et al. [63] compared the estimation accuracy of three SFAs, their proposed EKF and SFAs in [64], [65], using an IMU mounted on the KUKA Youbot robot while the accelerometer and magnetometer were calibrated using a 3D-ellipsoid fitting method [66]. The robot measured the reference (true) orientation during slow (18 degrees/s) and fast (45 degrees/s) trajectory tracking motions. Filippeschi et al. [49] performed an experimental study to compare five SFAs [67]–[71] for wrist position tracking. They used orientation and length of the trunk, upper arm, and forearm to estimate the wrist position. However, the accuracy of the SFAs was not directly comparable for the following reasons: (1) one method required visual reference for position tracking; (2) methods were different in terms of constraints of the kinematic chain; and (3) parameters of the methods were not selected systematically.

Table 1 Review of the previous literature surveys of the SFAs, including the tested algorithms, the gain selection procedure, the used reference system for validation, the type experiments, and the algorithm(s) concluded to have the best performance. Abbreviations used in the table are described in the table footnotes.

Study	SFAs	Filter Parameters	Reference	Experiments (duration in seconds)	Selected Filter
[63]	PEKF, [64], [65]	EC	Robot [72]	Slow & fast motions of robotic arm (≤45s)	PEKF
[49]	[67]–[71]	EC	MCS	Elbow, forearm & shoulder functional tasks (≤15s)	Acc.: [67] Corr.: [70]
[73]	[68], [74]–[76]	EC	MCS	Random motions (≤20), Treadmill walking (≤30s)	[74]
[77]	PEKF, KF	EC	MCS	Random head motions (≤35s)	PEKF
[78]	[64], [79]–[81]	EC	MCS	Static and dynamic tests in magnetically clean & disturbed environments (≤60s)	[81]
[82]	SDI, [64], [77]	EC	MCS	Daily routine tasks (≤60s), Walking (≤180s)	[77]
[83]	[64], [84]	EC	None	Single axis rotations (≤250s)	[84]
[79]	[85], [86]	EC	MCS	Daily routine tasks (≤60s), Walking (≤180s)	[85]
[87]	[64], [77], [88], XKF	OP	MCS	Slow, medium & fast random rotations (≤70s)	Slow/medium: XKF, Fast: [77]
[89]	[64], [65], [90]	OP	MCS	Quadcopter motion adopted from [91]	[65]
[92]	[64], [65], [93]–[96]	EC	MCS	Smartphone data during various activities (≤180s)	[96]
[97]	[64], [65]	EC	MCS	Various walking tests, adopted from [98]	[64]
[99]	[64], [65], [100], [101]	OP	Synthetic	-	[64], [65]
[102]	[103], modified [104]	EC	MCS	Material handling task (≤60s)	Modified [104]

- **Sensor Fusion Algorithms:** PEKF: Proposed Extended Kalman Filter by the study; XKF: Xesne proprietary Kalman Filter; SDI: Strap-down integration.
- **Filter Parameters:** EC: Selecting the sensor fusion algorithm's gain(s) by trial-and-error; OP: Selecting the sensor fusion algorithm's gain(s) by a rigorous search.
- **Reference:** MCS: Gold-standard camera motion-capture system. Synthetic: used synthetic IMU data.
- **Selected Filter:** Acc: Selected based on accuracy; Corr: Selected based on correlation.

Young [73] compared the EKF proposed in [68] with different Complementary Filters (CFs) presented in [74]–[76]. After calibrating sensors for offset and scale errors, the accuracy of the SFAs was evaluated during gentle random motions and over treadmill walking at a normal pace. They concluded that, in general, CFs with lower computational complexity could outperform KFs for human motion tracking, as CFs have no assumption about the process dynamics. Also, they showed that because of the lower computational complexity and minimal loss of accuracy, the use of non-optimal vector observation algorithms, such as TRi-axial Attitude Determination (TRIAD), is preferred compared to optimal ones such as the QUaternion ESTimator (QUEST). More recently, Sabitini [77] provided a general survey of SFAs, including algorithms based on vector observations and KFs, with great emphasis on practical aspects such as SFA gain selection.

Fan et al. [78] performed a systematic review of standard strategies for reducing the effect of magnetic disturbance on the accuracy and robustness of SFAs. They also compared the accuracy of five SFAs, [64], [79]–[81], and concluded that a "good" filter must have the following three features: (1) gyroscope drift compensation; (2) decoupling attitude from yaw estimation; and (3) an adaptive strategy to reject magnetic distortions. Similarly, Ligorio and Sabatini [79] reviewed the main magnetic disturbance compensation strategies used in KFs and showed that model-based approaches (estimating the magnetic disturbance at each iteration using a stochastic model) had the best performance.

Bergamini et al. [82] used routine manual tasks such as teeth/hair brushing and walking along a ∞-shaped pathway to compare the accuracy of strap-down integration with the CF proposed by Madgwick et al. [64] and the KF proposed by Sabatini [77]. This study showed that the tested CF and KF were significantly more accurate than strap-down integration for yaw estimation and that the two SFAs achieved similar accuracy. Using the optimal SFAs gains, Caruso et al. [87] analyzed the performance of four SFAs ([64], [77], [88], and Xesne proprietary KF) and concluded that the performance of SFAs depends on the experimental conditions, such as the rate of rotations during experiments. Michel et al. [92] compared the accuracy and robustness of six SFAs ([64], [65], [93]–[96]) using smartphone data during a variety of daily routine activities. They showed that the overall performance of the nonlinear CF proposed by Martin and Salaun [96] was best, but SFAs with a simpler structure and lower computational complexity, such as [64] and [65], could be highly beneficial for saving the battery life of the smartphone. See [105] for a more detailed study on the energy characterization of CF and KF.

However, the mentioned works only surveyed a limited number of SFAs, i.e., in total, 30 filters were tested in the abovementioned works, and only 4 of them were used in more than two studies. Therefore, in this chapter, we reviewed a wide range of SFAs for orientation tracking with IMUs, including vector observation algorithms, CFs, Linear KFs (LKFs), EKFs, and Complementary KFs (CKFs). However, we did not review fusing strategies such as the Unscented KF, Cubature KF, and Particle filter, or other technologies for orientation tracking, whether alone or together with IMUs. In summary, this review sought to answer the following question: how can IMU signals be fused for orientation tracking? To answer this question, we provided a survey on state-of-the-art strategies, including SFAs based on vector observation algorithms, CF, and LKF/EKF/CKF families.

2.3.2 IMU Model

This section presents the IMU model commonly used in developing SFAs [106], [107]. Gyroscope readout, y_G, can be modelled as the summation of the true angular velocity, ω, the bias b_G, and a white noise term, v_G, as in Equation 1,

$$y_{G,k} = K_G \omega_k + b_{G,k} + v_{G,k} \quad \text{Equation 1}$$

$$b_{G,k} = b_{G,k-1} + w_{b,k} \quad \text{Equation 2}$$

where K_G is the scale factor matrix, and Equation 2 models b_G as a first-order Markov process driven by white Gaussian noise, w_b. Accelerometer readout, y_A, can be modelled as the summation of the external non-gravitational acceleration, a, the gravitational acceleration, g, the bias b_A, and a white noise term, v_A, as in Equation 3,

$$y_{A,k} = K_A[a_k + g_k] + b_{A,k} + v_{A,k} \quad \text{Equation 3}$$

$$a_k = c_a a_{k-1} + w_{a,k} \quad \text{Equation 4}$$

where K_A is the scale factor matrix, and Equation 4 models a as a first-order low-pass filtered ($0 \leq c_a < 1$ is the cut-off frequency of the filter) white Gaussian noise process. The bias term b_A was commonly obtained through a calibration procedure [66], [108] or estimated during orientation tracking as part of the KF state vector [109], [110]. Finally, the magnetometer readout, y_M, can be

modelled as the summation of the true geomagnetic field, m, magnetic distortion, d, and a white noise term, w_M, as in Equation 5,

$$y_{M,k} = K_M m_k + d_k + w_{M,k} \quad \text{Equation 5}$$

$$d_k = c_d d_{k-1} + w_{d,k} \quad \text{Equation 6}$$

where K_M is the scale factor matrix, and Equation 6 models d as a first-order low-pass filtered ($0 \leq c_d < 1$ is the cut-off frequency of the filter) white Gaussian noise process.

2.3.3 Strap-down Integration

While strap-down integration is not an SFA on its own, we dedicate a separate section to it as it is the core of almost all CFs and KFs. The numerical strap-down integration of gyroscope readout, y_G, can be used to update the orientation with respect to a known orientation as in Equation 7 [111],

$$\begin{cases} q_{k+1} = \exp\left(\Omega(y_{G,k}) T_s\right) q_k \\ q_0 = q(0) \end{cases} \quad \text{Equation 7}$$

$$\Omega(y_G) = \frac{1}{2} \begin{bmatrix} 0 & -y_{G,x} & -y_{G,y} & -y_{G,z} \\ y_{G,x} & 0 & y_{G,z} & -y_{G,y} \\ y_{G,y} & -y_{G,z} & 0 & y_{G,x} \\ y_{G,z} & y_{G,y} & -y_{G,x} & 0 \end{bmatrix} \quad \text{Equation 8}$$

where q is the quaternion parametrization of orientation, $\Omega(y_G)$ is a 4×4 skew-symmetric matrix shown in Equation 8, $\exp(\cdot)$ is the matrix exponential operator, which can be estimated using the Taylor series or Padé approximation, T_s is the sampling period of the IMU, and $q(0)$ is the known initial orientation. Lee and Choi [112] showed that when using the Taylor series to calculate $\exp(\cdot)$, the approximation order highly depends on (1) the sampling rate of the IMU; and (2) the magnitude of the y_G. Equation 7 can also be extended to account for the relative angular velocity of (1) the Earth's frame with respect to the inertial frame; and (2) the navigation frame with respect to the Earth's frame [113].

Nevertheless, strap-down integration has two disadvantages: (1) the initial orientation must be known; and (2) the gyroscope bias, b_G, results in an increasing cumulative error in the estimated orientation due to the numerical integration (see [114] for comparison of the drifts obtained from the strap-down integration and a KF). To address the former, y_A and y_M, along with a vector

observation algorithm (described in Section 2.3.4), can be used to calculate $q(0)$. To address the latter, various SFAs have been developed to use y_A and/or y_M to correct the strap-down integration drift over time. Also, using SFAs, b_G can be estimated at each time instant based on a stochastic model, as in Equation 2, to correct the y_G before the strap-down integration. However, one must note that b_G is a function of environmental conditions, such as ambient temperature, and extra caution must be exercised when environmental conditions change drastically during data acquisition [115].

2.3.4 Vector Observation Algorithms

Vector observation algorithms, commonly used in spacecraft SFAs, estimate the rigid body absolute orientation with respect to a reference frame. To this end, two or more vectors measured in the local rigid body frame, as well as their counterpart in the desired reference frame, are required. In this setting, almost all vector observation algorithms are based on minimizing the cost function $\mathcal{J}(A) = \frac{1}{2}\sum_i a_i|b_i - Ar_i|^2$, known as the Wahba's problem [116], where A is the direction cosine matrix representing the rigid body orientation (to be estimated), b_i is a unit vector measured in local rigid body frame, r_i is the corresponding unit vector in the reference frame, and a_i is the weight associated with each vector observation. Markley and Mortari [117] provided an overview of the most popular algorithms for solving Wahba's problem and compared their accuracy and speed.

For orientation tracking with IMUs, vector observations (b_i) are the normalized y_A and y_M, and their reference counterparts (r_i) are the gravitational acceleration, ${}^G g$, and the Earth's geomagnetic field vector, ${}^G m$, respectively, where G represents the Earth's reference frame. In this setting, the TRIAD algorithm calculates the direction cosine matrix A using Equation 9 [76], [118],

$$w_1 = b_1/|b_1|,\ w_2 = (w_1 \times b_2)/|w_1 \times b_2|,\ w_3 = w_1 \times w_2$$
$$v_1 = r_1/|r_1|,\ v_2 = (v_1 \times r_2)/|v_1 \times r_2|,\ v_3 = v_1 \times v_2 \qquad \text{Equation 9}$$
$$A = w_1 v_1^T + w_2 v_2^T + w_3 v_3^T$$

In TRIAD, attitude is calculated using ${}^G g$ and is immune to magnetic disturbance. In contrast to TRIAD, QUEST [119] can accommodate more than two vector observations by selecting proper

weights a_i for sensors with different accuracies. However, in QUEST, magnetic disturbance can affect the attitude estimation as well as yaw angle.

Along with TRIAD, the Factored Quaternion Algorithm (FQA) [74] was designed to decouple y_A and y_M and cancel the effect of magnetic disturbance on attitude calculation. TRIAD and FQA produce similar solutions to the Wahba's problem, with the exception that the former produces a direction cosine matrix and the latter produces a quaternion [74]. Other variants of vector observation algorithms include: Davenport q-method [120]; fast optimal attitude matrix [121]; singular value decomposition-based method [122]; filter QUEST [123]; recursive QUEST [124]; fast linear quaternion attitude estimator [125]; recursive linear continuous quaternion attitude estimator [126]; quaternion-based iterated least-square [127]; and algebraic quaternion algorithm [128], [129]. The main advantage of the vector observation algorithms is that they can estimate the absolute orientation. However, as the vector observations (y_A and y_M) could be corrupted by a and d, these algorithms are not suitable for indoor orientation tracking during highly dynamic tasks.

2.3.5 Complementary Filters (CFs)

2.3.5.1 Foundations

For an accurate estimate of orientation, the accelerometer and magnetometer should be used during static conditions (low-frequency), while the gyroscope should be used during dynamic conditions (high-frequency). To do this, the CF structure includes a low-pass filter $\mathcal{L}(s)$ to remove the high-frequency estimations obtained by the accelerometer and magnetometer and a high-pass filter $\mathcal{H}(s)$ to remove the low-frequency estimations obtained by the gyroscope, as shown in Figure 3(a). Commonly, the two filters' structures have been selected such that $\mathcal{L}(s) = \frac{\mathcal{C}(s)}{\mathcal{C}(s)+s}$ and $\mathcal{L}(s) + \mathcal{H}(s) = 1$, where $\mathcal{C}(s)$ is a transfer function.

The simplest choice for $\mathcal{L}(s)$ and $\mathcal{H}(s)$ is a first-order low-pass and high-pass filter, respectively, with a cut-off frequency of k_P. To achieve this, we can set $\mathcal{C}(s) = k_P$ in $\mathcal{L}(s)$, which results in the basic CF structure shown in Figure 3(b) with solid lines in the time domain. Figure 3(c) shows the frequency response of the basic CF for three different values of k_P. The optimal value of k_P depends on the dynamics of motion. This is, for relatively slow motions, a larger k_P is preferred while for high dynamics, a smaller k_P should be chosen [130]. As shown in Figure

3(c), the slope of the frequency response plot of the low- and high-pass filters is not steep, and thus, the filter output contains components of both filters. To address this issue and to achieve steeper slopes with frequency responses in Figure 3(d), we can add an integrator with gain k_I to the basic CF structure, i.e., $\mathcal{C}(s) = k_P + \frac{k_I}{s}$, as shown with the dashed line in Figure 3(b).

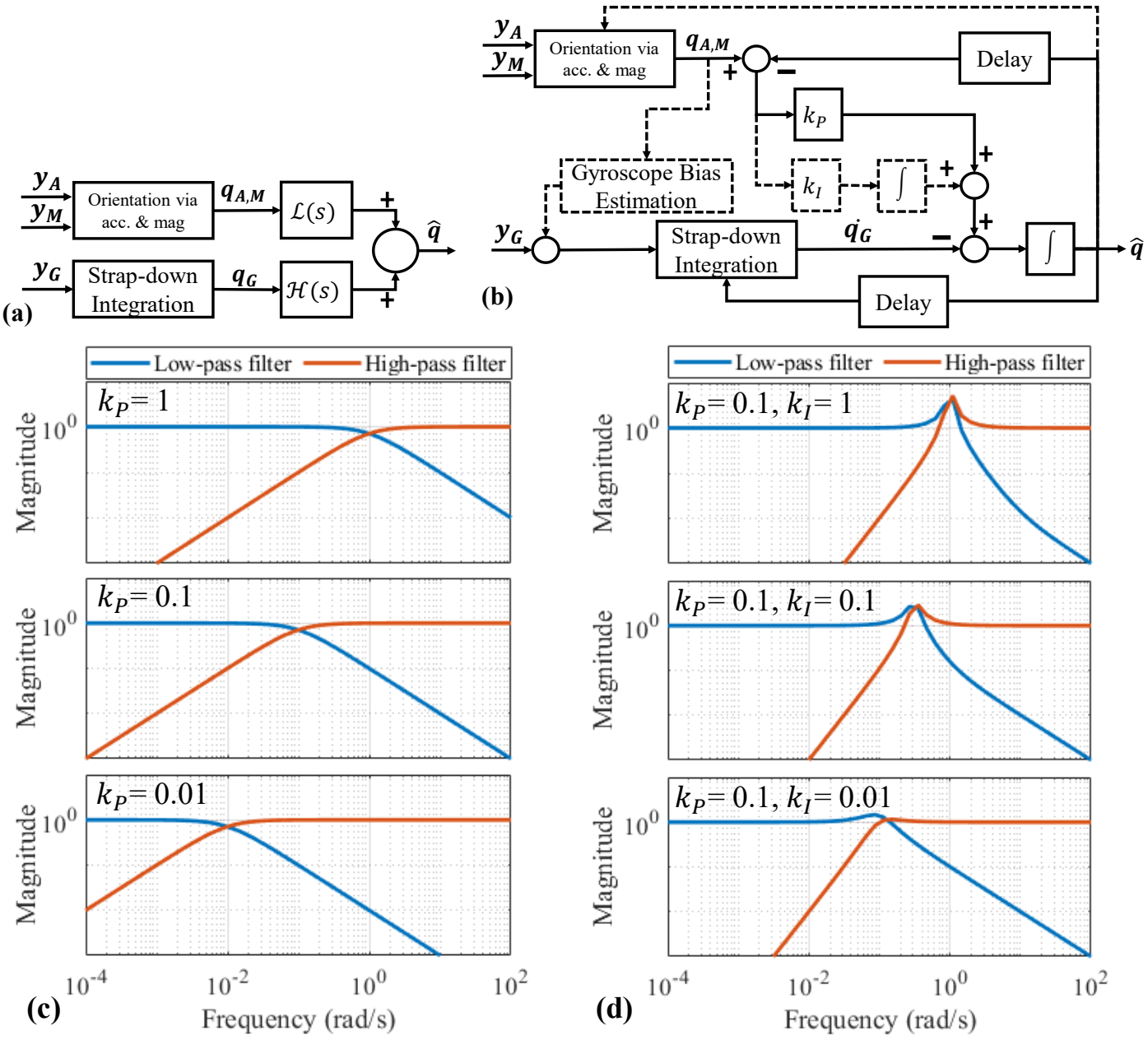

Figure 3 Flowchart and frequency response of a Complimentary Filter (CF). (a) The general structure of a CF; (b) Flowchart of the CF with low-pass filter transfer function defined as $\mathcal{L}(s) = \frac{\mathcal{C}(s)}{\mathcal{C}(s)+s}$ where $\mathcal{C}(s) = k_P + \frac{k_I}{s}$, and k_P and k_I are the proportional and integral gains, respectively; (c) Frequency response of the proportional CF, (d) Frequency response of the proportional-integral CF.

2.3.5.2 Literature survey of CFs

As the strap-down integration was used in almost all CFs developed for IMU orientation tracking, this section is focused on various approaches for (1) estimating the orientation via accelerometer and magnetometer; and (2) low- and high-pass filters' structure. See Table 2 for a comparison of CFs in the literature. Bachmann et al. [131] used the Gauss-Newton Algorithm (GNA) to modify the strap-down integration output based on a corrective term that minimized the error between the measured y_A and y_M and the projection of the ${}^{G}g$ and ${}^{G}m$ in IMU's sensor frame, SF, as in Equation 10,

$$q_{A,M}\left({}^{SF}_{G}\hat{q}_k\right) = [y_A, y_M] - \left[{}^{SF}_{G}\hat{q}_k^{*} \otimes {}^{G}g \otimes {}^{SF}_{G}\hat{q}_k \, , {}^{SF}_{G}\hat{q}_k^{*} \otimes {}^{G}m \otimes {}^{SF}_{G}\hat{q}_k\right] \quad \text{Equation 10}$$

where ${}^{SF}_{G}\hat{q}$ is the orientation of the IMU sensor frame with respect to the Earth's reference frame, $*$ and $\otimes$ are the quaternion conjugate and multiplication operations, respectively. Close variants of the same approach have been used in other works, including fast quaternion-based orientation optimizer [132]; Gradient Descent Algorithm (GDA)-based CF [64]; Levenberg-Marquardt algorithm-based CF [95], [133], [134]; GNA-based adaptive-gain CF [101]; geometrically-intuitive CF [135]; adaptive quaternion-based CF [136]; generalized linear quaternion-based CF [137]; and others [138]–[144].

The CF structure, which is shown in Figure 3(b), has been extensively revisited in the literature [65], [130], [145]–[149]. For instance, Calusdian et al. [130] used the proportional gain k_P to correct the strap-down integration output using the weighted error between the estimated orientations by CF at the previous time instant and the FQA. In CF proposed by Lai et al. [145], first, attitude was estimated using y_A as in Equation 11,

$$roll_{acc} = \tan^{-1}\left(y_{A,y}/y_{A,z}\right), pitch_{acc} = \tan^{-1}\left(y_{A,x}/\sqrt{{y_{A,y}}^2 + {y_{A,z}}^2}\right) \quad \text{Equation 11}$$

then, the proportional-integral CF in Figure 3(b) was employed to correct the strap-down integration output. Similarly, Liu and Zhu [111] proposed a CF based on the proportional-integral and multi-sample rotation vector concepts to eliminate the cumulative and noncommutativity errors of strap-down integration in high dynamics.

Mahony et al. [65] formulated the CF as a deterministic observer posed on the special orthogonal group *SO*(3). The proposed explicit CF does not require an algebraic reconstruction of

the attitude, as in vector observation algorithms, and due to its low computational complexity, it is ideal for embedded hardware platforms. Also, the explicit CF can work with only one vector observation (y_A or y_M). Similarly, Khosravian and Namvar [150] presented a nonlinear observer with asymptotic convergence based on a single vector observation (y_A or y_M). In general, a single vector observation can be used along with a thresholding scheme as in [142], [147] (also known as vector selection [106], [132]), or with fuzzy logic [151], [152], to reject imperfect measurements, such as rejecting y_A during high dynamic tasks or y_M during magnetic disturbance.

The stability properties of the explicit CF proposed in [65] were proven when the reference vectors are (1) stationary or (2) time-varying but the y_G is bias-free. Later, Grip et al. [153] proposed an improved explicit CF for cases when the reference vectors are time-varying and y_G is corrupted by bias. Also, Jensen [154] proposed a generalized version of the explicit CF by replacing the constant scalar gains with time-varying matrix gains. Because the gain tuning procedure for the explicit CF was based on trial-and-error, to provide a Kalman-like gain tuning capability for the filter, De Silva et al. [155] proposed the right-invariant formulation for the explicit CF with an intuitive gain tuning procedure based on the system's noise parameters.

Martin and Salaun [96] and Hua et al. [156] developed nonlinear observers by decoupling the yaw angle estimation from attitude estimation to minimize the effect of d on attitude. Fan et al. [157] and Wu et al. [158] proposed quaternion-based two-step CFs (step 1: estimate attitude by fusing y_G and y_A, step 2: estimate yaw using y_M). This allowed them to make attitude estimations immune to d and enable the filter to use two separate gains to minimize the effect of a and d in steps 1 and 2, respectively. Valenti et al. [128] introduced a vector observation algorithm for solving the Wahba's problem without singularity and, accordingly, developed a quaternion-based CF with attitude estimation immune to d. Marantos et al. [159] developed a CF based on a new analytical solution for Wahba's problem complemented with a gyroscope propagation and an adaptive gain regulation scheme to provide smooth orientation tracking in high dynamics. Yang et al. [160] formulated a linearly discrete dynamic model to relate the attitude to y_A and then developed a computationally efficient adaptive gain CF to combine the estimated attitude with strap-down integration output.

Chang et al. [161] first developed a smooth sliding-mode observer for attitude estimation using y_A, and then improved the observer estimations by including measurement noise and biases

[162]. El Hadri and Benallegue [163] proposed a nonlinear sliding-mode CF to achieve robust orientation tracking and b_G estimation under parametric uncertainties and modelling errors. Vasconcelos et al. [164] introduced a CF using Euler angle parametrization (stable for non-singular configurations) and b_G compensation and tuned the filter gains in the frequency domain to account for unmodeled disturbances found in the experimental setup. By estimating a virtual angular velocity for the rigid body using y_A and y_M, Tayebi et al. [165] developed a quaternion-based CF to track the orientation as well as an asymptotic estimate of b_G. Sheng and Zhang [166] proposed the application of a neural network-based proportional-integral-derivative controller for calculation of b_G based on the error between estimated orientation by strap-down integration and a vector observation algorithm. In the nonlinear CF introduced by Wu et al. [167], the error between y_A and the projection of ${}^G g$ in IMU sensor frame was used to estimate the b_G and correct the angular velocity before strap-down integration. However, this method does not provide an estimate of b_G when the IMU is motionless or y_A is parallel to ${}^G g$.

2.3.5.3 Modified Complementary Filters

Because the performance of a CF highly depends on its gains, Alves Neto et al. [168] proposed a CF using Euler angle parametrization and adaptive gains with values proportional to exp(-$|{}^G g - \|y_A\||$). Kottath et al. [169] presented the application of an ensemble of linear CFs with different gains to minimize the effect of gain value on the estimated orientation. In the proposed ensemble, the weighting factor associated with each CF was adaptively calculated based on the difference between the CF's and the ensemble's estimates. To adaptively compute the CF gains based on the error between the orientation obtained from y_A and y_M and CF output, Poddar and Narkhede [170] developed a non-linear CF aided with a Particle Swarm Optimization gain tuning scheme. It should be noted that the application of an adaptive gain tuning scheme or thresholding method for rejecting a and d cannot guarantee an accurate and robust estimation. For example, if gain tuning is used for an extended period of time to cancel the estimation errors from y_A during high dynamics, drift in attitude estimations will eventually occur because of b_G.

Table 2 Review of the state-of-the-art SFAs with a Complimentary Filter (CF) structure, including linear CF (LCK) and nonlinear CF (NCF). Abbreviations used in the table are described in the table footnotes.

Study	Year	Application	Method	Parametrization	b_G, a, d compensation	Notes (gain tuning or thresholding, etc.)
[131]	1999	HMT	GNA+CF	Q	-	-
[171]	2003	STC	NCF	Q	b_G	-
[84]	2006	AVTC	NCF	DCM	b_G	-
[165]	2007	-	NCF	Q	b_G	-
[65]	2008	RATC	NCF	DCM	b_G	-
[148]	2008	AVTC	NCF	Q	b_G	-
[168]	2009	MRTC	LCK	EA	-	$k_p \propto \exp(-\lvert {}^G g - \lVert y_A \rVert \rvert)$
[163]	2009	-	Sliding mode observer	EA	b_G	-
[132]	2009	HMT	GNA+CF	Q	-	a & d rejection with thresholding
[141]	2009	-	Azimuth-level detector CF	Q & DCM	-	-
[96]	2010	AVTC	NCF	Q	b_G	-
[145]	2010	-	NCF	EA	-	-
[64]	2011	HMT	GDA+CF	Q	-	-
[130]	2011	-	FQA+CF	Q	-	-
[133]	2011	Bio-logging	LMA+CF	Q	-	-
[164]	2011	SVTC	LCK	EA	-	-
[154]	2011	-	NCF	DCM	b_G	Time-varying gains
[146]	2011	MRTC	NCF	EA	b_G	-
[147]	2011	SVTC	NCF	EA	b_G	CF gain $\propto \lvert {}^G g - \lVert y_A \rVert \rvert$
[150]	2012	STC	NCF	DCM	-	-
[153]	2012	AVTC	NCF	DCM	b_G & b_A	-
[172]	2012	-	LCK	DCM	-	Using inverse sensor models to widen the frequency range
[173]	2012	-	TRIAD+LCK	DCM	b_G	-
[174]	2012	HMT	GDA+CF	Q	b_G	-
[175]	2012	HMT	LCK	DCM	-	CF gain $\propto$ duration of the experiment

Study	Year	Application	Method	Parametrization	b_G, a, d compensation	Notes (gain tuning or thresholding, etc.)
[176]	2012	MRTC	NCF	Q	-	-
[151]	2015	-	TRIAD+NCK	DCM	-	Adaptive gain tuning using fuzzy logic
[101]	2013	HMT	GDA+CF	Q	b_G	a & d rejection with thresholding
[134]	2014	HMT	Two-layer LMA+CF	Q	-	-
[81]	2011	HMT	GDA+CF	Q	b_G	-
[177]	2014	AVTC	PI controller+CF	EA	-	-
[156]	2014	AVTC	NCF	DCM	b_G	-
[152]	2014	HMT	LCK	EA	-	Adaptive gain tuning using fuzzy logic
[178]	2014	HMT	LCK	DCM	b_G	-
[143]	2015	Bicycle crank angle tracking	NCF + vertical acceleration update	Q	-	-
[166]	2015	AVTC	LCK	DCM	b_G estimation by neural network PID controller	-
[161]	2015	AVTC	Smooth 2nd order sliding mode observer	EA	-	-
[142]	2015	HMT	GDA+CF	Q	-	d rejection with thresholding
[128]	2015	AVTC	AQA+CF	Q	-	a rejection using LERP or SLERP + adaptive gain tuning
[179]	2015	AVTC	NCF	DCM	-	-
[135]	2016	HMT with smartphone	Geometrically-intuitive CF	Q	-	-
[158]	2016	-	Two-layer LCK	Q	-	d rejection with thresholding
[159]	2016	AVTC	Nonlinear SVD+CF	DCM	-	-
[167]	2016	RATC	NCF	DCM	b_G	-
[136]	2017	-	GDA+CF	Q	-	d rejection with thresholding
[169]	2017	AVTC	LCK	EA	b_G	Combining output of multiple fixed-gain CFs with MMAE
[170]	2017	AVTC	NCF	EA	-	Adaptive gain turning via Particle Swarm Optimization
[138]	2018	-	GDA+CF	Q	-	d rejection with thresholding

Study	Year	Application	Method	Parametrization	b_G, a, d compensation	Notes (gain tuning or thresholding, etc.)
[157]	2018	HMT	LCK	Q	-	a & d rejection with finite state machine
[139]	2018	RATC	FQA+CF	Q	-	Adaptive gain turning via GDA
[162]	2018	AVTC	Smooth 2nd order sliding mode observer	EA	b_G	-
[155]	2018	AVTC	Right invariant NCF	Q & DCM	b_G	CF gain $\propto$ system noise parameters
[160]	2018	AVTC	LCK	Q	-	CF gain $\propto \|y_G\|$
[180]	2018	-	MSRVA+CF	Q	b_G	-
[140]	2018	-	GDA+CF	Q	-	-
[137]	2019	AVTC	GDA+CF	Q	-	a & d rejection with thresholding
[144]	2019	-	GDA+CF	DCM	b_G	-
[181]	2019	Robot teleoperation	GDA+CF	Q	b_G	-
[149]	2019	AVTC	NCF	EA	b_G	Identified reliable y_G based on interquartile range of y_G previous samples
[182]	2020	HMT	GDA+CF	Q	-	d rejection
[183]	2020	HMT	GDA+CF	Q	-	y_G rejection during "no motion" state
[184]	2020	HMT	Two-layer LCK	Q	-	-
[185]	2020	-	LCF	Q	-	-
[186]	2020	AVTC	NCF	Q	-	a compensation by thresholding
[187]	2020	HMT	Extended CF	Q	b_G	d rejection with thresholding

- **Application:** STC: Spacecraft (satellite) tracking/control; HMT: Human motion tracking; MRTC: Mobile robot tracking/control; RATC: Robotic arm tracking/control; AVTC: Aerial vehicle tracking/control; SVTC: Surface vehicle tracking/control.
- **Method:** GNA: Gauss-Newton algorithm; GDA: Gradient descent algorithm; LMA: Levenberg-Marquardt algorithm; FQA: Factored quaternion algorithm; AQA: algebraic quaternion algorithm; LERP: Linear intERPolation; SLERP: Spherical Linear intERPolation; SVD: Singular value decomposition; MSRVA: Multi-sample rotation vector algorithm; MMAE: Multiple-model adaptive estimation.
- **Parametrization:** Q: Quaternion parametrization of orientation; EA: Euler angle parametrization of orientation; DCM: Direction cosine matrix parametrization of orientation.
- **Compensation:** b_G: Gyroscope bias; b_A: Accelerometer bias; a: external non-gravitational acceleration; d: magnetic disturbance.

2.3.6 Kalman Filters (KFs)

2.3.6.1 Foundations

Suppose that we describe the orientation tracking problem using linear or nonlinear discrete-time systems in Equation 12 and Equation 13, respectively,

$$\begin{aligned} x_{k+1} &= \mathcal{F}_k x_k + \mathcal{B}_k u_k + w_k \\ z_{k+1} &= \mathcal{H}_{k+1} x_{k+1} + v_{k+1} \end{aligned} \qquad \text{Equation 12}$$

$$\begin{aligned} x_{k+1} &= f_k(x_k, u_k, w_k) \\ z_{k+1} &= h_{k+1}(x_{k+1}, v_{k+1}) \end{aligned} \qquad \text{Equation 13}$$

where x, u, and z are states of the system (commonly the IMU orientation), input to the system (commonly y_G), and sensor measurements (commonly y_A and y_M), respectively; w and v are white Gaussian noise processes associated with system and measurement models with covariances $\mathcal{Q}$ and $\mathcal{R}$, respectively; $\mathcal{F}$ and $f(\cdot)$ are the state transition matrix and equation, respectively (also known as state propagation); and $\mathcal{H}$ and $h(\cdot)$ are the measurement prediction matrix and equation, respectively. Now, suppose that we show the estimation error, i.e., the error between the true state and the estimated state, of the linear system in Equation 12 by $\tilde{x}$ and our aim is to find the estimator that minimizes the weighted 2-norm of the expected value of $\tilde{x}$, i.e., $\min E[\tilde{x}^T \mathcal{T} \tilde{x}]$, where $\mathcal{T}$ is a positive definite weighting matrix. Then:

- If w_k and v_k are uncorrelated zero-mean white Gaussian processes, KF is the solution.
- If w_k and v_k are uncorrelated zero-mean white processes, KF is the best linear solution.
- For other cases, such as correlated/coloured noise or nonlinear system in Equation 13, the KF can be modified to answer the above problem [188].

In other words, the aim of using a KF is to estimate the state vector, x, based on our knowledge of the system model and the availability of the noisy input, u, and measurements, z. To this end, we can use LKF and EKF, as shown in Figure 4(a) and (b), to estimate the orientation using the linear and nonlinear systems in Equation 12 and Equation 13, respectively [188].

For orientation tracking applications, rigid body orientation is commonly considered to be the state vector. Also, (1) the strap-down integration is used to model the time-update equation, i.e., $\mathcal{F}$ or $f(\cdot)$; and (2) the difference between the measured and estimated acceleration and geomagnetic field is used to model the measurement-update equation, i.e., $\mathcal{H}$ or $h(\cdot)$. More

complex KFs have been introduced by including a, b_G, and/or d in the state vector (see Table 3 for a comparison of various KFs introduced in the literature).

2.3.6.2 Linear Kalman Filters (LKF)

Barshan and Durrant-Whyte [189] used y_G to build an LKF for estimating the yaw angle of a planar mobile robot. By inspection, they found an exponential model for b_G during the warm-up period and showed that the inclusion of this model reduced the estimation error by a factor of 5. Qi and Moore [47] proposed an LKF for GPS/IMU data fusion, where the GPS readouts were taken as the LKF measurements, and IMU readouts were taken as the additional information required for state propagation. Yun et al. [190] and Yean et al. [191] introduced LKFs where strap-down integration was used to build the time-update equation and the error between y_A/y_M and the projection of ${}^{G}g/{}^{G}m$ in IMU sensor frame, as in Equation 10, along with GNA and GDA were used to construct the measurement-update equation. Whole and Gebhard [192] extended this approach by switching between calculating the gradient of y_A and y_M under homogenous magnetic condition to calculating the gradient of y_A only under magnetic disturbance.

Lee and Park [86] used the optimal two-observation quaternion estimation method proposed in [193] along with a vector selection technique to estimate the orientation from y_A and y_M under quasi-static motions in magnetically homogeneous conditions and correct the predicted orientation by strap-down integration in an LKF structure. Seo et al. [194] proposed the application of the FQA to calculate the orientation using y_A and y_M and correct the strap-down integration output in a standard LKF. They also suggested a correction scheme using quaternion linear interpolation to combine the LKF and FQA outputs during static conditions which would eliminate the effect of b_G. Similarly, Valenti et al. [129], Guo et al. [195], Feng et al. [80], and Wu et al. [126] developed new algebraic quaternion estimators using y_A and y_M to formulate the measurement-update equation of a standard LKF. Some of these algebraic quaternion estimators made the attitude estimation immune to magnetic disturbance while providing higher computational efficiency compared to FQA.

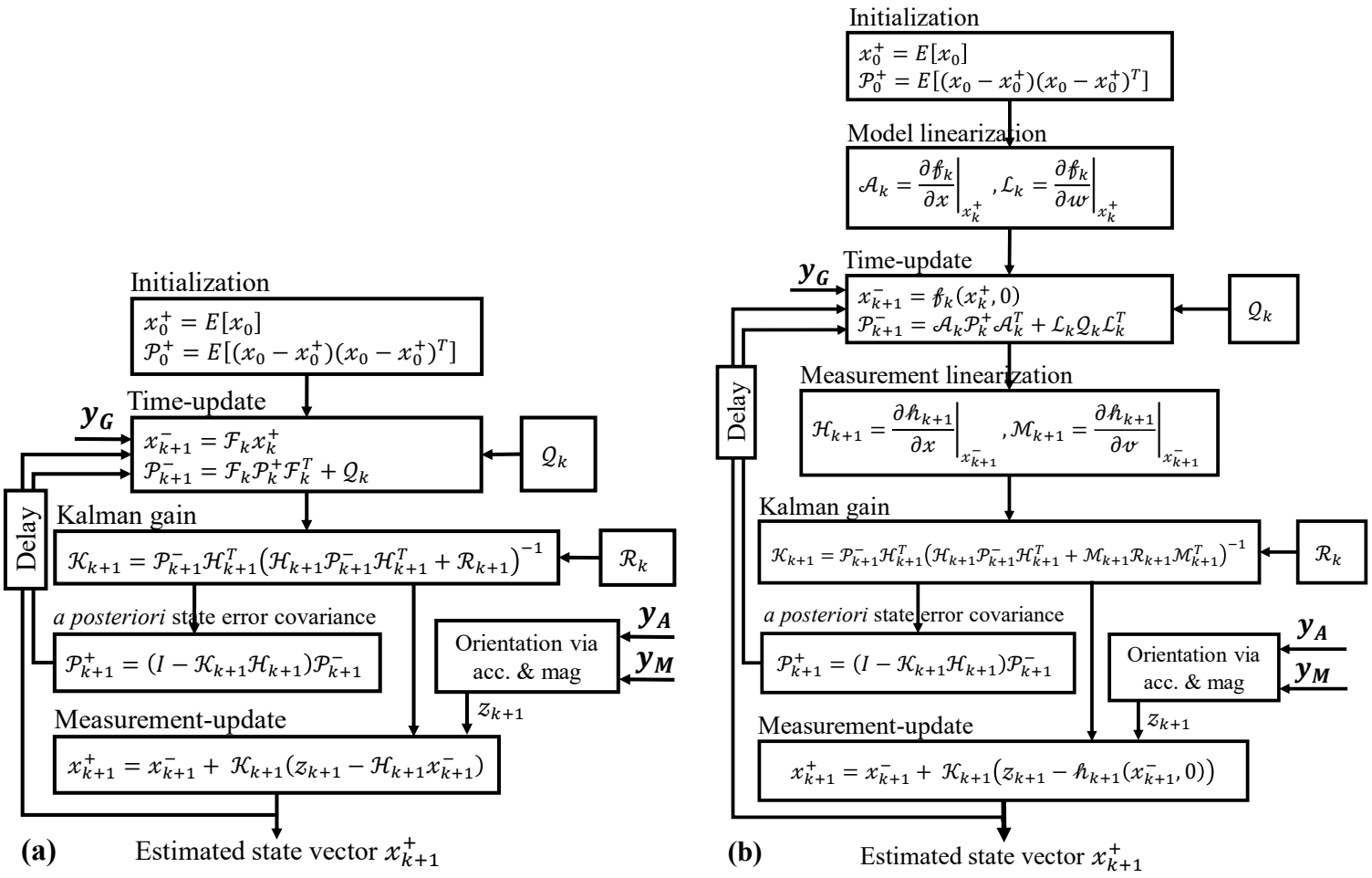

Figure 4 Flowchart of a general (a) Linear Kalman Filter and (b) Extended Kalman Filter. x is the state vector, z is the measurement vector. $\mathcal{P}$ is the state error covariance matrix. $\mathcal{F}$ and $f(\cdot)$ are the state transition matrix and equation, respectively. $\mathcal{H}$ and $h(\cdot)$ are the measurement prediction matrix and equation, respectively. $\mathcal{Q}$ and $\mathcal{R}$ are the system and measurement model covariance matrices, respectively. $\mathcal{K}$ is the Kalman gain.

Kim and Golnaraghi [196] proposed a magnetometer-free LKF in which the angular velocity used in strap-down integration and its bias were modelled as first-order Markov processes and included in the state vector. Also, the measurement-update equation was constructed using the error between (1) y_G and the estimated angular velocity, $\hat{\omega}$, plus bias; and (2) y_A and the projection of ${}^{G}g$ in IMU sensor frame. Also, Ligorio and Sabatini [104] developed a magnetometer-free LKF to estimate the attitude from the estimated gravitational acceleration, ${}^{G}\hat{g}$. However, these magnetometer-free LKFs limit the tracking to attitude only. Thus, other works [85], [197], [198] proposed two separate LKFs, or dual filtering, for estimating gravitational acceleration and geomagnetic field to compute the 3D orientation while eliminating the errors in yaw estimation from those of attitude estimation. For instance, Zhu and Zhou [67] and Zhu et al. [199] used an

LKF to estimate the gravitational acceleration, ${}^{G}\hat{g}$, and geomagnetic filed, ${}^{G}\hat{m}$, by propagating the state vector using y_G in time-update step and then comparing the state vector with y_A and y_M during measurement-update. Batista et al. [200], [201] extended the previous LKF structure by including b_G in the state vector and correcting the y_G accordingly during the time-update step.

Jurman et al. [202] constructed an adaptive LKF with Euler angles in its state vector. In this LKF, the state vector was propagated in time using strap-down integration and the Euler angles calculated from y_A (using Equation 11 for attitude) and y_M (using $\tan^{-1}(y_{M,y}/y_{M,x})$ for yaw) were used as the measurements. Sun et al. [203] included a with a first-order Markov process model in the state vector of their proposed LKF and used the modified acceleration (${}^{G}g$ + estimated a) in Equation 10 to build the measurement-update equation. In another approach, instead of an explicit modeling of a, Makni et al. [204], [205] proposed an adaptive LKF where the part of $\mathcal{R}$ associated with the accelerometer was estimated adaptively in real-time based on the LKFs accelerometer residual. Also, the proposed LKF was structured with energy consumption considerations in mind such that the gyroscope was turned off and re-activated alternately while the $\mathcal{Q}$ was adaptively tuned to compensate for the errors. Also, Rehbinder and Hu [206] proposed an SFA by switching between two LKFs similar to the high gain observer previously proposed by the same authors in [207], i.e., one for tracking under low accelerations and one for high accelerations.

2.3.6.3 Extended Kalman Filters (EKF)

Lefferts et al. [208] investigated the effect of constructing an EKF with different variations of quaternions as the state vector and concluded that including all elements of the quaternions and b_G could lead to singularity in calculating $\mathcal{Q}$. Koifman and Merhav [209] proposed the application of an EKF for real-time attitude estimation using y_G and y_M, investigated the effect of piecewise constant modeling of b_G on estimation error, and then devised a method for updating the corresponding elements of the covariance matrix when required. Vaganay and Aldon [210] proposed an EKF in which the state vector included roll and pitch angles as well as their drift rates, while the strap-down integration was performed out of EKF and as a part of the measurement update.

Marins et al. [90] and Yun and Bachmann [68], [211] investigated two approaches for EKF design using different measurement vectors: (1) using IMU readouts as the measurement; and (2) using the orientation (in quaternion) obtained by applying GNA or QUEST to y_A and y_M. They showed that in the former, the measurement-update equations were highly nonlinear functions of the state vector while in the latter, linear equations could be used to relate measurements to the state vector, which made the EKF suitable for real-time applications due to lower computational complexity. Also, Mazza et al. [212] introduced a similar magnetometer-free EKF but included b_G in the state vector. Sabatini [106] and Zhang et al. [213] included the accelerometer and magnetometer bias terms in the state vector of their proposed EKF and used their estimated values to correct the projection of ${}^{G}g$ and ${}^{G}m$ in IMU sensor frame during calculation of the predicted measurements.

Also, Sabatini [214] developed a similar EKF by substituting the bias terms in the previous EKF by b_G and d. Later, Sabatini [215] extended this work by introducing a variable-state-dimension EKF. This EKF switched between an EKF where a first-order Markov process was used to model d and a higher-order EKF where a second-order Markov process modeled the time rate of change of the magnetic field. This approach could make the propagation of state vector and calculation of the predicted measurements more realistic, particularly for long-duration tracking under magnetic disturbances. Following the same concept, Xu et al. [216] used a decision tree-based switching technique to develop an EKF capable of changing its measurement model between three modes (high y_G, high y_A, moderate y_A) to achieve robust tracking performance under different conditions.

2.3.6.4 Complementary Kalman Filters (CKF)

While it is common to use the KF structure to estimate the primary states directly, some works proposed the CKF structure, also known as the error-state KF [217], [218], to estimate the errors in the primary states [45], [219]. By defining the state vector as an error process, the *a priori* estimate of the state vector is always zero, and thus, the state transition, $\mathcal{F}$ or $f(\cdot)$, is zero, which simplifies the standard KF formulation. For instance, Foxlin [220], Setoodeh et al. [221], and Gebre-egziabher et al. [222] proposed CKFs by estimating the errors in gyroscope bias and Euler angles to correct y_G and the strap-down integration output before and after the strap-down integration, respectively. Gebre-egziabher et al. [222] also used the quaternion errors to develop a

similar CKF and showed that the quaternion parametrization has advantages such as more efficient gain tuning process and computations as compared to Euler angle parametrization. To achieve more robust estimates for indoor orientation tracking, Zhang and Reindl [223] added a magnetic disturbance rejection step to the CKF by Foxlin [220].

Roumeliotis et al. [217] introduced a smoothing filter, comprised of two CKFs, where the first CKF propagated the attitude estimate forward and then updated it via the absolute orientation obtained from the accelerometer and sun sensor, while the second CKF propagated the most recent estimate back in time to lower the uncertainty of the estimation. To estimate the errors in the attitude of a mobile robot moving on uneven terrains using y_A and the strap-down integration, Fuke and Krotkov [224] proposed the application of a CKF. Luinge and Veltink [109] developed an accelerometer-based CKF to estimate the error in gravitational acceleration and accelerometer offset by deriving the relationship between y_A and the state vector as well as calculating the angular velocity based on the direction of the y_A at each two successive time instants. Luinge and Veltink [114] also used both accelerometer and gyroscope to estimate the orientation error and gyroscope bias using the CKF structure. Later, the magnetometer was included in the CKF to prevent drift in the yaw angle, even under magnetic disturbances [107].

Hall et al. [225] proposed a CKF where y_G was used to propagate the error in orientation while y_A and GPS were used to perform the measurement-update. However, as the accelerometer and GPS had different sampling rates and reference frames, the proposed CKF took advantage of the incremental update concept [226], where the measurement update could be performed independently for each sensor. Kang et al. [227] developed a CKF to fuse a gyroscope and a vision system where a fading factor, tuned using fuzzy logic, has been applied to the Kalman gain, $\mathcal{K}$, to tune the tracking performance of the filter in response to the quality of the vision system data. Kannan [228] proposed a linear CKF where the compensation of the drift in the estimated orientation was performed via the time-update equation (using the orientation obtained by TRIAD from y_A and y_G) instead of the measurement-update equation. This approach resulted in a substantial improvement of the response and settling times of the proposed CKF.

Table 3 Review of the state-of-the-art SFAs with a Kalman Filter (KF) structure, including linear KF (LKF), extended KF (EKF), and Complimentary KF (CKF). Abbreviations used in the table are described in the table footnotes.

Study	Year	Application	Method	State vector components	Measurement-update	Notes (gain tuning or thresholding, etc.)
[208]	1982	STC	EKF	[Q, b_G]	[Line-of-sight attitude sensor]	-
[209]	1991	SVTC	EKF	[Velocity, ω, EA, altitude, wind gust velocity]	[y_G, y_M, airspeed sensor, barometric altimeter]	-
[210]	1994	MRTC	EKF	[Attitude]	[y_A, gyrometric attitude]	-
[189]	1995	MRTC	LKF	[Yaw]	[y_G]	-
[220]	1996	HMT	CKF	[eEA, eb_G]	[y_G, y_M]	$\mathcal{Q} \propto \max(y_G)$ $\mathcal{R} \propto$ slosh in fluid acc.
[224]	1996	MRTC	CKF	[eAttitude]	[y_A]	-
[217]	1999	MRTC	CKF	[eEA, eb_G]	[y_A, sun sensor]	-
[90]	2001	-	EKF	[Q, $\hat{\omega}$]	[y_G, y_A, y_M]	-
[90]	2001	-	GNA+EKF	[Q, $\hat{\omega}$]	[$\hat{q}$, y_G], $\hat{q}$ from GNA(y_A,y_M)	-
[47]	2002	SVTC	LKF	[GPS position, GPS receiver's clock range bias, b_G, b_A]	[Position, velocity, clock] errors from the algebraic GPS equations	-
[190]	2003	-	GNA+LKF	[Q, $\hat{\omega}$]	[$\hat{q}$, y_G], $\hat{q}$ from GNA(y_A,y_M)	-
[196]	2004	-	LKF	[Q, $\hat{\omega}$, b_G]	[y_G, y_A]	-
[67]	2004	HMT	LKF	[$\hat{g}$, $\hat{m}$]	[y_A, y_M]	-
[206]	2004	Walking robot motion tracking	Ensemble of two LKFs	[DCM(3)]	[y_A]	Switching between LKFs by $\lvert y_A \rvert$
[94]	2004	-	LKF	[Q, b_G]	[y_A] or [y_M]	Adaptive $\mathcal{Q}$
[109]	2004	HMT	CKF	[$e\hat{g}$, eb_A]	[y_A]	-
[229]	2004	-	LKF	[1D angle, ω]	[1D-y_G]	-
[221]	2004	-	CKF	[eEA, eb_G]	[EA from y_A & y_M]	-
[222]	2004	SVTC	CKF	[eEA, eb_G] OR [eQ, eb_G]	[EA from y_A & y_M]	Switching $\mathcal{Q}$ & $\mathcal{R}$ between two levels
[114]	2005	HMT	CKF	[eHelical angle/axis, eb_G]	[Attitude from y_A & y_G]	-
[45]	2005	-	CKF	[eQ, eb_G]	[Sun sensor]	-
[107]	2005	HMT	CKF	[eHelical angle/axis, eb_G, ed]	[Attitude from y_A & y_G, magnetic vector from y_M & y_G]	-

Study	Year	Application	Method	State vector components	Measurement-update	Notes (gain tuning or thresholding, etc.)
[106]	2006	HMT	EKF	[Q, b_A, b_M]	[y_A, y_M]	Switching $\mathcal{R}$ between two levels
[68]	2006	HMT	QUEST+EKF	[Q, $\hat{\omega}$]	[$\hat{q}$, y_G], $\hat{q}$ from QUEST(y_A,y_M)	-
[230]	2006	-	EKF	[Attitude, $\hat{\omega}$]	[$y_{A,x}$, $y_{A,y}$, y_G]	Adaptive acc. measurement equation
[199]	2007	-	LKF	[$\hat{g}$, $\hat{m}$]	[y_A, y_M]	Abandoning past estimations by forgetting factor
[202]	2007	-	LKF	EA	[EA from y_A & y_M]	Switching $\mathcal{R}$ between two levels
[218]	2007	-	CKF	[eQ, eb_G]	[y_A, y_M]	-
[225]	2008	AVTC	CKF	[eQ]	[$e\hat{q}$ from y_A & GPS]	Tuning $\mathcal{R}$ based on $\|y_A - {}^G g\|$
[231]	2008	SVTC	CKF	[eQ, eb_G]	[y_A, y_M]	-
[232]	2008	HMT	EKF	[eEA, b_G, b_A, d]	[y_A, y_M]	a & d rejection using vector selection + tuning $\mathcal{Q}$ & $\mathcal{R}$
[233]	2009	Surgical tool motion tracking	EKF	[Q, b_G]	[y_A, y_M]	-
[86]	2009	HMT	LKF	[Q]	[$\hat{q}$ from y_A & y_M using [193]]	a & d rejection using vector selection
[48]	2009	Augmented Reality	-	[EA, $\hat{\omega}$, $\dot{\hat{\omega}}$, b_G]	[$\hat{q}$, y_G], $\hat{q}$ from y_A & y_M	-
[234]	2009	HMT	EKF	[Velocity, $\hat{y}_A$, $\hat{\omega}$, b_G, Attitude]	[y_G, y_A]	-
[200]	2009	-	LKF	[$\hat{g}$, $\hat{m}$, b_G]	[y_A, y_M]	-
[110]	2010	-	CKF	[eQ, b_G, b_A]	[y_A, y_M]	Tuning $\mathcal{R}$ using residual in acc. measurement-update
[235]	2010	HMT	EKF+Particle Filter	[EA, b_G]	[EA from y_A & y_M]	-
[236]	2010	HMT	CKF	[eQ]	[y_A, y_M]	Tuning $\mathcal{R}$ based on $\|y_A - {}^G g\|$ & $\|y_M - {}^G m\|$
[237]	2011	-	CKF	[eEA, $e$velocity, eb_G, eb_A]	Velocity from GPS	$\mathcal{K}$ tuning by innovation-based adaptive estimation technique
[194]	2011	-	LKF	[Q]	[$\hat{q}$ from FQA(y_A,y_M)]	-
[203]	2011	HMT	LKF	[Q, a]	[y_M, y_A, $\|y_A\|$]	Switching $\mathcal{Q}$ between two levels
[238]	2011	HMT	EKF	[Q, b_G]	[y_A, y_M]	-
[239]	2011	HMT	CKF	[eEA, $e$position, $e$velocity, eb_G, b_A]	[Yaw from y_M, eb_G, Velocity from ZUPT]	Heuristic heading reduction [240]

Study	Year	Application	Method	State vector components	Measurement-update	Notes (gain tuning or thresholding, etc.)
[214]	2011	HMT	EKF	[Q, b_G, d]	[y_A, y_M]	-
[241]	2011	-	EKF	[Q]	[y_A]	-
[242]	2011	-	CKF	[eQ, eb_G, eK_G]	[eEA from y_A & y_M]	-
[243]	2011	-	EKF	[Q, b_G]	[y_A, y_M]	Tuning $\mathcal{R}$ based on $\left\|y_A - {}^{G}g\right\|$
[244]	2011	-	EKF	[DCM(1), DCM(3), b_G]	[y_A, y_M]	-
[245]	2011	HMT	CKF	[eEA, eb_G]	[y_M]	Quasi-static geomagnetic field detection
[246]	2012	Surgical tool motion tracking	Two LKFs + EKF	LKF1: [$\hat{g}$], LKF2: [$\hat{m}$], EKF: [Q, b_G]	LKF1: [y_A], LKF2: [y_M], EKF: [$\hat{q}$ from y_A & y_M]	-
[201]	2012	-	LKF	[$\hat{g}$, $\hat{m}$, b_G]	[y_A, y_M]	-
[212]	2012	HMT	EKF	[Q, b_G]	[$\hat{q}$ from y_A & y_M]	Switching $\mathcal{R}$ a piecewise linear function
[247]	2012	HMT/ SVTC	LKF	[$\hat{g}$]	[y_A]	-
[248]	2012	AVTC	EKF	[DCM(3), $\hat{\omega}$, b_G]	[y_A, y_G]	Switching $\mathcal{R}$ between two levels
[249]	2012	HMT	LKF	[Q]	[$\hat{q}$ from y_A & y_M]	a & d rejection using vector selection
[215]	2012	-	Variable state EKF	EKF1: [Q, b_G, d] EKF2: [Q, b_G, d, $\dot{d}$]	[y_A, y_G]	-
[250]	2013	-	CKF	[eEA, eb_G, K_G]	[eEA from y_A & y_M]	Switching $\mathcal{R}$ between three levels
[251]	2013	-	EKF	EKF 1: [DCM(3), a] EKF 2: [DCM(1), d]	EKF1: [y_A], EKF2: [y_M]	Resetting a and d by thresholding
[252]	2013	SVTC	CKF	[$e$position, $e$velocity, eEA, b_G, b_A]	[Position, velocity] from GNSS	-
[213]	2013	HMT	EKF	[Q, b_A, b_M]	[y_A, y_M]	Switching $\mathcal{R}$ between two levels
[253]	2013	-	EKF	[Q]	[y_A, y_M]	-
[204]	2014	-	LKF	[Q]	[y_A, y_M]	Tuning $\mathcal{R}$ based on acc. residuals
[254]	2014	HMT	Two-layer LKF	EKF1: [$\hat{g}$], EKF2: [Yaw]	EKF1: [y_A], EKF2: [y_M]	Innovation-based adaptive estimation tuning of $\mathcal{R}$ using fuzzy logic
[93]	2014	HMT with smartphones	EKF	[Q, b_G, a]	[y_A, y_M]	-
[255]	2014	AVTC	EKF	[Q, $\hat{\omega}$, b_G]	[$\hat{q}$ from y_A & y_M]	-
[256]	2014	HMT	Two-layer LKF	EKF1: [DCM(3)], EKF2: [DCM(1)]	EKF1: [y_A], EKF2: [y_M]	Switching $\mathcal{R}$ between two levels

Study	Year	Application	Method	State vector components	Measurement-update	Notes (gain tuning or thresholding, etc.)
[257]	2014	AVTC	CKF	[eEA, eb_G, ea, ed]	[y_A, y_M]	$\mathcal{P}_A \propto Error(a)$, $\mathcal{P}_M \propto Error(d)$
[258]	2015	Marine Satellite Tracking Antenna	LKF	[Q]	[y_A, y_M]	$\mathcal{Q} = \alpha\mathcal{Q}_0$, $\mathcal{R} = (1-\alpha)\mathcal{R}_0$
[104]	2015	HMT	LKF	[$\hat{g}$, a]	[y_A]	-
[85]	2015	HMT	LKF+LKF	LKF1: [$\hat{g}$, a], LKF2: [$\hat{m}$, d]	LKF1: [y_A], LKF2: [y_M]	-
[259]	2015	AVTC	GDA+LKF	[Q]	[y_A]	GDA step size $\propto y_G T_s$
[260]	2015	HMT	EKF	[Q]	[y_A]	Switching $\mathcal{R}$ between three levels
[261]	2015	HMT	LKF	[eYaw, eK_G, b_G]	[Yaw from y_M]	-
[228]	2015	HMT	LKF	[eEA, eb_G]	-	-
[53]	2015	-	Constrained-LKF	[$\hat{\omega}$, DCM, a, d]	[y_G, y_A, y_M]	-
[54]	2015	-	Constrained-EKF	[DCM(3), $b_{G,k}$]	[y_A]	Tuning $\mathcal{R}$ based on $\|y_A\|$
[205]	2016	-	LKF	[Q]	[y_A, y_M]	Tuning $\mathcal{R}$ based on accelerometer residuals
[262]	2016	AVTC	CF-EKF	[$e$position, $e$velocity, eEA, eb_G, eb_A, ed]	[Position, velocity] from GNSS	-
[129]	2016	-	LKF	[Q]	[Position, velocity] from GNSS	-
[263]	2016	HMT/ SVTC	Two-layer LKF	EKF 1: [$\hat{g}$], EKF 2: [$\hat{m}$]	EKF1: [y_A], EKF2: [y_M]	Switching $\mathcal{R}$ between three levels
[227]	2016	HMT	CKF	[eEA, eb_G]	[EA from vision system]	Adaptive fading factor by fuzzy logic
[264]	2016	HMT	LKF	[EA, b_G]	[Attitude from y_A]	$\mathcal{R} = \mathcal{R}_{nominal} + \|a\|^2$
[265]	2016	HMT	CKF	[eEA, eb_G]	[y_A, y_M]	Tuning $\mathcal{R}$ using Hidden Markov Model
[216]	2017	AVTC	EKF	[Q]	[y_A]	-
[266]	2017	SVTC	CKF	[EA, b_G]	[y_A, velocity from GPS]	-
[267]	2017	AVTC	EKF	[Q, b_G]	[y_A, y_M]	-
[195]	2017	AVTC	LKF	[Q]	[$\hat{q}$ from y_A & y_M]	-
[80]	2017	SVTC	LKF	[Q]	[$\hat{q}$ from y_A & y_M]	d rejection using vector selection
[198]	2017	-	Two-layer LKF	LKF1: [$\hat{g}$], LKF2: [$\hat{m}$]	LKF1: [y_A], LKF2: [y_M]	$\mathcal{R}_1 \propto \|a\|^2$, $\mathcal{R}_2 \propto \|d\|^2$

Study	Year	Application	Method	State vector components	Measurement-update	Notes (gain tuning or thresholding, etc.)
[268]	2017	-	EKF	[Q, $\hat{\omega}$]	[y_A, y_G]	-
[269]	2017	Marine satellite tracking antennas	CKF	[eQ, eb_G]	[y_A, y_M]	-
[270]	2017	Wearable robotic systems	EKF	[$\hat{\omega}$, $\dot{\omega}$, Q, $\dot{\mathrm{Q}}$, $\ddot{\mathrm{Q}}$, d, $\dot{d}$]	[y_G, y_A, y_M]	-
[191]	2018	HMT with smartphones	GDA+LKF	[Q]	[$\hat{q}$], $\hat{q}$ from GDA(y_A,y_M)	-
[271]	2018	-	CKF	[eEA, eb_G]	[y_A, y_G]	Tuning $\mathcal{R}$ using Hidden Markov Model
[126]	2018	-	LKF	[Q]	[$\hat{q}$ from y_A & y_M]	-
[192]	2018	-	GDA+LKF	[Q]	[$\hat{q}$], $\hat{q}$ from GDA(y_A,y_M)	$\mathcal{R} = \mathcal{R}_{nominal} + \alpha_k$ d rejection using vector selection
[272]	2018	HMT	Two-layer CKF	CKF1: [eAttitude], CKF2: [eYaw]	CKF1: [$e\hat{q}$ from y_A], CKF2: [$e\hat{q}$ from y_M]	Tuning $\mathcal{R}$ by variances of errors
[273]	2018	SVTC	EKF	[Position, velocity, Q, b_G, b_A]	[Position from GPS, $\hat{q}$ from y_A]	-
[274]	2018	SVTC	Two-step LKF	[Q, b_G]	Step1: [y_A, $y_{G,z}$], Step2: [y_M]	$\mathcal{R}_A \propto \exp(\left\|y_A - {}^{G}g\right\|^2)$ $\mathcal{R}_M \propto \exp(\left\|y_M - {}^{G}m\right\|^2)$
[197]	2019	-	LKF+LKF	LKF1: [$\hat{g}$], LKF2: [$\hat{m}$]	LKF1: [y_A], LKF2: [y_M]	-
[275]	2019	HMT	CKF	[eEA, b_G, d]	[y_A, y_M]	
[276]	2019	SVTC	CKF	[eEA, $e$velocity, $e$position]	[Velocity, Position] from GPS	Combined Sage-Husa [277] and Strong Tracking [278] KFs
[279]	2019	HMT	EKF	[Q]	[y_A, y_M]	$\mathcal{Q} \propto cosnt + \max(\|\omega\| - thr, 0)$ $\mathcal{R}_A \propto cosnt + \max(\left\|\|y_A\| - \|{}^{G}g\|\right\| - thr, 0)$ $\mathcal{R}_M \propto cosnt + \max(\left\|\|y_M\| - \|{}^{G}m\|\right\| - thr, 0)$
[280]	2020	HMT	EKF	[EA]	[EA] obtained by NCF	Innovation-based adaptive estimation tuning of $\mathcal{R}$
[281]	2020	MRTC	EKF	[Q, b_G]	[$\hat{q}$], $\hat{q}$ from TRIAD(y_A,y_M)	Tuning $\mathcal{R}$ by fuzzy logic
[282]	2020	HMT	LKF	[Q]	[y_A]	-
[283]	2020	HMT	Cascade LKF	LKF1: [DCM(3)], LKF2: [b_G]	LKF1: [y_A], LKF2: [y_A]	$\mathcal{R}_A \propto \|a\|^2 + \left\|y_A - {}^{G}g\right\|^2$

Study	Year	Application	Method	State vector components	Measurement-update	Notes (gain tuning or thresholding, etc.)
[284]	2020	HMT	GDA+EKF	[Q, b_G]	[$\hat{q}$], $\hat{q}$ from GDA(y_A,y_M)	GDA step size $\propto \|y_G\|, error(y_A, y_M)$
[285]	2020	SVTC	EKF	[Q]	[y_A, y_M]	Post-EKF error reduction by the proportional-integral controller
[286]	2020	AVTC	EKF	[Position, velocity, Q, b_G, b_A, LiDAR bias]	[Position, velocity, y_A]	-
[287]	2020	RATC	CKF	[eEA, eb_G]	[y_A, y_M]	Adaptive tuning of $\mathcal{R}$ using ellipsoidal method

- **Application:** STC: Spacecraft (satellite) tracking/control; HMT: Human motion tracking; MRTC: Mobile robot tracking/control; RATC: Robotic arm tracking/control; AVTC: Aerial vehicle tracking/control; SVTC: Surface vehicle tracking/control; GNSS: Global Navigation Satellite System.
- **Method:** GNA: Gauss-Newton algorithm; GDA: Gradient descent algorithm; FQA: Factored quaternion algorithm, QUEST: QUaternion ESTimator; TRIAD: TRi-axial Attitude Determination; ZUPT: Zero-Velocity-Update strategy.
- **State vector components:** Q: Quaternion parametrization of orientation; EA: Euler angle parametrization of orientation; DCM: Direction cosine matrix parametrization of orientation.
- **Measurement-update:** b_G: Gyroscope bias; b_A: Accelerometer bias; b_M: Magnetometer bias; a: external non-gravitational acceleration; d: magnetic disturbance; $\hat{q}$: Orientation used in measurement-update of KF; $\hat{\omega}$: Estimated angular velocity; $\hat{g}$: Estimated gravitational acceleration; $\hat{m}$: Estimated geomagnetic field.
- **Notes:** $\mathcal{Q}$: System model covariance matrix; $\mathcal{R}$: Measurement model covariance matrix; $\mathcal{P}$: State error covariance matrix; $\mathcal{K}$: Kalman filter gain.

2.3.6.5 Modified Kalman Filters

Ren and Kazanzides [233], [246] proposed a two-layer filtering scheme such that two LKFs in the first layer were designed to estimate ${}^{G}\hat{g}$ and ${}^{G}\hat{m}$ from y_A and y_M, respectively, and an EKF in the second layer was used to correct the predicted orientation by strap-down integration using the orientation calculated by vector observations from the first layer. Music et al. [235] introduced a two-layer filter where in the first layer, a standard EKF estimated orientation using strap-down integration and direct Euler angle calculation from y_A and y_M, while the estimated orientation in the second layer (calculated using a Particle Filter) was used to present extra information to EKF and improve the overall performance. Sabatelli et al. [253] developed a two-layer filter where the first and second layers used y_A and y_M, respectively, to correct the propagated orientation by the strap-down integration. Also, Dang and Nguyen [251] proposed a two-layer filter where in the first layer, an EKF estimated the third column of direction cosine matrix (associated with attitude) and a while in the second layer, an EKF with similar structure estimated the first column of direction cosine matrix (associated with yaw angle) and d. Such structures have the benefit of eliminating the effect of magnetic disturbance from the attitude estimations.

2.3.6.6 Adaptive gain tuning of Kalman Filters

KF performance highly relies on an accurate definition of the system and measurement models, as well as noise covariance matrices (commonly, $\mathcal{Q}$ and $\mathcal{R}$ are defined before the estimation starts and remain fixed during the tracking process). However, in reality, $\mathcal{Q}$ and $\mathcal{R}$ could change over time due to the time-varying nature of the errors, such as orientation tracking during slow (quasi-static) and fast motions. Therefore, adaptive KFs have been proposed to respond to the changes in the nature of the error by tuning $\mathcal{Q}$ and $\mathcal{R}$ in real-time [288].

For example, in the covariance scaling technique, $\mathcal{Q}$ or $\mathcal{R}$ are scaled by the factor $\mathcal{S}_k > 1$ to put more weight on the *a priori* state vector x^-, or measurements, respectively [289]. $\mathcal{S}_k$ can be tuned using the magnitude of y_A, y_G, and/or y_M at some predefined levels [106], [212], or the magnitude of the predicted residuals [289]. For example, Suh [110] and Suh et al. [230] customized the application of the covariance scaling technique for a CKF and EKF, respectively, such that instead of applying a small $\mathcal{S}_k$ to all elements of $\mathcal{Q}$ or $\mathcal{R}$ to guard against a (and rely more on y_G), first, the direction of the a was estimated, and small weights were supplied only for the affected axes. Sun et al. [236] included an adaptive scheme in their standard CKF to weight $\mathcal{R}$ based on the

error between magnitude and direction of y_A (y_M) with its reference value recorded during static (magnetically undisturbed) condition. Later, this method was extended by Johnson and Sathyan [290] to include b_G estimation. Tong et al. [271] proposed the application of a hidden Markov Model recognizer to identify the measurement disturbances and adjust $\mathcal{R}$ of their proposed CKF adaptively. Also, Jamil et al. [291] used an Artificial Neural Network to eliminate the errors in y_A and y_G by adjusting $\mathcal{R}$.

In the innovation adaptive estimation technique, the innovation sequence, that is, the difference between the real measurement and its predicted value by the KF, is used in an algorithm known as the covariance matching to tune the value of $\mathcal{Q}$, $\mathcal{R}$, or $\mathcal{K}$ such that the actual value of the innovation sequence covariance matrix matches its theoretical value [237], [292]. Finally, in the multiple-model adaptive estimation technique, a bank of KFs (each using a different $\mathcal{Q}$ or $\mathcal{R}$) runs in parallel to calculate the *a posteriori* state estimate x^+ based on the weighted combination of the predicted state by each KF (KF weights could be obtained based on the probability density function of the innovation sequence covariance matrix) [293].

2.3.7 Lessons learned

Numerous works proved the efficiency of SFAs in compensating the limitations associated with the strap-down integration or vector observation algorithms for orientation tracking with IMUs. In this section, we listed the lessons learned during the literature survey. The general flowchart of an SFA in Figure 5 includes features that could improve the accuracy and robustness of the orientation estimation.

2.3.7.1 Gyroscope and Strap-down Integration

strap-down integration of y_G is the core of almost all CFs and KFs. Therefore, the accuracy of the propagated orientation in time via strap-down integration is vital to the accuracy and robustness of any SFA, especially when aiding sensors' recordings, i.e., y_A and y_M, are not reliable, such as tracking under high dynamics or magnetically disturbed environments. To improve the accuracy of strap-down integration, the following must be considered:

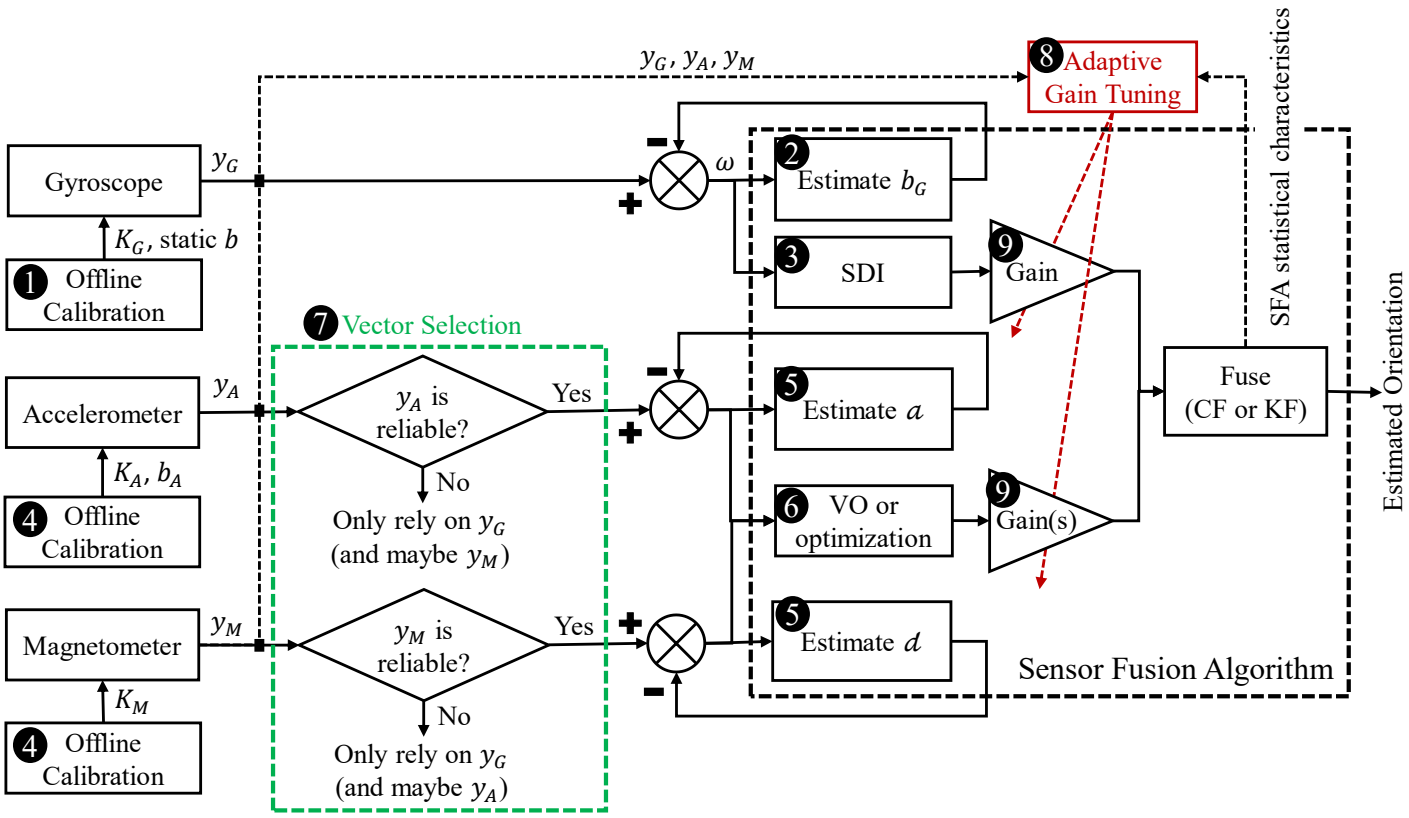

Figure 5 Flowchart of a general SFA containing offline calibration of sensors, vector selection for imperfect measurement rejection, and adaptive gain tuning. Block 1 and 4 show the offline calibration of the gyroscope, accelerometer, and magnetometer; block 2 shows the online estimation of the gyroscope bias; block 3 shows strap-down integration (SDI); block 5 shows the online estimation of the external non-gravitational acceleration and magnetic disturbance; block 6 shows the orientation estimation with accelerometer and magnetometer; blocks 7 and 8 show the adaptive gain tuning of the SFA; and block 9 shows the fusion gains.

1. Use a gyroscope with low bias.
2. Correct the gyroscope's static bias and scale factor (block 1 in Figure 5). For the static bias, before any data acquisition, the IMU must be turned on and put at rest for a while (commonly specified by the manufacturer, and if not, at least 20 minutes according to [82]). This will ensure that the gyroscope has reached ambient temperature, and the estimated static bias will not change significantly due to temperature change. Then, y_G must be measured when the IMU is at rest to obtain an estimate of the static bias. Finally, the estimated static bias must be removed from y_G recorded during data acquisition.
3. Use stochastic models [107], [214] or heuristics [81] to estimate the time-varying b_G in real-time (block 2 in Figure 5). A first-order Markov process, as in (1b), can be used for this purpose. According to the principle of pseudo-noise injection, estimating b_G can

improve the accuracy and robustness of the orientation tracking, even for short trials where b_G does not have time to change drastically [104].

4. Use an accurate estimation of $\exp(\cdot)$ for the strap-down integration in Equation 7 (block 3 in Figure 5). For example, using a first-order Taylor series showed inaccurate results under low sampling frequencies [112].

2.3.7.2 Accelerometer and magnetometer

During long-duration trials, the use of an accelerometer and magnetometer are crucial to an SFA, as they can correct the cumulative error of the strap-down integration. Thus, consider the following for these aiding sensors:

1. Evaluate the calibration of these sensors (blocks 4 in Figure 5). Various procedures have been introduced in the literature to verify and possibly re-calibrate accelerometers [66], [108], [294] and magnetometers [295]. These procedures use *ad hoc* tests to estimate the scale factors K_A and K_M (in Equation 3 and Equation 5), as well as the bias terms of these sensors, which can be later used to correct y_A and y_M.
2. Use online stochastic models, e.g., first-order Markov processes as in Equation 4 and Equation 6, to estimate a and d, respectively, and correct y_A and y_M (blocks 5 in Figure 5). This correction is effective for motions with high dynamics or in magnetically disturbed environments [104], [106], [107].

2.3.7.3 Dealing with magnetic disturbance

Magnetic disturbance can significantly affect the yaw angle estimation, which in turn may affect the attitude estimation. Thus, consider the following when formulating an SFA:

1. Decouple the attitude estimation from y_M or yaw angle (block 6 in Figure 5). For example, use TRIAD, instead of QUEST, as the vector observation algorithm in CF or KF, or use two-layer filters as in [134], [158], [198], [263], [274].
2. Use vector selection to detect and reject imperfect measurements (block 7 in Figure 5). When the geomagnetic field is disturbed, the field strength and dip angle change significantly. Therefore, magnetic disturbance can be identified by applying thresholds to the field strength and/or dip angle. In such cases, the propagated orientation by strap-down integration can be declared as the estimated orientation without any correction, see [78] for

more details. A similar approach can be applied to y_A to reduce the effect of non-gravitational acceleration.

2.3.7.4 Adaptive gain tuning

Gain tuning plays a significant role in the performance of any SFA; if gains are selected improperly, the SFA could even diverge. Therefore, consider the following regarding SFA gains:

1. Use an online gain turning strategy to adaptively put more weight on the most reliable source of information (block 8 in Figure 5). For instance, to reduce the effect of correction via the magnetometer and rely more on the gyroscope, when the magnetic disturbance is detected using a vector selection, the CF gain or KF measurement covariance matrix should be adjusted accordingly.
2. Decouple the gains associated with the gyroscope, accelerometer, and magnetometer (blocks 9 in Figure 5). Generally, developing a KF with a different gain for each sensor is easy. However, in most well-recognized CFs, such as [64], [65], the same gain is used to weight accelerometer and magnetometer. In such cases, both sensors will be declared reliable or unreliable at the same time, while one can be more reliable than the other one.
3. Select the filter gains rigorously. Although filter gains found by trial-and-error might result in acceptable estimations under certain working conditions, the filter performance will not be guaranteed for other situations. Therefore, filter gains must be evaluated under various motion patterns, intensities, and durations.

2.3.7.5 Beyond EKF

Violation of the assumptions that were used to formulate a filter can degrade its performance. Thus, consider the following two extensions for KFs:

1. When execution time is not a consideration, use unscented KF instead of EKF. As EKF uses linearization to propagate the mean and covariance of the state vector, its performance can deteriorate for highly nonlinear systems.
2. Use robust filtering techniques when adaptive gain tuning is not possible. For example, the H_∞ filter formulates an estimation strategy that bounds the worst-case estimation error by adaptively weighting the state error covariance matrix [188]. Also, the H_∞ filter assumes

that the process and measurement noises are energy bounded signals, and drops the Gaussian distribution assumption for noises in formulating the standard KF.

2.4 Conclusions

A survey of the literature showed that IMUs could track the orientation of the body segments using SFAs. Also, we concluded that for an SFA to be effective, the embedded sensors must be calibrated (offline), error sources of the embedded sensors must be estimated and removed from the sensors' readouts (online), and the gains of the SFA must be tuned adaptively. Moreover, we identified the need for benchmarking studies as the main gap in the literature.

Thus, to ensure that the estimated orientation has high accuracy and robustness under various motion patterns and intensities, Chapter 4 introduces a general framework for adaptive gain regulation of SFAs. Also, to ensure high accuracy for long-duration tasks, Chapter 5 presents two new SFAs that estimate the error sources of the sensors embedded in an IMU and correct the IMU readouts before being used for orientation estimation. Chapter 5 also contains a comprehensive benchmarking study to identify the most effective fusing strategy.

Nevertheless, the estimated orientation with SFAs describes the IMU sensor frame orientation with respect to a global reference frame. Thus, before delving into orientation estimation with IMUs, Chapter 3 introduces two procedures for sensor-to-segment calibration. Using these procedures, we can track the orientation of the body segments (i.e., anatomical frames of the segments) using IMUs.

Chapter 3

Sensor-to-Segment Calibration

This chapter provides two methods for sensor-to-segment calibration, enabling us to transform IMU data from its sensor frame to the anatomical frame of the body. Portions of this chapter have been adopted and/or edited from:

M. Nazarahari, H. Rouhani, "Semi-automatic sensor-to-body calibration of inertial sensors on lower limb using gait recording," IEEE Sensors Journal, Vol. 19(24), pp. 12465 - 12474, 2019.

M. Nazarahari, A. Noamani, N. Ahmadian, H. Rouhani, "Sensor-to-body calibration procedure for clinical motion analysis of lower limb using magnetic and inertial measurement units," Journal of Biomechanics, Vol. 85, pp. 224-229, 2019.

3.1 Introduction

IMUs have been extensively used as an ideal tool for ambulatory human motion analysis because of their lightweight, small size, and long battery life [39], [57], [296], [297]. Also, the accuracy and reliability of IMUs have been validated in various biomedical applications against gold-standard in-lab MCSs [298]. However, Anwary et al. showed that proper selection of attachment site/orientation of the IMU would affect the inter-participant repeatability of the gait assessment. Therefore, an effective methodology is required for virtual re-orientation of the IMU to obtain accurate and repeatable results, particularly for IMU applications in the free-living environment when an inexperienced user attaches the IMU over body segments. Also, IMUs measure the body

acceleration and angular velocity in their frame of reference instead of the anatomical frame (AF) of body segments, as recommended by the International Society of Biomechanics (ISB) [299]. Thus, to obtain clinically meaningful joint angles, the sensor frame (SF) of the IMU must be transformed into the AF of its corresponding segment through a calibration procedure.

Information provided by the IMU during a specific functional task, e.g., single-axis rotation of a segment (e.g., knee flexion) or static posture (e.g., quiet standing), can be used for sensor-to-segment calibration. For example, Palermo et al. presented a calibration approach based on two predefined static postures to align IMUs attached to the lower limb with their corresponding AFs [300]. Favre et al. proposed passive flexion/extension (FE) and abduction/adduction (AA) of the knee for shank IMU calibration [301]. Then, they calibrated the thigh IMU such that the anatomical knee joint angle was equal to zero during the standing posture. "Outwalk" procedure proposed a comprehensive protocol for IMU attachment, AF definition, and a multi-step calibration [302]. Seel et al. proposed an optimization-based approach to calibrate thigh and shank IMUs based on arbitrary motions of the leg [303]. Recently, estimation of IMUs' orientations during a T-pose or N-pose was suggested to align IMU frames with the "known" orientation of each segment in that posture [304], [305].

The main limitations of the above-mentioned sensor-to-segment calibration procedures could be summarized as follows: (1) an experienced operator was required to perform specific, usually demanding, procedures [300], [302]; (2) an IMU was calibrated based on another IMU readout [303]; (3) IMU orientation had to be estimated, which could be error-prone, especially when a magnetometer was used [304]–[306]; or (4) an ad hoc tool was required [307]. Therefore, the mentioned procedures limit the ambulatory measurement capabilities of the IMUs for human motion analysis in a free-living environment.

Considering the limitations of the previously introduced calibration procedures, the first objective of this chapter was to develop and validate an accurate and repeatable calibration procedure for IMUs attached to the pelvis, hip, knee, and foot. Then, we aimed to investigate whether it is at all necessary to perform an *extra*, *calibration-specific*, *functional movement* for sensor-to-segment calibration of the IMUs attached to the thigh, shank, and foot, or whether it is sufficient to use the data collected during the main gait analysis trials for sensor-to-segment calibration. In particular, this chapter aimed at filling the gap between developed technologies for

human lower limb motion analysis using IMUs and clinical gait analysis in the free-living environment by introducing simple yet effective sensor-to-segment calibration procedures.

For this purpose, we hypothesized that if the IMUs were aligned with their corresponding AFs, hip FE or walking along a straight line could replicate a single-axis rotation in the sagittal plane for the thigh, shank, and foot IMUs. This hypothesis was based on (1) the definition of AFs according to the ISB recommendation [16]; and (2) the thigh, shank, and foot motion pattern during straight walking. Thus, the proposed calibration procedures included (1) hip FE or AA; or (2) straight walking for eight steps together with three to five seconds of quiet standing. Also, to assess the effect of the number of steps on calibration accuracy and repeatability, straight walking for five steps was also considered. The accuracy and repeatability of the proposed calibration procedures were evaluated in an experimental study with ten able-bodied participants to validate the mentioned hypothesis. Also, the results were compared with the literature. Finally, the effect of the proposed calibration procedures on clinical joint angle measurement was evaluated during over-ground walking.

3.2 Measurement Setup

Three IMUs (MTws, Xsens Technologies, The Netherlands) were attached to rigid plastic plates equipped with four retro-reflective markers (Figure 6(a)). Each IMU included a tri-axial accelerometer (range: ±16g) and a tri-axial gyroscope (range: ±2000 degrees/s). The plates were fixed over the thigh, shank, and foot segments using medical tape. IMUs recorded data with a sampling frequency of 100 Hz synchronously and transferred wirelessly to a computer. After data collection and before performing the calibration, the axes of the sensor frames of all three IMUs were rotated to match the coordinate system shown in Figure 6(a). Also, a MCS (VICON, Oxford Metrics Group, UK) with eight cameras was used as the reference system to record the 3D position of the plate markers and 11 markers attached on anatomical landmarks of the thigh, shank and foot segments (according to [308]), synchronized with IMUs. The MCS was used for validation of the purposed calibration only.

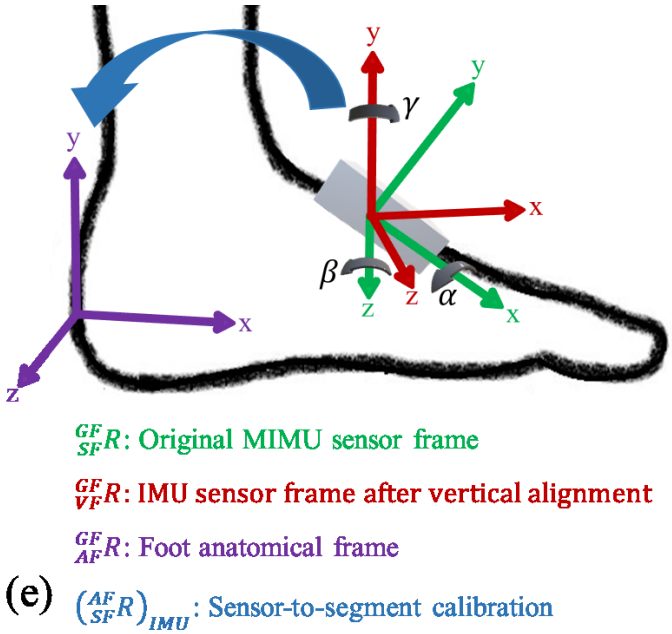

Figure 6 (a) and (b) The measurement system, including IMUs, plates, and retro-reflective markers on anatomical landmarks of sacrum, thigh, shank, and foot, (c) hip flexion/extension, (d) hip abduction/adduction, and (e) IMU sensor frame and foot AF.

3.3 Sensor-to-Segment Calibration

The AFs, which were obtained using anatomical landmarks [308] along with the joint coordinate system defined in [309], were utilized to measure clinically meaningful 3D rotations of lower limb joints, as recommended by the ISB [299]: (1) knee: flexion/extension (K_{FE}), abduction/adduction (K_{AA}), and internal/external rotation (K_{IE}); and (2) ankle: dorsi/plantar flexion (A_{DP}), inversion/eversion (A_{IV}), and internal/external rotation (A_{IE}).

In general, an IMU's sensor frame, SF, (shown in green in Figure 6(e)) must be aligned with the AF of its corresponding segment (shown in purple in Figure 6(e)) using a calibration procedure to measure clinically meaningful kinematics: ${}^{GF}_{SF}R$ and ${}^{GF}_{AF}R$ represent the rotation matrices of SF and AF with respect to the global frame of the laboratory (GF). To align SF with AF, this chapter presents the following calibration procedures: (1) quiet standing for three to five seconds followed by twenty hip FE or AA as seen in Figure 6(c) and (d); and (2) quiet standing for three to five seconds followed by eight steps of level walking (with arbitrarily selected speed) on a straight line. Then, *Vertical Calibration* followed by *Heading Calibration* is required to obtain the rotation matrix of the sensor-to-body calibration $({}^{AF}_{SF}R)_{IMU}$ using IMUs' readouts (Figure 6(e)). *Vertical* and *Heading Calibration* procedures are described below [23].

I) We defined *Vertical Calibration* as finding the required transformation $({}^{VF}_{SF}R)$ for aligning IMU's vertical axis with the gravitational acceleration during the quiet standing period (Figure 6(e)). ${}^{VF}_{SF}R$ was composed of rotations around the x-axis and z-axis of the original IMU SF (shown with α and β in Figure 6(e), respectively) and was obtained by Equation 14:

$$
\begin{aligned}
&y_{VF} = \left(y_{A,x}, y_{A,y}, y_{A,z}\right) \rightarrow y_{VF} = y_{VF}/\|y_{VF}\| \\
&z_{VF} = [1\ 0\ 0]^T \times y_{VF} \rightarrow z_{VF} = z_{VF}/\|z_{VF}\| \\
&x_{VF} = y_{VF} \times z_{VF} \rightarrow x_{VF} = x_{VF}/\|x_{VF}\| \\
&{}^{VF}_{SF}R = [x_{VF}\ y_{VF}\ z_{VF}]
\end{aligned}
\qquad \text{Equation 14}
$$

where $\left(y_{A,x}, y_{A,y}, y_{A,z}\right)$ was the mean value of the accelerometer readouts during the quiet standing period. ${}^{VF}_{SF}R$ was an orthogonal matrix that aligned the y-axis of the IMU with the gravitational acceleration, assuming that the x-axis of the IMU lies in the sagittal plane of the body during the quiet standing period [310], [311]. The possible errors caused by assuming an x-axis in the sagittal plane of the body during *Vertical Calibration* will be canceled out by *Heading Calibration* automatically. Also, it should be noted that Equation 14 was similar to other static orientation estimation methods which use accelerometer readouts. However, in contrast to similar methods which calculate the Euler angles required for ${}^{VF}_{SF}R$ (shown with α and β in Figure 6(e)), Equation 14 was formulated to calculate the rotation matrix required for *Vertical Calibration* directly and eliminate the extra step of converting Euler angles to the rotation matrix. Next, *Heading Calibration* must be performed.

II) We defined *Heading Calibration* as finding a single-axis rotation (${}^{AF}_{VF}R$) around the y-axis (shown with γ in Figure 6(e)) to align the x-axis and z-axis of the vertically aligned IMU frame (${}^{GF}_{VF}R$) with the sagittal and frontal planes of the AF, respectively. We hypothesized that if each IMU was aligned with its corresponding AF, hip FE or walking along a straight line could replicate a single-axis rotation (around z-axis) for the thigh, shank, and foot IMUs. Thus, the angular velocity recorded by each IMU during repetitive hip FE or straight walking in its x-z plane was used to determine the optimal single-axis rotation around the y-axis, which aligns the x-axis and z-axis of the IMU with the sagittal and frontal planes of the AF, respectively. For this purpose, Principal Component Analysis [33] was used to determine the single-axis rotation around the y-axis, which maximized the variations of angular velocity around the z-axis during repetitive hip FE or straight walking as in Equation 15:

$$\gamma = \tan^{-1}\left(\frac{C(2,1)}{C(1,1)}\right)$$

$${}^{AF}_{VF}R = \begin{bmatrix} \cos\gamma & 0 & \sin\gamma \\ 0 & 1 & 0 \\ -\sin\gamma & 0 & \cos\gamma \end{bmatrix} \qquad \text{Equation 15}$$

where C is the Principal Component coefficient matrix, γ is the single-axis rotation around the y-axis (Figure 6(e)), and ${}^{AF}_{VF}R$ is the *Heading Calibration* matrix. The Principal Component coefficient matrix can be obtained with the "pca" function in MATLAB. Since the gyroscope readouts were not used to estimate the IMU orientation, gyroscope drift will not affect the proposed calibration [312]. Then, the final calibration matrix (${({}^{AF}_{SF}R)}_{IMU}$) was calculated by Equation 16 [23]:

$${({}^{AF}_{SF}R)}_{IMU} = {}^{AF}_{VF}R \cdot {}^{VF}_{SF}R \qquad \text{Equation 16}$$

Finally, the orientation of the AF obtained from IMU was determined by Equation 17:

$${({}^{GF}_{AF}R)}_{IMU} = {({}^{GF}_{SF}R)}_{IMU} \cdot {({}^{AF}_{SF}R)}^{T}_{IMU} \qquad \text{Equation 17}$$

3.4 Experimental Study

The accuracy and repeatability of the proposed calibration procedures were evaluated through an experimental study with ten able-bodied participants (all male, 24±3 years old, 75±6 kg, 178±5 cm). The Research Ethics Board Committee of the University of Alberta approved the study

protocol, and written consent was obtained from all participants. During the experimental study, participants performed the following movements twice (two repetitions): straight walking for five steps, straight walking for eight steps, active hip FE (20 times), passive knee FE (performed by study coordinator), passive knee AA (performed by study coordinator), quiet standing for five seconds, and quiet sitting for five seconds. Knee FE/AA and quiet standing/quiet sitting data were used to compare the proposed calibration procedures with the literature [300], [301] when applied to the AF definitions identical to those in the present study. To avoid any bias in the walking pattern of the participants, they were not informed that their movement would be used for calibration. At the end of the session, participants walked in an oval-shaped path for 40 seconds. The above procedure was recorded as the *Test* session. Then the sensors were removed and attached again to the body, and the same procedure was repeated as the *Retest* session.

3.5 Data Analysis

3.5.1 Performance Evaluation of the Calibration Using MCS

A plate frame (PF) was constructed based on the three markers of each rigid plate. Then the orientations of the three plates ($({}^{GF}_{PF}R)_{MCS}$) were recorded at each time instant by the MCS. The misalignment between the IMU's SF and the plate frame (${}^{PF}_{SF}R$) for each body segment was estimated according to [313]. To this end, the misalignment between the normal vector to the plate (using plate markers and MCS) and the gravitational acceleration (using accelerometer) were calculated when the plate was placed over a level surface horizontally and vertically. Then the rotation matrix (${}^{PF}_{SF}R$) which would correct this misalignment was computed. Additionally, the true orientation of the AF of each segment $({}^{GF}_{AF}R)_{MCS}$ was determined based on markers on anatomical landmarks according to [308]. Therefore, a reference for the calibration matrix ($({}^{AF}_{SF}R)_{MCS}$) was obtained using the MCS to transform each IMU's SF to its corresponding AF during the quiet standing period as in Equation 18:

$$({}^{AF}_{SF}R)_{MCS} = ({}^{GF}_{AF}R)^{T}_{MCS} \cdot ({}^{GF}_{PF}R)_{MCS} \cdot {}^{PF}_{SF}R \qquad \text{Equation 18}$$

Then the difference between the estimated calibration matrix ($({}^{AF}_{SF}R)_{IMU}$) obtained from IMU readouts and the reference ($({}^{AF}_{SF}R)_{MCS}$) obtained using the MCS was quantified as a helical angle [23] as in Equation 19:

$$\theta = \cos^{-1}\left(\frac{\text{trace}\left(\left({}^{AF}_{SF}R\right)^{T}_{MCS} \cdot \left({}^{AF}_{SF}R\right)_{IMU}\right) - 1}{2}\right) \qquad \text{Equation 19}$$

The smaller the θ, the closer $\left({}^{AF}_{SF}R\right)_{IMU}$ and $\left({}^{AF}_{SF}R\right)_{MCS}$. Note that the above approach provides a fair assessment of calibration accuracy and repeatability by isolating the calibration errors from other sources of error, such as IMU orientation estimation, as discussed in [23].

3.5.2 Test/Retest Repeatability

θ was calculated for each repetition during *Test* and *Retest* sessions for hip FE and AA, and straight walking for five-step (PC5) and eight-step (PC8) cases to assess the *Test/ Retest* repeatability. Then the obtained θ was compared between the two repetitions of each session and between the *Test* and *Retest* sessions.

3.5.3 Effect of Quiet Standing Duration on Vertical Calibration

To assess the effect of quiet standing duration on the repeatability of *Vertical Calibration*, the helical angle associated with the *Vertical Calibration* rotation matrix ${}^{VF}_{SF}R$ (see Equation 14) was calculated for different durations of quiet standing (1, 2, 3, and 4 seconds) for foot IMU of all participants and compared via statistical test.

3.5.4 Effect of the Number of Repetitions/Steps and Performance Comparison with the Literature

Participants were asked to perform hip FE (or AA) 20 times continuously. Then, Principal Component Analysis was applied to every k (k = 1, ⋯, 20) consecutive motions starting from the first motion. The mean and standard deviation values of θ associated with each k consecutive motion were calculated to evaluate the effect of the number of repetitions of active hip FE (or AA) on the accuracy and repeatability of functional calibration. Also, participants were asked to walk for (1) five steps (PC5); and (2) eight steps (PC8) to investigate the effect of the number of steps on calibration accuracy and repeatability. Statistical analysis (see Section 3.5.6) was employed to compare the accuracy and repeatability of the proposed calibration procedures with the literature [300], [301].

3.5.5 Effect of the Calibration on 3D Joint Angle Measurement

The orientations of the thigh, shank and foot AFs were obtained based on both IMU and MCS recordings during 40 seconds of walking. Then knee and ankle clinical joint angles were obtained using both systems. To isolate the error in 3D joint angle estimation due to the calibration from other sources of error, such as errors of the algorithm that estimate orientation using IMU readouts [64], [212], [314], we used orientation estimations based on the plate frames ($({}^{GF}_{PF}R)_{MCS}$) measured by the MCS instead of using IMU readouts to determine the orientation of IMUs as in Equation 20:

$$({}^{GF}_{SF}R)_{MCS} = ({}^{GF}_{PF}R)_{MCS} \cdot {}^{PF}_{SF}R \qquad \text{Equation 20}$$

where $({}^{GF}_{SF}R)_{MCS}$ is the orientation of an IMU obtained from the plate frame measured by the MCS. To this end, the plate frame orientation was transformed into the IMU orientation by applying the previously calculated misalignment between the plate and IMU frames. To calculate $({}^{GF}_{PF}R)_{MCS}$, the direction of the vectors connecting three plate markers was calculated in the MCS reference coordinate system. The vector cross product of these vectors was calculated at each time instant to obtain the orientation of the plate frame ($({}^{GF}_{PF}R)_{MCS}$). Finally, the orientation of each AF was obtained by the proposed calibration as in Equation 21:

$$({}^{GF}_{AF}R)_{IMU} = ({}^{GF}_{SF}R)_{MCS} \cdot ({}^{AF}_{SF}R)^{T}_{IMU} \qquad \text{Equation 21}$$

where $({}^{AF}_{SF}R)_{IMU}$ is the calibration matrix calculated by Equation 16 using IMU readouts. To assess the accuracy of the proposed calibration on 3D lower limb joint angle measurement, these angles were calculated based on the following: (1) IMU SFs when no calibration was applied ($({}^{GF}_{SF}R)_{MCS}$ according to Equation 20); (2) IMU SFs when the proposed calibration was applied ($({}^{GF}_{AF}R)_{IMU}$ according to Equation 21); and (3) AFs constructed by anatomical landmark markers ($({}^{GF}_{AF}R)_{MCS}$) (served as reference angles).

The error between the reference and estimated (with/without calibration) joint angles was calculated during walking trials for the knee (K_{FE}, K_{AA}, K_{IE}), and ankle (A_{DP}, A_{IV}, A_{IE}) joints. Then the offset error (mean value of the error during quiet standing) and root-mean-square of the error time-series (RMSE) were calculated for each joint as in Equation 22:

$$RMSE = \sqrt{\frac{1}{T-1}\sum_{i=1}^{T}\left(J_{MCS,i} - J_{IMU,i} - \mu\right)^2} \qquad \text{Equation 22}$$

where T is the duration of the trial, J_{MCS} and J_{IMU} are the reference and estimated joint angles time-series, respectively, and μ is the offset between J_{MCS} and J_{IMU}. Also, the reference and the estimated range of motions were determined for each joint [314]. Finally, statistical analysis (see Section 3.5.6) was performed on the offset error, RMSE, and range-of-motion values to assess the effectiveness of the calibration for clinical gait analysis [23].

3.5.6 Statistical Analysis

We compared the accuracy and repeatability of the (1) calibration procedures (based on metric θ) and (2) joint kinematic measurement (based on offset error, RMSE, and range-of-motion). To this end, we used the Jarque-Bera test [315] to verify the normality of the distribution of θ (significance level = 5%). Jarque-Bera test is a two-sided goodness-of-fit test for evaluating the hypothesis that the test data comes from a normal distribution with an unknown mean and variance. Then, we evaluated the equality of the variance for two data sets with normal distributions using the Bartlett test. Next, based on the tested normality and equality of variance, the following statistical tests were applied to detect significant differences among calibration procedures. Repeatability of the metric θ between *Test/ Retes*t sessions was tested via paired t-test (significance level = 5%). Paired t-test determines whether the mean difference between *Test* and *Retest* sessions is zero. Accuracies of each two calibration procedures were compared together via Wilcoxon signed-rank test (significance level = 5%). Inter-participant repeatability of the calibration procedures (variance of the obtained metric θ among all participants) was compared via a two-sample F-test.

3.6 Results

Calibration using hip FE tended to be more accurate (smaller mean value of θ) and repeatable (smaller standard deviation of θ) than hip AA for both thigh and shank IMUs (Figure 7). That is, by increasing the number of repetitions, a decreasing trend can be observed in the mean value and standard deviation of θ for the thigh and shank IMUs. However, a significant difference was not observed.

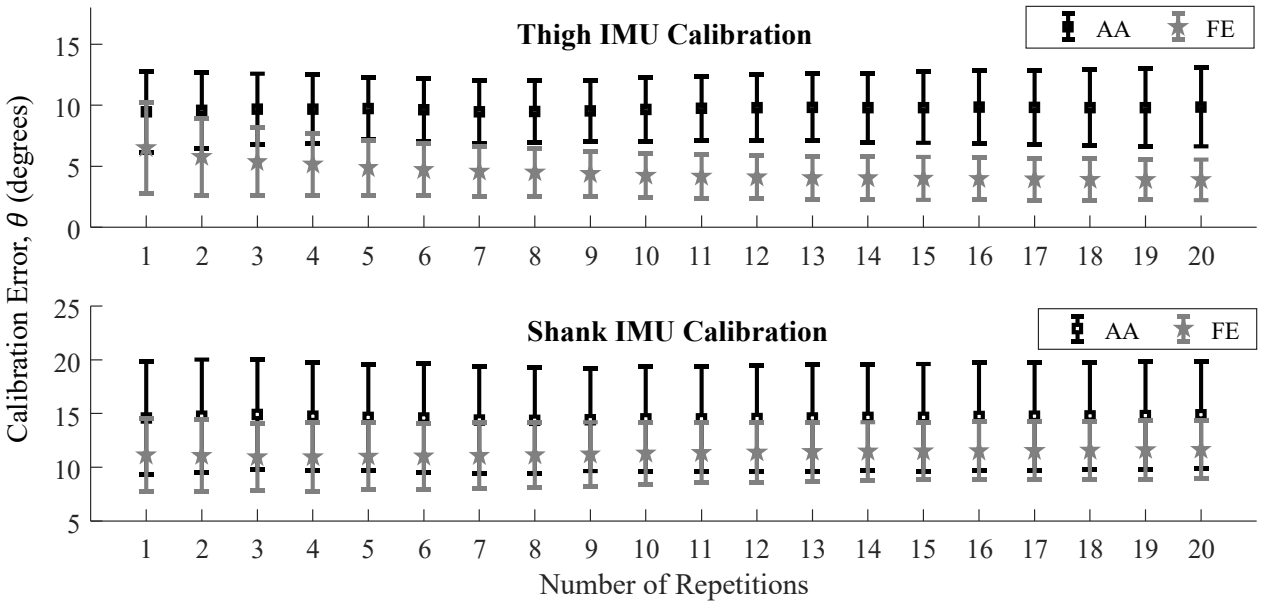

Figure 7 The helical angle (θ) between calibration matrices obtained by the sensor-to-segment calibration and the gold-standard MCS, obtained with a different number of repetitions of hip flexion/extension (FE) and abduction/adduction (AA) for (a) thigh and (b) shank IMUs calibration during the *Test* session. The results are presented as mean and standard deviation among participants.

Figure 8 shows the changes in the pattern of $\theta_{k+1} - \theta_k$ (k is the number of hip FE or AA repetitions, and each curve represents one participant). By increasing the number of repetitions, the dependency of the functional calibration outcome (θ) to the number of repetitions decreases for both thigh and shank IMUs. Specifically, by performing ten or more calibration movements, the change in the metric θ ($\theta_{k+1} - \theta_k$) was less than 0.5 degrees for more than 90% of the participants for both thigh and shank IMUs. Therefore, for calibration of the thigh and shank IMUs, we recommend five seconds of quiet standing followed by at least ten active hip FE.

A paired t-test showed no significant difference among *Vertical Calibration* rotation matrices associated with different durations of quiet standing for the straight walking calibration procedure. Thus, recording of quiet standing for 1 second is enough for the calibration; however, to cancel out the effect of small motions during quiet standing on IMU readouts, we recommend recording an extended period of quiet standing (three to five seconds) to capture the IMUs' readouts in a motionless period.

For hip FE, except for the thigh IMU, no significant difference was observed in metric θ between either two repetitions in a session or between *Test* and *Retest* sessions. For the straight walking procedure, for all IMUs, no significant difference ($p<0.05$) was observed in metric θ neither between the two repetitions in a session nor between *Test* and *Retest* sessions.

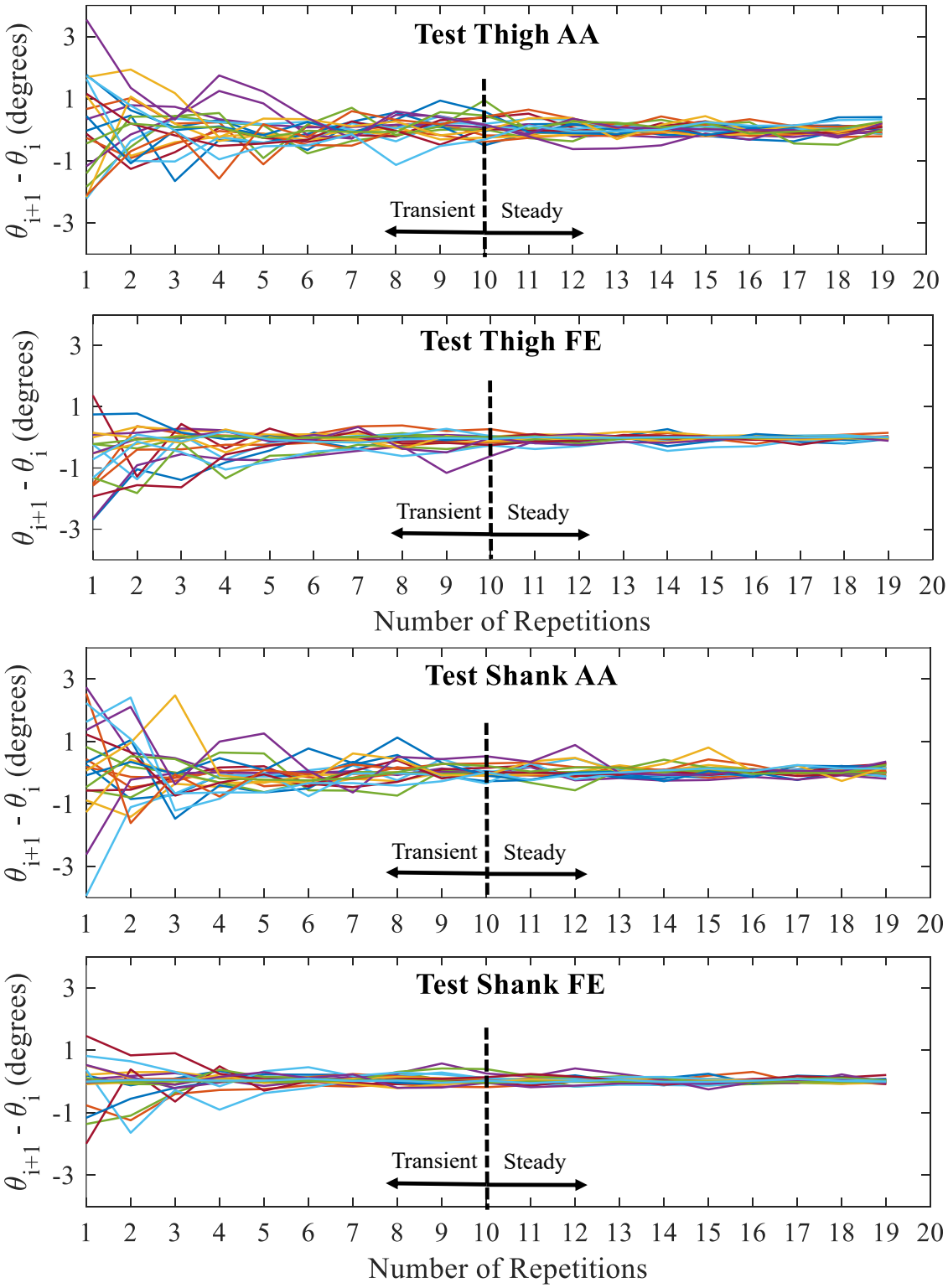

Figure 8 Changes in $\theta_{k+1} - \theta_k$ (θ represents the helical angle between calibration matrices obtained by the sensor-to-segment calibration and the gold-standard MCS) for different number of repetitions of hip flexion/extension (FE) and abduction/adduction (AA) for all participants during the *Test* session. The same pattern was observed for the *Retest* session. Each curve represented the results obtained for one participant.

Comparing straight walking for five and eight steps, Figure 9 shows that similar accuracies were obtained with both PC5 and PC8; medians of the accuracies (PC5, PC8) for the thigh, shank, and foot segments were (5.8, 6.2), (16.3, 16.5), and (12.1, 11.8) degrees, respectively. Thus, it can be concluded that taking three more steps would not improve the calibration accuracy. However, standard deviations of the accuracies (PC5, PC8) for the thigh, shank and foot segments were (9.9, 9.6), (19.3, 17.5), and (5.4, 4.8) degrees, respectively. Therefore, straight walking for eight steps (PC8) showed more reliable results, and thus, it was selected as the proposed calibration movement in this work. According to Figure 9, calibration of thigh IMU resulted in the lowest calibration error, while the highest calibration error (in terms of both median and standard deviation of accuracy) was obtained for shank IMU. This result was expected as the shank IMU SF has the highest misalignment with the shank AF.

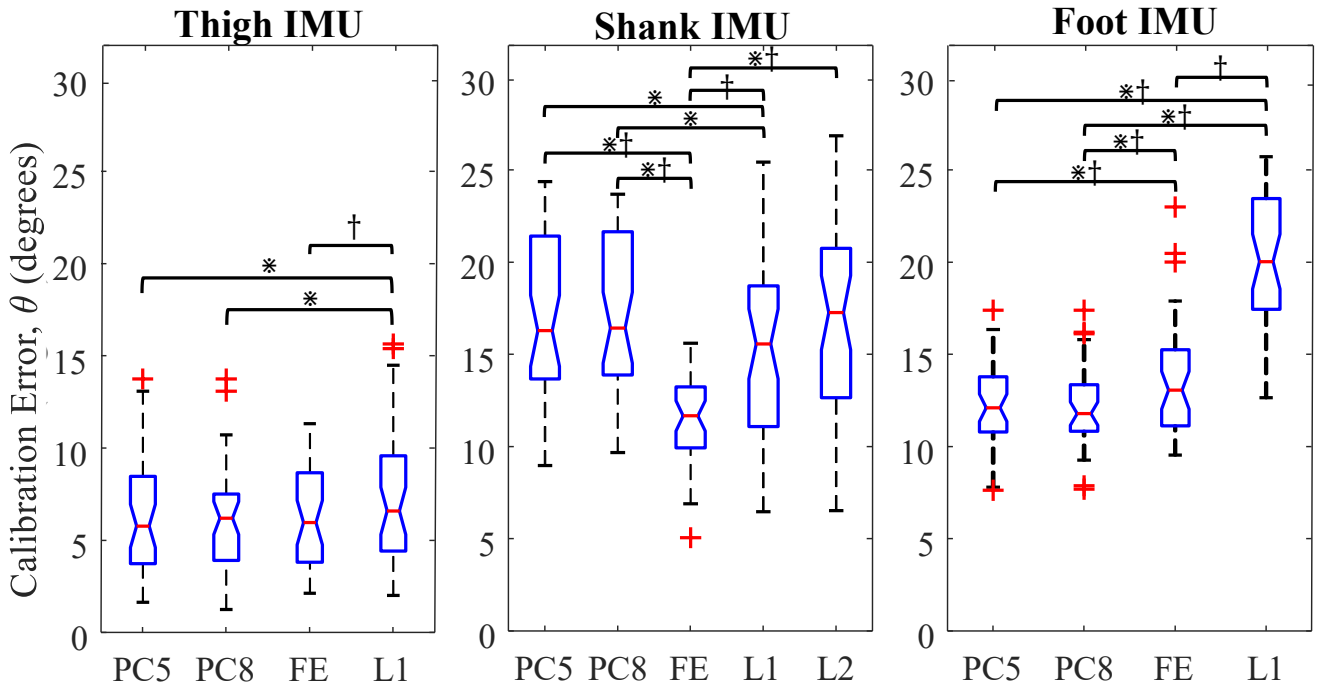

Figure 9 Comparison of the accuracy and inter-participant repeatability of the proposed calibration procedures (indicated by FE, and PC5 and PC8 for five-step (PC5) and eight-step (PC8), respectively) with the calibration procedures proposed in the literature; a combination of standing and sitting postures indicated by L1 [300], and passive knee FE and AA indicated by L2 [301]. The metric θ for thigh, shank, and foot IMUs is presented as box-plot for all participants (the central mark, bottom, and top edges, and + sign show the median, 25th and 75th percentiles, and outliers, respectively). Significant differences ($p<0.05$) between the accuracy and repeatability of two groups of data are shown with ⁎ and †, respectively.

As outlined in Figure 9, while there was no significant difference between PC8 and hip FE accuracy for the thigh IMU, PC8 aligned the thigh IMU significantly more accurately than the

combination of static postures (L1) [300]. Additionally, for thigh IMU, PC8 tended to have lower inter-participant repeatability than hip FE while it tended to have higher inter-participant repeatability than L1 [300]; standard deviations of the calibration accuracy were 9.6, 7.5, and 15.2 degrees for PC8, hip FE, L1 [300], respectively.

For shank IMU, both hip FE and L1 [300] performed significantly more accurate calibration than the PC8; medians of the calibration accuracies were 16.4, 11.7, and 15.6 degrees for PC8, hip FE, L1 [300], respectively. However, PC8 tended to be more repeatable than L1 [300] for the shank IMU; standard deviations of the calibration accuracy were 17.5 and 23 degrees for PC8 and L1 [300], respectively. Also, hip FE obtained significantly higher inter-participant repeatability compared to all other procedures. For the foot IMU, PC8 was significantly more accurate than hip FE and L1 [300]; medians of the calibration accuracies were 11.8, 13.1, and 20 degrees for PC8, hip FE, and L1 [300], respectively. Also, PC8 resulted in the highest inter-participant repeatability for foot IMU compared to hip FE and L1 [300]. Finally, foot IMU, hip FE performed significantly more repeatable than the method in L1 [300].

Although the study coordinator tried to align IMUs visually with body segments, Figure 10(a) shows that PC8 was still needed to reduce the crosstalk among IMU axes during active hip FE (i.e., a single-axis rotation around the z-axis), particularly for shank and foot IMUs. It is worth mentioning that the combination of *Vertical* and *Heading* alignments ensures highly accurate and repeatable calibration even for randomly placed IMUs. Figure 10(b) and Table 4 show that the proposed calibration procedures improved the accuracy and repeatability of the clinical joint angle estimation significantly. Using hip FE, the offset errors of H_{IE}, K_{AA}, K_{IE}, A_{IV}, and A_{IE} were significantly lower ($p<0.05$) than not performing the calibration (Table 4(a)). In addition, Table 4(a) shows that hip FE resulted in more repeatable results for H_{AA}, H_{IE}, K_{IE}, A_{DP}, A_{IV}, and A_{IE}, indicated by the smaller standard deviation (among participants) of the offset error. Moreover, by applying hip FE calibration, K_{AA}, A_{DP}, A_{IV}, and A_{IE} angles were estimated with significantly lower RMSE than not performing the calibration. According to Table 4(b), using PC8, the offset errors for K_{AA}, K_{IE}, A_{IV}, and A_{IE} angles reduced from 8.6, 26.3, 23.3, 21.2 to 4.2, 17.1, 9.1 and 14.8 degrees, respectively. Also, RMSE values significantly reduced for K_{AA}, A_{DP}, A_{IV}, and A_{IE} angles after applying PC8. Furthermore, Table 4(b) shows that PC8 made joint angle estimation significantly more repeatable for K_{AA}, A_{DP}, and A_{IE} angles. Finally, as outlined in Table 4(b), although the range-of-motions of the estimated joint angles with calibration were still significantly

different from the reference ones, they tended to be more repeatable and accurate than those estimated without calibration.

3.7 Discussions

This chapter presented two sensor-to-segment calibration procedures to align IMUs attached to the thigh, shank, and foot segments with their corresponding AFs for IMUs applications in the free-living environment. The proposed procedures consisted of (1) three to five seconds of neutral standing followed by twenty hip FE; or (2) three to five seconds of neutral standing followed by straight walking for eight steps. Acceleration readouts during quiet standing were used for *Vertical Alignment* (aligning the vertical axis of the IMU frame with the gravitational acceleration), while the planar angular velocity of IMUs during hip FE/straight walking was utilized for *Heading Alignment* (aligning the x-axis and z-axis of IMUs with sagittal and frontal planes of the body).

PC8 (calibration using straight walking), unlike the previously suggested ones [300]–[302], [316], [317], did not need any calibration-specific movement or presence of an expert operator or utilizing an ad hoc tool, which limits the out-of-lab capabilities of the IMUs. Indeed, the precision of performing calibration-specific movements such as hip FE, which sometimes require the supervision of an experienced operator, may considerably affect the calibration accuracy and repeatability. Our experimental validation showed that IMU motion during verbally instructed '*straight*' walking could be used as '*single-axis rotation*' for sensor-to-segment calibration without further supervision, at least for able-bodied participants. Therefore, we recommended the PC8 as a reliable procedure for sensor-to-segment calibration in free-living environments. However, the application of a semi-automatic motion such as walking for patients with gait impairment must be further investigated. In particular, for such patients, alternative procedures such as the proposed hip FE or passive knee FE/AA [301] can be utilized.

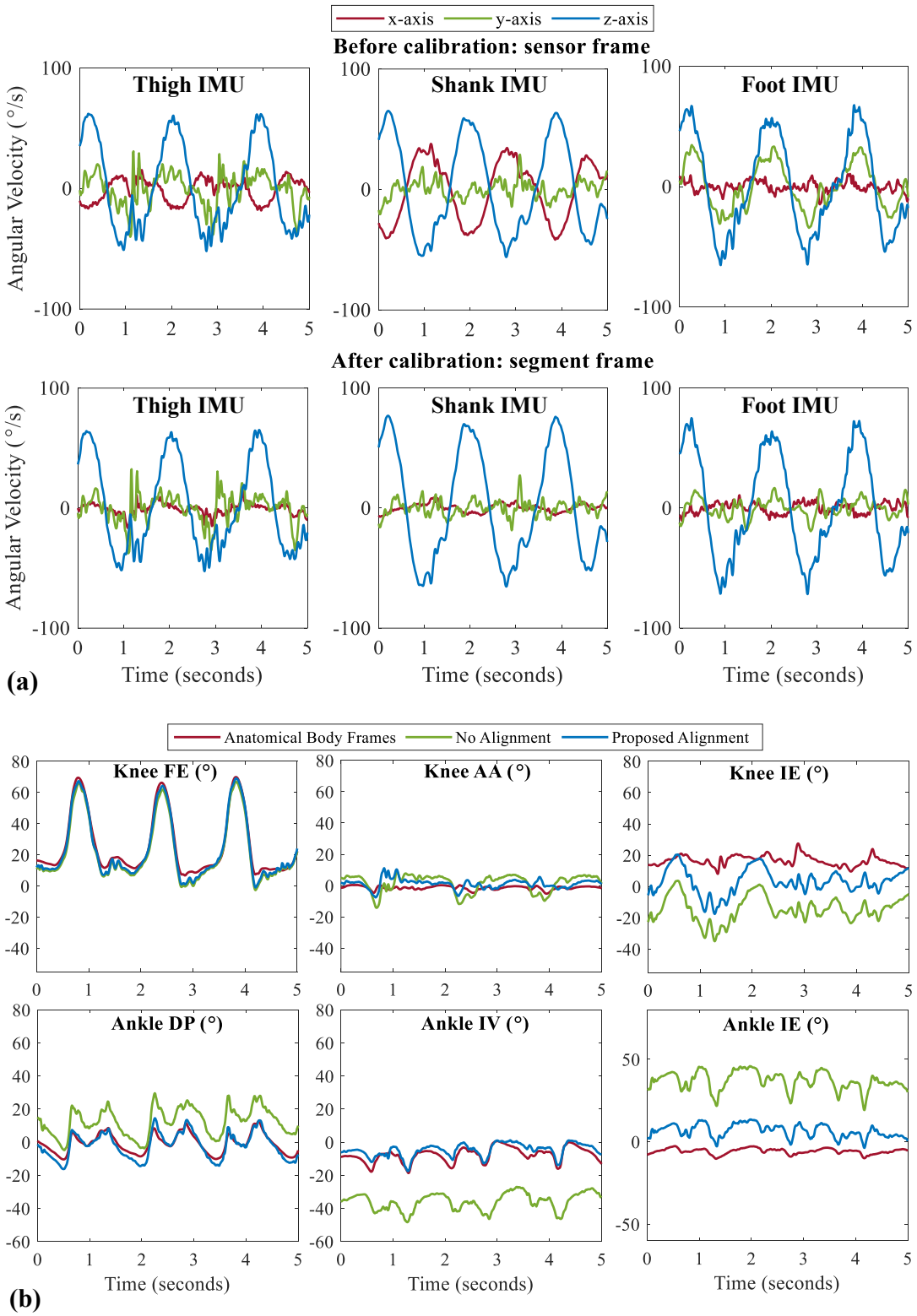

Figure 10 (a) 3D angular velocities of thigh, shank, and foot during active hip FE in IMU (before calibration) and AF (after calibration) frames; (b) 3D estimated (with and without calibration) and reference joint angles of knee and ankle during a representative gait trial. In both figures, straight walking was used for the calibration.

Table 4 Mean (standard deviation) values of the offset and RMSE of the joint angle errors and range-of-motion of the estimated and reference joint angle time-series. The offset error and RMSE values present the difference between the estimated joint angles with calibration ((a) Hip FE and (b) PC8) or without calibration (None), and the reference joint angles obtained based on anatomical frames measured by MCS.

(a) Hip FE versus no calibration

	Offset error		RMSE		Range-of-motion		
	Hip FE	**None**	**Hip FE**	**None**	**Hip FE**	**None**	**Reference**
K_{FE}	4.7 (3.6)	4.5 (2.6)	2.7 (0.8)	2.8 (1.0)	85.0 (5.8)†	85.7 (7.3)†	76.7 (4.5)
K_{AA}	4.2 (2.8)	8.6 (4.0)⋆	3.6 (1.0)	6.1 (1.9)⋆‡	28.0 (5.3)†	33.9 (7.1)†	10.3 (2.5)
K_{IE}	12.8 (9.4)	26.3 (13.9)⋆‡	8.0 (3.3)	8.3 (3.0)	40.4 (7.9)†	45.2 (8.9)†	27.5 (4.5)
A_{DP}	2.8 (1.8)	4.8 (3.3)‡	3.2 (1.0)	5.5 (1.0)⋆	53.3 (13.3)†	60.4 (18.3)†	38.5 (10.1)
A_{IV}	9.4 (3.0)	23.3 (4.9)⋆‡	2.7 (1.1)	5.7 (1.3)⋆	35.7 (5.3)	46.1 (9.9)†	32.0 (6.1)
A_{IE}	8.9 (5.0)	21.2 (9.9)⋆‡	4.7 (2.0)	7.0 (2.7)⋆	24.7 (11.7)†	35.1 (14.7)†	16.6 (7.8)

(b) PC8 versus no calibration

	Offset error		RMSE		Range-of-motion		
	PC8	**None**	**PC8**	**None**	**PC8**	**None**	**Reference**
K_{FE}	3.5 (2.5)	4.5 (2.6)	2.6 (0.8)	2.8 (1.0)	85.1 (5.4)†	85.7 (7.3)†‡	76.7 (4.5)
K_{AA}	4.2 (2.9)	8.6 (4.0)⋆	3.5 (1.0)	6.1 (1.9)⋆‡	30.2 (5.2)†‡	33.9 (7.1)†‡	10.3 (2.5)
K_{IE}	17.1 (9.1)	26.3 (13.9)⋆	8.1 (3.5)	8.3 (3.0)	42.1 (3.8)†	45.2 (8.9)†‡	27.5 (4.5)
A_{DP}	2.7 (1.9)	4.8 (3.3)‡	3.6 (1.0)	5.5 (1.0)⋆	51.1 (13.1)†	60.4 (18.3)†‡	38.5 (10.1)
A_{IV}	9.1 (3.5)	23.3 (4.9)⋆	3.3 (1.4)	5.7 (1.3)⋆	38.4 (7.0)†	46.1 (9.9)†‡	32.0 (6.1)
A_{IE}	14.8 (5.3)	21.2 (9.9)⋆‡	4.7 (1.9)	7.0 (2.7)⋆	26.6 (10.7)†	35.1 (14.7)†‡	16.6 (7.8)

⋆ indicates the procedure with significantly lower accuracy ($p<0.05$)
‡ indicates the procedure with significantly lower repeatability ($p<0.05$)
† indicates the range-of-motion which is significantly different from its corresponding reference range of motion ($p<0.05$)

3.7.1 Repeatability and Accuracy of the Calibration Procedure

The accuracy of the proposed calibration procedures was not affected by the marker and IMU attachments during *Test* and *Retest* sessions, except for the thigh IMU with hip FE. Also, our results showed that performing at least ten consecutive hip FE movements will reduce the dependency of the calibration outcome on the number of repetitions. Moreover, taking eight steps during straight walking (PC8) only improved the repeatability of the calibration and did not affect the calibration accuracy. Also, Figure 9 shows that both hip FE and PC8 had comparable accuracy and inter-participant repeatability with more sophisticated procedures proposed in the literature [300], [301]. In contrast to some previous studies, our proposed procedures calibrated each IMU independently and as such, errors in the calibration of one IMU will not propagate to another one. Finally, it is worth mentioning that the accuracy of calibration depends on the choice of AF

definition. Thus, inter-participant repeatability is a better metric for comparing calibration procedures, as it does not depend on the definition of AFs.

3.7.2 3D Joint Angle Estimation

Although the IMUs were visually aligned with segments during attachment, both hip FE and PC8 significantly reduced the offset error of K_{AA}, K_{IE}, A_{IV}, and A_{IE} angles, and RMSEs of K_{AA}, A_{DP}, A_{IV}, and A_{IE} angles, see Table 4. It should be noted that erroneous identification of AFs can lead to propagation of error in joint kinetics estimation as well [318], [319]. In particular, as the shank IMU was placed over the bony surface of the tibia (significant misalignment with the shank AF), the effect of the calibration was prominent for knee and ankle joint angle estimation, suggesting the necessity of a calibration procedure at least for the shank IMU.

3.7.3 Limitations and Future Works

The accuracy and repeatability of proposed sensor-to-segment calibration procedures were investigated for only ten able-bodied participants and should be further investigated with more participants, specifically for individuals with various movement disorders. Also, considering the planar cyclic motion of the arms during walking, the application of straight walking for sensor-to-segment calibration of IMUs attached to the hand, forearm, and upper arm should be investigated. Finally, considering the current developments in the areas of machine learning [320], [321] and optimization [303], [322][323], [324], as an alternative to analytical procedures such as the presented calibration procedure, a machine-learning-based procedure can be employed to obtain the sensor-to-segment transformation matrix. For this purpose, the orientation of the true AF obtained by the MCS can be used in the training phase.

3.8 Conclusion

We showed that twenty consecutive hip FE movements or eight steps of straight walking, together with three to five seconds of quiet standing, can be used as an effortless yet accurate and repeatable sensor-to-segment calibration to obtain clinically meaningful lower limb joint angles using IMUs. Straight walking is not the most accurate calibration for the shank segment; the medians of the calibration accuracies were 16.4 and 11.7 degrees for straight walking and hip FE. However, the calibration accuracy and repeatability obtained by straight walking are still comparable with most of the suggested calibration-specific movements/postures in the literature. Also, as the functional

movements and the calculations required for obtaining the segment-to-segment transformation are performed before the main trial (where biofeedback is provided), the proposed procedures can be implemented in real-time. Nevertheless, the proposed procedures' ability to achieve more accurate and repeatable transformations must be validated for a clinical population in the future. Having a reliable sensor-to-segment calibration, in Chapter 4, we introduce a general framework for adaptive gain regulation of SFAs to obtain an accurate and robust estimation of IMU sensor frame orientation.

Chapter 4

Adaptive Gain Regulation of SFAs

This chapter provides the details of a general framework for optimal adaptive gain regulation of SFAs for accurate and robust body segment orientation tracking with IMUs. Portions of this chapter have been adopted and/or edited from:

M. Nazarahari, H. Rouhani, "Adaptive Gain Regulation of Sensor Fusion Algorithms for Orientation Estimation with Magnetic and Inertial Measurement Units," IEEE Transactions on Instrumentation and Measurement, Vol. 70, 2020.

4.1 Introduction

Using sensor-to-segment calibration methods discussed in Chapter 3, the readouts of IMUs can be used to obtain the lower limb joint angles in anatomically meaningful frames. However, to calculate joint angles, first, we have to estimate the orientation of the body segments using IMU readouts. To achieve an accurate and robust estimation of the IMU orientation, as discussed in Section 2.3, many studies have introduced SFAs that combine accelerometer, gyroscope, and magnetometer readouts. Nevertheless, the performance of such SFAs depends highly on their gains, and poor initialization or incorrect adjustment of the gains would degrade the SFAs' performance.

Although the statistical properties of the sensors could be used to estimate the gains of some SFAs, due to the complexity of the (1) noise mechanism; and (2) SFA structure, there is not

always a clear one-to-one relationship between statistical properties and SFA gains. Therefore, to obtain the optimal gains of SFAs with various structures, a general framework is needed.

Furthermore, while one set of SFA gains may result in good accuracy for a certain motion, another set of gains may be required for a different condition [325]. To address this issue, previous works have proposed two adaptive gain regulation schemes with a focus on KFs: (1) vector selection technique (VST); and (2) innovation adaptive estimation (IAE).

In VST, the magnitude of the accelerometer, gyroscope, and magnetometer readouts will be used to change the value of the process and/or measurement noise covariance matrices between two predefined levels using a hard-switch [106], [326]. However, to the best of the authors' knowledge, no one has (1) presented a general framework for finding the optimal levels; or (2) assessed the effect of using a hard-switch with more than two levels, or more complex switching schemes on accuracy and robustness of SFAs, specifically CFs.

In IAE, the process or measurement noise covariance matrix evolves with time, based on the statistical information obtained from the innovation sequence (the difference between real and estimated measurements) [327]. Commonly, the IAE approach has been coupled with a fuzzy system to adjust one of the noise covariance matrices [328], [329]. However, the IAE approach is limited to KFs and is only able to adjust the covariance matrix associated with process or measurement noise while the other one is constant. Moreover, all adjustments in the IAE approach are made around the predefined nominal covariance matrix. Thus, there is still a need for a general framework to determine the nominal process and measurement noise covariance matrices.

Therefore, the main contribution of this chapter is the development of a general framework for structuring an optimal gain regulation scheme for any SFA. For this purpose, we optimized the SFA gains toward minimizing the error between the estimated (obtained from an SFA) and true (obtained from an MCS) orientations. We employed Particle Swarm Optimization [330] to solve the optimization problem. In particular, we implemented four adaptive gain regulation schemes: (1) VST1: hard-switch between two levels; (2) VST2: hard-switch between three levels; (3) VST3: a general approximator using a Mamdani fuzzy inference system; and (4) IAE: innovation-based tuning of process noise covariance matrix. The first three schemes have been tested for two KFs and two CFs from the literature, while the last scheme has been evaluated for a KF only.

4.2 Materials and Methods

4.2.1 Sensor Fusion Algorithms

The performance of four different SFAs [64], [65], [88], [107], [195] was evaluated using the optimal fixed value of their gains (hereafter, referred to as fixed optimal gain (FOG)) or adaptive gain regulation schemes, VST1, VST2, VST3, and IAE. The selected SFAs included representatives of both KF and CF families with structures and gains in Figure 11 and Table 5, respectively. The SFA gains in Table 5 are described in the following paragraphs of this section and identified with red symbols in Figure 11. Here, we avoided describing the selected SFAs in detail and refer the interested reader to the original articles. However, we used the same notation as it was used in the original articles. Also, to distinguish these SFAs from one another, we named them as first author(year). It should be noted that not all SFA gains can be tuned intuitively, e.g., the initial error covariance matrix $\mathcal{P}_0$ in KFs. Therefore, in the current work, we applied adaptive gain tuning to the gains that directly control the effect of the accelerometer, gyroscope, and magnetometer on the estimated orientation while using the optimal fixed value for other gains.

In Madgwick(2011) [64], first, the estimated orientation at the previous time step was projected forward in time using strap-down integration of angular velocity (block 1 in Figure 11(a)). Then, a single-iteration gradient-descent algorithm was used to estimate the orientation from accelerometer and magnetometer readouts (block 2 in Figure 11(a)). Finally, the latter estimation, weighted by gain β (block 3 in Figure 11(a)), was used to correct the former estimation and compute the SFA output at the current step. Moreover, the gyroscope drift was estimated at each time step and then weighted by gain ζ to correct the angular velocity before strap-down integration (block 4 in Figure 11(a)). Therefore, gains β and ζ control the performance of the Madgwick(2011), i.e., gain β plays the role of both process and measurement covariance matrices in a KF. However, through several preliminary tests, we concluded that the effect of gain ζ on performance was negligible for the tested IMUs. Therefore, in the present work, we applied the adaptive gain regulation scheme to gain β only, while using an optimal fixed value for gain ζ (Table 5).

The general structure of the Mahony(2008) [65] is similar to Madgwick(2011), as shown in Figure 11(a), except for using a different formulation for calculating the orientation from

accelerometer and magnetometer readouts (block 2 in Figure 11(a)). Mahony(2008) uses two gains: k_p adjusts the weight of the correction via accelerometer and magnetometer, and k_i adjusts the weight of the estimated gyroscope drift [65]. Therefore, similar to Madgwick(2011), we applied the adaptive gain regulation scheme to k_p only, while using the optimal fixed value for gain k_i (Table 5).

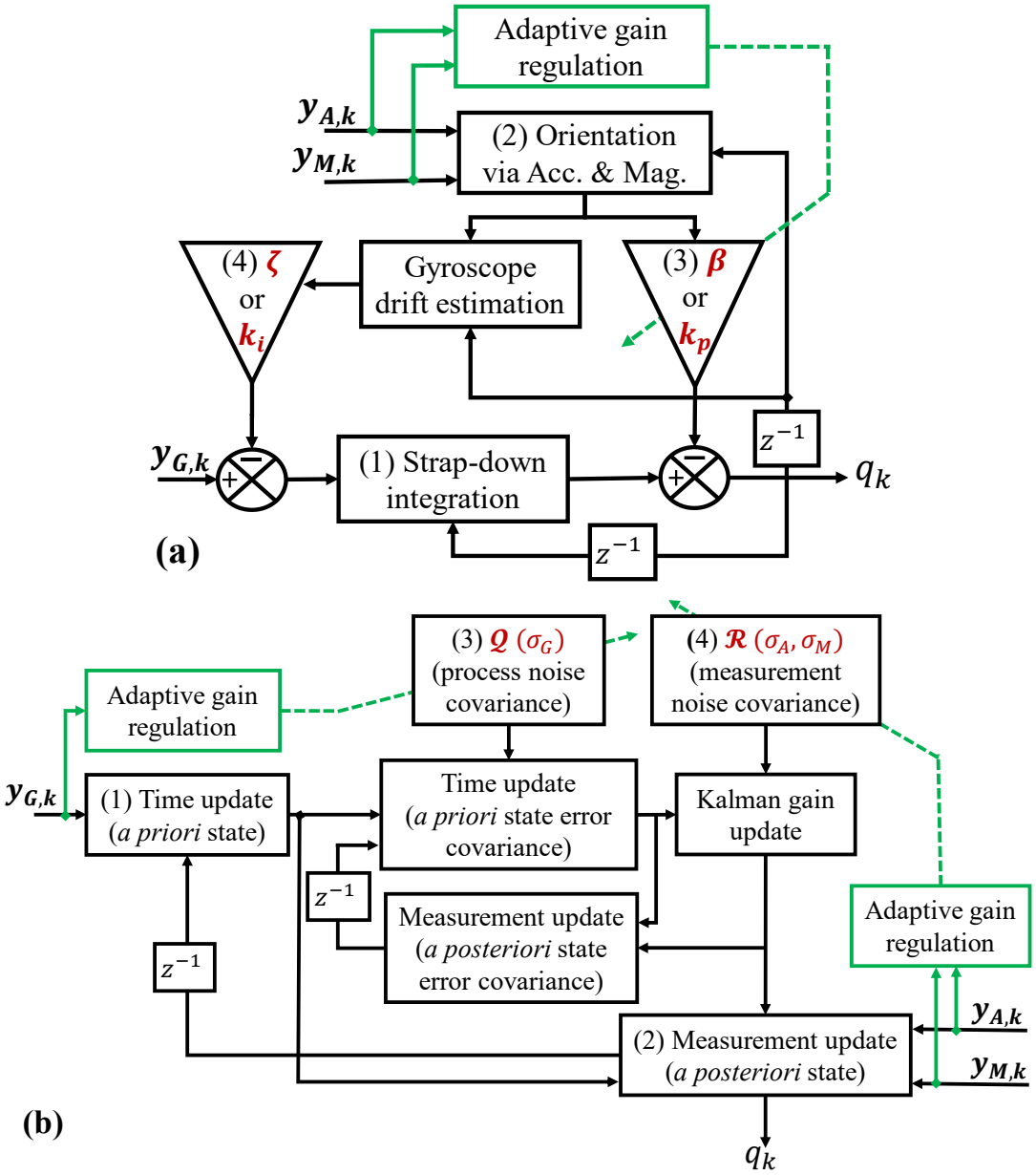

Figure 11 Block diagram of two families of SFAs implemented in this paper where SAF gains and adaptive gain regulation schemes are shown with red and green, respectively. (a) Madgwick(2011) [64] and Mahony(2008) [65], (b) Guo(2017) [195] and Roeternberg(2005) [88]. $y_{G,k}$, $y_{A,k}$, $y_{M,k}$, q_k, and z^{-1} are the angular velocity, acceleration, magnetic field, estimated orientation and delay operator, respectively.

To assess the effectiveness of the adaptive gain regulation schemes for KFs, two KFs were tested, a direct KF (Guo(2017)) [195] and an indirect KF (Roeternberg(2005)) [88], [107]. While there are more complex forms of KFs for estimation of nonlinear systems, e.g., Unscented/Cubature KF, or systems with periodic nature, Taylor-Fourier KF [331], in the present work, we only evaluated Guo(2017) and Roeternberg(2005) as they were designed for orientation tracking where linear state-space model can be used to describe the tracking equations and signals are non-periodic in general.

In Guo(2017), the quaternion parametrization of the orientation was considered as the state vector, and the quaternion-based strap-down integration was used to develop the process model (block 1 in Figure 11(b)). Also, the measurement model was obtained by solving Wahba's problem formed by accelerometer and magnetometer readouts (block 2 in Figure 11(b)). Moreover, the gains, i.e., process and measurement noise covariance matrices (blocks 3 and 4 in Figure 11(b)), were defined as $\mathcal{Q} = [\sigma_G^2 \times I_{3\times3}]$ and $\mathcal{R} = [\sigma_A^2 \times I_{3\times3}\ 0_{3\times3};\ 0_{3\times3}\ \sigma_M^2 \times I_{3\times3}]$, respectively, where σ_G, σ_A, and σ_M represent the variance of the gyroscope, accelerometer, and magnetometer readouts, respectively. Therefore, we applied the adaptive gain regulation scheme to σ_G, σ_A, and σ_M, to control the effect of the three sensors on the estimated orientation, while using the optimal fixed value for the other Guo(2017) parameter, i.e., the initial error covariance matrix $\mathcal{P}_0$ (Table 5).

The Roeternberg(2005) implemented in the "ahrsfilter" system object in MATLAB Sensor Fusion and Tracking Toolbox (MathWorks, USA) is based on the Indirect Complementary KF proposed in [107]. Roeternberg(2005) used a 12-element state vector to track the orientation error, the gyroscope bias, the linear acceleration error, and the magnetic disturbance error. These elements were considered to account for the possible errors in the general-purpose IMU model that has been commonly used in the literature, e.g., see [106], [107]. This model contains terms representing the error level associated with the gyroscope bias, non-gravitational acceleration, and magnetic disturbance. These errors depend not only on the IMU manufacturing quality but also on the motion's pattern and intensity during the movement. Thus, they cannot be estimated via an offline calibration and must be estimated during orientation tracking.

In Roeternberg(2005), the *a priori* estimate, and therefore the state transition matrix, was always zero. This is because the state vector was defined in terms of the error of the mentioned

quantities and not the quantities themselves. Also, the measurement model was developed by considering the effect of the gyroscope bias, orientation error, and magnetic disturbance on the inclination and magnetic vector estimates (block 2 in Figure 11 (b)). Similar to Guo(2017), we applied the adaptive gain regulation scheme to gains σ_G, σ_A, and σ_M, while using the optimal fixed value for other Roeternberg(2005) parameters, i.e., the initial error covariance matrix $\mathcal{P}_0$, gyroscope drift noise ζ (variance of the gyroscope offset drift), linear acceleration noise ξ (variance of the linear acceleration noise), magnetic disturbance noise γ (variance of the magnetic disturbance noise), magnetic disturbance decay factor σ, and expected magnetic field strength m_{exp} [332] (Table 5).

4.2.2 Adaptive Gain Regulation Schemes

4.2.2.1 Hard-switch Between Two or Three Levels

As the simplest case of adaptive gain regulation, we implemented a hard-switch between two (VST1) or three (VST2) levels, as shown in Figure 12(a) and (b), respectively. In VST1 and VST2, each SFA gain changes between two or three predefined levels, i.e., G_1, G_2, and G_3, based on a predefined threshold value S (or S_1 and S_2). As the IMU readouts are the only information available during orientation tracking (for a general SFA), we applied the threshold to the deviation of IMU readouts from a (recorded) reference value to select the proper gain at each time instant. Notably, as described in Table 5, for Madgwick(2011) and Mahony(2008), we tuned the gains β and k_p, respectively, based on the deviation of the sensed acceleration and magnetic field from their reference value at the beginning of the test. For Guo(2017) and Roeternberg(2005), we tuned σ_G, σ_A, and σ_M in the same manner. Thus, for Madgwick(2011) and Mahony(2008) with one tunable gain, only one hard-switch was designed for each SFA; whereas, for KFs, three separate hard-switches were designed to regulate the gains σ_G, σ_A, and σ_M.

For instance, a hard-switch with two levels (Figure 12(a)), formulated as Equation 23, was used to regulate the gain β for Madgwick(2011):

$$\beta = \begin{cases} \beta_1, & \left|\left\|\mathrm{y}_{A,k}\right\| - \left\|y_{A,stat}\right\|\right| < S_A \cap \left|\left\|\mathrm{y}_{M,k}\right\| - \left\|\mathrm{y}_{M,stat}\right\|\right| < S_M \\ \beta_2, & \text{otherwise} \end{cases} \quad \text{Equation 23}$$

Table 5 Gains of each (SFA, gain regulation scheme) optimized via the Particle Swarm Optimization (MF: membership function).

SFA	Gain regulation	# decision variables	Description of SFA gains
Madgwick(2011) [64]	FOG	2	(β, ζ)
	VST1	5	$(\beta_1, \beta_2, S_A, S_M, \zeta)$
	VST2	8	$(\beta_1, \beta_2, S_{A_1}, S_{M_1}, \beta_3, S_{A_2}, S_{M_2}, \zeta)$
	VST3	24	Parameters of the MFs $(L_1, L_2, M_1, M_2, M_3, M_4, H_1, H_2)$ for 2 inputs and 1 output
Mahony(2008) [65]	FOG	2	(k_p, k_i)
	VST1	5	$(k_{p_1}, k_{p_2}, S_A, S_M, k_i)$
	VST2	8	$(k_{p_1}, k_{p_2}, S_{A_1}, S_{M_1}, k_{p_3}, S_{A_2}, S_{M_2}, k_i)$
	VST3	24	Parameters of the MFs $(L_1, L_2, M_1, M_2, M_3, M_4, H_1, H_2)$ for 2 inputs and 1 output
Guo(2017) [195]	FOG	4	$(\mathcal{P}_0, \sigma_G, \sigma_A, \sigma_M)$
	VST1	10	$(\mathcal{P}_0, \sigma_{G_1}, \sigma_{G_2}, S_G, \sigma_{A_1}, \sigma_{A_2}, S_A, \sigma_{M_1}, \sigma_{M_2}, S_M)$
	VST2	16	$(\mathcal{P}_0, \sigma_{G_1}, \sigma_{G_2}, S_{G_1}, \sigma_{G_3}, S_{G_2}, \sigma_{A_1}, \sigma_{A_2}, S_{A_1}, \sigma_{A_3}, S_{A_2}, \sigma_{M_1}, \sigma_{M_2}, S_{M_1}, \sigma_{M_3}, S_{M_2})$
	VST3	48	Parameters of the MFs $(L_1, L_2, M_1, M_2, M_3, M_4, H_1, H_2)$ for 3 inputs and 3 outputs
	IAE	51	Parameters of the MFs $(L_1, L_2, M_1, M_2, M_3, M_4, H_1, H_2)$ for 3 inputs and 3 outputs + $(\mathcal{P}_0, \sigma_A, \sigma_M)$
Roeternberg(2005) [88]	FOG	9	$(\mathcal{P}_0, \sigma_G, \sigma_A, \sigma_M, \zeta, \xi, \gamma, \sigma, m_{exp})$
	VST1	15	$(\mathcal{P}_0, \sigma_{G_1}, \sigma_{G_2}, S_G, \sigma_{A_1}, \sigma_{A_2}, S_A, \sigma_{M_1}, M_2, S_M, \zeta, \xi, \gamma, \sigma, m_{exp})$

where β_1 and β_2 are the values of gain β at each level, $\|y_{A,k}\|$ and $\|y_{M,k}\|$ are the norm of the acceleration and magnetic field at each time instant, respectively, $\|y_{A,stat}\|$ and $\|y_{M,stat}\|$ are the norm of the acceleration and magnetic field at rest (measured when the IMU was motionless at the beginning of the experiment), and S_A and S_M are the switching thresholds for the acceleration and magnetic field, respectively. Then, the values of gains G_i and switching thresholds S_i were optimized based on the framework described in Section 4.2.3. For VST2, a hard-switch with three levels (Figure 12(b)) can be designed similarly.

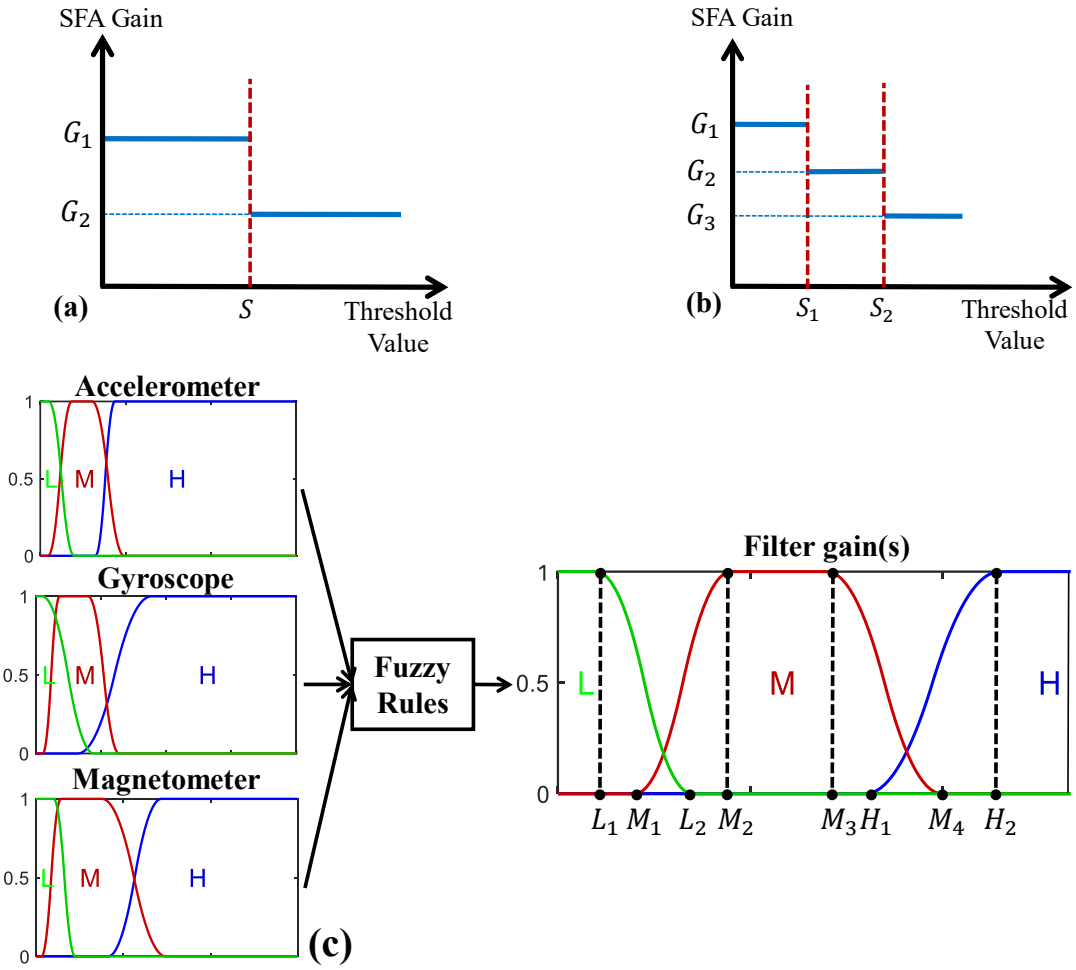

Figure 12 Structure of the three general-purpose adaptive gain regulation schemes: (a) VST1: hard-switch between two levels, (b) VST2: hard-switch between three levels, and (c) VST3: a general approximator using a Mamdani fuzzy inference system.

4.2.2.2 Fuzzy Inference System

Theoretically, there are two disadvantages with a hard-switch gain regulation scheme: (1) the resolution in which the SFA gain can be tuned is always limited by the number of switching levels;

and (2) the change in the value of the gain(s) is sudden and significant which may result in SFA instability. To address these limitations, we have to increase the number of switching levels, which will increase the number of decision variables of the optimization problem. Therefore, we proposed the application of a general approximator using a Mamdani fuzzy inference system [333] for adaptive gain regulation, as shown in Figure 12(c). Theoretically, the fuzzy inference system can tune the SFA gain(s) with significantly higher resolution and provide a soft-switch between different levels. However, the fuzzy inference system-based gain regulation is computationally more expensive than hard-switching parameters. Also, the fuzzy inference system has more parameters to be tuned compared to VST1 and VST2. Thus, more data with higher variability is required to optimize these parameters and avoid overfitting.

To construct the targeted relationship between the inputs (IMU readouts) and outputs (SFA gain(s)), we customized the fuzzy inference system structure for each SFA. For Madgwick(2011) and Mahony(2008), we combined accelerometer and magnetometer readouts using fuzzy rules to tune the SFA gain β and k_p, respectively. For example, as shown in Figure 12(c), the following rules were used for Madgwick(2011) and Mahony(2008):

- IF accelerometer belongs to L_{acc} AND magnetometer belongs to L_{mag} THEN gain belongs to H_{gain}.
- IF accelerometer belongs to M_{acc} AND magnetometer belongs to M_{mag} THEN gain belongs to M_{gain}.
- IF accelerometer belongs to H_{acc} OR magnetometer belongs to H_{mag} THEN gain belongs to L_{gain}.

where H, M, and L show high, medium, and low membership function, and subscripts *acc/mag* and *gain* show the deviation of the accelerometer/magnetometer readout from its reference value (similar to Equation 23) and gain value, respectively. Therefore, at each time instant, the degree to which the IMU readouts belong to each membership function H, M, and L will be determined, and rules will be fired accordingly to determine the filter gain. For KFs, we used each of the gyroscope, accelerometer, and magnetometer readouts separately to tune the SFA gains, i.e., σ_G, σ_A, and σ_M (three rules were defined for each gain σ_G, σ_A, and σ_M).

As mentioned previously, three membership functions were used to describe fuzzy inference system input and output variables: L for small magnitudes; M for medium magnitudes; and H for large magnitudes of the input and output values, as shown in Figure 12(c). The three membership functions, L, M, and H, were created using S-shape, Π-shaped, and Z-shaped spline-based functions, respectively. As shown in Figure 12(c), the S- and Z-shape functions allow obtaining infinitely low and high gain values (compared to a bell- or Π-shaped, which only covers a limited range of parameters), respectively, while the Π-shaped covers the medium range for gain values; see [334] for more details on the selected functions. Also, the final value of SFA gain will be obtained based on the *Aggregation* and *Defuzzification* methods mentioned at the end of this section. These S-shaped, Π-shaped, and Z-shaped functions were defined by eight parameters (L_1, L_2, M_1, M_2, M_3, M_4, H_1, H_2), as shown in Figure 12(c). The initial structure of the fuzzy inference system was generated using the fuzzy c-means clustering technique with the following parameters.

- *AND operator*: minimum of the fuzzified input values.
- *OR operator*: maximum of the fuzzified input values.
- *Implication method*: minimum (truncating the consequent membership function at the antecedent result value).
- *Aggregation method*: maximum of the consequent fuzzy sets.
- *Defuzzification method*: centroid of the area under the output fuzzy set.

4.2.2.3 Innovation Adaptive Estimation

In IAE, the value of $\mathcal{Q}_k$ or $\mathcal{R}_k$ can be tuned at each time step by calculating the discrepancy matrix D_k as in [335], [336]. In this work, we applied the IAE to the process noise covariance matrix $\mathcal{Q}_k$, while using the optimal fixed value for measurement noise covariance matrix $\mathcal{R}_k$ and initial error covariance matrix $\mathcal{P}_0$. Also, the IAE was only implemented for Guo(2017), as the covariance matrix $\mathcal{Q}_k$ was not directly accessible in Roeternberg(2005).

To implement IAE, after calculating the D_k, a fuzzy inference system was used to update the value of $\mathcal{Q}_k$ to reduce the discrepancy between actual and predicted measurements at step k as follows.

- IF $D_k(i,i) \cong 0$ THEN do not change $\mathcal{Q}_k(i,i)$.
- IF $D_k(i,i) > 0$ THEN decrease $\mathcal{Q}_k(i,i)$.

- IF $D_k(i,i) < 0$ THEN increase $Q_k(i,i)$.

As mentioned previously, in the Guo(2017), Q_k was defined as $Q_k = [\sigma_G^2 \times I_{3\times3}]$. Therefore, three single-input single-output fuzzy inference systems were designed with the three rules mentioned above to adjust the value of each diagonal element of Q_k based on the corresponding diagonal element of D_k. It should be noted that there was no direct correspondence between the dimensions of D_k and Q_k, i.e., D_k was 4×4 while Q_k was 3×3. Therefore, we used only the first three diagonal elements of the D_k as inputs of fuzzy inference systems similar to [335], [336].

4.2.3 Gain Optimization Framework

We proposed the following general framework to optimize (1) the gains of the four mentioned SFAs (FOG); or (2) the gains (G_i) and switching thresholds (S_i) of the gain regulation schemes (VST1, VST2, VST3, and IAE). This framework optimized the desired decision variables (Table 5) by comparing the estimated orientation by an SFA and the true orientation obtained by the reference MCS, as shown in Figure 13(a). Notably, gain regulation between a set of experimentally selected (and not optimal) values can generate inaccurate results. For example, previous comparative studies, e.g., Valenti et al. [128], Del Rosario et al. [135], and Feng et al. [80], obtained lower accuracy and robustness for SFAs with non-optimized parameters compared to the results presented by their developers, as they used experimentally selected gains.

As shown in Figure 13(a), to optimize the gain regulation schemes, the error between estimated and true orientations must be calculated. This error was defined as in Equation 24,

$$ {}_{E}R_k = \left({}^{GF_{MCS}}_{PF}R_k\right)^T \cdot {}^{GF_{MCS}}_{GF_{IMU}}R \cdot {}^{GF_{IMU}}_{SF}R_k \cdot \left({}^{PF}_{SF}R\right)^T \qquad \text{Equation 24} $$

where ${}^{GF_{IMU}}_{SF}R_k$ and ${}^{GF_{MCS}}_{PF}R_k$ are the estimated orientation (obtained by IMU) and true orientation (obtained by MCS), respectively, at time step k with respect to their global coordinate system (superscript: GF). ${}^{GF_{MCS}}_{PF}R_k$ was calculated from three markers on each plate using the MCS. Also, ${}^{GF_{MCS}}_{GF_{IMU}}R$ is the fixed transformation matrix between global coordinate systems of IMU and MCS and was calculated according to Equation 25,

$$ {}^{GF_{MCS}}_{GF_{IMU}}R = {}^{GF_{MCS}}_{PF}R_{k_{avg}} \cdot {}^{PF}_{SF}R \cdot \left({}^{GF_{IMU}}_{SF}R_{k_{avg}}\right)^T \qquad \text{Equation 25} $$

where ${}^{GF_{IMU}}_{SF}R_{k_{avg}}$ and ${}^{GF_{MCS}}_{PF}R_{k_{avg}}$ are the orientations of the IMU and plate, averaged over the quiet standing period at the beginning of the test, and obtained according to [337]. Finally, to account for the possible fixed misalignment between IMU and plate local frames due to the IMU attachment inaccuracies, ${}^{PF}_{SF}R$ was calculated according to [24].

Then, the estimation error rotation matrix obtained by Equation 24, ${}_{E}R_{k}$, was converted to Euler angles (roll, pitch, yaw), and the estimation error value equal to $\text{Error}_{\text{roll}} + \text{Error}_{\text{pitch}} + \text{Error}_{\text{yaw}}$ was fed back to a Particle Swarm Optimization routine as the cost function value. The Particle Swarm Optimization routine was selected for optimization as it was shown to be a powerful solver for continuous problems with non-convex search space [321], [338]. Particle Swarm Optimization has a stochastic nature in which the particles can be perturbed randomly to avoid local minima. The parameters of the Particle Swarm Optimization were selected as follows: maximum number of iterations = 50; population size = 50; inertia weight = 0.73; inertia weight damping ratio = 0.99; personal learning coefficient = 1.50; and global learning coefficient = 1.50.

As indicated in Table 5, for FOG, VST1, and VST2, the gains of the SFA or gain regulation schemes were directly used as the decision variables of the Particle Swarm Optimization routine. However, for VST3 and IAE, parameters of the membership functions (L_1, L_2, M_1, M_2, M_3, M_4, H_1, H_2) were used as the decision variables. Additionally, the membership functions of each input/output of the fuzzy inference system in VST3 and IAE were subject to the following seven constraints: (1) IF $L_2 < L_1$ THEN $L_2 = L_1$; (2) IF $L_2 < M_1$ THEN $L_2 = M_1$; (3) IF $M_2 < M_1$ THEN $M_2 = M_1$; (4) IF $M_3 < M_2$ THEN $M_3 = M_2$; (5) IF $M_4 < M_3$ THEN $M_4 = M_3$; (6) IF $M_4 < H_1$ THEN $M_4 = H_1$; (7) IF $H_2 < H_1$ THEN $H_2 = H_1$. These constraints ensure that the membership functions maintain the targeted shape, and there is an overlap between the stretches of the consecutive membership functions to cover the whole range of inputs/outputs.

The described optimization procedure was performed for 16 rounds for each (SFA, gain regulation scheme). In the first four optimization rounds, random numbers were used as the initial population and range for decision variables. Then, the obtained results were used as a part of the initial population (plus random initial population to avoid premature convergence) for the next optimization rounds. Also, the optimized gains were used to adjust the acceptable range for the gains in future optimization rounds. After 16 separate rounds of optimization, the optimized values

(minimum error for the training data set) for FOG, VST1, VST2, VST3, or IAE for each SFA were selected and applied to the testing data set (training and testing sets are described in Section 4.2.5).

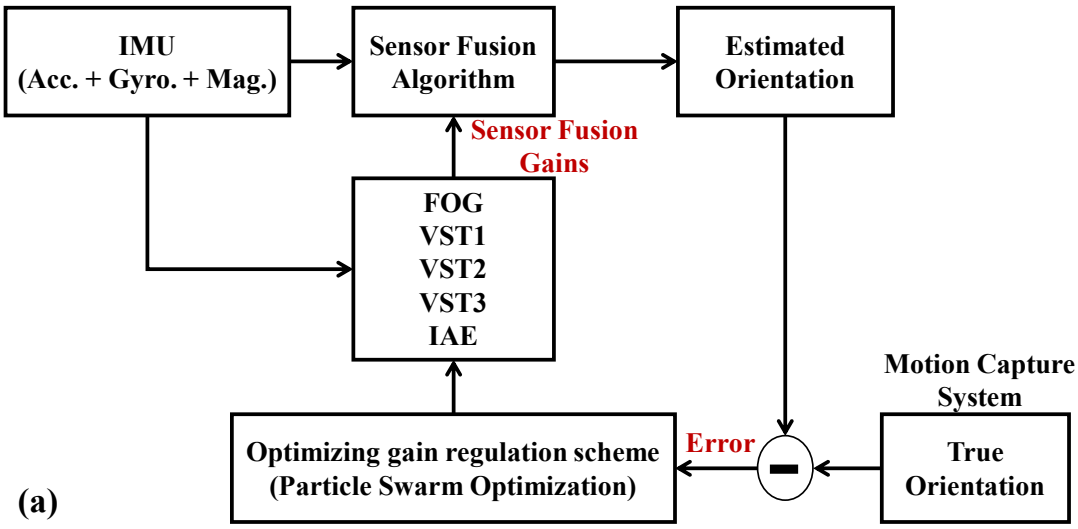

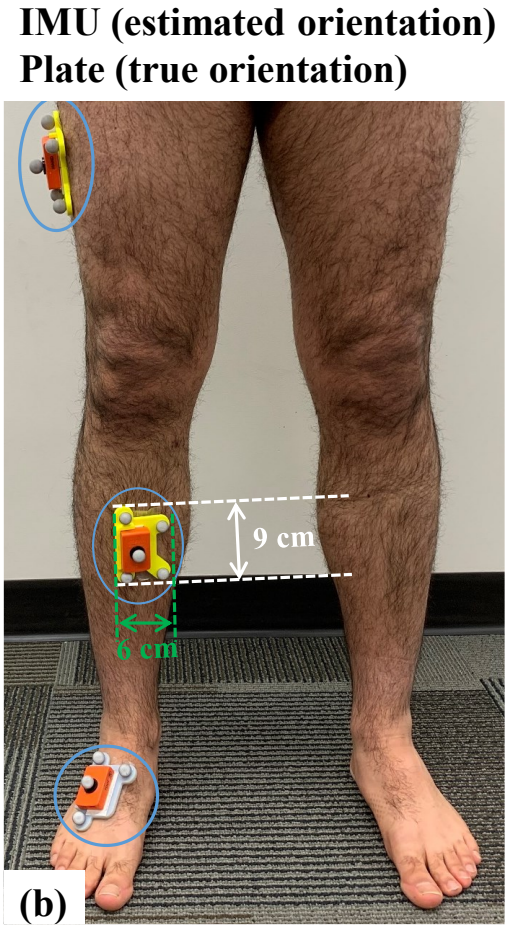

Figure 13 (a) Structure of the proposed framework for optimizing the parameters of the adaptive gain regulation schemes, (b) Experimental setup including three IMUs attached to the thigh, shank, and foot along with plate-mounted reflective markers tracked by the MCS.

4.2.4 Experimental Procedure

The effectiveness of the FOG, as well as the four gain regulation schemes, VST1, VST2, VST3, and IAE, were assessed by measuring the orientation estimation error (roll, pitch, yaw) through an experimental study with nine able-bodied participants (all male, 26±2 years old, 74±6 kg, 177±4 cm). The Research Ethics Board Committee at the University of Alberta approved the study protocol, and written consent was obtained from all participants. During the experiments, participants performed the following movements: quiet standing (60 seconds); straight walking (5 meters); turning; straight walking (2.5 meters); vertical jumping (two times); straight walking (2.5 meters); turning; hopping with both legs (three times); turning; walking the 5-meter corridor back-and-forth three times with U-turns at the end; quiet standing (30 seconds). Participants were instructed to take 2 seconds of quiet standing after each task (one complete trial was 131±7 seconds on average).

We aimed to evaluate the accuracy and robustness of orientation estimation accuracy of SFAs together with adaptive gain regulation under a wide range of motion intensities and patterns and in long durations. Therefore, we had to recruit only able-bodied individuals for our experimental study. Nevertheless, we made no assumption about the performed motions for orientation estimation. Thus, the same level of accuracy is expected for other applications, such as the motion tracking of participants with motor dysfunction. Experiments were performed on three separate days, three participants each day, while the same IMUs were attached to each segment during all experiments. This procedure was performed to assess the accuracy and robustness of orientation estimation in different environmental conditions, e.g., room temperature. In addition to keeping the IMUs motionless for 10 minutes before each data collection (to allow them to reach a stable condition), the first 30 seconds of each experiment were used to allow the SFAs to converge to a stable condition without the need for a drastic change in SFA gain(s) during motion.

4.2.5 Data Analysis

Three-fold cross-validation was performed using the experimental data recorded in three separate days to assess the effectiveness of the FOG, VST1, VST2, VST3, and IAE. In other words, the IMU data of the three participants in each day were used to perform the optimization (training data set), and the data of the remaining six participants (testing data set) were used to evaluate the

performance of each SFA combined with each gain regulation scheme. This procedure was repeated for all combinations of (IMU, SFA, gain regulation scheme).

The performance of each combination was quantified as the RSME (the difference between true and estimated angles) of the roll, pitch, and yaw angles associated with orientation estimation error ${}_{E}R_{k}$. Then, for each (IMU, SFA) combination, we compared the performance of the gain regulation schemes in terms of accuracy (median of RMSE among all testing data set) and robustness (standard deviation of RMSE among all testing data set). The non-parametric Wilcoxon rank-sum test (significance level = 5%) was employed to find the significant differences between the obtained errors of each two schemes as the equality of variance and/or normal distribution conditions have not been met. Also, standard deviations of RMSEs were compared via the two-sample F-test.

4.2.6 Computation Complexity

The execution time for each SFA combined with FOG, VST1, VST2, VST3, and IAE was measured in milliseconds by measuring the total execution time of one trial and dividing the result by the number of samples in that trial. This procedure was repeated 500 times for each (SFA, gain regulation) combination, and the average value was recorded. Also, the execution time of other operations, such as loading the data or allocating memory to variables, which were performed at the initialization phase of running each SFA and not repeated per sample, were recorded separately and included in the runtime per sample. All codes were executed with MATLAB R2018b (MathWorks, USA) on a desktop PC with the following characteristics: CPU: Intel Core i7-4770; and RAM: 12 GB.

4.3 Results

Figure 14 shows a representative graph of the 3D-angle-estimation errors obtained from the thigh, shank, and foot IMUs using Madgwick(2011) combined with FOG, VST1, and VST2. According to Figure 14, Madgwick(2011) errors depended on the location of the IMU under investigation, i.e., the errors of the shank and foot IMUs were generally larger compared to the errors of the thigh IMU. Using FOG, the Madgwick(2011) performance depended on both the IMU location and trial duration. For instance, for the foot IMU, 3D errors were small during the first 10 seconds and then increased over time. However, both VST1 and VST2 resulted in reduced tracking error (during

motion) and convergence error (during motionless periods) compared to the FOG for all three IMUs. This observation could be because VST1 and VST2 enabled the Madgwick(2011) to rely more on accelerometer and magnetometer during short periods with little motion between activities to reduce the drift caused by strap-down integration.

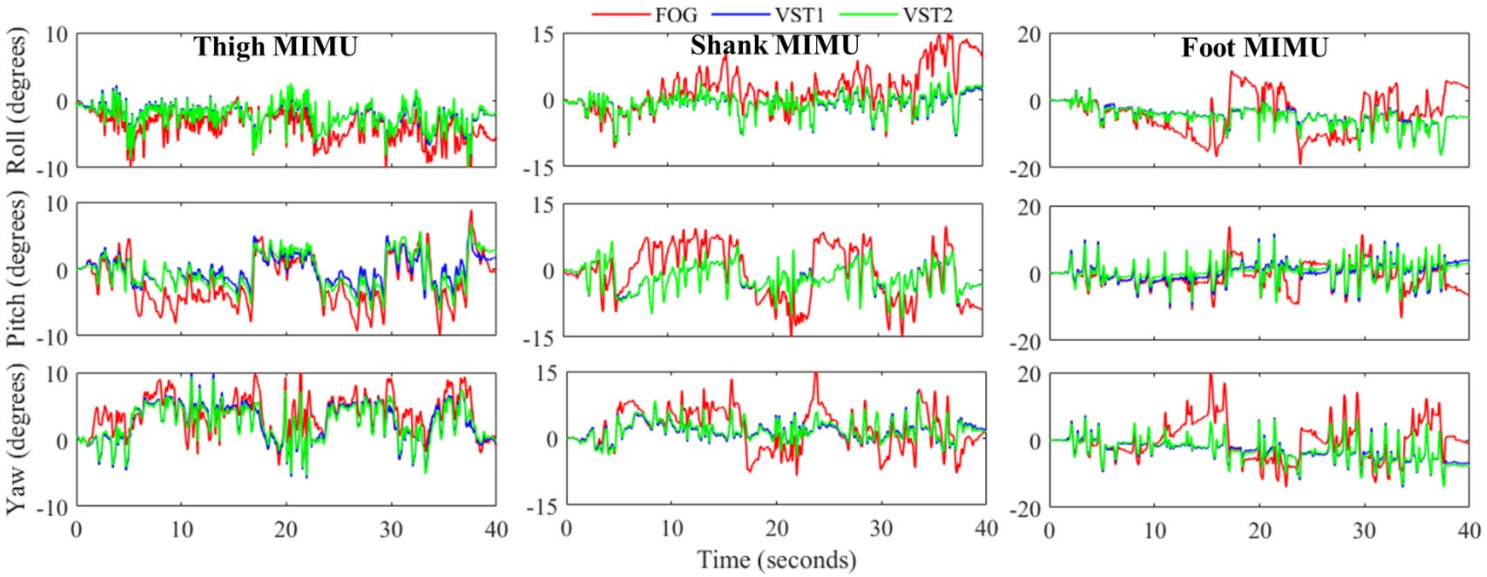

Figure 14 A representative graph of the errors in 3D-angle-estimation obtained for thigh, shank, and foot IMUs and Madgwick(2011) [64] using FOG, VST1, VST2 (test data of one participant). The trial includes walking, vertical jumping, and hopping.

Table 6 shows the gain values of the Madgwick(2011) optimized for IMUs on each body segment using the data of the first three participants. According to Table 6, the optimized value of the gains varies among IMUs, and the optimal gains for one IMU may result in poor performance for another IMU. Thus, the gains for each IMU must be optimized separately. Additionally, by comparing the SFA gains, β, obtained for FOG, VST1, and VST2, we observed that the adaptive gain regulation allowed the Madgwick(2011) to use higher values of β during motionless and magnetically undisturbed situations (β_1: which resulted in rapid convergence and gyroscope drift cancellation) and use low values of β during intensive activities (β_2: to rely on gyroscope mainly).

According to Table 7(a) and Figure 15(a), adaptive gain regulation not only significantly ($p<0.05$) reduced the RMSE of the orientation estimation but often resulted in significantly more robust estimation for Madgwick(2011). For example, while the RMSEs reported as median (interquartile range) across participants for foot IMU using FOG were 7.7(3.3), 5.3(2.9), and 7.5(3.6) degrees for roll, pitch, and yaw angles, respectively, applying the VST1 to Madgwick(2011) reduced the errors to 4.6(1.8), 3.1(0.8), and 4.3(1.2) degrees, respectively.

Moreover, for shank and foot IMUs, Madgwick(2011) with FOG resulted in poor performance for some participants, shown as outliers in Figure 15(a).

According to Table 7(b), for Mahony(2008), for the shank IMU, all adaptive gain regulation schemes resulted in significantly ($p<0.05$) higher accuracy and robustness compared to FOG. For the foot IMU, VST1 and VST2 obtained significantly higher accuracy compared to FOG and VST3. For example, the estimation errors were decreased from 9.3(1.6), 7.3(1.0), and 8.2(1.2) degrees for FOG to 4.2(2.4), 3.1(0.7), and 4.5(2.1) degrees for VST2 for roll, pitch, and yaw angles, respectively (Figure 15(b)). For the thigh IMU, a trend was not observed, and adaptive gain regulation schemes did not always perform better than FOG.

Table 8(a) shows that, for Guo(2017), VST2 achieved significantly ($p<0.05$) lower RMSE compared to FOG and often other adaptive gain regulation schemes. Specifically, the maximum RMSE among participants did not exceed 4.9 degrees (yaw) for VST2, while FOG and IAE resulted in maximum RMSEs of 9.3 (yaw) and 8.1 (roll) degrees, respectively (Figure 15(c)). Moreover, VST1 to VST3 often showed significantly more accurate and robust performance than both FOG and IAE, except for the yaw angle of the thigh IMU. According to Table 8(b), for Roeternberg(2005), unlike for the thigh IMU, VST1 significantly ($p<0.05$) outperformed FOG in terms of accuracy, robustness, or both for shank and foot IMUs. For example, for the shank IMU, the maximum RMSEs among participants were decreased from 4.3, 9.0, 7.8 degrees for FOG to 3.1, 3.5, 4.5 degrees for VST1 for roll, pitch, and yaw angles, respectively (Figure 15(d)).

Table 9 shows that for both Madgwick(2011) and Mahony(2008), while the execution times of VST1 and VST2 were similar, the highest execution times were associated with VST3 and, in both cases, less than 0.5 milliseconds, which is 20 times faster than the sampling period of the IMUs (10 milliseconds). For Guo(2017), while the VST1 and VST2 were nearly 7 times slower than FOG, they were still 10 times faster than the sampling period of the IMUs. As was expected, the highest execution times were recorded for Roeternberg(2005), which were still nearly 5 times faster than the sampling period of the IMUs. Also, according to Table 9, the obtained execution times are comparable to the internal sampling period (1 millisecond) of the IMU embedded systems. Therefore, wireless data transfer from IMU to the computer is the slowest link (sampling period of 10 milliseconds). Thus, the worst-case scenario for the total time required to sample and transfer data and calculate the orientation will be 13.1 (1+10+2.1) milliseconds.

Table 6 Optimal gains of the Madgwick(2011) [64] (FOG) or adaptive gain regulation schemes (VST1 and VST2) for thigh, shank, and foot IMUs associated with the estimated angles shown in Figure 14.

Gain regulation	IMU	Gain values
FOG		β, ζ
	Thigh	0.073, 6e-04
	Shank	0.004, 6e-06
	Foot	0.003, 1e-12
VST1		$\beta_1, \beta_2, S_A, S_M, \zeta$
	Thigh	0.082, 1e-05, 0.122, 0.051, 1e-12
	Shank	0.050, 1e-05, 0.064, 0.085, 9e-05
	Foot	0.045, 1e-12, 0.019, 0.404, 1e-25
VST2		$\beta_1, \beta_2, S_{A_1}, S_{M_1}, \beta_3, S_{A_2}, S_{M_2}, \zeta$
	Thigh	0.089, 0.005, 0.135, 0.052, 1e-18, 0.200, 0.201, 2e-14
	Shank	0.082, 1e-03, 0.067, 0.086, 1e-18, 0.150, 0.128, 1e-04
	Foot	0.050, 0.006, 0.100, 0.200, 1e-18, 0.204, 0.207, 1e-25

4.4 Discussions

IMUs are an accurate and robust alternative for stationary MCSs, with promising out-of-lab applications. However, for applications such as joint angle measurement or segment velocity/position estimation, the orientation of the body segments must first be estimated using an SFA. These SFAs have been validated for real IMU data in applications such as tracking and/or control of spacecraft (satellite), human motion, mobile robots, robotic arms, and aerial vehicles.

Previously, Nez et al. [325] showed that the KF gains must be selected rigorously. Otherwise, its performance could deteriorate. They also showed that the values of these gains, which could be identified through optimization, were relatively different from those obtained by the Allan Variance method [339]. The reason could be that the optimized gains implicitly account for sources of error, such as modeling or calibration errors [325]. However, their approach was only suitable for specific activities with a similar movement intensity. To address this issue, some researchers have proposed switching the gain values between different levels [340]–[342].

Table 7 Statistical comparison of the accuracy and robustness of different gain regulation schemes for (a,b) Madgwick(2011) and (c,d) Mahony(2008). Each gain regulation scheme significantly ($p<0.05$) outperformed the methods named in its associated column. The gain regulation scheme names were summarized as F: fixed optimal gain (FOG), V1: hard-switch between two levels (VST1), V2: hard-switch between three levels (VST2), V3: fuzzy inference system (VST3).

(a) Accuracy of Madgwick(2011) [64]

	Roll				**Pitch**				**Yaw**			
	FOG	**VST1**	**VST2**	**VST3**	**FOG**	**VST1**	**VST2**	**VST3**	**FOG**	**VST1**	**VST2**	**VST3**
Thigh	-	F	F	F	-	F, V2	F	F, V2	-	F	F	F
Shank	-	F	F, V1	F, V2	-	F	F	F	-	F	F	F
Foot	-	F	F	F	-	F	F	F	-	F	F	F

(b) Robustness of Madgwick(2011) [64]

	FOG	**VST1**	**VST2**	**VST3**	**FOG**	**VST1**	**VST2**	**VST3**	**FOG**	**VST1**	**VST2**	**VST3**
Thigh	-	-	F	-	-	-	-	-	-	-	F, V1	F, V1
Shank	-	F	F	F	-	F	F	F	-	F	F	F
Foot	-	F	F	F	-	F	F	F	-	F	F	F

(c) Accuracy of Mahony(2008) [65]

	FOG	**VST1**	**VST2**	**VST3**	**FOG**	**VST1**	**VST2**	**VST3**	**FOG**	**VST1**	**VST2**	**VST3**
Thigh	-	-	F, V1, V3	F	-	-	-	-	V2	V2	-	V2
Shank	-	F	F	F	-	F	F	F	-	F	F	F
Foot	-	F, V3	F, V3	-	-	F, V3	F, V3	-	-	F, V3	F, V3	-

(d) Robustness of Mahony(2008) [65]

	FOG	**VST1**	**VST2**	**VST3**	**FOG**	**VST1**	**VST2**	**VST3**	**FOG**	**VST1**	**VST2**	**VST3**
Thigh	-	-	V1	-	V2	V2	-	V2	V3	-	-	-
Shank	-	F	F, V1, V3	F	-	F	F	F	-	F	F	F, V1, V2
Foot	V1	-	V1	V1	V1	-	V1	V1	V1	-	V1	V1

However, in all of these works, the structure of the switching schemes was designed for KFs, and the gains were not selected systematically, which could deteriorate the SFA's performance [325]. Therefore, we proposed a general framework to optimize the structure and parameters of adaptive gain regulation schemes for SFAs (KFs and CFs). Through an extensive experimental study, we showed that adaptive gain regulation of SFAs is of crucial importance, regardless of the SFA structure or complexity. To ensure that the results were not affected by the experimental setup, we used (1) three different IMUs attached to three different body segments; and (2) collected the data of nine participants during various activities in three different days (to minimize the effect of environmental condition on IMU readouts).

4.4.1 Adaptive Gain Regulation Technique Selection

A gain regulation scheme can be selected based on (1) highest estimation accuracy (lowest median RMSE across all participants); (2) highest estimation robustness (lowest standard deviation of RMSE across all participants); (3) simplest structure (lowest number of tunable parameters), see Table 5. According to Table 7(a,b) and Figure 15(a), the application of all adaptive gain regulation techniques for Madgwick(2011) resulted in significantly higher accuracy (and oftentimes robustness) compared to FOG for all IMUs and angles. Therefore, we concluded that for Madgwick(2011), VST1 with the simplest structure would suffice. Table 7(c,d) shows that no technique outperformed others in all angles for the thigh IMU for Mahony(2008). However, VST2 resulted in significantly higher accuracy (and oftentimes robustness) compared to FOG for all estimated angles of the shank and foot IMUs. Therefore, we concluded that for Mahony(2008), VST2 is the best choice.

When Guo(2017) was implemented for the shank and foot IMUs, VST2 achieved significantly lower RMSEs compared to FOG and IAE for all angles, and some angles compared to VST1 and VST3 (Table 8(a,b)). Additionally, for both shank and foot IMUs, VST2 was significantly more robust than FOG and IAE. For thigh IMU, VST2 resulted in significantly lower RMSEs compared to FOG and other gain regulation schemes except for pitch angle estimation via VST1 and VST3. Therefore, we recommend VST2 as the gain regulation scheme for Guo(2017).

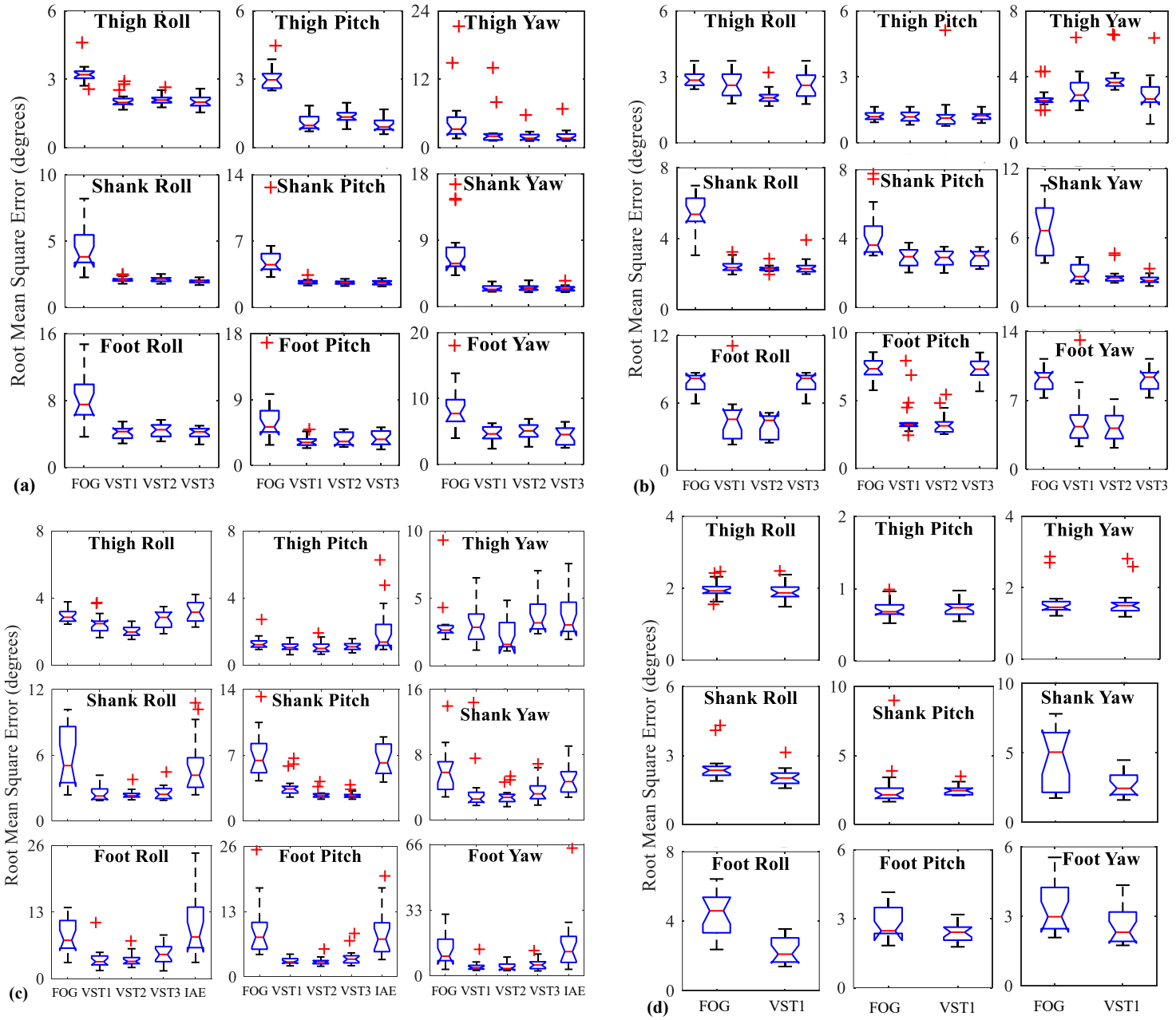

Figure 15 Boxplot of the RMSE (difference between true and estimated orientation) for (a) Madgwick(2011) [64], (b) Mahony(2008) [65], (c) Guo(2017) [195], and (d) Roeternberg(2005) [88]. Each boxplot presents the RMSE values of all testing data set (18 samples = data of six study participants for each cross-validation × 3-fold cross-validation). Also, Table 7 and Table 8 show the significant differences resulted from the statistical analysis for each SFA.

Table 8 Statistical comparison of the accuracy and robustness of different gain regulation schemes for (a,b) Guo(2017) and (c,d) Roeternberg(2005). Each gain regulation scheme significantly ($p<0.05$) outperformed the methods named in its associated column. The gain regulation scheme names were summarized as F: fixed optimal gain (FOG), V1: hard-switch between two levels (VST1), V2: hard-switch between three levels (VST2), V3: fuzzy inference system (VST3), I: innovation adaptive estimation (IAE).

(a) Accuracy of Guo(2017) [195]

	Roll					**Pitch**					**Yaw**				
	FOG	**VST1**	**VST2**	**VST3**	**IAE**	**FOG**	**VST1**	**VST2**	**VST3**	**IAE**	**FOG**	**VST1**	**VST2**	**VST3**	**IAE**
Thigh	-	F,I	F,V1,V3,I	I	-	-	F,I	F,I	I	-	V3	-	F,V1,V3,I	-	-
Shank	-	F,I	F,I	F,I	-	-	F,I	F,V1,I	F,V1,I	-	-	F,I	F,I	F,I	-
Foot	-	F,I	F,I	F,I	-	-	F,V3,I	F,V3,I	F, I	-	-	F,I	F,V1,I	F,I	-

(b) Robustness of Guo(2017) [195]

	FOG	**VST1**	**VST2**	**VST3**	**IAE**	**FOG**	**VST1**	**VST2**	**VST3**	**IAE**	**FOG**	**VST1**	**VST2**	**VST3**	**IAE**
Thigh	I	I	V1,V3,I	I	-	I	F,I	I	F,I	-	-	-	-	-	-
Shank	-	F,I	F,V1,I	F,I	-	-	F	F,V1,I	F,V1,I	-	-	-	F,V1,I	F,V1	V1
Foot	-	F,I	F,I	F,I	-	-	F,I	F,I	F,I	-	I	F,I	F,I	F,I	-

(c) Accuracy of Roeternberg(2005) [88]

	FOG	**VST1**	**FOG**	**VST1**	**FOG**	**VST1**
Thigh	-	-	-	-	-	-
Shank	-	F	-	-	-	F
Foot	-	F	-	-	-	F

(d) Robustness of Roeternberg(2005) [88]

	FOG	**VST1**	**FOG**	**VST1**	**FOG**	**VST1**
Thigh	-	-	-	-	-	-
Shank	-	F	-	F	-	F
Foot	-	-	-	F	-	-

Table 9 Execution times (in milliseconds) of different (SFA, gain regulation scheme) combinations. N/A shows that the (SFA, gain regulation scheme) combination was not evaluated.

SFA	FOG	VST1	VST2	VST3	IAE
Madgwick(2011) [64]	0.185	0.201	0.198	0.401	N/A
Mahony(2008) [65]	0.137	0.186	0.185	0.403	N/A
Guo(2017) [195]	0.111	0.675	0.716	1.028	0.478
Roeternberg(2005) [88]	1.644	2.100	N/A	N/A	N/A

As executing the proposed optimization framework for finding the Roeternberg(2005) gains required considerably longer runtimes compared to other SFAs, we did not assess VST2 and VST3 for Roeternberg(2005). Figure 15(d) and Table 8(c,d) show that while FOG and VST1 performed almost the same in terms of accuracy and robustness for the thigh IMU, VST1 outperformed FOG significantly in terms of accuracy, robustness, or both, for the shank and foot IMUs. Also, as shown in Figure 15(d), for both shank and foot IMUs, the maximum RMSEs were decreased, and the interquartile ranges were also reduced while using VST1, indicating higher robustness of VST1 compared to FOG. Therefore, we recommend the application of VST1 with Roeternberg(2005) for segment orientation estimation.

Also, according to Figure 15, for all SFAs, the thigh and foot IMUs had the smallest and highest errors, respectively. Notably, higher errors for foot IMU orientation tracking was expected as the SFA performance could be negatively affected by the following: (1) the foot IMU was closer to the ground, thus, the metals used in the building structure caused higher magnetic disturbances (see [343] for more details); and (2) the foot IMU experienced a higher acceleration compared to the other two IMUs which could affect the accelerometer's ability in the orientation estimation. Yet, VST1 and VST2 showed to be effective in achieving high performance for the foot IMU.

4.4.2 SFAs Execution Time

According to Table 9, the execution time of Madgwick(2011), Mahony(2008), Guo(2017), and Roeternberg(2005) with FOG was at most 0.016, 0.049, 0.605, and 0.456 milliseconds faster than employing VST1 or VST2. However, in the worst-case scenario, such as Roeternberg(2005) with VST1, the SFA execution time was 2.1 milliseconds. At the same time, a normal gait motion has a frequency content of up to 6 Hz [344] and is usually tracked at a sampling rate of around 100 Hz

(sampling period of 10 milliseconds). Therefore, even the most time-consuming SFA, Roeternberg(2005) with VST1, will be able to track the gait motion in real-time.

4.4.3 Overfitting During Optimization

One may expect the adaptive gain regulation schemes to perform the same or better than FOG. This is because if FOG has the best performance for an SFA, the adaptive gain regulation schemes could also converge to the FOG structure. However, in some cases, the adaptive gain regulation schemes performed poorly for the testing data set, shown as outliers with larger error values in Figure 15. A possible reason for this condition is overfitting. As adaptive gain regulation schemes have more parameters than FOG, they can be more flexible during optimization with the training data set, resulting in overfitting. In other words, while the SFA, together with adaptive gain regulation, had a very small error during training, it will not be able to track the orientation with high accuracy during testing. To address this issue, in practical applications, in addition to the training data set, a validation data set must be used to check whether overfitting happened during training, similar to the training of supervised classifiers [321].

4.4.4 Limitations and Future Works

First, the performance of the adaptive gain regulation schemes was evaluated for four representative SFAs and should be further investigated for others, specifically Unscented KF, Cubature KF, and Particle Filter. Also, the application of SFAs such as Taylor-Fourier KF, which showed to be effective in state estimation of periodic systems combined by adaptive gain tuning, must be investigated. Second, the accuracy and robustness of the adaptive gain regulation schemes were investigated for four activities (quiet standing, walking, vertical jumping, and hopping) and should be further investigated in other activities with various intensities and patterns. In particular, the performance assessment must be carried out for trials with longer durations, e.g., a standard 6-minute walking test. Third, gain regulation was performed only based on the accelerometer/gyroscope/magnetometer signal magnitude. In the future, more complex schemes that combine signal magnitude with other measures, such as the statistical properties of the SFA, must be developed. Specifically, time or temperature-dependent models could be developed to regulate the gyroscope-related gains. Finally, for VST3, the effect of using other membership functions used in the literature on the performance of the adaptive gain regulation must be evaluated.

4.5 Conclusions

We presented a general framework for designing an optimal adaptive gain regulation scheme applicable to both families of SFAs: CFs (Madgwick(2011) [64] and Mahony(2008) [65]) and KFs (Guo(2017) [195] and Roeternberg(2005) [88], [107]). Our experimental study proved that the performance of all four tested SFAs highly depended on the selection of SFA gains, regardless of the SFA structure or complexity. Also, in almost all cases, optimal adaptive gain regulation based on IMU signal intensity, i.e., determining which source of information (gyroscope, accelerometer, and/or magnetometer) can be relied on at each time instant, resulted in significantly more accurate and repeatable results. Moreover, for the first time, our experimental study results showed that an optimized simple gain regulation scheme such as switching gains between two or three levels was sufficient, and there was no need for a more complex scheme such as a Mamdani fuzzy inference system. While adaptive grain regulation can improve the SFA performance for short-duration tasks, there is still a need for estimating the error sources of sensors embedded in an IMU to achieve acceptable performance for long-duration dynamic tasks. Thus, Chapter 5 presents two KFs in which the error sources of the sensors were estimated and the IMU readouts were corrected using these estimations before orientation tracking.

Chapter 5

Novel Linear/Extended Kalman Filter for Orientation Tracking with IMUs

This chapter provides the details of a linear Kalman filter and a robust extended Kalman filter for accurate and robust body segment orientation tracking with IMUs. Portions of this chapter have been adopted and/or edited from:

M. Nazarahari, H. Rouhani, "Sensor Fusion Algorithms for Orientation Tracking via Magnetic and Inertial Measurement Units: An Experimental Comparison Survey," Information Fusion, Vol. 76, pp. 8-23, 2021.

M. Nazarahari, H. Rouhani, "A Full-State Robust Extended Kalman Filter for Orientation Tracking During Long-duration Dynamic Tasks Using Magnetic and Inertial Measurement Units," Submitted to IEEE Transactions on Neural Systems and Rehabilitation Engineering, Vol. 29, pp. 1280 - 1289, 2021.

5.1 Introduction

Our survey of SFAs found three main limitations in the literature: (1) constant gains were used for the developed SFAs; (2) the effect of gyroscope bias (Equation 2), external non-gravitational acceleration (Equation 4), and magnetic disturbance (Equation 6) on the estimation orientation was ignored; and (3) performance of every newly developed SFA was evaluated only in a specific

testing condition. Thus, in Chapter 4, we introduced a general framework for online gain tuning of SFAs to adaptively put more weight on the most reliable source of information. Also, in this chapter, we present two novel full-state KFs (an LKF and a robust EKF) and a comprehensive benchmarking study that compares our proposed SFAs with previously developed SFAs using a common experimental setting. We also published the codes and part of the dataset to enable other researchers to compare their works with the literature toward creating a comprehensive online repository for SFAs.

5.1.1 Benchmarking Sensor Fusion Algorithms

Our survey study identified a need for benchmarking studies for orientation tracking with IMUs [22]. The reason is that each SFA's performance was assessed in limited test scenarios in terms of motion duration, pattern, and intensity. Also, other contributing factors, such as the optimal SFA gains or manufacturing quality of the tested IMUs, were not considered in assessments. As a result, contradictory results on the performance of SFAs have been reported in various studies. In Section 2.3.1.1, we surveyed 14 benchmarking studies [49], [63], [92], [97], [99], [102], [73], [77]–[79], [82], [83], [87], [89] that had a focus on the experimental comparison of SFAs. However, one cannot make a general conclusion about the SFAs' accuracy and robustness based on these works, as each of them showed at least one of the following limitations:

1. They assessed the accuracy of only a limited number of SFAs (maximum of six filters in [92]). In total, 30 filters were tested in these works, while only 4 were compared with other filters in more than two studies.
2. They used different IMU technologies. IMUs can have different sensitivities to various sources of error, which affect the accuracy and robustness of the SFAs, e.g., the thermal gradient can make an IMU less suitable for outdoor orientation tracking [44].
3. They selected the SFAs gains experimentally. As shown in the literature [25], [325], SFA gains must be selected rigorously. Otherwise, the SFA performance may deteriorate severely. Only 3 (out of 14) of the previous experimental comparison studies reported a rigorous search for finding the SFAs gains.
4. They evaluated SFAs in different testing conditions, i.e., motions with various patterns and intensities or evaluated SFAs in tasks with different durations. Notably, some SFAs do not contain effective strategies to compensate for the cumulative errors of the strap-down

integration in long-duration trials and perform poorly after a short period. Thus, the test results from one study could not be directly compared to another study.

5. They have not published all the data/codes online. Thus, other researchers cannot compare the newly developed SFA against the previous ones.

5.1.2 Contributions

This chapter aims to build upon our survey and present an experimental comparison among a wide range of well-recognized and highly cited SFAs from the literature. Notably, the following procedure was considered to address the limitation of the previous surveys: we evaluated the performance of 37 SFAs from the literature, including examples of CFs, LKFs, EKFs, CKFs, against the gold-standard MCS in an extensive experimental study with multiple trials including various short- and long-duration dynamic tasks using optimal adaptive gain tuning for each SFA (obtained using Particle Swarm Optimization [330]). In addition, in this chapter, we proposed a novel full-state LKF, full-state robust EKF, square-root unscented KF (SRUKF) with four different sigma-point definitions [345], and square-root cubature KF (SRCKF) [346], [347] for IMU orientation estimation. In contrast to analyzed KFs, the novel proposed full-state LKF/EKF state vector includes all accelerometer, gyroscope, and magnetometer source noises to enable orientation tracking under dynamic activities in long-duration trials. The SRCKF and SRUKF were also purposed to address the challenges related to the linearization of orientation estimation equations performed in EKF. We compared the performance of these LKF, EKF, SRUKF, and SRCKF against the MCS during the same short- and long-duration dynamic tasks. However, fusing strategies such as Particle Filters or the use of other technologies alone or together with IMUs for orientation tracking were not included in this comparison. In the end, sample IMU and MCS data, as well as the SFAs implementations, were shared via an online repository (https://www.ncbl.ualberta.ca/codes).

5.2 Experimental Comparison

The details of the orientation parametrization and IMU mathematical model are described in Section 2.3.1 and Section 2.3.2, respectively.

5.2.1 Selected Sensor Fusion Algorithms (SFAs)

To conduct an experimental comparison among SFAs from all families shown in Figure 16, we had to ensure that the selected algorithms were implemented correctly. To this end, we performed an exhaustive search in online repositories to find SFAs implemented by their authors or requested the codes of highly-cited SFAs from their corresponding authors. All codes have been converted to MATLAB functions (if implemented initially with another coding language). Also, to distinguish these SFAs from one another, we named them as first author(year)

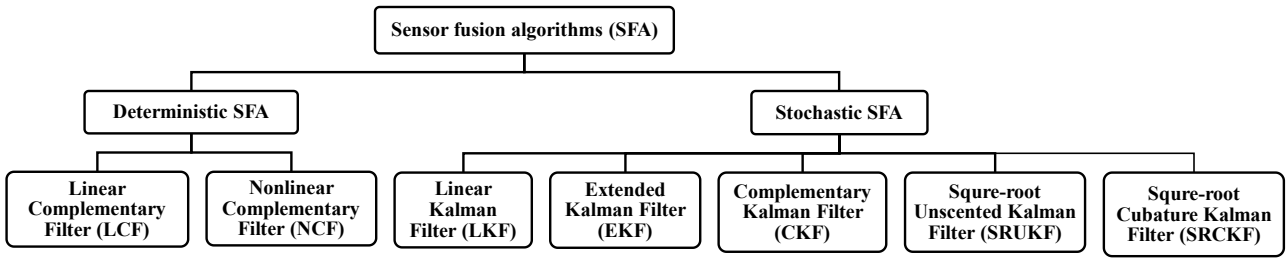

Figure 16 The proposed taxonomy of the SFAs benchmarked in this study.

In addition to the SFAs previously introduced in the literature, we proposed a novel full-state LKF, robust EKF, SRUKF, and SRCKF. Our proposed LKF (hereafter referred to as Nazarahari(2020)) and EKF (hereafter referred to as Nazarahari(2021)) were designed by including b_G, a, and d in the IMU model (see Equation 2, Equation 4, and Equation 6) in the state vector as described in Section 5.2.1.1 and Section 5.2.1.2, respectively. With this new formulation, the raw IMU readouts (i.e., y_G, y_A, y_M) can be corrected before being used for orientation estimation. We hypothesized that this correction would make the proposed SFAs more accurate for long-duration dynamic tasks where the Earth's magnetic field is disturbed. Also, we implemented SRUKF and SRCKF, which have been little implemented in the past for IMU orientation estimation. In the SRUKF (with four different sigma point definitions) and SRCKF formulation, time- and measurement-update equations were adopted from an implemented EKF [348] with mediocre performance. Then, instead of linearization steps in the EKF [348], we implemented SRUKF and SRCKF, according to [349] and [347], respectively, to investigate the effect of unscented transform and spherical-radial cubature rule in dealing with nonlinear orientation estimation equations.

Table 10 presents the list of implemented SFAs (37 in total), sorted based on their publication year. Although we acknowledge that providing the details of these algorithms in this

paper can be useful, due to a large number of implemented/tested SFAs, we refer the interested reader to the original articles for algorithm details. Nevertheless, we categorized the implemented SFAs in Table 11 and briefly described their general structure, orientation parametrization, time- and measurement-update in case of a KF, and modifications proposed to improve their performance. The implemented SFAs in this paper can be divided into two general families: CFs and KFs, and a detailed survey and flowchart of these families can be found in Section 2.3 [22].

5.2.1.1 Proposed Full-state Linear Kalman Filter

The IMU model in Section 2.3.2 was used to develop a novel full-state LKF.

LKF Prediction Model

Figure 4(a) shows the flowchart of an LKF. The state vector of the proposed LKF, x, was composed of the estimated orientation of the IMU, expressed as a unit quaternion $q_k = \left(q_{0,k}\ q_{1,k}\ q_{2,k}\ q_{3,k}\right)^T$, non-gravitational acceleration, gyroscope drift, and magnetic disturbance, as in Equation 26. Then, the evolution of the state vector was written based on the strap-down integration of angular velocity, ω_k:

$$x_{k+1}^- = [q_{k+1} \quad a_{k+1} \quad b_{G,k+1} \quad d_{k+1}]^T = \mathcal{F}_k x_k^+$$
$$= \begin{bmatrix} \exp(\Omega(\omega_k)T_s) & 0_{4\times3} & 0_{4\times3} & 0_{4\times3} \\ 0_{3\times4} & c_a I_{3\times3} & 0_{3\times3} & 0_{3\times3} \\ 0_{3\times4} & 0_{3\times3} & I_{3\times3} & 0_{3\times3} \\ 0_{3\times4} & 0_{3\times3} & 0_{3\times3} & c_d I_{3\times3} \end{bmatrix} x_k^+ \qquad \text{Equation 26}$$

where $\mathcal{F}_k$ is the state transition matrix and T_s is the sampling period of the IMU. $\Omega(\omega_k)$ is a 4×4 skew-matrix defined as in Equation 27,

$$\Omega(\omega_k) = \frac{1}{2}\begin{bmatrix} 0 & -\omega_{x,k} & -\omega_{y,k} & -\omega_{z,k} \\ \omega_{x,k} & 0 & \omega_{z,k} & -\omega_{y,k} \\ \omega_{y,k} & -\omega_{z,k} & 0 & \omega_{x,k} \\ \omega_{z,k} & \omega_{y,k} & -\omega_{x,k} & 0 \end{bmatrix} \qquad \text{Equation 27}$$

where ω_k is the corrected angular velocity, i.e., $y_{G,k} - b_{G,k}^+$. Also, $\exp(\cdot)$ in Equation 26 is the matrix exponential operation, which can be approximated by Padé approximation [350] or Taylor-series. Next, the *a priori* error covariance matrix, $\mathcal{P}_{k+1}^-$ was calculated according to Figure 4(a). To this end, the system model covariances matrix, $\mathcal{Q}_k$, was obtained under the assumption that

$\mathcal{w}_q$, $\mathcal{w}_a$, $\mathcal{w}_{b_G}$, and $\mathcal{w}_d$ are uncorrelated with one another, see [80], [106] for more details, as in Equation 28,

$$\mathcal{Q}_k = \begin{bmatrix} {T_s}^2/4\,\Xi_k {\sigma_G}^2 I_{3\times3} {\Xi_k}^T & 0_{4\times3} & 0_{4\times3} & 0_{4\times3} \\ 0_{3\times4} & {\sigma_{a,\mathcal{w}}}^2 T_s I_{3\times3} & 0_{3\times3} & 0_{3\times3} \\ 0_{3\times4} & 0_{3\times3} & {\sigma_{b_G,\mathcal{w}}}^2 T_s I_{3\times3} & 0_{3\times3} \\ 0_{3\times4} & 0_{3\times3} & 0_{3\times3} & {\sigma_{d,\mathcal{w}}}^2 T_s I_{3\times3} \end{bmatrix} \quad \text{Equation 28}$$

where σ_G, $\sigma_{a,\mathcal{w}}$, $\sigma_{b_G,\mathcal{w}}$, and $\sigma_{d,\mathcal{w}}$ are the variance of the white Gaussian noises affecting gyroscope readouts, estimated non-gravitational acceleration, estimated gyroscope drift, and estimated magnetic disturbance, respectively.

LKF Correction Model

The *a posteriori* estimate of orientation q_k^+ corrected via the accelerometer (y_A) and magnetometer (y_M) readouts was considered as the measurements, z_{k+1}. To calculate z_{k+1}, the gradient descent optimization technique was used similar to [64]: the difference between the estimated acceleration and geomagnetic field and the accelerometer and magnetometer readouts expressed in Equation 29 and Equation 30 should be minimized when the *a posteriori* state x_k^+ have an accurate estimate,

$$\mathcal{f}_A = \left(a + {}^{SF}_{G}q^* \otimes {}^{G}g \otimes {}^{SF}_{G}q\right) - y_A \quad \text{Equation 29}$$

$$\mathcal{f}_M = \left(d + {}^{SF}_{G}q^* \otimes {}^{G}m \otimes {}^{SF}_{G}q\right) - y_M \quad \text{Equation 30}$$

where $\mathcal{f} = [\mathcal{f}_A\ \mathcal{f}_M]^T$ is the objective function which should be minimized, ${}^{G}g$ and ${}^{G}m$ are the gravitational acceleration and the reference geomagnetic vector in the Earth reference frame (G), ${}^{SF}_{G}q$ is the orientation of the IMU sensor frame with respect to the Earth's reference frame, and $\otimes$ is the quaternion multiplication [64]. By simplifying Equation 29 and Equation 30, the objective function $\mathcal{f}$ can be obtained as in Equation 31,

$$\mathcal{f} = \begin{bmatrix} a_x + 2(q_1q_3 - q_0q_2) - y_{A,x} \\ a_y + 2(q_0q_1 + q_2q_3) - y_{A,y} \\ a_z + 2(0.5 - q_1^2 - q_2^2) - y_{A,z} \\ d_x + 2m_x(0.5 - q_2^2 - q_3^2) + 2m_y(q_0q_3 + q_1q_2) + 2m_z(q_1q_3 - q_0q_2) - y_{M,x} \\ d_y + 2m_x(q_1q_2 - q_0q_3) + 2m_y(0.5 - q_1^2 - q_3^2) + 2m_z(q_0q_1 + q_2q_3) - y_{M,y} \\ d_z + 2m_x(q_0q_2 + q_1q_3) + 2m_y(q_2q_3 - q_0q_1) + 2m_z(0.5 - q_1^2 - q_2^2) - y_{M,z} \end{bmatrix} \quad \text{Equation 31}$$

Then, the *a posteriori* state x_k^+ could be corrected via one iteration of gradient descent optimization as in Equation 32 to obtain z_{k+1},

$$z_{k+1} = x_k^+ - \mu \nabla \mathbb{f}(x_k^+) = x_k^+ - \mu \cdot \mathcal{J}_{\mathbb{f}}^T \cdot \mathbb{f}(x_k^+) \qquad \text{Equation 32}$$

where μ is the learning rate of the gradient descent and $\mathcal{J}_{\mathbb{f}}$ is the Jacobian of the function $\mathbb{f}$ as in Equation 33,

$$\mathcal{J}_{\mathbb{f}} = \frac{\partial \mathbb{f}}{\partial x} = \begin{bmatrix} H_A & I_{3\times3} & 0_{3\times6} \\ H_M & 0_{3\times6} & I_{3\times3} \end{bmatrix} \qquad \text{Equation 33}$$

and H_A and H_M were derived based on Equation 31 as in Equation 34,

$$H_A = 2\begin{bmatrix} -q_2 & q_3 & -q_0 & q_1 \\ q_1 & q_0 & q_3 & q_2 \\ 0 & -2q_1 & -2q_2 & 0 \end{bmatrix}$$

$$H_M = 2\begin{bmatrix} m_y q_3 - m_z q_2 & m_y q_2 + m_z q_3 & -2m_x q_2 + m_y q_1 - m_z q_0 & -2m_x q_3 + m_y q_0 + m_z q_1 \\ -m_x q_3 + m_z q_1 & m_x q_2 - 2m_y q_1 + m_z q_0 & m_x q_1 + m_z q_3 & -m_x q_0 - 2m_y q_3 + m_z q_2 \\ m_x q_2 - m_y q_1 & m_x q_3 - m_y q_0 - 2m_z q_1 & m_x q_0 + m_y q_3 - 2m_z q_2 & m_x q_1 + m_y q_2 \end{bmatrix} \qquad \text{Equation 34}$$

Equation 32 shows that the measurement vector is in fact a corrected version of the *a posteriori* state x_k^+. Therefore, the measurement transition matrix H_{k+1} is equal to the identity matrix. Finally, the measurement covariance matrix, $\mathcal{R}_{k+1}$ must be determined to calculate the Kalman gain, $\mathcal{K}_{k+1}$. To this end, first, we calculate the covariance matrix associated with accelerometer and magnetometer as in Equation 35,

$$\Sigma_{A,M} = \begin{bmatrix} {\sigma_A}^2 I_{3\times3} & 0_{3\times3} \\ 0_{3\times3} & {\sigma_M}^2 I_{3\times3} \end{bmatrix} \qquad \text{Equation 35}$$

where σ_A and σ_M are the standard deviation of the accelerometer and magnetometer readouts, respectively [106]. Then, as z_{k+1} is a nonlinear function of accelerometer and magnetometer readouts, we used the first-order Taylor series using the Jacobian of z_{k+1} to measurement covariance matrix as in Equation 36 [351],

$$\mathcal{R}_{k+1} = \mathcal{L} \cdot \Sigma_{A,M} \cdot \mathcal{L}^T \qquad \text{Equation 36}$$

where $\mathcal{L}$ is the Jacobian matrix of z_{k+1} and could be obtained as in Equation 37,

$$\mathcal{L} = \frac{\partial z_{k+1}}{\partial [y_A, y_M]} = \begin{bmatrix} \mu {H_A}^T & \mu {H_M}^T \\ \mu I_{3\times3} & 0_{3\times3} \\ 0_{3\times3} & 0_{3\times3} \\ 0_{3\times3} & \mu I_{3\times3} \end{bmatrix} \qquad \text{Equation 37}$$

5.2.1.2 Proposed Full-state Robust Extended Kalman Filter

The IMU model in Section 2.3.2 was used to develop a novel full-state robust EKF.

EKF Prediction Model

Figure 4(b) shows the flowchart of an EKF. The state vector of the proposed LKF, x, was composed of the estimated orientation of the IMU, expressed as a unit quaternion $q_k = \left(q_{0,k}\ q_{1,k}\ q_{2,k}\ q_{3,k}\right)^T$, non-gravitational acceleration, gyroscope drift, and magnetic disturbance, as in Equation 26. Then, the evolution of the state vector over time, $\mathbb{f}_k(x_k^+, 0)$, was written based on the strap-down integration of angular velocity, ω_k, similar to the proposed LKF, Equation 26. Also, $\exp(\cdot)$ in Equation 26 is the matrix exponential operator, which was computed by the second-order Taylor series approximation, as suggested by Lee and Choi [112],

$$\exp(\Omega(\omega_k)T_s) = I_{4\times4} + \Omega(\omega_k)T_s + \frac{1}{2}\Omega(\omega_k)^2{T_s}^2 \qquad \text{Equation 38}$$

Next, to calculate the *a priori* error covariance matrix $\mathcal{P}_{k+1}^-$, the system equation was linearized, as shown in Figure 4(b),

$$\mathcal{A}_k = \frac{\partial \mathbb{f}_k}{\partial x}\Big|_{x_k^+} = \begin{bmatrix} \exp(\Omega(\omega_k)T_s) & 0_{4\times3} & \mathcal{F}_k & 0_{4\times3} \\ 0_{3\times4} & c_a I_{3\times3} & 0_{3\times3} & 0_{3\times3} \\ 0_{3\times4} & 0_{3\times3} & I_{3\times3} & 0_{3\times3} \\ 0_{3\times4} & 0_{3\times3} & 0_{3\times3} & c_d I_{3\times3} \end{bmatrix} \qquad \text{Equation 39}$$

$$\mathcal{L}_k = \frac{\partial \mathbb{f}_k}{\partial w}\Big|_{x_k^+} = I_{13\times13}$$

where $\mathcal{F}_k$ was calculated as in Equation 40,

$$\mathcal{F}_k = \frac{{T_s}^2}{4} q_k^+ {\omega_k}^T + \frac{T_s}{2}\begin{bmatrix} q_{1,k}^+ & q_{2,k}^+ & q_{3,k}^+ \\ -q_{0,k}^+ & q_{3,k}^+ & -q_{2,k}^+ \\ -q_{3,k}^+ & -q_{0,k}^+ & q_{1,k}^+ \\ q_{2,k}^+ & -q_{1,k}^+ & -q_{0,k}^+ \end{bmatrix} = \frac{{T_s}^2}{4} q_k^+ {\omega_k}^T + \frac{T_s}{2}\Xi_k \qquad \text{Equation 40}$$

Also, the process covariances matrix, Q_k, was obtained similar to Equation 28.

EKF Correction Model

Similar to the proposed LKF, accelerometer (y_A) and magnetometer (y_M) readouts were considered as the sensor measurements, z_{k+1}. To calculate the predicted measurements, $\mathbb{h}_{k+1}(x_{k+1}^-, 0)$, we

used the following idea: assuming that the IMU is at rest in a magnetically undisturbed environment, the estimated measurements $\hat{y}_A$ and $\hat{y}_M$ could be estimated based on the gravitational acceleration (^{G}g) and the geomagnetic vector (^{G}m) in the Earth's reference frame (G), respectively, according to Equation 41,

$$\hat{y}_A = {}^{SF}_{G}q^* \otimes [0 \ {}^{G}g] \otimes {}^{SF}_{G}q$$
$$\hat{y}_M = {}^{SF}_{G}q^* \otimes [0 \ {}^{G}m] \otimes {}^{SF}_{G}q \quad \text{Equation 41}$$

where ${}^{SF}_{G}q$ is the orientation of the IMU sensor frame with respect to the Earth's reference frame, $*$ and $\otimes$ are the quaternion conjugate and multiplication operations, respectively [64]. Therefore, the measurement equation can be written as $\hbar_{k+1}(x^-_{k+1}, 0) = [\hat{y}_A \ \hat{y}_M]^T$ using Equation 41. Then, Equation 41 was extended to the general case in which the IMU is moving in a magnetically disturbed environment using the predicted non-gravitational acceleration (a_k) and magnetic disturbance (d_k) as in Equation 42,

$$\hat{y}_A = \begin{bmatrix} a_x + 2(q_1q_3 - q_0q_2) \\ a_y + 2(q_0q_1 + q_2q_3) \\ a_z + 2(0.5 - q_1^2 - q_2^2) \end{bmatrix}$$
$$\hat{y}_M = \begin{bmatrix} d_x + 2m_x(0.5 - q_2^2 - q_3^2) + 2m_y(q_0q_3 + q_1q_2) + 2m_z(q_1q_3 - q_0q_2) \\ d_y + 2m_x(q_1q_2 - q_0q_3) + 2m_y(0.5 - q_1^2 - q_3^2) + 2m_z(q_0q_1 + q_2q_3) \\ d_z + 2m_x(q_0q_2 + q_1q_3) + 2m_y(q_2q_3 - q_0q_1) + 2m_z(0.5 - q_1^2 - q_2^2) \end{bmatrix} \quad \text{Equation 42}$$

where $(q_0 \ q_1 \ q_2 \ q_3)$ are the components of ${}^{SF}_{G}q$, $(m_x \ m_y \ m_z)$ are the components of ${}^{G}m$, ${}^{G}g$ is (0, 0, 1), and the index $k+1$ and superscript "–" (the *a priori* estimate) were dropped for brevity. Next, to calculate the Kalman gain, $\mathcal{K}_{k+1}$, the measurement equation was linearized as in Equation 43,

$$\mathcal{H}_{k+1} = \left.\frac{\partial \hbar_{k+1}}{\partial x}\right|_{x^-_{k+1}} = \begin{bmatrix} H_A & I_{3\times3} & 0_{3\times6} \\ H_M & 0_{3\times6} & I_{3\times3} \end{bmatrix}$$
$$\mathcal{M}_{k+1} = \left.\frac{\partial \hbar_{k+1}}{\partial v}\right|_{x^-_{k+1}} = I_{6\times6} \quad \text{Equation 43}$$

where H_A and H_M were derived based on definitions of $\hat{y}_A$ and $\hat{y}_M$ as in Equation 44,

$$H_A = 2\begin{bmatrix} -q_2 & q_3 & -q_0 & q_1 \\ q_1 & q_0 & q_3 & q_2 \\ 0 & -2q_1 & -2q_2 & 0 \end{bmatrix}$$

Equation 44

$$H_M = 2\begin{bmatrix} m_y q_3 - m_z q_2 & m_y q_2 + m_z q_3 & -2m_x q_2 + m_y q_1 - m_z q_0 & -2m_x q_3 + m_y q_0 + m_z q_1 \\ -m_x q_3 + m_z q_1 & m_x q_2 - 2m_y q_1 + m_z q_0 & m_x q_1 + m_z q_3 & -m_x q_0 - 2m_y q_3 + m_z q_2 \\ m_x q_2 - m_y q_1 & m_x q_3 - m_y q_0 - 2m_z q_1 & m_x q_0 + m_y q_3 - 2m_z q_2 & m_x q_1 + m_y q_2 \end{bmatrix}$$

Also, the measurement covariance matrix, $\mathcal{R}_{k+1}$, was obtained as in Equation 45,

$$\mathcal{R}_{k+1} = \begin{bmatrix} {\sigma_A}^2 I_{3\times 3} & 0_{3\times 3} \\ 0_{3\times 3} & {\sigma_M}^2 I_{3\times 3} \end{bmatrix} \qquad \text{Equation 45}$$

where σ_A and σ_M are the standard deviation of the accelerometer and magnetometer readouts, respectively. Finally, the unit-norm property of the *a posteriori* quaternion, q_{k+1}^+, was preserved by a normalization step, i.e., dividing q_{k+1}^+ by its Euclidean norm [106].

Robust EKF

This section presents the procedure for converting the EKF formulation to the robust EKF using the structure of a H_∞ filter. To build a H_∞ filter, we assume that in the state-space model in Equation 13, the process and measurement noises are energy bounded $l_2[0,\infty)$ signals, i.e., $\sum_{k=0}^{\infty} {w_k}^T w_k < \infty$ and $\sum_{k=0}^{\infty} {v_k}^T v_k < \infty$. Then, the purpose of the H_∞ filter is to find an estimation strategy that minimizes the H_∞ norm of the mapping between $x_0 - x_0^+$, w_k, v_k and the estimation error [352]. It was shown that a closed-form solution for optimal H_∞ filter is available for only limited cases [353]. Therefore, a suboptimal solution that bounds the worst-case estimation error is commonly treated in the literature by satisfying the objective function in Equation 46,

$$\frac{\sum_{j=0}^{k} \left\| x_j - x_j^+ \right\|_2^2}{\|x_0 - x_0^+\|_{P_0^{-1}}^2 + \sum_{j=0}^{k} \left\| w_j \right\|_{Q^{-1}}^2 + \sum_{j=0}^{k} \left\| v_j \right\|_{\mathcal{R}^{-1}}^2} < \gamma^2 \qquad \text{Equation 46}$$

where $\gamma > 0$ is a user-specified scaler and determines the worst-case estimation error upper bound, the notation $\|a\|_W^2$ is the square of the weighted l_2 norm of a, i.e., $\|a\|_W^2 = a^T W a$, $\mathcal{P}_0$ is the initial covariance of the estimation error, and other parameters carry a similar definition as in the EKF [352]. Then, a closed-form solution to the suboptimal H_∞ filter can be formulated as a robust EKF [352], [354], using the structure of the EKF derived in the previous two sections, except for the *a posteriori* error covariance matrix equation which is given by Equation 47,

$$\mathcal{P}_{k+1}^{+} = \mathcal{P}_{k+1}^{-} - \mathcal{P}_{k+1}^{-}[\mathcal{H}_{k+1}^{T}\ I_{13\times13}]\mathcal{L}_{k+1}^{-1}\begin{bmatrix}\mathcal{H}_{k+1}\\ I_{13\times13}\end{bmatrix}\mathcal{P}_{k+1}^{-}$$

$$\mathcal{L}_{k+1} = \begin{bmatrix}\mathcal{R}_{k+1} & 0_{6\times13}\\ 0_{13\times6} & -\gamma^{2}I_{13\times13}\end{bmatrix} + \begin{bmatrix}\mathcal{H}_{k+1}\\ I_{13\times13}\end{bmatrix}\mathcal{P}_{k+1}^{-}[\mathcal{H}_{k+1}^{T}\ I_{13\times13}]$$

Equation 47

5.2.2 Sensor Fusion Algorithms' (SFAs') Gains

Table 10 lists the gains associated with the implemented SFAs. It has been shown that an SFA's performance highly depends on its gains [325], [364] and that adaptive gain tuning could significantly improve the accuracy and reliability of an SFA [25]. Therefore, to perform a fair comparison between the implemented SFAs, a similar procedure to Chapter 4 was followed to find the optimal adaptive gain tuning scheme for each SFA. Notably, for each SFA, an optimization routine (Figure 13(a)) was executed to find a two-level hard-switch for intuitively tunable gains of an SFA using IMU readouts, i.e., y_A, y_G, and y_M.

As described in Chapter 4, each two-level hard-switch adjusts one of the intuitively tunable gains of an SFA between two predefined levels G_1 and G_2 by applying a threshold S to (1) deviation of $\|y_{A,k}\|$ from $\|y_{A,stat}\|$ measured during a static condition; (2) deviation of $\|y_{M,k}\|$ from $\|y_{M,stat}\|$ measured during an undisturbed magnetic condition; and (3) $\|y_{G,k}\|$ (assuming $\|y_{G,k}\| \approx 0$ during a static condition). Note that for some SFAs, the gain associated with each of the accelerometer, magnetometer, and gyroscope sensors is different and tunable; for example, see the implemented KFs in Table 10. For these SFAs, three two-level hard-switches were designed to tune the gains associated with accelerometer, magnetometer, and gyroscope separately as in Equation 48, Equation 49, and Equation 50:

Table 10 The list of the implemented SFAs and their gains. Abbreviations/symbols used in the table are described in the table footnotes. Please see the original paper related to each SFA for details of the algorithms and gains. Subscripts 1 and 2 show that the gain value was adaptively tuned to level 1 or 2 as described in Section 5.2.2, while for gains with no number subscript, the fixed optimal values were used.

Study	Name	SFA Gains
[355]	Markely(2003)	$(\mathcal{P}_0, \sigma_{G_1}, \sigma_{G_2}, S_G, \sigma_{A_1}, \sigma_{A_2}, S_A, \sigma_{M_1}, \sigma_{M_2}, S_M, \sigma_{b_G})$
[107]	Roeternberg(2005)	$(\mathcal{P}_0, \sigma_{G_1}, \sigma_{G_2}, S_G, \sigma_{A_1}, \sigma_{A_2}, S_A, \sigma_{M_1}, \sigma_{M_2}, S_M, \zeta, \xi, \gamma, \sigma, m_{exp})$
[356]	Choukroun(2006)	$(\mathcal{P}_0, \sigma_{G_1}, \sigma_{G_2}, S_G, \sigma_{A_1}, \sigma_{A_2}, S_A, \sigma_{M_1}, \sigma_{M_2}, S_M)$
[106]	Sabatini(2006)	$(\mathcal{P}_0, \sigma_{G_1}, \sigma_{G_2}, S_G, \sigma_{A_1}, \sigma_{A_2}, S_A, \sigma_{M_1}, \sigma_{M_2}, S_M, \sigma_{b_A}, \sigma_{b_M})$
[65]	Mahony(2008)	$(k_{p_1}, k_{p_2}, S_A, S_A, k_i)$
[96]	Martin(2010)	$(l_a, l_c, l_d, \sigma, n, o)$
[110]	Suh(2010)	$(\mathcal{P}_0, \mathcal{P}_{b_G}, \mathcal{P}_{b_A}, \sigma_{G_1}, \sigma_{G_2}, S_G, Q_{b_G}, Q_{b_A}, M_1, M_2, \gamma, \sigma_{M_1}, \sigma_{M_2}, S_M)$
[64]	Madgwick(2011) (MIMU)	$(\beta_1, \beta_2, S_A, S_M, \zeta)$
[64]	Madgwick(2011) (IMU)	$(\beta_1, \beta_2, S_A, \zeta)$
[95], [133]	Fourati(2011)	$(k_{A_1}, k_{A_2}, S_A, k_{M_1}, k_{M_2}, S_M, \beta)$
[156]	Hua(2014)	$(k_1, k_2, k_3, k_4, k_b, \Delta)$
[93]	Renaudin(2014)	$(\mathcal{P}_0, \sigma_{G_1}, \sigma_{G_2}, S_G, \sigma_{A_1}, \sigma_{A_2}, S_A, \sigma_{M_1}, \sigma_{M_2}, S_M)$
[128]	Valenti(2015)	$(\sigma_{b_G}, \alpha_A, e_1, e_2, \sigma_{M_1}, \sigma_{M_2}, S_M, S_G, S_A, S_b)$
[85]	Ligorio(2015)	LKF1: $(\mathcal{P}_A, \sigma_{G_1}, \sigma_{G_2}, S_G, \sigma_{A_1}, \sigma_{A_2}, S_A, c_{A_a}, c_{A_b})$ LKF2: $(\mathcal{P}_M, \sigma_{G_1}, \sigma_{G_2}, S_G, \sigma_{M_1}, \sigma_{M_2}, S_M, c_{M_a}, c_{M_b})$
[54]	Hyyti(2015)	$(\mathcal{P}_{DCM}, \mathcal{P}_{b_G}, \sigma_{G_1}, \sigma_{G_2}, S_G, \sigma_b, \sigma_{A_f}, \sigma_A)$
[159]	Marantos(2016)	$(w_{A_1}, w_{A_2}, S_A, w_{M_1}, w_{M_2}, S_M, Tot, S_G)$
[135]	DelRosario(2016)	$(\mu_{A_s}, \mu_{A_d}, S_A, \mu_{M_s}, \mu_{M_d}, w_L)$
[158]	Wu(2016)	$(\gamma_{A_1}, \gamma_{A_2}, S_A, Thr_A, \gamma_{M_1}, \gamma_{M_2}, S_M, Thr_M)$
[129]	Valenti(2016)	$(\mathcal{P}_0, \sigma_{G_1}, \sigma_{G_2}, S_G, \sigma_{A_1}, \sigma_{A_2}, S_A, \sigma_{M_1}, \sigma_{M_2}, S_M)$
[348]	Chen(2017)	$(\mathcal{P}_0, \sigma_{G_1}, \sigma_{G_2}, S_G, \sigma_{A_1}, \sigma_{A_2}, S_A, \sigma_{M_1}, \sigma_{M_2}, S_M, c_a, c_d, \sigma_{b_G})$
[357]	FouratiMartin(2011)	$(k_{A_1}, k_{A_2}, S_A, k_{M_1}, k_{M_2}, S_M, \beta)$
[195]	Guo(2017)	$(\mathcal{P}_0, \sigma_{G_1}, \sigma_{G_2}, S_G, \sigma_{A_1}, \sigma_{A_2}, S_A, \sigma_{M_1}, \sigma_{M_2}, S_M)$
[272]	DelRosario(2018)	$(c_a, c_m, N_S, N_L, N_m, \sigma_{G_1}, \sigma_{G_2}, S_G, \xi_a, \xi_{xy})$
[126]	Wu(2018)	$(\mathcal{P}_0, \sigma_{Q_y}, \sigma_{G_1}, \sigma_{G_2}, S_G, \sigma_{A_1}, \sigma_{A_2}, S_A, \sigma_{M_1}, \sigma_{M_2}, S_M)$
[137]	Wu(2019)	$(w_A, w_M, \sigma_{G_1}, \sigma_{G_2}, S_G, X)$
[358]	Suh(2019)	$(\sigma_{G_1}, \sigma_{G_2}, S_G, \sigma_{A_1}, \sigma_{A_2}, S_A, \sigma_{M_1}, \sigma_{M_2}, S_M)$
[185]	Justa(2020)	$(\sigma_{A_1}, \sigma_{A_2}, S_A, \sigma_{M_1}, \sigma_{M_2}, S_M)$
[359]	Wu(2020)(Plain)	$(\mathcal{P}_0, \sigma_{G_1}, \sigma_{G_2}, S_G, \sigma_{A_1}, \sigma_{A_2}, S_A, \sigma_{M_1}, \sigma_{M_2}, S_M, \mu)$
[359]	Wu(2020)(Recursive)	$(\mathcal{P}_0, \sigma_{G_1}, \sigma_{G_2}, S_G, \sigma_{A_1}, \sigma_{A_2}, S_A, \sigma_{M_1}, \sigma_{M_2}, S_M, \mu)$
[360]	GyroLib(2020)	$(\mathcal{P}_0, \sigma_{G_1}, \sigma_{G_2}, S_G, \sigma_{A_1}, \sigma_{A_2}, S_A, \sigma_{M_1}, \sigma_{M_2}, S_M, \sigma_{b_G})$
Proposed	Nazarahari(2020)	$(\mathcal{P}_0, \sigma_{G_1}, \sigma_{G_2}, S_G, \sigma_{A_1}, \sigma_{A_2}, S_A, \sigma_{M_1}, \sigma_{M_2}, S_M, c_a, c_d, \sigma_a, \sigma_{b_G}, \sigma_d, \mu)$
Proposed	Nazarahari(2021)	$(\mathcal{P}_0, \sigma_{G_1}, \sigma_{G_2}, S_G, \sigma_{A_1}, \sigma_{A_2}, S_A, \sigma_{M_1}, \sigma_{M_2}, S_M, c_a, c_d, \sigma_a, \sigma_{b_G}, \sigma_d, \gamma)$
Proposed	SRCKF (cubature points [347])	$(\mathcal{P}_0, \sigma_{G_1}, \sigma_{G_2}, S_G, \sigma_{A_1}, \sigma_{A_2}, S_A, \sigma_{M_1}, \sigma_{M_2}, S_M, c_a, c_d, \sigma_{b_G})$
Proposed	SRUKF1 (sigma points [349])	$(\mathcal{P}_0, \sigma_{G_1}, \sigma_{G_2}, S_G, \sigma_{A_1}, \sigma_{A_2}, S_A, \sigma_{M_1}, \sigma_{M_2}, S_M, c_a, c_d, \sigma_{b_G}, \alpha, \beta)$
Proposed	SRUKF2 (sigma points [361])	$(\mathcal{P}_0, \sigma_{G_1}, \sigma_{G_2}, S_G, \sigma_{A_1}, \sigma_{A_2}, S_A, \sigma_{M_1}, \sigma_{M_2}, S_M, c_a, c_d, \sigma_{b_G}, \kappa)$
Proposed	SRUKF3 (sigma points [362])	$(\mathcal{P}_0, \sigma_{G_1}, \sigma_{G_2}, S_G, \sigma_{A_1}, \sigma_{A_2}, S_A, \sigma_{M_1}, \sigma_{M_2}, S_M, c_a, c_d, \sigma_{b_G}, w_0)$
Proposed	SRUKF4 (sigma points [363])	$(\mathcal{P}_0, \sigma_{G_1}, \sigma_{G_2}, S_G, \sigma_{A_1}, \sigma_{A_2}, S_A, \sigma_{M_1}, \sigma_{M_2}, S_M, c_a, c_d, \sigma_{b_G}, w_n)$

- **Abbreviations:** LKF: linear Kalman filter; SRCKF: square-root cubature Kalman filter; SRUKF: square-root unscented Kalman filter.
- **Symbols:** $\mathcal{P}_0$: initial state error covariance matrix; G: gyroscope-related gain/threshold; A: accelerometer-related gian/threshold; M: magnetometer-related gian/threshold; σ_{b_G}: gyroscope bias gain.
- **Proposed**: We originally proposed Nazarahari(2020) and Nazarahari(2021) in this work, and the other SFAs, labeled as proposed, were previously introduced in the literature, but we originally implemented them for IMU orientation estimation.

$$\sigma_A = \begin{cases} \sigma_{A_1}, & \left|\|y_{A,k}\| - \|y_{A,stat}\|\right| < S_A \\ \sigma_{A_2}, & \text{otherwise} \end{cases} \quad \text{Equation 48}$$

$$\sigma_M = \begin{cases} \sigma_{M_1}, & \left|\|y_{M,k}\| - \|y_{M,stat}\|\right| < S_M \\ \sigma_{M_2}, & \text{otherwise} \end{cases} \quad \text{Equation 49}$$

$$\sigma_G = \begin{cases} \sigma_{G_1}, & \|y_{G,k}\| < S_G \\ \sigma_{G_2}, & \text{otherwise} \end{cases} \quad \text{Equation 50}$$

where σ_A, σ_M, σ_G are the values of gains for the accelerometer, magnetometer, and gyroscope sensors, respectively, $\|y_{A,stat}\|$ and $\|y_{M,stat}\|$ are the norm of the acceleration and geomagnetic field at rest (measured when the IMU is motionless at the beginning of the experiment), and S_A, S_M, and S_G are the switching thresholds for the acceleration, geomagnetic field, and angular velocity, respectively. On the other hand, for some SFAs, the same intuitively tunable gain is applied to two or more sensors; for example, see gains of Madgwick(2011) [64] or Mahony(2008) [65] in Table 10. For these SFAs, a single two-level hard-switch was designed to adjust the tunable gain. For instance, for Madgwick(2011) [64], we used Equation 23 to tune the gain β. Note that not all the gains of an SFA are tunable in an intuitive manner. Thus, as shown in Table 10, adaptive gain tuning was only applied to specific intuitively tunable gains (mostly the gains that control the weights associated with accelerometer/magnetometer/gyroscope estimations), while for the remaining gains, their fixed optimal values were found and used similar to [25].

Table 11 The selected the state-of-the-art SFAs with (a) a CF structure (including linear CF (LCF) and nonlinear CF (NCF)), and (b) KF structure (including linear KF (LKF), extended KF (EKF), complimentary KF (CKF), square-root unscented KF (SRUKF), and square-root cubature KF (SRKKF)). Abbreviations/symbols used in the table are described in the table footnotes.

(a) Deterministic SFAs

Study	Method	Parametrization	b_G, a, d compensation	Notes
[65]	NCF	$[q]$	b_G	-
[96]	NCF	$[q]$	b_G	-
[64]	GDA+CF	$[q]$	b_G	MIMU: uses both y_A, y_M; IMU: only uses y_A
[95], [133]	LMA+CF	$[q]$	-	-
[156]	NCF	DCM	b_G	-
[128]	AQA+CF	$[q]$	-	a rejection using LERP or SLERP + adaptive gain tuning
[159]	Nonlinear SVD+CF	[DCM]	-	-
[135]	Geometrically-intuitive CF	$[q]$	-	-
[158]	Two-layer LCF	$[q]$	-	d rejection with thresholding
[357]	LMA+CF	$[q]$	-	d rejection with thresholding
[137]	GDA+CF	$[q]$	-	a & d rejection with thresholding
[185]	LCF	$[q]$	-	-

(b) Stochastic SFAs

Study	Method	State vector components	Measurement-update	Notes
[355]	Multiplicative EKF	$[q, b_G]$	$[y_A, y_M]$	-
[107]	CKF	[eHelical angle/axis, eb_G, ed]	[Attitude from y_A & y_G, magnetic vector from y_M & y_G]	-
[356]	LKF	$[q]$	$[\hat{q}]$, $\hat{q}$ from y_A & y_M	-
[106]	EKF	$[q, b_A, b_M]$	$[y_A, y_M]$	Switching $\mathcal{R}$ between two levels
[110]	CKF	$[eq, b_G, b_A]$	$[y_A, y_M]$	Tuning $\mathcal{R}$ using residual in acc. measurement-update
[93]	EKF	$[q, b_G, a]$	$[y_A, y_M]$	-
[85]	LKF+LKF	LKF1: $[\hat{g}, a]$, LKF2: $[\hat{m}, d]$	LKF1: $[y_A]$, LKF2: $[y_M]$	-
[54]	Constrained-EKF	[DCM(3), b_G]	$[y_A]$	Tuning $\mathcal{R}$ based on $\|y_A\|$
[129]	LKF	$[q]$	$[\hat{q}]$, $\hat{q}$ from AQA(y_A,y_M)	-
[348]	EKF	$[q, b_G, a]$	$[y_A, y_M]$	-
[195]	LKF	$[q]$	$[\hat{q}]$, $\hat{q}$ from y_A & y_M	-
[272]	Two-layer CKF	CKF1: [eAttitude], CKF2: [eYaw]	CKF1: [$e\hat{q}$ from y_A], CKF2: [$e\hat{q}$ from y_M]	Tuning $\mathcal{R}$ by variances of errors
[126]	LKF	$[q]$	$[\hat{q}]$, $\hat{q}$ from y_A & y_M	-
[358]	CKF	$[eq]$	$[y_A, y_M]$	d rejection with thresholding
[360]	LKF	$[q, b_G]$	$[y_A, y_M]$	-

Study	Method	State vector components	Measurement-update	Notes
[359]	GDA+LKF	$[q]$	$[\hat{q}]$, $\hat{q}$ from GDA(y_A,y_M)	a rejection with thresholding; two versions are proposed: Plain and Recursive
Proposed	GDA+LKF	$[q, b_G, a, d]$	$[\hat{q}]$, $\hat{q}$ from GDA(y_A,y_M)	-
Proposed	Robust EKF	$[q, b_G, a, d]$	$[y_A, y_M]$	-
Proposed	SRUKF	$[q, b_G, a]$	$[y_A, y_M]$	Basic SFA equations from [348]; SRUKF structure based on [349]; Four sets of sigma points: SRUKF1 [349], SRUKF2 [361], SRUKF3 [362], SRUKF4 [363]
Proposed	SRCKF	$[q, b_G, a]$	$[y_A, y_M]$	Basic SFA equations from [348]; SRCKF structure based on [347]

- **Method:** GDA: Gradient descent algorithm; LMA: Levenberg-Marquardt algorithm; AQA: algebraic quaternion algorithm; LERP: Linear intERPolation; SLERP: Spherical Linear intERPolation;
- **Orientation Parametrization:** q: Quaternion; EA: Euler angles; DCM: Direction cosine matrix.
- **IMU Model parameters:** b_G: Gyroscope bias; b_A: Accelerometer bias; b_M: Magnetometer bias; a: external non-gravitational acceleration; d: magnetic disturbance; $\hat{q}$: Orientation used in measurement-update of KF; $\hat{g}$: Estimated gravitational acceleration; $\hat{m}$: Estimated geomagnetic field.

Notes: $\mathcal{R}$: Measurement model covariance matrix in KFs; e: Error of the parameter of interest in CKFs.

5.2.3 Gain Optimization for Sensor Fusion Algorithms

To obtain the optimal gains for each SFA (whether two-level hard-switch or fixed gains), we performed the procedure described in Chapter 4:

1. We used IMU readouts to estimate the orientation using an SFA (using non-optimal gains): $\hat{q}$ (quaternion, parametrization).
2. We compared the estimated orientation ($\hat{q}$) with the reference orientation obtained by MCS, q, and calculated the error in estimated orientation as q_e.
3. We transformed the error quaternion q_e to Euler angles and fed the estimation error equal to RMS($\text{roll}_{\text{error}}$) + RMS($\text{pitch}_{\text{error}}$) + RMS($\text{yaw}_{\text{error}}$) (RMS: root-mean-square) as the cost function to a Particle Swarm Optimization [330] routine to be minimized.
4. The Particle Swarm Optimization routine changed the SFA gains toward improving the estimation orientation $\hat{q}$ and minimizing the estimation error.

The Particle Swarm Optimization routine was executed in 8 rounds for each SFA. In the first 4 rounds, random numbers were used as the initial population and range for SFA gains. The obtained results were then used as a part of the initial population (plus random initial population to avoid premature convergence) for the next rounds. The parameters of the Particle Swarm Optimization were selected as follows: maximum number of iterations = 50, population size = 50,

inertia weight = 0.73, inertia weight damping ratio = 0.99, personal learning coefficient = 1.50, and global learning coefficient = 1.50. The training data set (used to optimized SFA gains as described above) and the testing data set (used to evaluate the SFA performance) are discussed in Section 5.2.7.

5.2.4 Measurement setup

An IMU (MTws, Xsens Technologies, The Netherlands) was attached to a rigid plastic plate equipped with four retro-reflective markers (Figure 13(b)) and fixed over the foot using double-sided medical tape. The IMU included a tri-axial accelerometer (range: ±16g), a tri-axial gyroscope (range: ±2000 degrees/s), and a tri-axial magnetometer (range: ±1.9 Gauss). The IMU recorded data with a sampling frequency of 100 Hz and transferred it wirelessly to a computer. Also, a MCS (VICON, Oxford Metrics Group, UK) with eight cameras was used as the reference system to record the 3D position of the plate markers synchronized with IMUs. The MCS was used to measure the reference orientation of the plate based on its markers. Before any data processing, signals were low-pass filtered using a zero-phase 4th-order digital Butterworth filter with a cut-off frequency of 30 Hz. Furthermore, the least-square approach presented in [365], [366] was employed to reduce the noise of the data recorded by the MCS.

5.2.5 Comparing Estimated and Reference Orientations

As described above, the estimated orientation was calculated using an SFA, while the reference orientation was obtained by tracking the plate markers using the MCS. Thus, we represent the direction cosine matrix parametrization of the estimated (IMU) and reference (MCS) orientations by ${}^{GF_{IMU}}_{SF}R_k$ and ${}^{GF_{MCS}}_{PF}R_k$, respectively, at each time step k with respect to their global reference frames GF_{IMU} and GF_{MCS}. Here, SF and PF show the local frames of the IMU and plate. Then, the estimation error between IMU and MCS can be calculated as in Equation 24. Then, the estimation error ${}_{E}R_k$ in Equation 24 was converted into Euler angles and used as the input of the Particle Swarm Optimization routine as described in Section 5.2.3.

5.2.6 Experimental Procedure

Some of the previous experimental comparison studies did not evaluate the performance of the implemented SFAs in testing conditions close to real-life scenarios. These studies considered motions with limited (1) range of motion; (2) intensity and pattern; and (3) testing duration; see

[22] for more details. In contrast, in the current study, we evaluated the SFAs performance in an extensive experimental study with nine able-bodied participants (all male, 26±2 years old, 74±6 kg, 177±4 cm). The Research Ethics Board Committee at the University of Alberta approved the study protocol, and written consent was obtained from all participants. The experimental protocol included two phases:

Phase I: quiet standing (60 seconds), straight walking (5 meters), turning, straight walking (2.5 meters), vertical jumping (two times), straight walking (2.5 meters), turning, hopping with both legs for 5 meters, turning, walking the 5-meter corridor back-and-forth three times with U-turns at the end, quiet standing (30 seconds). Also, participants were instructed to have 2 seconds of quiet standing between every two tasks (one complete trial was 131±7 seconds on average).

Phase II: quiet standing (60 seconds), walking (normal-pace) the 5-meter corridor back-and-forth for 75 seconds with U-turns at the end, walking (normal-pace) the 5-meter corridor back-and-forth for 75 seconds making an ∞-shape, quiet standing (5 seconds), repeating the above two walking periods with a fast pace, quiet standing for 30 seconds (one complete trial was 393±3 seconds in average). The first participant's data were discarded in *Phase II* as the IMU data were not recorded correctly.

Phase I was performed to evaluate the accuracy and reliability of the implemented SFAs under various motion patterns/intensities. *Phase II* was performed to assess the performance of the SFAs during highly dynamic long-duration tasks. Experiments have been performed on three separate days, three participants per day, to assess SFAs' accuracy and reliability in different environmental conditions, e.g., room temperature. Also, the IMU was kept motionless for 10 minutes before data collection to ensure that it has reached a stable condition. Furthermore, each trial's first 30 seconds were used to allow the SFAs to converge to a stable orientation without a need for a drastic change in SFAs' gains during the test.

5.2.7 Gain Optimization vs. Testing

Three-fold cross-validation was performed using the experimental data of *Phase I*. Notably, the IMU data of one participant from each day in *Phase I* (for example, participants 1, 4, 7 from days 1, 2, and 3, respectively) were used as the "training data set" to find the optimal gains for each SFA according to the procedure described in Section 5.2.3. The data of the remaining six participants in *Phase I* and all eight participants in *Phase II* were used as the "testing data set" to

evaluate the performance of the SFAs. Then, the same procedure was repeated twice for each of the two sets of three participants from *Phase I*. As a result, the number of testing results in each fold was: *Phase I*: 18 samples (test data of six participants for each fold × 3-fold cross-validation) and *Phase II*: 24 samples (test data of eight participants for each fold × 3-fold cross-validation).

5.2.8 Performance Evaluation

Previous studies have shown that offline calibration of the accelerometer, gyroscope, and magnetometer plays a significant role in improving the performance of SFAs [357]. Unfortunately, the recorded data in this study could not be used to calibrate the accelerometer and magnetometer. However, to investigate the effect of the gyroscope static bias on SFA performance, we measured the estimation error in two conditions:

1. Raw IMU data were low-pass filtered and used to find optimal gain and test SFAs.
2. The gyroscope static bias was removed from the low-pass filtered data before gain optimization and testing. Gyroscope static bias was estimated as the mean value of y_G during quiet standing at the beginning of each trial as the foot-worn IMU could be considered motionless during this period.

The estimation error of each SFA was quantified as the RMS of the Quaternion Angle Difference (QAD) as in Equation 51 [357], [367]:

$$e = \text{RMS}(\cos^{-1}(2\langle q \cdot \hat{q}\rangle^2 - 1)) \qquad \text{Equation 51}$$

where e is the RMS of QAD, q and $\hat{q}$ are the reference (MCS) and estimated (IMU) orientations in quaternion parametrization, respectively, and $\cdot$ is inner (or dot) product. QAD provides a single quantity representing the distance between two rotations, which can be used in statistical analysis to find SFAs with a significantly lower estimation error (or higher accuracy). Notably, we compared the accuracy (median of RMS(QAD) among all testing data set) of each SFA between with and without gyroscope static bias removal using the Wilcoxon rank-sum test (significance level = 5%). Also, we compared the accuracy (median of RMS(QAD) among all testing data set) of the SFAs after gyroscope static bias removal against one another using the Kruskal-Wallis test (significance level = 5%) and post-hoc multiple-comparison test with Tukey-Kramer correction.

Finally, the execution time for the selected SFAs from each family was recorded in milliseconds by measuring the total execution time of one trial and dividing the result by the

number of samples in that trial. This procedure was repeated 300 times for each SFA, and the median value was reported. All execution times were measured by using MATLAB R2020a (MathWorks, USA) on a desktop PC with the following characteristics: CPU: i7-9700K (3.60 GHz), RAM: 32 GB (2400 MHz).

5.3 Results and Discussions

5.3.1 Gyroscope Static Bias Removal

Table 12 compares the [25%,50% (median),75%] percentiles of the RMS(QAD) with and without gyroscope static bias removal and identifies significant ($p<0.05$) differences between them. According to Table 12, for all the implemented CFs, except Markely(2003) in *Phase I* and Marantos(2016) in both *Phases I and II*, removing the gyroscope static bias significantly ($p<0.05$) reduced the RMS(QAD). In other words, gyroscope static bias removal must be performed to achieve accurate estimations with CFs. Note that while some CFs such as Madgwick(2011) and Mahony(2008) have built-in mechanisms to estimate and remove gyroscope bias b_G during estimation (see Table 11), static bias removal still resulted in significantly ($p<0.05$) higher accuracy for them. Notably, for *Phase II* with long-duration trials, the maximum median RMS(QAD) among all CFs, except for Markely(2003) and Marantos(2016), was reduced from 48.3 to 5.8 degrees. Also, *Phase II* results should be indeed paid more attention to than *Phase I* because trials' durations were longer in *Phase II*. Thus, the cumulation of strap-down integration errors had a more prominent impact on *Phase II* results.

As Table 12 shows, in *Phase I*, all the implemented LKFs, except for GyroLib(2020), Valenti(2016), and Suh(2019), showed significantly ($p<0.05$) lower RMS(QAD) after gyroscope static bias removal. However, in *Phase II*, only 6 (out of 11) LKFs showed significantly ($p<0.05$) higher accuracy after static bias removal. Among LKFs with no performance improvement after static bias removal in *Phase II*, none had a built-in online b_G estimation mechanism, while among LKFs with performance improvement, only 3 (out of 6) had a built-in online b_G estimation mechanism. Therefore, we can not conclude based on the current results whether including an online b_G estimation can compensate for the lack of static bias removal. However, static bias removal did not significantly ($p<0.05$) lower performance in any of the LKFs. Thus, we recommend removing gyroscope static bias before starting estimations with LKFs.

Table 12 [25%,50% (median),75%] percentiles of the RMS of the quaternion angle difference (QAD) for all testing data in *Phase I* and *Phase II* with and without (removed) gyroscope static bias. For each SFA in each *Phase*, significantly ($p<0.05$) lower RMS(QAD), i.e., higher accuracy, between with and without static bias is indicated with †.

Sensor Fusion Algorithm		*Phase I*		*Phase II*	
		With Gyro Bias	**Without Gyro Bias**	**With Gyro Bias**	**Without Gyro Bias**
CF	Marantos(2016)	[9.0,10.9,19.2]	[8.2,10.9,23.2]	[27.3,30.7,33.7]	[20.8,24.8,28.7]
	DelRosario(2016)	[7.3,28.8,33.3]	[1.7,2.0,2.5]†	[33.9,42.5,49.1]	[3.9,4.3,4.9]†
	Markely(2003)	[1.9,2.1,2.4]	[2.0,2.1,2.4]	[31.1,33.0,38.1]	[19.1,28.4,31.5]†
	Wu(2016)	[3.5,3.7,4.4]	[1.8,2.0,2.6]†	[23.7,44.9,52.8]	[4.1,5.0,22.5]†
	Wu(2019)	[9.1,10.9,15.7]	[1.6,1.8,2.1]†	[24.7,33.5,46.0]	[3.9,4.3,4.7]†
	Valenti(2015)	[6.4,7.3,7.5]	[1.6,1.8,2.0]†	[27.8,29.9,31.2]	[3.8,4.3,4.4]†
	Hua(2014)	[5.3,8.5,11.6]	[1.6,1.6,1.9]†	[17.1,27.7,31.2]	[3.0,3.6,4.4]†
	Fourati(2011)	[5.1,6.0,7.6]	[1.6,1.8,1.9]†	[19.4,23.2,27.4]	[3.5,4.0,4.4]†
	FouratiMartin(2011)	[6.0,6.8,7.7]	[1.6,1.8,2.1]†	[13.2,18.5,22.0]	[3.1,3.6,3.9]†
	Madgwick(2011)(MIMU)	[4.8,5.8,8.0]	[1.7,1.9,2.2]†	[47.5,48.3,49.1]	[5.0,5.8,10.7]†
	Madgwick(2011)(IMU)	[3.3,4.1,6.3]	[1.6,1.8,2.1]†	[42.0,45.3,46.1]	[3.7,4.3,19.1]†
	Mahony(2008)	[6.6,7.4,7.4]	[1.6,1.8,1.9]†	[26.9,28.9,30.1]	[3.8,4.2,4.3]†
	Martin(2010)	[6.6,7.4,7.6]	[1.7,1.9,2.7]†	[25.7,27.7,30.5]	[3.5,4.2,4.7]†
	Justa(2020)	[2.8,3.4,4.3]	[1.7,2.1,3.1]†	[5.9,8.1,12.4]	[3.2,3.5,4.0]†
LKF	Wu(2020)(Plain)	[3.5,4.4,7.4]	[2.0,2.5,3.3]†	[9.4,16.0,39.8]	[6.2,15.0,27.6]
	Wu(2020)(Recursive)	[3.1,3.8,5.0]	[1.8,2.0,2.4]†	[7.3,7.8,10.9]	[3.9,4.8,5.2]†
	GyroLib(2020)	[2.0,2.2,2.3]	[1.9,2.4,2.7]	[10.1,21.6,47.0]	[3.5,8.3,15.3]†
	Ligorio(2015)	[3.7,4.5,6.5]	[1.6,2.3,2.7]†	[7.7,21.8,34.8]	[4.0,4.7,6.9]†
	Valenti(2016)	[7.3,8.2,10.2]	[2.1,10.4,14.5]	[21.8,23.3,27.6]	[16.7,21.9,44.2]
	Wu(2018)	[3.3,4.2,5.3]	[1.8,2.2,2.7]†	[9.4,11.2,16.2]	[12.6,14.8,16.1]
	Guo(2017)	[3.5,3.8,4.2]	[1.6,2.1,2.3]†	[8.6,11.6,14.8]	[6.7,9.9,13.7]
	Renaudin(2014)	[3.0,3.4,4.1]	[1.5,1.8,1.9]†	[5.8,7.9,14.5]	[3.1,3.6,3.9]†
	Choukroun(2006)	[3.4,3.9,4.2]	[1.7,1.9,1.2]†	[12.0,17.5,28.7]	[3.5,4.0,4.2]†
	Nazarahari(2020)	[3.7,4.1,4.9]	[1.7,1.8,2.1]†	[12.8,17.7,24.6]	[3.6,4.1,4.4]†
	Suh(2019)	[35.5,36.2,39.7]	[34.0,37.1,38.2]	[49.2,50.1,52.8]	[48.1,51.0,52.3]
EKF **CKF** **SRCKF** **SRUKF**	DelRosario(2018)	[6.1,6.7,7.0]	[1.6,1.8,2.0] †	[26.6,28.7,30.3]	[3.8,4.2,4.3]†
	Hyyti(2015)	[5.6,8.4,14.0]	[2.7,5.5,10.1]	[41.1,46.3,53.5]	[24.4,45.5,50.5]
	Chen(2017)	[2.2,2.4,3.2]	[2.3,2.6,3.4]	[5.2,9.4,23.4]	[6.3,10.0,22.1]
	Sabatini(2006)	[3.1,4.2,5.3]	[1.6,1.7,1.9]†	[7.4,12.0,15.4]	[2.7,3.2,3.7]†
	Suh(2010)	[3.0,3.3,4.0]	[1.8,2.1,2.4]†	[8.2,10.2,20.9]	[5.6,6.5,7.6]†
	Roeternberg(2005)	[2.3,3.0,3.6]	[1.6,1.7,2.0]†	[8.9,44.1,46.5]	[3.2,4.1,5.3]†
	Nazarahari(2021)	[2.3,2.7,2.9]	[1.6,1.8,2.1]†	[13.0,15.9,20.4]	[3.5,3.7,4.3]†
	SRCKF	[2.8,3.8,4.3]	[1.7,1.9,2.1]†	[5.1,6.6,9.2]	[3.0,3.6,5.0]†
	SRUKF1	[5.5,6.0,6.4]	[1.6,1.8,1.9]†	[26.0,27.6,29.2]	[3.8,4.0,4.2]†
	SRUKF2	[5.5,6.6,7.0]	[1.6,1.7,1.9]†	[26.3,28.0,29.2]	[3.8,4.1,4.2]†
	SRUKF3	[2.7,3.0,3.2]	[1.6,1.8,1.9]†	[11.8,14.8,16.5]	[3.6,3.8,4.2]†
	SRUKF4	[4.0,8.1,9.3]	[1.7,1.9,2.3]†	[14.7,25.6,31.9]	[3.5,3.9,4.2]†

Finally, according to Table 12, all SFAs from EKF, CKF, SRCKF, and SRUKF families, except for Hyyti(2015) and Chen(2017), significantly ($p<0.05$) higher accuracies were obtained

after static bias removal in both *Phases*. Notably, for *Phase II*, the maximum median RMS(QAD) among all these SFAs, except for Hyyti(2015) and Chen(2017), was reduced from 44.1 to 6.5 degrees. In contrast to LKFs, both Hyyti(2015) and Chen(2017) (that had built-in online b_G estimation) showed no performance improvement after static bias removal. Thus, we can hypothesize that including an online b_G estimation can compensate for the lack of gyroscope static bias removal for EKFs. However, as the evidence for this hypothesis is not strong with the current results (only 2 EKFs), we avoid drawing a general conclusion in this regard.

5.3.2 Sensor Fusion Algorithms Comparison

Table 13 presents the statistical comparison among the RMS(QAD) associated with *Phase I* and *Phase II* for the implemented SFAs. The following paragraphs present, discuss and compare the results obtained with each family of SFAs as classified in Figure 16 and Table 11.

Complementary Filters: Table 13(a) shows that for CFs, Hua(2014), FouratiMartin(2011), and Justa(2020) achieved a higher score than other SFAs in terms of the number of times they were significantly ($p<0.05$) more accurate than other CFs. Also, CFs identified with * in Table 13(a) obtained lower maximum error compared to the other CFs. Figure 17 shows the estimation errors presented in terms of Euler angles for these CFs. Figure 17(a) shows that in *Phase I*, the median roll/pitch/yaw errors were roughly 2 degrees for all the selected CFs, and none had obvious lower errors. However, DelRosario(2016), Martin(2010), and Justa(2020) had the lowest inter-repeatability among participants, indicated by their interquartile range (75% percentile – 25% percentile) of errors. For *Phase II*, Figure 17(b) shows that all the selected CFs had median angle errors of roughly 5 degrees or less, except for Madgwick(2011)(MIMU), which also had the highest interquartile range of error (i.e., lowest inter-repeatability). In conclusion, while Figure 17 shows slight performance differences between these selected CFs, Table 13 shows no significant difference between them, except for Madgwick(2011)(MIMU). Therefore, other factors, such as the number of gains that require tuning or SFA execution time, must be considered to select the best CF.

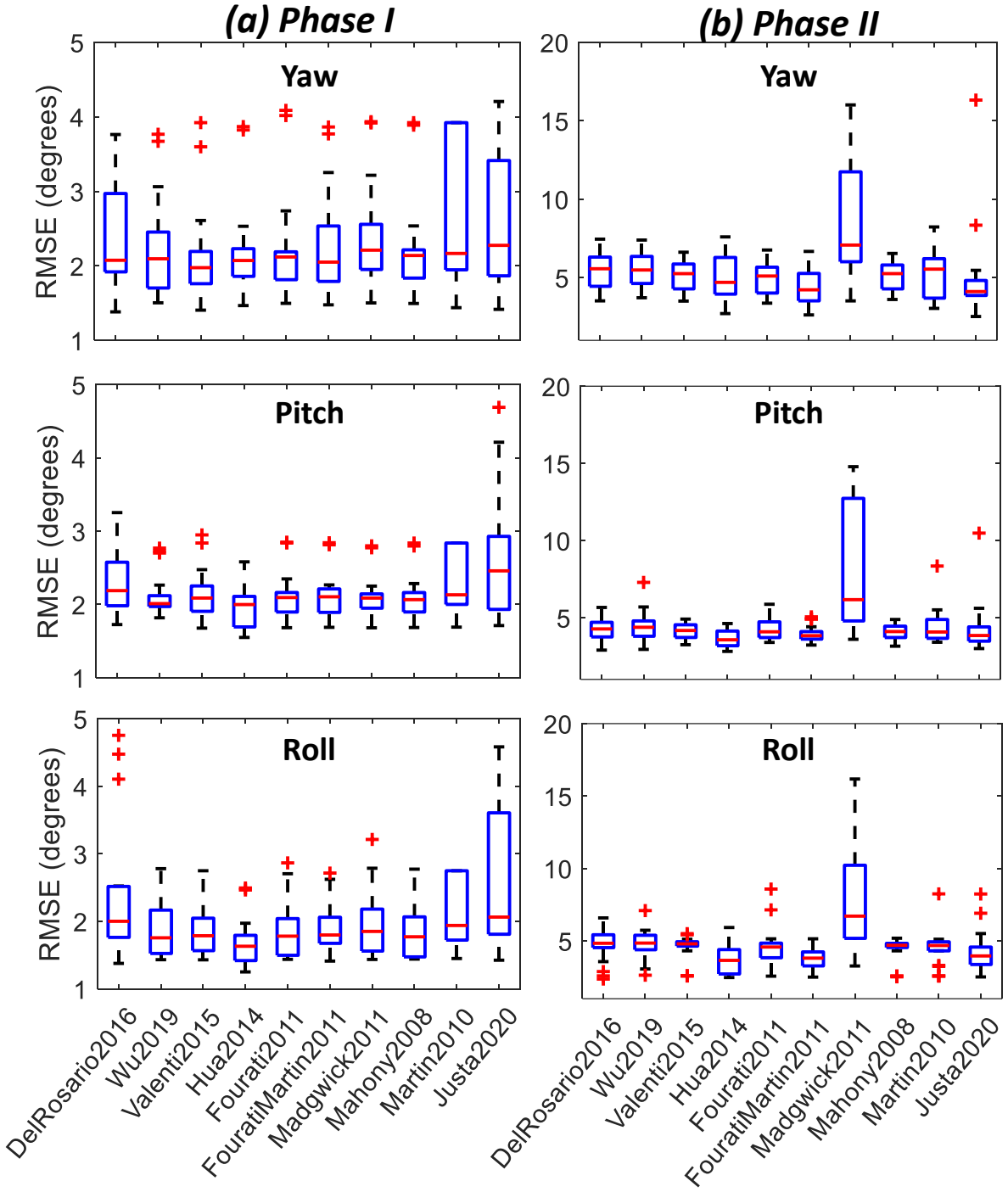

Figure 17 Boxplot ([25%, 50%, 75%] percentiles, red + shows outliers) of the RMSE obtained by the implemented SFAs from the complementary filter (CF) family presented in Euler angle parametrization for (a) *Phase I* and (b) *Phase II*. Each boxplot presents the RMS values of all testing data set (18 samples for *Phase I* and 24 samples for Phase II).

Linear Kalman Filters: Table 13(b) shows that for LKFs, Renaudin(2014), Choukroun(2006), and Nazarahari(2020) (the proposed LKF) achieved a higher score than other

SFAs in terms of the number of times they were significantly ($p<0.05$) more accurate than other LKFs. Also, Figure 18 shows the LKFs estimation errors presented in Euler angles for LKFs identified with * in Table 13(b). Figure 18(a) shows that in *Phase I*, the median roll/pitch/yaw errors were between 2 to 3 degrees for all the selected LKFs, while Renaudin(2014) tended to have lower median roll and yaw errors compared to others. Also, Figure 18(a) shows that Renaudin(2014) and Ligorio(2015) tended to have the smallest and largest interquartile ranges, respectively. For *Phase II*, Figure 18(b) shows that the median errors were roughly 5 degrees, except for Wu(2018) and Guo(2017), which also had the highest interquartile range (i.e., lowest inter-repeatability). Similar to *Phase I*, Renaudin(2014) showed the lowest median angle errors and interquartile range among LKFs. In conclusion, Table 13(b) and Figure 18 show the obvious superiority of Renaudin(2014) (with 10 gains), followed by Choukroun(2006) (with 10 gains) and Nazarahari(2020 (with 16 gains), among all LKFs.

Nonlinear Kalman Filters: Table 13(c) shows that for EKFs, CKFs, SRCKF, and SRUKFs, DelRosario(2018) (CKF), Sabatini(2006) (EKF), and the proposed SRUKF3 achieved a higher score than other SFAs in terms of the number of times they were significantly ($p<0.05$) more accurate than other SFAs in these families. Also, Figure 19 shows the estimation errors presented in Euler angles for these SFAs identified with * in Table 13(c). Figure 19(a) shows that in *Phase I*, the median roll/pitch/yaw errors were roughly 2 degrees or less for these SFAs, except for Suh(2010). These SFAs showed a similar interquartile range, except for pitch angle errors of SRUKFs, where lower interquartile ranges were obtained. For *Phase II*, Figure 19(b) shows that all these SFAs had median angle errors of roughly 5 degrees or less, except for Suh(2010). Also, Suh(2010), Roeternberg(2005), and SRCKF had the highest interquartile range (i.e., lowest inter-repeatability). Moreover, Figure 19(c) shows that by converting the Chen(2017) structure from an EKF to SRUKF/SRCKF, accuracy has significantly increased in *Phase I* and *Phase II*. In conclusion, Figure 19 shows the superiority of Sabatini(2006) in terms of median angle error, specifically in *Phase II*.

Table 13 Statistical comparison of the RMS of the quaternion angle difference (QAD) among SFAs in one family for all testing data in *Phase I* and *Phase II* after gyroscope static bias removal. Significantly ($p<0.05$) lower RMS(QAD), i.e. higher accuracy, for an SFA in a row compared to the ones in columns are identified with † for *Phase I* and with and ‡ for *Phase II*. * shows SFAs from each family with the lowest maximum error. The last column (score) shows the number of times an SFA significantly outperformed other SFAs in its family for *Phase I* and *Phase II* cumulatively.

(a) Complementary Filters	Maran.	DelRos.	Markely	Wu2016	Wu2019	Valenti	Hua	Fourati	Fourati Martin	Madg. (MIMU)	Madg. (IMU)	Mahony	Martin	Justa	**Score**
Marantos(2016)		-	-	-	-	-	-	-	-	-	-	-	-	-	0
DelRosario(2016)*	†,‡		‡	-	-	-	-	-	-	-	-	-	-	-	3
Markely(2003)	-	-		-	-	-	-	-	-	-	-	-	-	-	0
Wu(2016)	†,‡	-	-		-	-	-	-	-	-	-	-	-	-	2
Wu(2019)*	†,‡	-	‡	-		-	-	-	-	-	-	-	-	-	3
Valenti(2015)*	†,‡	-	‡	-	-		-	-	-	-	-	-	-	-	3
Hua(2014)*	†,‡	-	‡	‡	-	-		-	-	‡	-	-	-	-	**5**
Fourati(2011)*	†,‡	-	‡	-	-	-	-		-	-	-	-	-	-	3
FouratiMartin(2011)*	†,‡	-	‡	‡	-	-	-	-		‡	-	-	-	-	**5**
Madgwick(2011)(MIMU)*	†	-	-	-	-	-	-	-	-		-	-	-	-	1
Madgwick(2011)(IMU)	†,‡	-	‡	-	-	-	-	-	-	-		-	-	-	3
Mahony(2008)*	†,‡	-	‡	-	-	-	-	-	-	-	-		-	-	3
Martin(2010)*	†,‡	-	‡	-	-	-	-	-	-	-	-	-		-	3
Justa(2020)*	†,‡	-	‡	‡	-	-	-	-	-	‡	-	-	-		**4**

(b) Linear Kalman Filters	Wu2020 (Plain)	Wu2020 (Rec.)	GyroLib	Ligorio	Valenti	Wu2018	Guo	Renau.	Chouk.	Nazar.	Suh	**Score**
Wu(2020)(Plain)		-	-	-	-	-	-	-	-	-	†,‡	2
Wu(2020)(Recursive)*	-		-	-	‡	‡	-	-	-	-	†,‡	4
GyroLib(2020)	-	-		-	‡	-	-	-	-	-	†,‡	3
Ligorio(2015)*	-	-	-		‡	‡	-	-	-	-	†,‡	4
Valenti(2016)	-	-	-	-		-	-	-	-	-	-	0
Wu(2018)*	-	-	-	-	-		-	-	-	-	†	1
Guo(2017)*	-	-	-	-	-	-		-	-	-	†,‡	2
Renaudin(2014)*	†,‡	-	‡	-	†,‡	‡	‡		-	-	†,‡	**7**
Choukroun(2006)*	‡	-	-	-	†,‡	‡	‡	-		-	†,‡	**5**
Nazarahari(2020)*	‡	-	-	-	†,‡	‡	‡	-	-		†,‡	**5**
Suh(2019)	-	-	-	-	-	-	-	-	-	-		0

(c) Complementary/ Extended/ Unscented/ Cubature Kalman Filters	DelRo.	Hyyti	Chen	Sabatini	Suh	Roeter.	Nazar,	SRCKF	SRUKF1	SRUKF2	SRUKF3	SRUKF4	**Score**
DelRosario(2018)*		†,‡	†,‡	-	-	-	-	-	-	-	-	-	4
Hyyti(2015)	-		-	-	-	-	-	-	-	-	-	-	0
Chen(2017)	-	-		-	-	-	-	-	-	-	-	-	0
Sabatini(2006)*	-	†,‡	†,‡		‡	-	-	-	-	-	-	-	**5**
Suh(2010)*	-	-	-	-		-	-	-	-	-	-	-	0
Roeternberg(2005)*	-	†,‡	†,‡	-	-		-	-	-	-	-	-	4
Nazarahari(2021)*	-	†,‡	†,‡	-	‡	-		-	-	-	-	-	**5**
SRCKF*	-	†,‡	†,‡	-	‡	-	-		-	-	-	-	5
SRUKF1*	-	†,‡	†,‡	-	‡	-	-	-		-	-	-	5
SRUKF2	-	†,‡	†,‡	-	‡	-	-	-	-		-	-	5
SRUKF3*	-	†,‡	†,‡	-	‡	-	-	-	-	-		-	**5**
SRUKF4*	-	†,‡	‡	-	‡	-	-	-	-	-	-		4

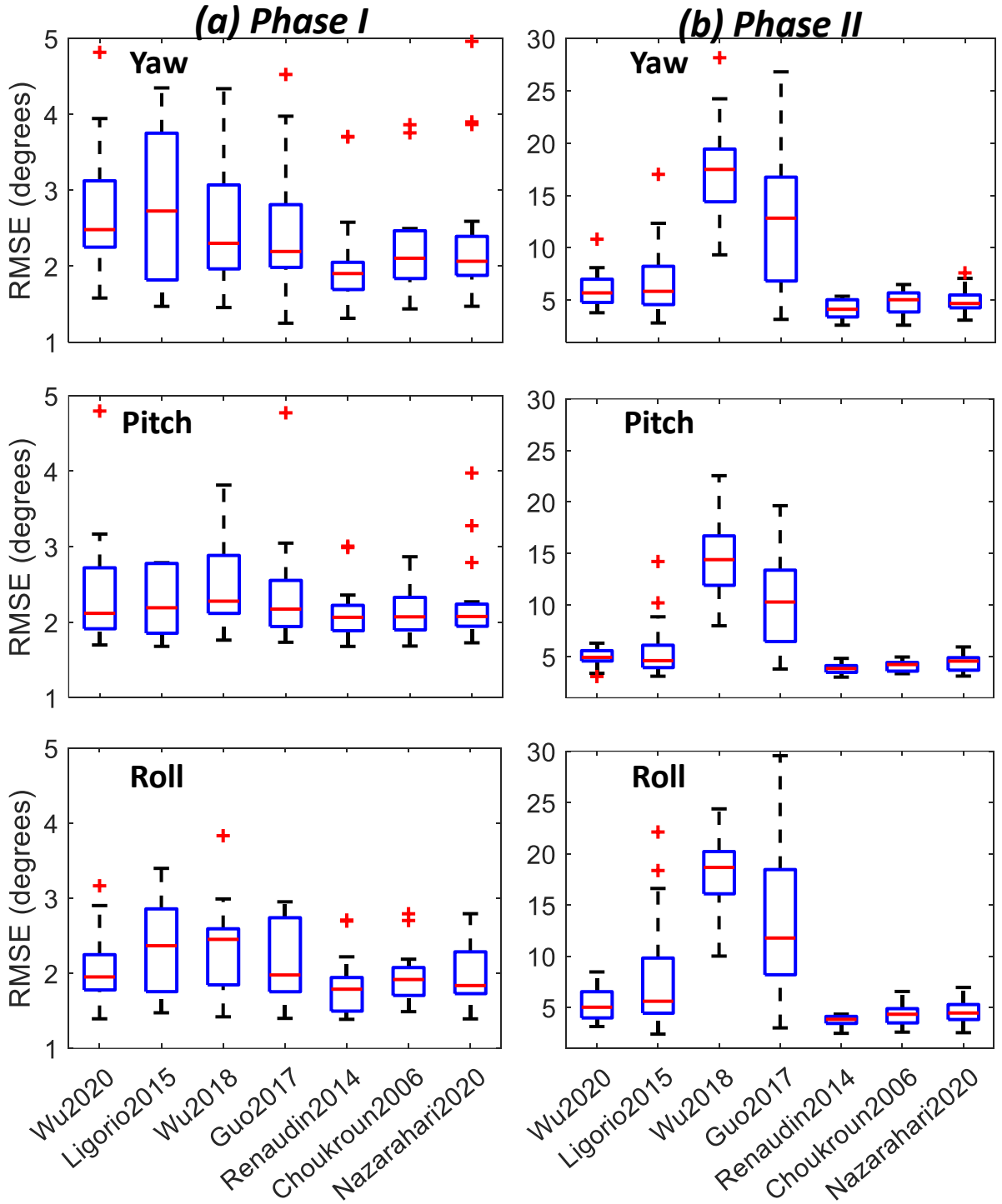

Figure 18 Boxplot ([25%, 50%, 75%] percentiles, red + shows outliers) of the RMSE obtained by the implemented SFAs from the linear Kalman filter (LKF) family presented in Euler angle parametrization for (a) *Phase I* and (b) *Phase II*. Each boxplot presents the RMS values of all testing data set (18 samples for *Phase I* and 24 samples for *Phase II*).

5.3.3 Selecting the Best Sensor Fusion Algorithm

The three SFAs from each family with the highest score in Table 13 were selected and compared against one another in terms of accuracy (based on RMS(QAD)) and execution time. Statistical analysis only showed significantly ($p<0.05$) lower RMS(QAD) for Sabatini(2006) compared to DelRosario(2018) and Nazarahari(2020) in *Phase II*. Figure 20 shows the estimation errors presented in terms of Euler angles for these nine selected SFAs. Figure 20(a) shows that in *Phase I*, the median roll/pitch/yaw errors were roughly 2 degrees or less for all SFAs, and none has obvious lower errors for all three angles. However, by comparing the interquartile range of errors, we observed that Justa(2020) tended to have the lowest repeatability. For *Phase II*, Figure 20(b) shows that the selected nine SFAs had median angle errors of less than 5 degrees for Euler angles. Also, the interquartile ranges were mostly similar, specifically for pitch and yaw.

Table 14 shows the execution times (in milliseconds) for the selected nine SFAs. According to Table 14, execution times ranged from 10.10 milliseconds for Justa(2020) to 291.46 milliseconds for SRUKF3. As expected, the families with the shortest execution times can be sorted as follows: CFs (the first three rows in Table 14), CKF (DelRosario(2018)), LKF (the second three rows in Table 14), EKF (Sabatini(2006)), and finally SRUKF. Yet, Sabatini(2006) (EKF) had shorter execution times compared to Nazarahari(2020) (LKF), which shows the effect of state-vector size and measurement-update equation structure on the execution time. Also, as expected, SRUKF3 had the highest execution time because it performs calculations on multiple sigma points at each time instant (compared to other KFs that propagate one state-vector in time). In conclusion, while Figure 20 shows slight performance differences among the selected nine SFAs, none performed significantly better than all others. However, when the execution time is not a factor, Sabatini(2006) should be selected as it tended to have lower angle errors (Figure 20). When the execution time is a factor, Hua(2014) or Justa(2020) should be selected.

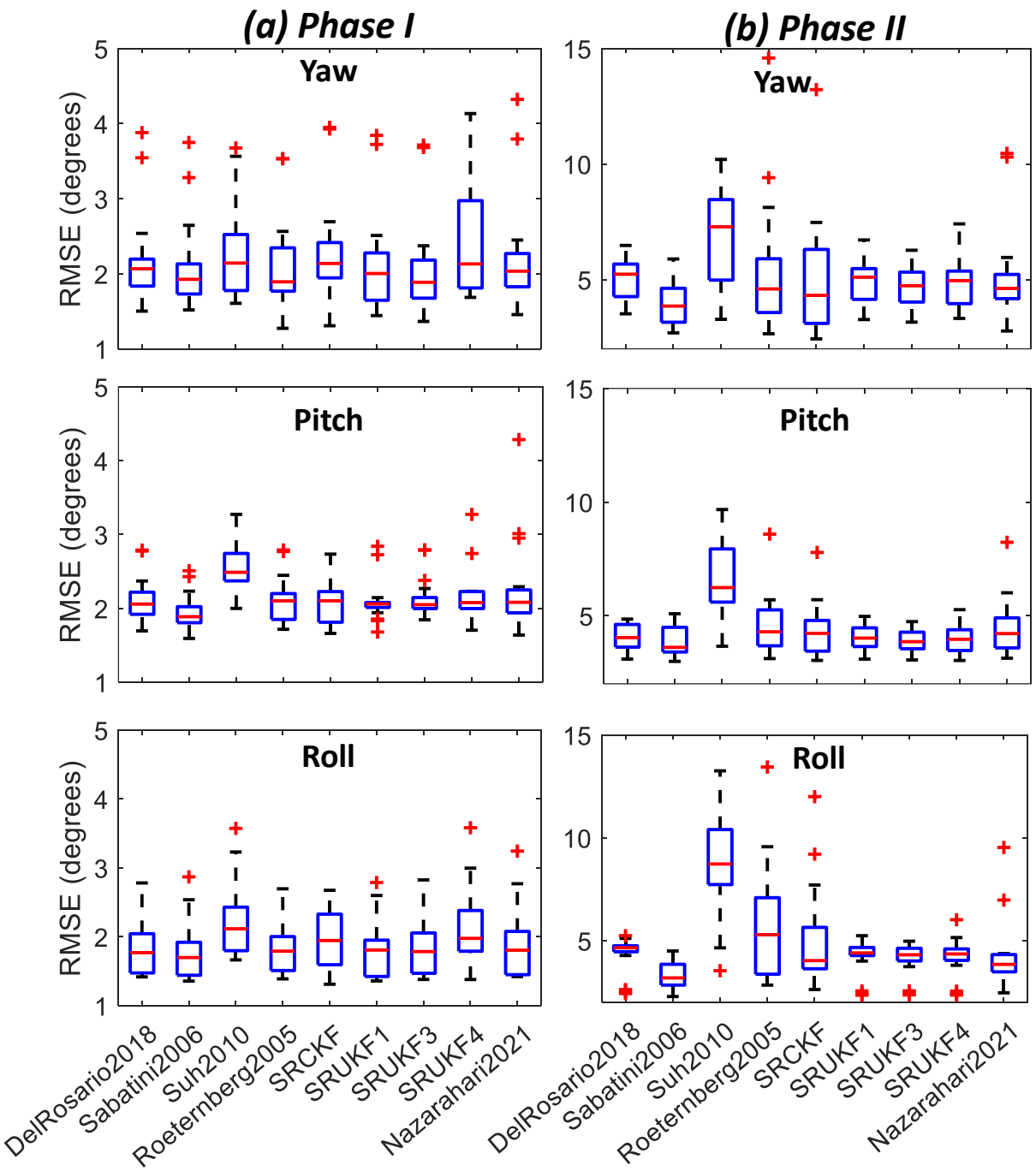

Figure 19 Boxplot ([25%, 50%, 75%] percentiles, red + shows outliers) of the RMSE obtained by the implemented SFAs from the extended, complementary, unscented, and cubature Kalman filter families presented in Euler angle parametrization for (a) *Phase I* and (b) *Phase II*. Each boxplot presents the RMS values of all testing data set (18 samples for *Phase I* and 24 samples for *Phase II*).

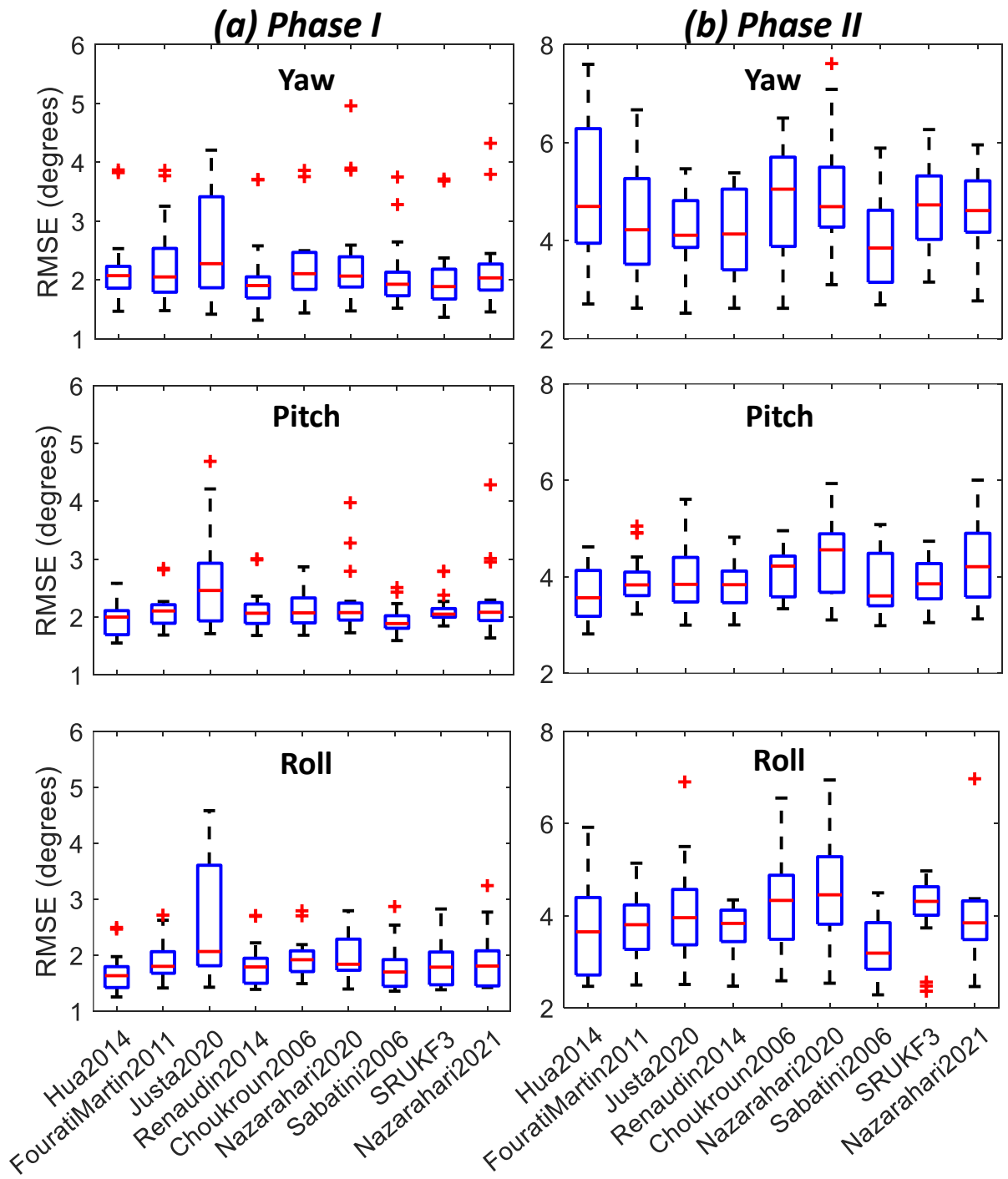

Figure 20 Boxplot ([25%, 50%, 75%] percentiles, red + shows outliers) of the RMSE obtained by three SFAs with the highest accuracy from each family presented in Euler angle parametrization for (a) *Phase I* and (b) *Phase II*. Each boxplot presents the RMS values of all testing data set (18 samples for *Phase I* and 24 samples for *Phase II*).

Table 14 Median of the execution times (in milliseconds) for the three SFAs with the highest accuracy in each family reported in diagonal elements. Also, for each SFA (each row), other SFAs with significantly longer execution times are identified with †. The last column (score) shows the number of times one SFA was significantly faster than other SFAs (the higher, the better).

	Hua	FouratiMartin	Justa	Renaudin	Choukroun	Nazarahari(2020)	Sabatini	SRUKF3	Nazarahari(2021)	**Score**
Hua(2014)	10.71	†	-	†	†	†	†	†	†	7
FouratiMartin(2011)	-	25.70	-	†	†	†	†	†	†	6
Justa(2020)	†	†	10.10	†	†	†	†	†	†	**8**
Renaudin(2014)	-	-	-	38.95	†	†	†	†	†	5
Choukroun(2006)	-	-	-	-	55.68	†	†	†	†	4
Nazarahari(2020)	-	-	-	-	-	99.21	-	†	-	1
Sabatini(2006)	-	-	-	-	-	†	75.83	†	†	3
SRUKF3	-	-	-	-	-	-	-	291.46	-	0
Nazarahari(2021)	-	-	-	-	-	†	-	†	78.59	2

5.3.4 Conceptual Comparison Between Families

The main differences between the SFAs tested in this paper are how to (1) estimate the orientation using IMU readouts (i.e., y_G, y_A, y_M) and (2) weight the estimated orientation from each sensor before fusing them. While the former difference can be considered as the SFA property, the latter can be attributed to the SFA family. Notably, CFs and KFs (including various sub-families) use a deterministic and stochastic approach to tune the fusing weight. In CFs, the fusing weight is determined by the user, while in KFs, the Kalman gain (i.e., the fusing weight) is calculated in each iteration based on gyroscope/accelerometer/magnetometer noises as well as the state error covariance matrix to achieve the optimal estimation. This property makes CFs computationally more efficient (see Table 14), while optimality is not guaranteed.

Among KF families, the major difference is how to model the system (commonly, strap-down integration using y_G) and measurement (commonly, orientation estimation using y_A and y_M) equations. LKFs use linear models for system and measurement equations, while EKF benefits from the nonlinear system and/or measurement equations. Thus, EKF includes a linearization step, which can result in inaccuracies for a highly nonlinear system. Thus, SRUKF and SRCKF have been proposed to use unscented or cubature transformation to propagate state vector and state error covariance matrix in time and avoid linearization. As a result, as we move from LKF toward SRUKF/SRCKF, theoretically, both the accuracy and computational complexity (i.e., execution

time) will increase. Comparing Figure 18 and Figure 19, we observe that in *Phase II*, the maximum errors obtained by LKFs were under 30 and 25 degrees for yaw/roll and pitch angles, while for EKFs/SRUKFs/SRCKF, the maximum errors were less than 15 and 10 degrees for yaw/roll and pitch angles. However, this higher accuracy came at a greater computational cost (Table 14).

5.3.5 Limitations and Future Works

This chapter presents the first step toward building a comprehensive online repository for sharing data and codes for SFAs that can be used to estimate the IMU orientation. However, a number of limiting factors are associated with the current work, and further steps must be taken in the future to address them. First, we only tested 37 SFAs, while our previous survey listed 250 SFAs in the literature [22]. Thus, in the future, more SFAs must be included in the comparison to identify algorithms with the highest accuracy/repeatability, particularly Particle Filters [188]. Also, we encourage other scientists to publish their codes/data, similar to [64], [357], which then can be aggregated into a universal online repository.

Second, this study only presents results related to one foot-mounted IMU. Therefore, data collection with other IMUs, with different manufacturing qualities must be performed. The reason is that the accelerometer, gyroscope, and magnetometer calibration and noise can play a crucial role in SFAs performance, as it was shown in this study and by the others [49], [79], [82], [357], [368].

Third, while the used experimental data was extensive (nine participants, short- and long-duration trials), they were all (1) in the context of human motion analysis; (2) performed in an indoor environment; and (3) shorter than 10 minutes. Thus, in the future, IMU data collected in other scenarios, such as a mobile robot or robotic arm motion tracking and aerial/surface/underwater vehicle navigation, must be analyzed; yet, the limitation with such applications is how to track the reference orientation. Also, trials with longer duration are essential, but they substantially increase the data processing and analysis time.

Lastly, our collected data cannot be used to perform offline accelerometer and magnetometer calibration, similar to [66], [108], [294], [295]. However, having the required data for this purpose is essential, as it can reveal the ability of an SFA to handle sensor inaccuracies that may occur after manufacturing an IMU (for example, due to impact during tests).

5.4 Conclusions

We compared the estimated orientation with 37 SFAs from CF, LKF, EKF, CKF, SRUKF and SRCKF families and shared the codes and sample data on our laboratory website. Comparing the performance of SFAs against one another after gyroscope static bias removal, we observed slight differences between CFs, except for Marantos(2016), Markely(2003), Wu(2016), and Madgwick(2011). Notably, for CFs, Hua(2014), FouratiMartin(2011), and Justa(2020) showed high accuracy for short- and long-duration trials. For SFAs from the LKF family, Renaudin(2014), Choukroun(2006) and Nazarahari(2020) have the highest accuracies. Finally, among SFAs from EKF/CKF/SRUKF/SRCKF families, Sabatini(2006), DelRosario(2018), and SRUKF3 had higher accuracies. For long-duration trials in *Phase II*, the selected nine SFAs (the best three from each of CF, LKF, EKF/CKF/SRUKF/SRCKF families) had median angle errors of less than 5 degrees for Euler angles. Also, the execution times ranged from 10.10 milliseconds for Justa(2020) to 291.46 milliseconds for SRUKF3. Thus, when the execution time is not a factor, Sabatini(2006) should be selected as it tended to have lower errors. On the other hand, when the execution time is a factor, Hua(2014) 16 or Justa(2020) should be selected.

At this point, we can track the orientation of IMU attached to body segments by combining the SFAs proposed in this chapter with adaptive gain regulation in Chapter 4. Then, we can use the proposed sensor-to-segment calibration procedures (Chapter 3) to estimate the orientation of the anatomical frames of proximal and distal segments. Finally, we can calculate clinically meaningful lower limb joint angles in real-time, which can be provided as biofeedback during therapeutic gait training. Nevertheless, in the future, the validity of the proposed technologies in measuring lower limb joint angles with clinically meaningful higher accuracy and repeatability compared to the literature must be validated for a clinical population.

Chapter 6

Temporal Gait Event Detection

This chapter provides the details of a real-time robust algorithm for temporal gait event detection. Portions of this chapter have been adopted and/or edited from:

M. Nazarahari, A. Khandan, H. Rouhani, "Foot Kinematic Features Measured with Inertial Measurement Units: An Inherently Robust Approach to Real-time Gait Event Detection," Submitted, 2021.

6.1 Introduction

By combining the technical contributions in Chapter 3, Chapter 4, and Chapter 5, joints angles can be measured in real-time, and the proper biofeedback can be provided. Nevertheless, to fully exploit the benefits of an instrumented biofeedback-based training, temporal gait events, including initial contact (IC, i.e., heel-strike) and terminal contact (TC, i.e., toe-off) of the foot with the ground, must be detected with high accuracy and robustness in real-time.

Usually, the algorithms developed for gait detection using IMU implement heuristic rules to identify prominent morphological features in acceleration and/or angular velocity time-series recorded by the shank- or foot-worn IMU. For example, morphological features such as zero-crossing and local minima/maxima of the angular velocity, the norm of the 3D acceleration, and first-derivative of the norm of the 3D angular velocity of the foot or the shank ($y_{G_F,y}$ or $y_{G_S,y}$) were investigated to identify the most accurate indicators of IC and TC [369]. In [370], IC and TC were

identified as the minima of the shank flexion/extension angle and the minima of its angular velocity, respectively.

Heuristic constraints (e.g., thresholds) were also added to gait detection algorithms to improve their robustness. For example, in [371], the true TC was detected as local minima of $y_{G_S,y}$ which was at least 100 ms farther from the last detected IC. Similarly, in [372], a TC was detected when a set of heuristic rules were satisfied and the $y_{G_S,y}$ magnitude was smaller than a predefined threshold. Recently, eight heuristic algorithms for gait event detection were compared in [373]. The results show that none of the previous algorithms could simultaneously achieve the highest accuracy and robustness for both IC and TC. Thus, [373] proposed the combination of two previously introduced algorithms that used $y_{G_S,y}$ morphological features and heuristic constraints for gait event detection.

Despite the successful implementation of such heuristic algorithms for normal and impaired gaits, a literature review showed that previous works have at least one of the following limitations. First, the main goal of the previous works was to maximize the temporal accuracy of the detected events with respect to events obtained by a gold-standard reference system. Thus, the robustness of the algorithms defined in terms of sensitivity and precision was neglected. Second, in some algorithms, the construct of heuristic rules or constraints requires offline data processing, making the algorithm unsuitable for real-time implementation. These limitations were because the heuristic rules were mainly focused on the morphology of the time-series and not the reconstructed motion of the foot during gait (e.g., foot contact with and rolling on the ground). We hypothesize that IC and TC detection based on kinematic features of the foot motion measured by the IMU can result in a robust gait event detection in various experimental conditions or for altered gait.

Thus, we present a novel algorithm for robust real-time gait event (IC and TC) detection based on foot kinematics, which minimally depends on the morphology of the IMU readout time-series. Our goal is to detect IC and TC with sensitivity and precision of 100% using an algorithm with minimum delay (1 sample), to make the proposed algorithm suitable for providing biofeedback in real-time to the user in rehabilitative gait training or for control of neural prostheses or exoskeletons.

6.2 Materials and methods

6.2.1 Measurement setup

Four IMUs (MTws, Xsens Technologies, The Netherlands) were attached to rigid plastic plates and fixed over both feet and shanks using double-sided medical tape (Figure 21). The IMU included a tri-axial accelerometer (range: ±16g), a tri-axial gyroscope (range: ±2000 degrees/s), and a tri-axial magnetometer (range: ±1.9 Gauss). Also, wearable pressure insoles (Pedar-X, Novel, DE) were employed as the reference system to detect IC and TC during gait (Figure 21). Previous studies showed high accuracy and robustness of pressure insoles measurements when compared with the gold-standard force platform measurements [374]. Thus, they have been successfully used for gait analysis in the past [375]. Both IMU and pressure insole recorded data synchronously with a sampling frequency of 100 Hz.

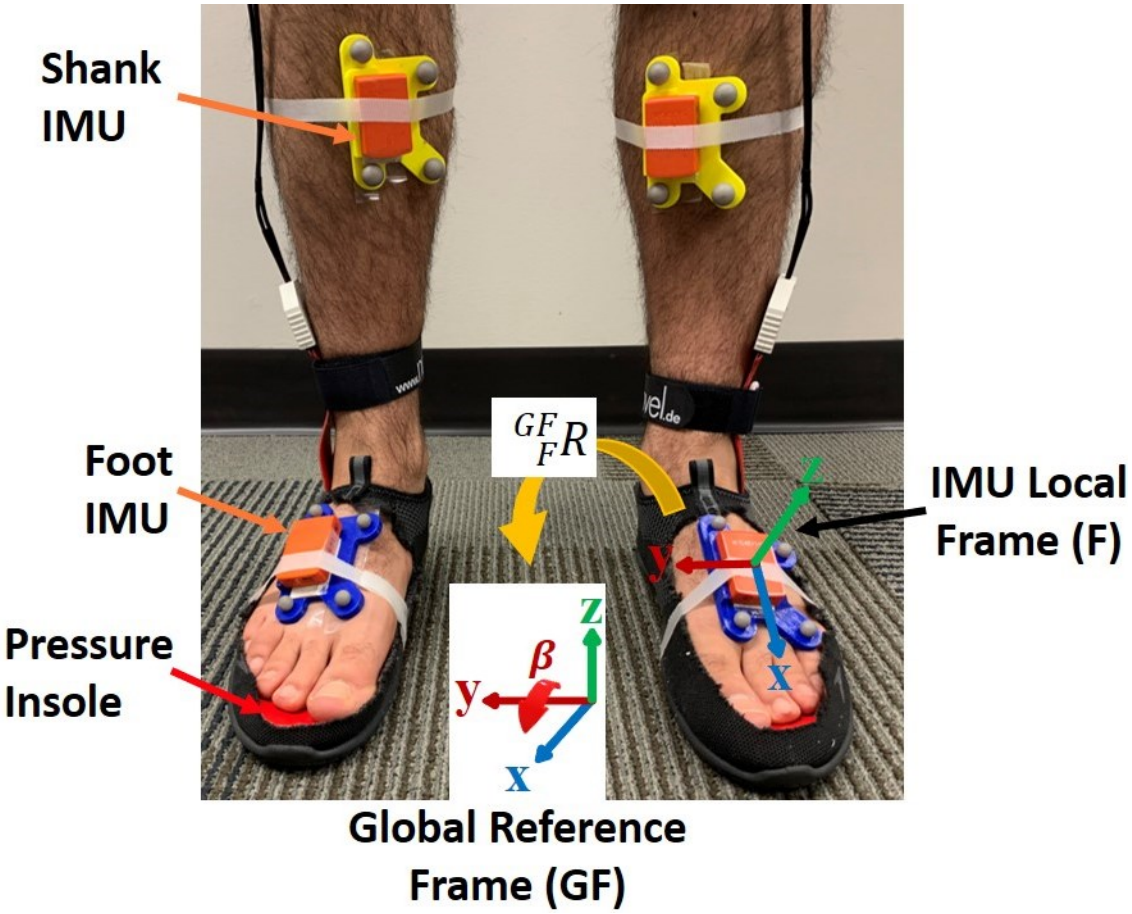

Figure 21 Experimental setup including foot- and shank-worn IMUs and pressure insoles (underneath the foot) to detect the true gait events (i.e., IC and TC).

6.2.2 Gait Event Detection

Reference temporal events: Following previous studies [376], [377], a threshold of 20 N was applied to the resultant vertical ground reaction force measured by the pressure insoles to detect IC (the force profile passed above the threshold) and TC (the force profile passed below the threshold).

Proposed heuristic algorithm for gait event detection using IMU data: Previous works used local minima/maxima of the acceleration or angular velocity time-series or their time derivates. However, these acceleration and angular velocity time-series contain several local minima/maxima depending on the sensor hardware, individual's gait characteristics, or footwear-ground conditions, making the detection of IC and TC sensitive to these factors (see Figure 22). In particular, to detect a local minimum/maximum in the time-series, its value must be compared with previous and future data samples (note that access to each sample in the future means a delay for a real-time system). Thus, for real-time detection of IC and TC where no access to the data samples in the future (except for the next sample) is allowed, every observed local minimum/maximum can be falsely detected as an IC or TC event. As such, IC and TC detection using jerky time-series with multiple local minima/maxima in the proximity of the true IC and TC is prone to false detection.

Thus, we suggest detecting IC and TC based on how IC and TC are visually identified when we look at the foot's recorded motion. Thus, we identified IC and TC based on the foot inclination angle in the sagittal plane (pitch angle or β in Figure 21). To this end, we obtained the rotation matrix that quantifies the foot orientation with respect to a global reference frame, ${}^{GF}_{F}R$:

$$ {}^{GF}_{F}R = {}^{GF}_{F}R_z(\gamma) \times {}^{GF}_{F}R_y(\beta) \times {}^{GF}_{F}R_x(\alpha) = \begin{bmatrix} (1,1) & (1,2) & (1,3) \\ (2,1) & (2,2) & (2,3) \\ -\sin(\beta) & (3,2) & (3,3) \end{bmatrix} \quad \text{Equation 52} $$

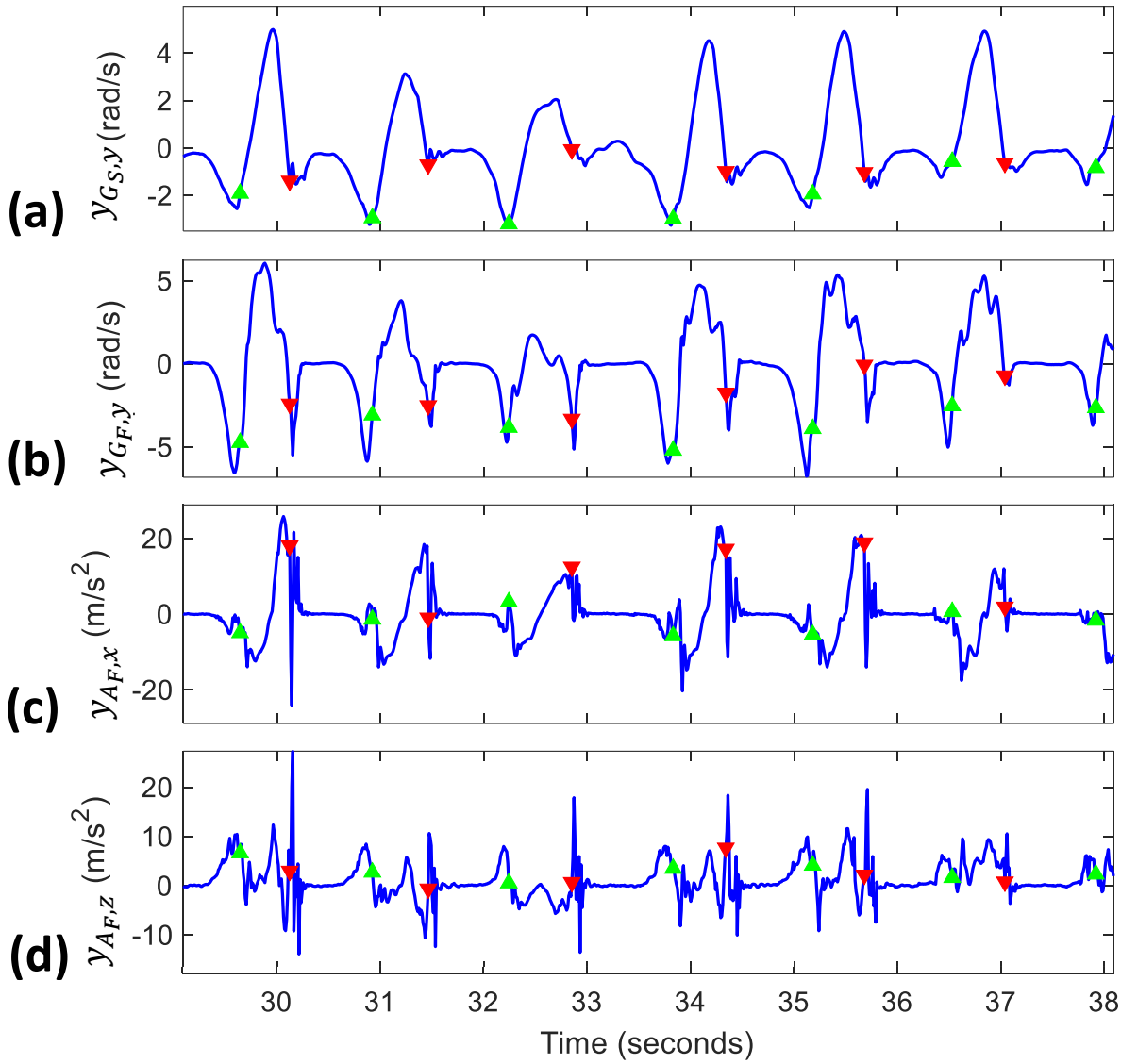

Figure 22 A representative time-series of the angular velocity of the shank ($y_{G_S,y}$) and foot ($y_{G_F,y}$) in the sagittal plane, foot acceleration in the anterior-posterior ($y_{A_F,x}$) and vertical ($y_{A_F,z}$) directions, and sine of the foot pitch angle, $-\sin(\beta)$. Ture IC (▼) and TC (▲) events obtained from reference pressure insoles are identified in the figure.

where α, β, and γ are the foot angle in the c oronal plane (roll angle), sagittal plane (pitch angle), and transverse plane (yaw angle), respectively. We used only $-\sin(\beta)$ corresponding to the element (3,1) of ${}^{GF}_{F}R$ to detect its local minima and maxima, corresponding to IC and TC, respectively, as shown in Figure 23(c). By using $-\sin(\beta)$, we avoided the calculation of Euler angles which might show singularity. However, before using $-\sin(\beta)$, two corrections must be applied to ${}^{GF}_{F}R$:

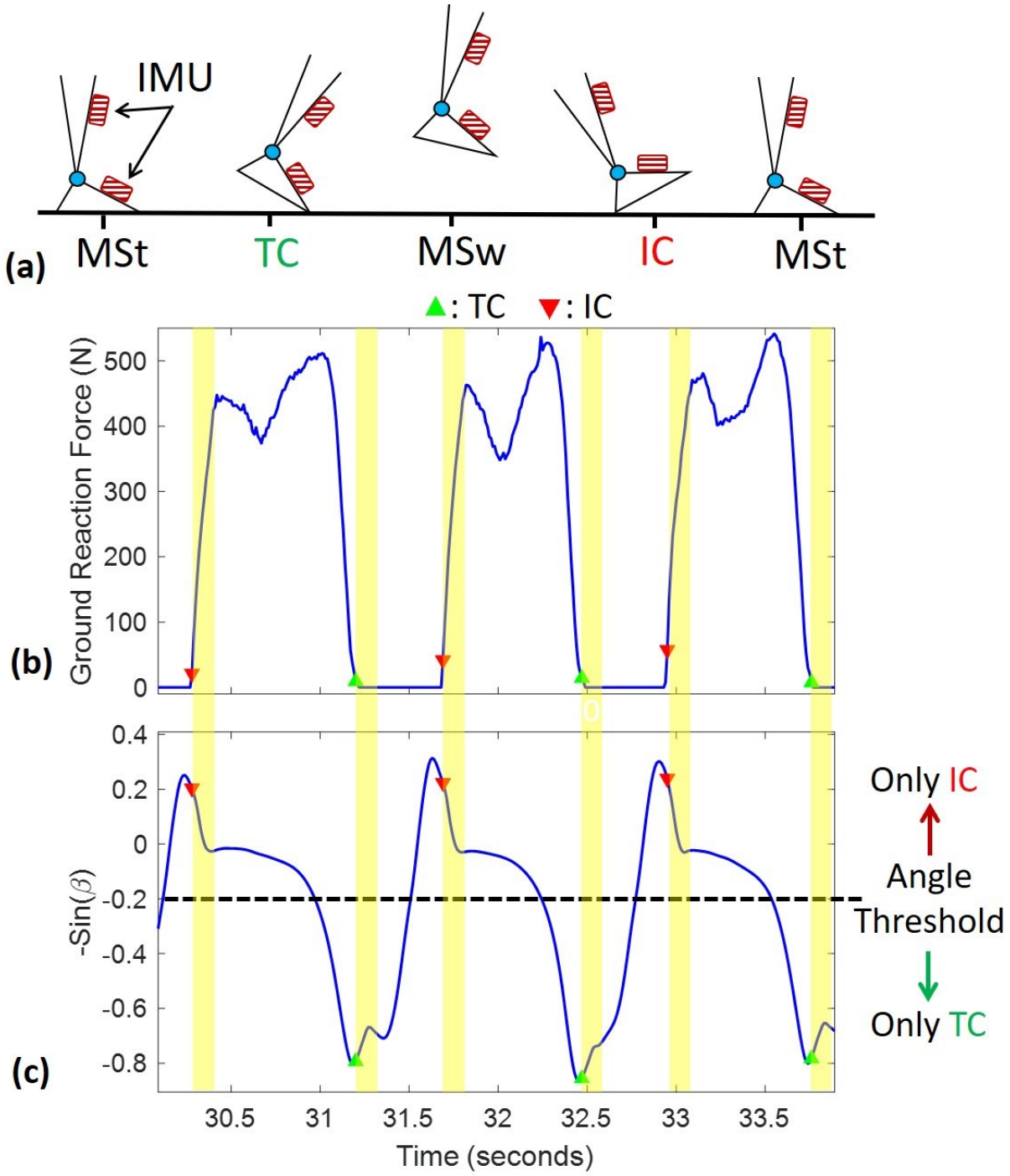

Figure 23 (a) Temporal events during a gait cycle: MSt: mid-stance, TC: terminal contact, MSw: mid-swing, IC: initial contact; (b) the resultant ground reaction force profile measured with pressure insoles; and (c) the sine of foot pitch angle measured by an IMU. True events are identified in the figure. The foot angle threshold, which determines what event to be detected, is shown with a dashed line. The yellow shades identify the time constraint, which prohibits detecting new gait events for a period of time after one event has been detected.

1. ${}^{GF}_{F}R$ depends on the definition of the global reference frame and IMU attachment over the foot (IMU local frame). Thus, to make robust pitch angle measurements, we multiplied the

calculated ${}^{GF}_{F}R_k$ by ${}^{F}_{GF}R_{k=1}$. Thus, the pitch angle at k = 1 (corresponding to the quiet standing at the beginning of the trial) became zero, regardless of global reference frame definition or IMU attachment, and we only tracked pitch angle changes with respect to this initial orientation.

2. For a fixed global reference frame, pitch angle depends on the motion direction. Thus, at each time sample, we multiplied ${}^{GF}_{F}R$ by ${}^{F}_{GF}R_z(\gamma)$ where γ is the yaw angle in Equation 52 to ensure that pitch angle has the same pattern, regardless of motion direction.

Thus, we used the following heuristic algorithm (see Algorithm 1 for the pseudocode) to detect IC and TC:

- TC: The following conditions must be satisfied:

  (1) the current sample is at least 150 ms after the previous TC,

  (2) $-\sin(\beta)$ < -0.2 (corresponding to foot angle of ≈ 11 degrees with respect to the initial angle, i.e., 0 degrees),

  (3) the previous sample was a local minimum.

- IC: The following conditions must be satisfied:

  (1) at least one TC is detected before the last IC,

  (2) the current sample is at least 150 ms after the previous IC,

  (3) $-\sin(\beta)$ > -0.2,

  (4) the previous sample was a local maximum.

To detect local minima and maxima in real-time in a robust manner, we used the following customized algorithm: Sample k is a local minimum if and only if,

(1) $-\sin(\beta)_k <- \sin(\beta)_{k-1\ to\ k-15}$ and $-\sin(\beta)_k <- \sin(\beta)_{k+1}$ and,

(2) at least 80% of $-\sin(\beta)_{k-i}\,(i = 1 \cdots 15)$ show a decreasing trend with respect to $-\sin(\beta)_{k-i-1}$.

The local maximum was found similarly. This method ensured that the delay in detection of the local minima/maxima was only 1 sample.

Heuristic algorithms from literature for gait event detection using IMU data: we implemented five algorithms from the literature (adopted from [369], [373], [371], [372], and

[378]) and compared their accuracy and robustness with our proposed algorithm. These algorithms, among others introduced in the literature, were selected as (1) they were proposed to be implemented in real-time; (2) they used $y_{G_S,y}$ or $y_{G_F,y}$ which have a smoother time-series compared to foot or shank acceleration; (3) they included various constraints to reject false events; and (4) they showed higher temporal accuracy and reliability during experimental studies compared to other algorithms. In particular, [371] showed higher temporal accuracy and/or robustness compared to [372], [379], and [373] showed higher temporal accuracy and/or robustness compared to [371], [372], [379]–[382].

Algorithm 1 Pseudocode of the proposed heuristic algorithm for gait event detection

Input: $-\sin(\beta)$

Initialization: IC is empty, TC is empty, flag = 0
for k = 16 **to** N **do** (N is the number of samples)
  if flag == 0
    if k – TC(end) > 15 (150 ms, Fs = 100 Hz)
      if $-\sin(\beta)_k$ < -0.2
        if $k-1$ **is** a local minimum
          TC(end+1) = k
          flag = 1
        end if
      end if
    end if
  end if

  if flag == 1
    if k – IC(end) > 15 (150 ms, Fs = 100 Hz)
      if $-\sin(\beta)_k$ > -0.2
        if $k-1$ **is** a local maximum
          IC(end+1) = k
          flag = 0
        end if
      end if
    end if
  end if
end for
Output: IC and TC

6.2.3 Experimental study

To validate the accuracy and robustness of the proposed algorithm, an experimental study was conducted with seven able-bodied participants (all male, 26±3 years old, 72±13 kg, 177±6 cm). Research Ethics Board Committee of the University of Alberta approved the study protocol, and written consent was obtained from all participants. The participants wore sandals embedding

pressure insoles, and IMUs were attached to their feet and shank using medical tapes. They were asked to perform the following activities: (1) walk over the ground in an oval-shaped path (large and small diameters: $\approx$ 3 m and 1 m) for 2 minutes with self-selected speed; (2) walk over the treadmill for 2 minutes with self-selected speed; (3) run over the treadmill for 1.5 minutes with self-selected speed; and (4) walk over an inclined treadmill (slope: 10%) for 1.5 minutes with self-selected speed. Each trial included 10 seconds of quiet standing at the beginning and the end. Also, the first and last two/three gait cycles were deleted to remove transient patterns in the gait data. The third participant's data of over-ground walking were discarded as the pressure insoles data were not recorded correctly.

6.2.4 Data analysis

In this work, we used foot orientation (${}^{GF}_{F}R$) obtained by the LKF that we previously proposed in Chapter 5 using IMU's raw data. However, ${}^{GF}_{F}R$ can be tracked with other SFAs with an RMSE of less than 4 degrees for β.

To measure the *temporal accuracy* of the proposed algorithm and those from the literature, we calculated the mean and standard deviation of the differences (measured in number of samples) between detected events using implemented algorithms and reference events obtained from pressure insoles. To assess the robustness of heuristic algorithms, we calculated the sensitivity, Se, and precision, Pr, as,

$$Se = \frac{TP}{TP+FN} \times 100 \quad \text{and} \quad Pr = \frac{TP}{TP+FP} \times 100 \qquad \text{Equation 53}$$

where TP, FN, and FP are true positives, false negatives, and false positives, respectively. TPs are the reference events detected by the heuristic algorithms, FNs are the reference events missed by the heuristic algorithms, and FPs are the extra false events detected by the heuristic algorithms. We considered a tolerance window of $\pm$500 ms (50 samples) around each reference event to identify TP, FN, and FP [373]. Finally, the agreement of the proposed algorithm with pressure insoles in detecting gait events was assessed using Bland-Altman analysis [383].

6.3 Results

A total of 1039, 1491, 1848, and 1177 reference ICs/TCs were recorded from all participants for the four performed activities. Figure 24 shows a representative sample of $-\sin(\beta)$ recorded during

these four activities as well as the detected (using the proposed algorithm) and reference (using the pressure insoles) IC and TC.

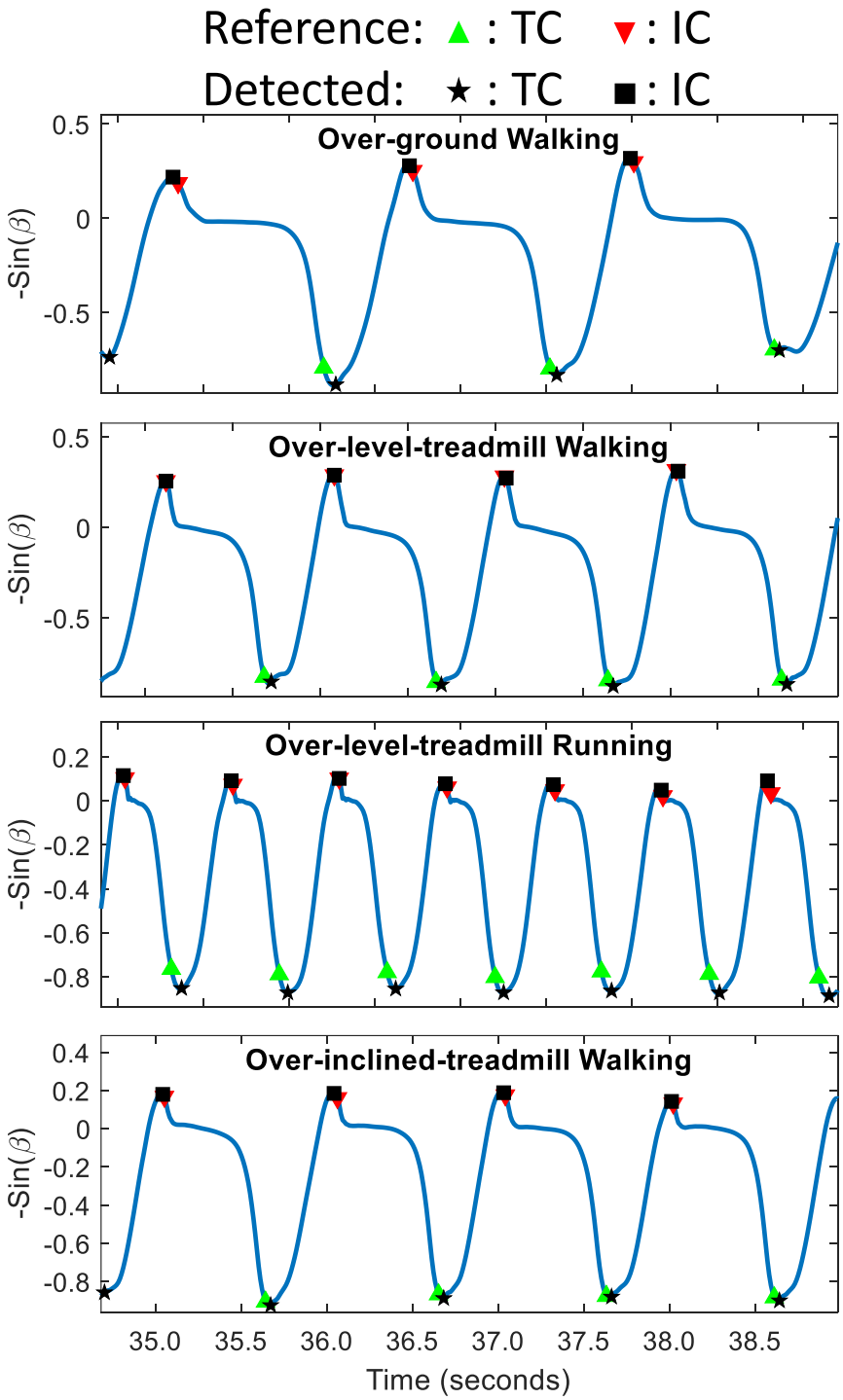

Figure 24 Representative patterns of sine of foot pitch angle for (a) over-ground walking; (b) over-level-treadmill walking; (c) over-level-treadmill running; and (d) over-inclined-treadmill walking. True and detected events are identified in the figure.

According to Table 15, for over-ground walking, algorithms proposed in [371], [372], and [378] obtained the highest temporal accuracy (mean$\pm$standard deviation: 1$\pm$1 samples) in detecting IC, while TC detected by our algorithm had the highest accuracy (5$\pm$5 samples). For over-level-treadmill walking, all algorithms showed similar temporal accuracy in detecting IC, while our algorithm had the highest accuracy in detecting TC (4$\pm$4 samples). For over-level-treadmill running, our algorithm showed to be the most accurate in detecting IC (0$\pm$3 samples), while [369] had the highest accuracy for TC (-3$\pm$3 samples). Finally, for over-inclined-treadmill walking, our algorithm showed the highest temporal accuracy (IC: 0$\pm$4 samples and TC: 4$\pm$4 samples) compared to the literature. In addition, the Bland-Altman plots in Figure 25 show that the detected events had a high temporal agreement with the reference events. Notably, the percentage of detected events with temporal error beyond the limits of agreement (mean±1.96×standard deviation) was less than 8.4% (TC during over-inclined-treadmill walking) in the worst case scenario.

According to Table 15, our proposed algorithm achieved a sensitivity, Se, and precision, Pr, of 100$\pm$0%, meaning all reference events were correctly detected, and no extra event was detected. [372] and [378] showed the second-highest Se and Pr during over-level/inclined-treadmill walking, while for over-ground walking and over-level-treadmill running, [378] and [369], respectively, had the second-highest Se and Pr.

Table 15 Temporal accuracy (in terms of the number of samples, Fs = 100 Hz), sensitivity, Se, and precision, Pr, of the implemented algorithms for IC and TC detection during various walking modalities, presented as mean±standard deviation among participants. Positive mean errors correspond to delays in the event detection with respect to the reference pressure insoles.

(a) Over-ground Walking						
Algorithm	Initial Contact (IC)			Terminal Contact (TC)		
	Accuracy	Se %	Pr %	Accuracy	Se %	Pr %
Mariani et al. [369]	-2±4	100±0	69±12	-6±12	100±0	85±10
Gouwanda et al. [371]	1±1	100±1	100±1	N/A	N/A	N/A
Catalfamo et al. [372]	1±1	100±0	100±0	-5±10	88±10	88±10
Perez-Ibarra et al. [373]	-4±4	96±4	94±6	-11±8	94±4	92±10
Maqbool et al. [378]	1±1	100±1	100±0	-7±5	85±10	100±1
Proposed	-4±2	100±0	100±0	4±3	100±0	100±0
(b) Over-level-treadmill Walking						
Algorithm	Initial Contact (IC)			Terminal Contact (TC)		
	Accuracy	Se %	Pr %	Accuracy	Se %	Pr %
Mariani et al. [369]	2±4	100±0	92±14	-4±10	100±0	94±9
Gouwanda et al. [371]	2±1	100±1	100±0	N/A	N/A	N/A
Catalfamo et al. [372]	2±1	100±0	100±0	-7±4	100±0	100±0
Perez-Ibarra et al. [373]	-2±2	94±16	95±9	10±4	93±15	94±11
Maqbool et al. [378]	2±1	100±0	100±0	-7±4	100±0	100±0
Proposed	-1±4	100±0	100±0	4±3	100±0	100±0
(c) Over-level-treadmill Running						
Algorithm	Initial Contact (IC)			Terminal Contact (TC)		
	Accuracy	Se %	Pr %	Accuracy	Se %	Pr %
Mariani et al. [369]	3±4	100±0	100±0	-3±3	94±15	100±0
Gouwanda et al. [371]	4±1	100±0	97±9	N/A	N/A	N/A
Catalfamo et al. [372]	4±1	100±0	100±0	4±3	100±0	100±0
Perez-Ibarra et al. [373]	0±4	80±23	99±1	12±5	81±24	100±0
Maqbool et al. [378]	4±1	100±0	100±0	4±2	88±32	100±0
Proposed	0±3	100±0	100±0	6±5	100±0	100±0
(d) Over-inclined-treadmill Walking						
Algorithm	Initial Contact (IC)			Terminal Contact (TC)		
	Accuracy	Se %	Pr %	Accuracy	Se %	Pr %
Mariani et al. [369]	2±5	100±0	90±14	-4±10	100±0	96±8
Gouwanda et al. [371]	3±2	100±0	100±0	N/A	N/A	N/A
Catalfamo et al. [372]	3±2	100±0	100±0	-7±4	100±0	100±0
Perez-Ibarra et al. [373]	-1±3	99±1	87±16	10±7	99±1	87±16
Maqbool et al. [378]	3±2	100±0	100±0	-7±4	100±0	100±0
Proposed	0±4	100±0	100±0	4±3	100±0	100±0

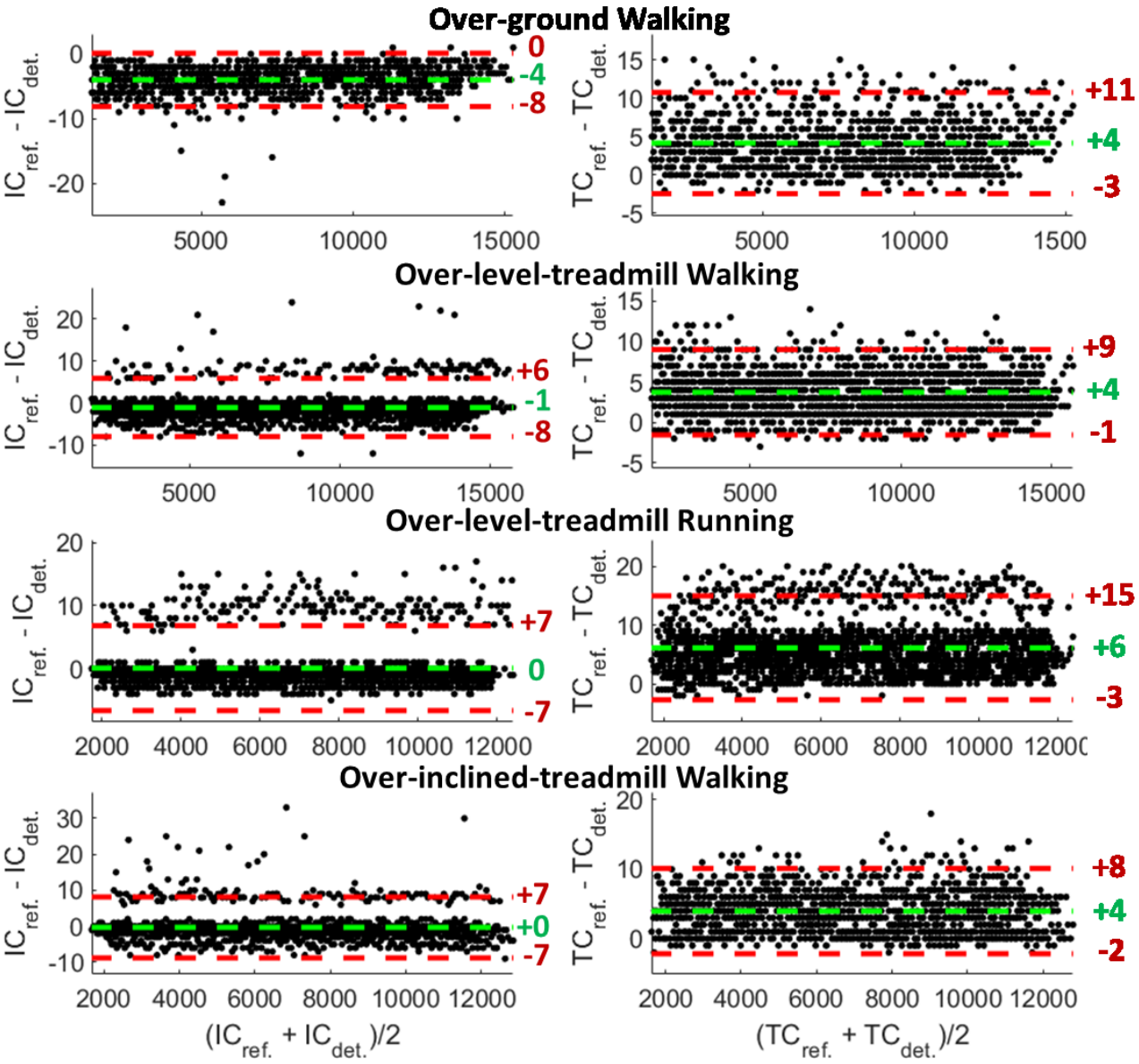

Figure 25 Bland-Altman plots of initial contact (IC) and terminal contact (TC) for four different walking modalities. Errors were calculated based on the number of samples (Fs = 100 Hz). Positive errors correspond to delays in detecting events using our real-time algorithm with respect to the reference pressure insoles. Mean error and limits of agreement (mean±1.96×standard deviation) are identified with a green line and red lines, respectively.

6.4 Discussion

In this study, we presented a heuristic algorithm for robust real-time detection of IC and TC based on the reconstruction of foot motion during various walking modalities rather than morphological features of the IMU readouts. In contrast to previous studies where the temporal accuracy of the detected events was the main target, the goal of the current study was to develop an algorithm with

sensitivity and precision of 100% to only detect true ICs/TCs. This is the first step toward creating a gait event detection algorithm for providing real-time biofeedback on gait phases for control of neural prostheses that use the functional electrical stimulation technology or exoskeletons since false detection of gait phases can result in harmful actuation of the neural prostheses or exoskeleton. Also, biofeedback-based gait rehabilitation strategies require reliable biofeedback since false detection of gait phases can affect the compliance and adherence of the user.

6.4.1 A robust signal for event detection

Various time-series measured/derived from foot- or shank-worn IMUs were used in the literature for gait event detection. Noisy time-series such as acceleration, jerk, or angular acceleration naturally have several consecutive local minima/maxima that are sensitive to gait characteristics, sensor technology, and footwear-ground interaction, and thus gait event detection based on these time-series would inherently lack sensitivity and precision. Also, choosing one local minima/maxima among several in a narrow window requires comparing it with other neighboring minima/maxima. This requires analyzing the time-series after the targeted minima/maxima that is not allowed in real-time gait event detection. Therefore, smooth time-series derived from IMUs are expected to obtain more robust gait event detection. It is not surprising that the shank and foot angular velocities have been more popular in the literature for gait event detection [369]–[371], [373], [380], [384]. Yet, raw angular velocity time-series have multiple local minima/maxima, which can be detected as gait events incorrectly.

To achieve the highest robustness in detecting IC and TC, the vertical positions of the heel and toe might be the most meaningful kinematic features, i.e., the minimum of heel/toe vertical position happens at IC/TC. Indeed, when measured by an MCS, heel and toe vertical positions showed accurate and robust results [377], [385]. Nevertheless, heel and toe position tracking using IMUs is not straightforward. First, a corrective mechanism must be used to remove the integration drift due to the numerical integration of the acceleration [386]. Second, preliminary measurements are required to determine the relative position of the heel and toe with respect to mid-foot, where IMUs can be attached reliably. One may wonder if IC/TC can be detected based on the mid-foot vertical position (to avoid the preliminary measurements). Figure 26 shows that for a representative over-level-treadmill trial, the mid-foot vertical position calculated with IMUs does not contain any prominent feature associated with the reference TC.

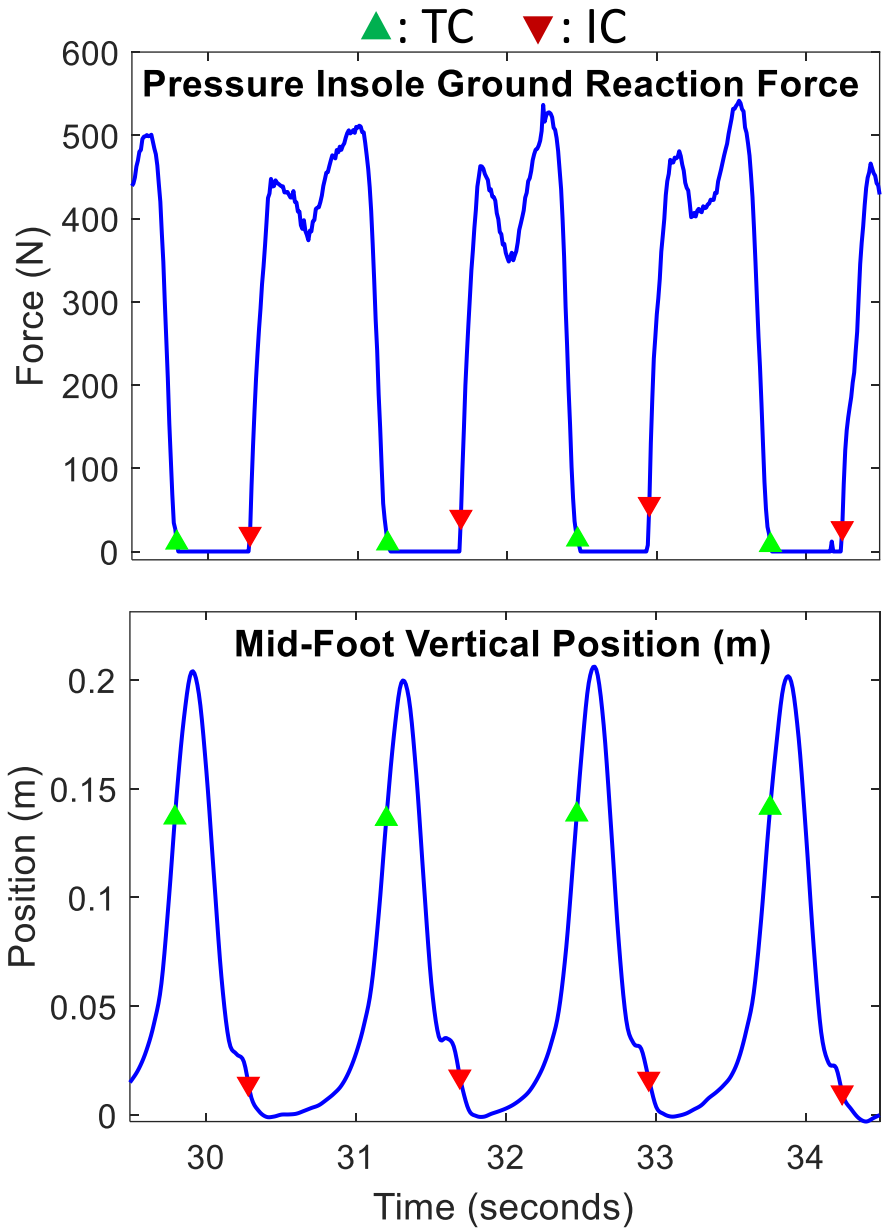

Figure 26 Representative patterns of the resultant ground reaction force profile measured with pressure insoles and mid-foot vertical position measured with IMU. Reference events are identified in the figure.

To address these limitations, we introduced the sine of the foot angle in the sagittal plane, $-\sin(\beta)$, for IC/TC detection. Figure 24 shows that $-\sin(\beta)$ has a clear pattern with prominent kinematic features associated with IC/TC in different walking modalities. Also, our previous works showed that foot orientation could be tracked with IMUs with sufficient accuracy in long-duration trials [22], [26]. To this end, SFAs such as Kalman Filters with adaptive gain regulation are suggested [25].

6.4.2 Heuristic algorithms for event detection

Heuristic gait event detection algorithms contain two parts: rules and constraints. Rules are used to identify prominent features, e.g., local minima/maxima, in a time-series, while constraints (thresholds) are used to remove false events. Time constraints prohibit searching for a new event for a period of time after detecting an event of the same type or another type. Magnitude constraints limit the search for features to specific areas of the signal that are smaller/larger than a threshold. In this work, rules and constraints (threshold values) were determined based on foot biomechanics during gait and validated among all participants. For algorithms from the literature, we either used the suggested values by their authors or tested several values to improve their performance.

Thresholds used in a time constraint depend on the gait speed. Thus, in contrast to [378] and [371] where large thresholds (300 ms and 350 ms, respectively) were used, we used a small threshold (150 ms as shown in yellow shades in Figure 23(b) and (c)) to ensure both very slow and very fast motions (e.g., running) can be analyzed reliably. Also, in contrast to [373], where a tight magnitude constraint was used to differentiate stance and swing phases, we used a biomechanically meaningful threshold ($-\sin(\beta)$ greater/smaller than -0.2 corresponding to the foot angle of ≈ 11 degrees with respect to the initial angle) to identify the periods when the heel-to-toe vector has a positive (corresponding to IC) or negative (corresponding to TC) angle with the horizontal plane. Figure 23(c) shows that this threshold is nearly 0.4 ($\approx$ 23 degrees) farther than the foot angle associated with IC/TC, which ensures high sensitivity and precision, simultaneously. The final constraint in our algorithm ensures that IC and TC are detected in order, and not multiple events of the same type are detected consecutively, similar to [373], [378].

Real-time implementation is another challenge in designing a robust algorithm. Offline local minima/maxima detection can be done by comparing the value of a time-series in an instant with that of other instants in the past and the future. However, to minimize the delay in event detection for real-time applications, we only used the value of $-\sin(\beta)$ in only 1 data sample from the future. For previously published algorithms, this resulted in the detection of multiple false local minima/maxima where the value of time-series decreased or increased only even for 1 sample in the opposite direction of its trend. To fix this issue, we designed an additional rule that not only evaluated the value of $-\sin(\beta)$ for local minima/maxima detection but also looks for a decreasing/increasing trend among previous samples to ensure that a true event is detected.

The inclusion of all the mentioned considerations differentiated our proposed algorithm from those in the literature and ensured its high robustness, Se and Pr of 100%, in gait event detection, at least for the unimpaired gait. In addition, the Bland-Altman plots in Figure 25 show that the detected events had a high temporal agreement with the reference events. Notably, the percentage of detected events with temporal error beyond the limits of agreement (mean$\pm$1.96$\times$standard deviation) was (2.3%, 3.6%), (7.1%, 2.3%), (8.4%, 6.5%), (5.8%, 2.8%) for (IC, TC) and for over-ground walking, over-level-treadmill walking, over-level-treadmill running, and over-inclined-treadmill walking, respectively. In conclusion, Table 15 shows that our proposed kinematically meaningful rules and constraints resulted in not only Se and Pr of 100%, but also a temporal accuracy higher than or comparable to the literature.

6.5 Conclusion

We used foot orientation, which provides physiologically meaningful kinematic features corresponding to our observational recognition of IC and TC, to detect temporal gait events. We conducted an experimental study to validate our algorithm, including seven participants performing four walking/running activities. By analyzing 5,555 ICs/TCs recorded during the tests, only our algorithm achieved a sensitivity and precision of 100%. Our obtained temporal accuracy (mean±standard deviation of errors ranging from 0±3 to 6±5 time samples; sampling frequency: 100 Hz) was better than or comparable to those reported in the literature. Thus, using the technical contributions in the previous/current chapters, we can measure lower limb joint angles and temporal gait events and provide biofeedback during therapeutic gait training. In the future, we must validate our proposed gait event detection algorithm with a higher sample size of able-bodied individuals and patients with gait impairment. Also, while we tried to make a fair comparison with the literature by tuning the thresholds of the implemented algorithm, further investigation with clinical data is required to confirm the current finding. In Chapter 7, we introduce a novel algorithm to assess the effect of gait training by monitoring patients' daily activities in their natural living environment.

Chapter 7

Daily Activity Monitoring with IMUs

This chapter provides the details of a daily activity monitoring algorithm that can be used to track the efficacy of rehabilitation on enhancing the functional capacity of stroke survivors. Portions of this chapter have been edited/adopted from:

M. Nazarahari, H. Rouhani, "Detection of Daily Postures and Walking Modalities Using a Single Chest-mounted Tri-axial Accelerometer," Medical engineering & physics, Vol. 57, pp. 75-81, 2018.

7.1 Introduction

Quantitative assessment of physical activities during daily life plays a significant role in evaluating the functional ability in healthy individuals and patients suffering from obesity, recurrent falling, Parkinson's disease, and back pain [387]–[391]. Notably, the functional capacity of patients during their daily life could reveal the efficacy of the instrumented biofeedback-based walking training. Thus, in this chapter, we propose a novel algorithm to monitor daily activities using a wearable IMU.

Najafi et al. [390], [392] adopted the trunk inclination angle, obtained from the integration of the angular velocity and discrete wavelet transform, to detect postural transitions (PT) from accelerometer and gyroscope signals of a chest-mounted sensor. In such algorithms, the efficiency of both PT and walking detection can be affected negatively by the improper selection of threshold

values. The acceleration patterns obtained from the signal vector magnitude (SVM) were also used to differentiate between stand-to-sit (StSi) and sit-to-stand (SiSt) transitions [393], [394]. However, these approaches (1) did not include an algorithm for the detection of StSi and SiSt instants (before classification); and (2) relied on discrete wavelet transform calculation with a high computational load.

Distinguishing activity from rest periods by detecting time intervals when the signal magnitude area is greater or smaller than a threshold was performed in [391], [395]–[397]. However, this method can be error-prone when the participant performs an activity slowly. Multiple-sensor daily activity assessment algorithms have also been presented [396], [398], [399] to provide more information and make activity classification more accurate; however, attaching several sensors to an individual's body for a long period can be cumbersome. Fusion of different sensors recording (accelerometer, gyroscopes, and barometers) also has found applications in physical activity analysis [400], [401]. However, gyroscopes, unlike accelerometers, have high power consumption and are prone to measurement drift. Also, Massé et al. [402], [403] showed that the barometer sensor must be selected with caution, as not all of them can differentiate between the altitude of the trunk during sitting and standing postures. Therefore, accelerometers are still a preferred choice for physical activity analysis as they provide robust information about daily activity independent of other sensors.

Several groups have attempted to detect level walking using an accelerometer [389], [390], [399]. Godfrey et al. [389] used only a single chest-mounted accelerometer for PT and walking detection. Nevertheless, this method was not able to distinguish level walking from walking upstairs/downstairs. Sekine et al. [404], [405] presented the application of discrete wavelet transform and fractal analysis for non-level walking classification. While both methods provided measures for discrimination between walking modalities, no classification rate between the three walking modalities was reported. Recently, Nyan et al. [406] developed a reliable technique to classify level/ non-level walking from the spatial correlation of discrete wavelet transform coefficients. In addition to a high computation load, the method was not capable of counting the number of steps.

The main objective of this chapter was to develop and validate a novel method for the detection and classification of a wide range of physical activities, including standing, sitting, lying,

level walking (with slow, normal, and fast speeds), and walking upstairs and downstairs using a single chest-mounted accelerometer. The key features of our proposed method are: (1) detection and classification of an inclusive range of physical activities with higher accuracy, sensitivity and specificity compared to the literature in various movement habits among different individuals; and (2) detection of and counting the number of steps during level walking, walking upstairs and downstairs, using the same chest-mounted accelerometer. To this end, we applied the biomechanical characteristics of each PT and walking modality to extract robust metrics for the detection and classification of daily activities.

7.2 Materials and Methods

7.2.1 Experimental Method

Two separate experimental studies were conducted in the laboratory and outdoors involving healthy participants. *Study I* was conducted in the presence of an MCS as a gold standard reference system to validate the accuracy of the proposed algorithm in (1) measuring trunk inclination angle and vertical displacement during PTs; and (2) detecting the occurrence time of PTs. *Study II* was conducted to evaluate the performance of the proposed algorithm in long-term analysis of a wide range of physical activities in a free-living environment. Research Ethics Board Committee of the University of Alberta approved the study protocol, and written consent was obtained from all participants.

Study I: Main daily activities, including lying, sitting, standing, and level walking, were evaluated in ten healthy participants (all male, 27±12 years old). The protocol of this study was as follows: sitting on the mattress (height = 10 cm, start point of the test), lying on the mattress, sitting on the mattress, standing, sitting on the first chair (height = 61 cm), standing, sitting on the second chair (height = 50 cm), standing, walking, sitting on the first chair, standing, sitting on the second chair, standing, sitting on the mattress, lying on a mattress, and repeating all these activities once again. For the first five participants, only one chair (height = 50 cm) was used for StSi/SiSt during the experiment, while for the rest, two chairs (heights = 61 and 51 cm) were used.

Study II: The experiment was conducted at the university campus as a free-living environment. Ten healthy participants (7 males and 3 females, 26±2 years old) were involved. They performed eight activities: standing, sitting, level walking (slow-, normal-, and fast-paced),

walking upstairs, walking downstairs, and lying in a self-selected order. Specifically, for level walking, participants were asked to walk with self-selected slow, normal, and fast speeds to evaluate the robustness of the proposed method for detecting walking periods with various speeds. During all tests, the study coordinator recorded the participants' activities with a hand-held camera.

7.2.2 Data Collection

During both experiments, an IMU (Physilog, GaitUp, Switzerland) was fixed on the participants' chest (over sternum) using medical tape. The benefits of attaching the IMU to the chest are: (1) the flat bony surface of the sternum facilitates repeatable sensor attachment by even unskillful users; and (2) the chest-mounted sensor minimally interferes with daily routines, in comparison with sensors on the sacrum, thigh, or even pocket. In this study, only the tri-axial accelerometer (range: $\pm$11g) of the sensor module was used in our proposed method (gyroscope was only used to implement methods presented in the literature). The sampling frequency was 100 Hz, and the data was recorded on an internal memory card. After completing data collection, the data were transferred from the memory card to a computer for further analysis (MATLAB, MathWorks, USA). The sensor frame was defined such that the *x*-axis pointed forward (anterior direction), *y*-axis pointed upward, and *z*-axis pointed toward the right (lateral direction).

An MCS (Motion Analysis Corporation, USA) with eight infrared cameras sampling at 100 Hz was used as a gold standard reference system, and its recordings were synchronized with the IMU in study I. Three retro-reflective markers were placed on the sensor box to measure its 3D movement. Four markers were placed on heels and toes bilaterally to measure the gait cycles. The markers over the sternum were used to validate the height change during StSi/SiSt calculated by the IMU, and the foot markers were used to identify the number of steps. To assess the validity of the results obtained by the accelerometer, the MCS recordings were analyzed to determine the number of PTs and the start/end of each PT. The PT instants were defined as the average of the start and the end times detected by MCS (e.g., for StSi transition, the start time was defined as the start of the leaning forward phase from standing posture and the end time was defined as the end of leaning backward phase after sitting on the chair [392]).

7.2.3 Postural Transition Detection and Classification

Our proposed method for PT detection and classification is shown in Figure 27. We used the trunk inclination angle as the primary metric for PT detection. This angle was estimated as the angle between the gravitational component of the vertical acceleration ($GA_{y_{A,v}}$) measured by the accelerometer and the gravity vector (g):

$$\theta = \arccos(GA_{y_{A,v}}/\mathrm{g}) \qquad \text{Equation 54}$$

The $GA_{y_{A,v}}$ was obtained by applying a second-order elliptical IIR low-pass filter with the cut-off frequency, passband ripple, and stopband ripple of 0.25 Hz, 0.01 dB, and -100 dB, respectively, to the accelerometer readout ($y_{A,v}$) in the vertical axis.

7.2.4 Lie-to-sit (LySi) and Sit-to-lie (SiLy)

The trunk inclination does not increase beyond 70 degrees during activities other than lying [391]. Thus, the trunk inclination angle was used to detect the SiLy and LySi instants. Also, the sign of the gradient of $y_{A,v}$ at these SiLy/LySi instants was used to distinguish SiLy from LySi. Notably, the frontal (instead of vertical) axis of the accelerometer was used to measure gravity during lying. To discard unknown movements (labeled with trunk inclination beyond 70 degrees), the algorithm detected a short static period with the measured frontal acceleration associated with the gravity after (before) any SiLy (LySi) transition.

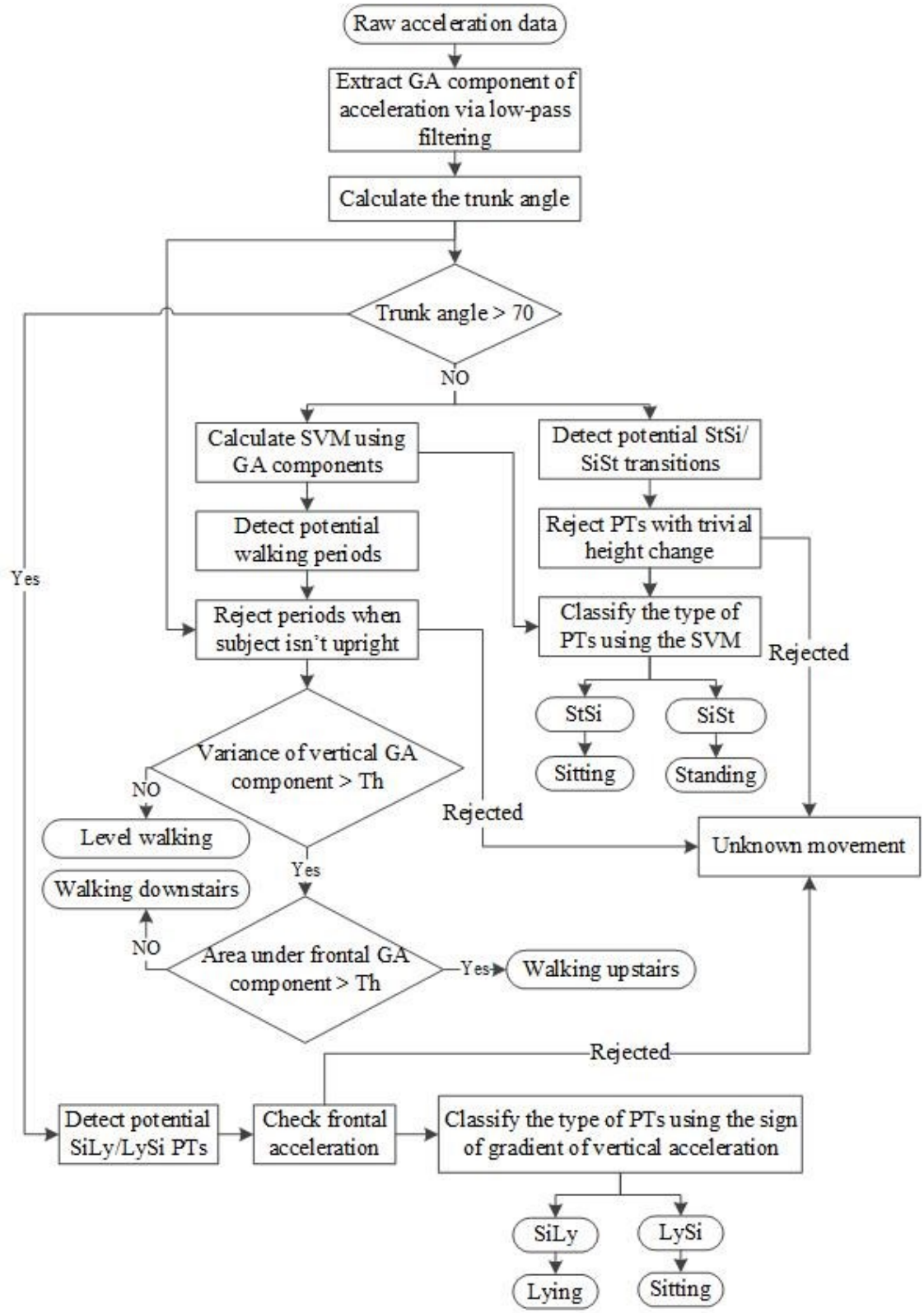

Figure 27 The flowchart of the proposed method for determining the body posture from the raw data obtained from a chest-mounted accelerometer. SVM refers to signal vector magnitude, PT to postural transition, and GA to the gravitational component of the accelerometer recordings.

7.2.5 Stand-to-sit (StSi) and Sit-to-stand (SiSt)

We detected the incidence of StSi/ SiSt transitions using a threshold of 20 degrees on the trunk inclination angle. To cope with the challenge of tuning this threshold, we proposed a novel approach to improve the robustness of StSi/SiSt detection against false detections when the threshold is set small (here, 20 degrees). In this method, we used the vertical displacement of the chest (ΔY) to reject the false detections. Note that the chest height decreases/increases about the thigh length during the StSi/SiSt transitions. As such, detected StSi/SiSt transitions while the calculated ΔY was considerably smaller than (less than 50%) the thigh length of the participants were rejected. ΔY was calculated by double integration of the vertical acceleration relative to the global reference frame ($y^{g}_{A,v}$) similar to [39]:

$$y^{g}_{A,v}(t) = -GA_{y_{A,f}}(t)\sin\big(\theta(t)\big) + GA_{y_{A,v}}(t)\cos\big(\theta(t)\big) \quad \text{Equation 55}$$

$$\Delta Y = \iint_{t_1}^{t_2} y^{g}_{A,v}(t)dt \quad \text{Equation 56}$$

To reduce the integration drift in Equation 56, the $[t_1, t_2]$ interval was selected to be short, and the mean value of accelerations was removed before integration. Subsequently, the StSi/SiSt transition time was detected as the time difference between the nearest local minima in trunk inclination angle before and after the detected StSi/SiSt.

Then, to distinguish StSi from SiSt, we used the 'acceleration pattern' during StSi/SiSt transitions (Figure 28). To obtain the 'acceleration pattern,' the SVM was calculated using the GA components of accelerometer readout:

$$SVM = \sqrt{{GA_{y_{A,f}}}^2 + {GA_{y_{A,v}}}^2 + {GA_{y_{A,l}}}^2} - \mathrm{g} \quad \text{Equation 57}$$

where $GA_{y_{A,f}}$, $GA_{y_{A,v}}$, and $GA_{y_{A,l}}$ are the frontal, vertical, and lateral GA components of the accelerometer readouts. Figure 28 shows that while $y_{A,v}$ and $y_{A,f}$ did not directly provide distinctive patterns between StSi and SiSt, SVM showed a negative (positive) peak followed by a positive (negative) peak during StSi (SiSt) [4]. Instead of using the order of the negative and positive peaks in SVM (proposed in [393], [394]), in our algorithm, the cumulative integration of SVM was calculated over the transition time, and the sign of cumulative numerical integration of SVM was used to distinguish StSi from SiSt. Unknown movements (e.g., bowing or squats) were

not considered as StSi/SiSt since they did not pass the following two conditions simultaneously: (1) trunk inclinations lower than 70 degrees; and (2) ΔY about the thigh length during the transition.

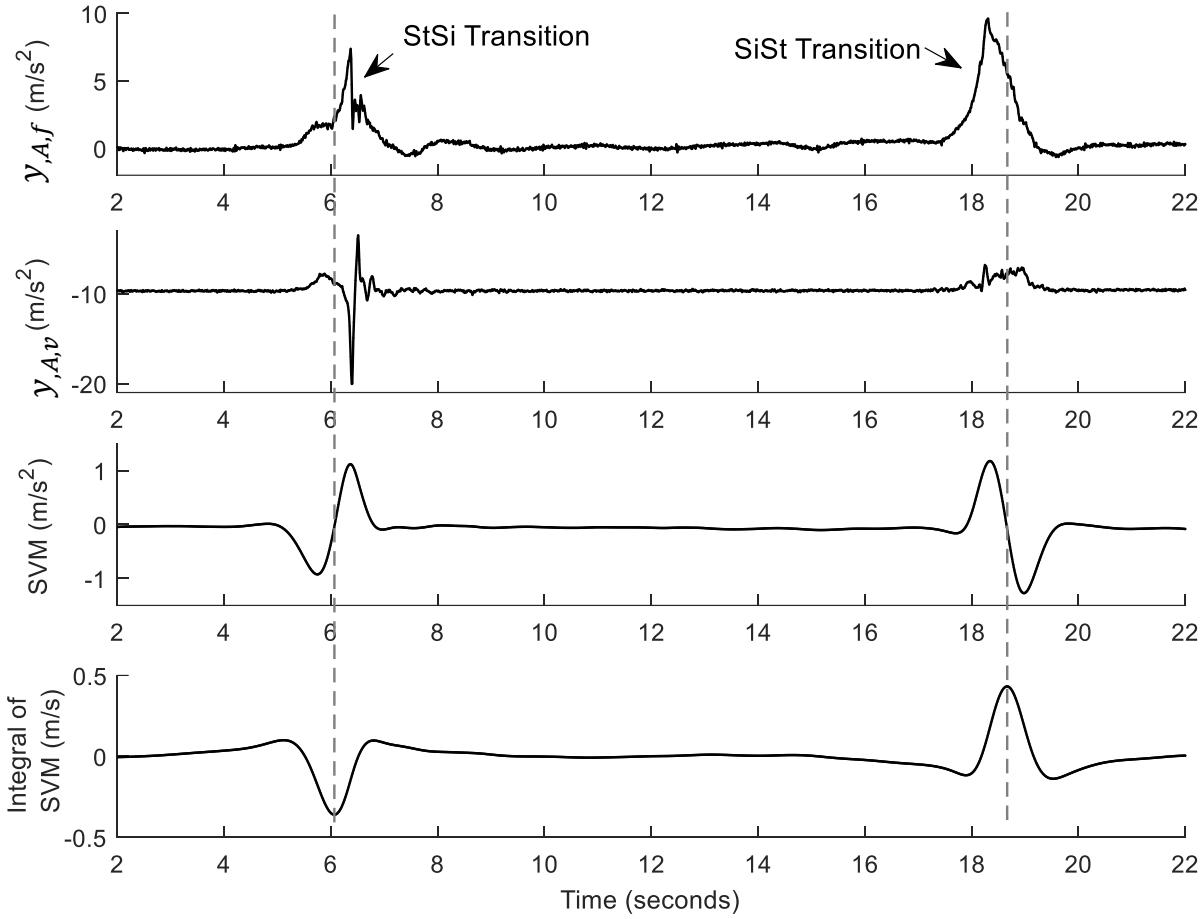

Figure 28 Representative time-series of the accelerometers recording in the vertical ($y_{A,v}$) and frontal (anterior-posterior) ($y_{A,f}$) directions, signal vector magnitude (SVM), and cumulative numerical integration of SVM during StSi and SiSt transitions. During a StSi transition (when the negative peak in the SVM time-series occurs before the positive peak), a large negative peak can be observed in the cumulative integration of SVM at the StSi instant, while the reverse occurs at the SiSt instant. The vertical dashed lines represent the detected postural transitions using the proposed method.

7.2.6 Walking

We used the successive positive peaks of SVM beyond a predefined threshold to detect walking periods. To decrease the dependency of our proposed method on the threshold value, we compared the trunk inclination angle at the walking interval to a small threshold. Then, we rejected the walking periods when the participant was not in an upright posture.

Trunk inclination was also used as the primary metric to detect walking upstairs/downstairs. Naturally, trunk inclination during level walking helps to keep the center of

mass of the body inside the base of support and maintain the balance [407], [408]. Moreover, during non-level walking, the trunk has to incline further compared to level walking to maintain balance due to both horizontal and vertical displacement of the body. The more change in the trunk inclination, the more change in the $GA_{y_{A,v}}$. As a result, the variance of the $GA_{y_{A,v}}$ would be larger in periods associated with walking upstairs/downstairs in comparison to level walking (Figure 29). Moreover, $GA_{y_{A,f}}$ showed positive values for walking upstairs, and mixed positive and negative values for walking downstairs. Therefore, as a novel method, we proposed to use cumulative numerical integration to calculate the area under $GA_{y_{A,f}}$ and classify the non-level walking (upstairs or downstairs) using a single threshold. Similar to level walking, we determined the number of steps during non-level walking based on the successive positive peaks of the SVM. Moreover, as walking was detected by at least three successive peaks in the SVM signal within a pre-defined step duration, unknown movements performed in an un-repeated fashion were discarded.

7.2.7 Data Analysis

To evaluate the performance of our proposed method for PT detection, similar to [390], the sensitivity, specificity, and accuracy of each PT detection were calculated using PT detected by the cameras as a reference. Also, the correlation coefficient was used to compare ΔY time-series obtained by accelerometer using our proposed method and ΔY obtained by cameras. To compare the results obtained by our method to those obtained by other methods, we implemented three methods for PT identification in the literature on our collected datasets. The results were presented as mean±SD (standard deviation) for each metric.

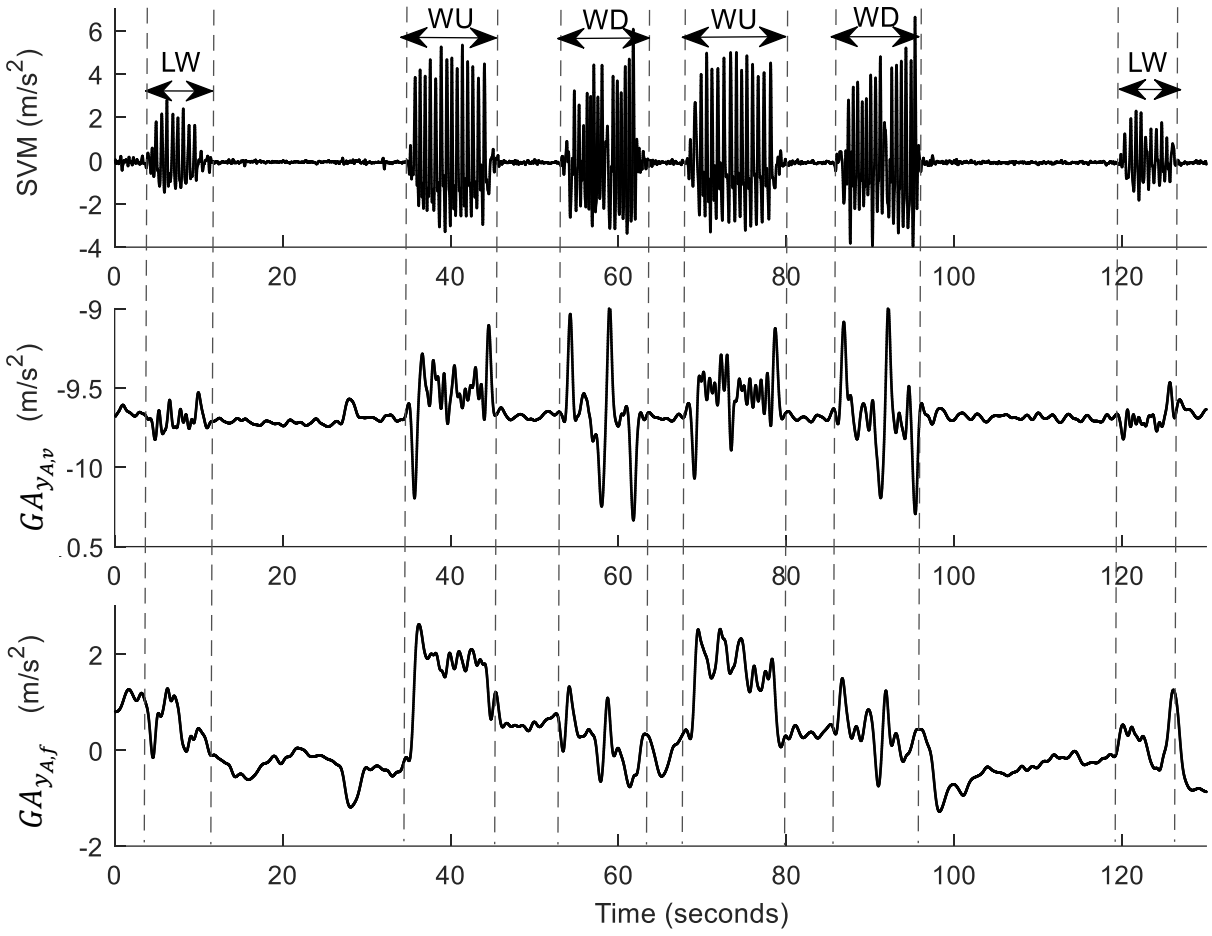

Figure 29 Representative time-series of the gravitational component of the accelerometer recordings (GA) during level walking (LW), walking upstairs (WU), and walking downstairs (WD). The variance of the vertical GA component is higher in WU/WD periods in comparison to LW. The frontal GA component values are positive during WU, while both positive and negative values were observed during WD. The vertical dashed lines represent the detected postural transitions using the hand-held proposed method.

7.3 Results

7.3.1 Study I: Experiments in Laboratory Environment

The completion time for data collection for each participant was 250±41 seconds. 29 SiLy, 28 LySi, 74 StSi, and 77 SiSt transitions and 250 gait cycles were performed by all participants during the study I. A representative acceleration pattern and the associated vertical displacement of the trunk obtained by MCS are shown in Figure 30. The SiLy and LySi transitions were detected and classified with an accuracy of 100±0%. Also, the proposed method obtained the accuracy, sensitivity, and specificity of 99±3%, 100±0%, and 98±5%, respectively, for StSi identification and 98±3%, 98±4%, and 97±5% for SiSt identification (Table 16(a)). The time differences

between the actual (obtained from MCS) and detected transition instants obtained by the proposed method and other methods in the literature, applied on our dataset, are also presented in Table 16(c). Our proposed method detected the SiLy/LySi and StSi/SiSt instants with an error of less than 0.3 seconds and 0.2 seconds, respectively, relative to the transition instants obtained by the MCS.

Correlation analysis was performed to evaluate the accuracy of the vertical displacement estimation using Equation 56 during StSi and SiSt transitions. The correlation coefficients between the vertical displacement of the trunk (ΔY) obtained by the accelerometer using our proposed method and that obtained by cameras were 0.94±0.10, 0.96±0.06, and 0.94±0.08 for seat heights of 10 (mattress), 50, and 61 cm, respectively.

Table 16 Comparison between the proposed method and other methods in detection of postural transitions: (a) accuracy, sensitivity, and specificity for detection and classification of StSi and SiSt transitions, (b) accuracy for detection of level walking and step counting, and (c) time difference between the LySi/SiLy and StSi/SiSt instants obtained by the accelerometer and those obtained by MCS. The results are presented as mean±standard deviation among all participants.

(a) StSi/SiSt detection and classification

	Accuracy (%)		**Sensitivity (%)**		**Specificity (%)**	
	StSi	**SiSt**	**StSi**	**SiSt**	**StSi**	**SiSt**
The proposed method	99±3	98±3	100±0	98±4	98±5	97±5
Najafi et al. [392]	81±12	83±12	82±13	82±11	81±12	84±14
Godfrey et al. [389]	88±10	91±11	88±10	92±10	89±12	90±12
Bidargaddi et al. [393]	95±5	93±4	95±8	97±5	95±8	89±5
Alternative method[1]	96±8	93±8	97±10	94±7	95±7	92±10

(b) Level walking detection and step counting

	Accuracy (%)		
	low threshold value, high detection rate	high threshold value, low detection rate	low threshold value, rejection using trunk tilt
The proposed method	83±11	86±9	96±3
Najafi et al. [390]	83±10	87±9	92±6
Godfrey et al. [389]	82±10	87±7	96±5

(c) Time difference (in seconds) between detected and actual SiLy/LySi and StSi/SiSt instants

	SiLy/LySi	**StSi/SiSt**
The proposed method	0.28±0.21	0.18±0.15
Najafi et al. [390]	0.45±0.25	0.18±0.12
Godfrey et al. [389]	0.33±0.26	0.18±0.13

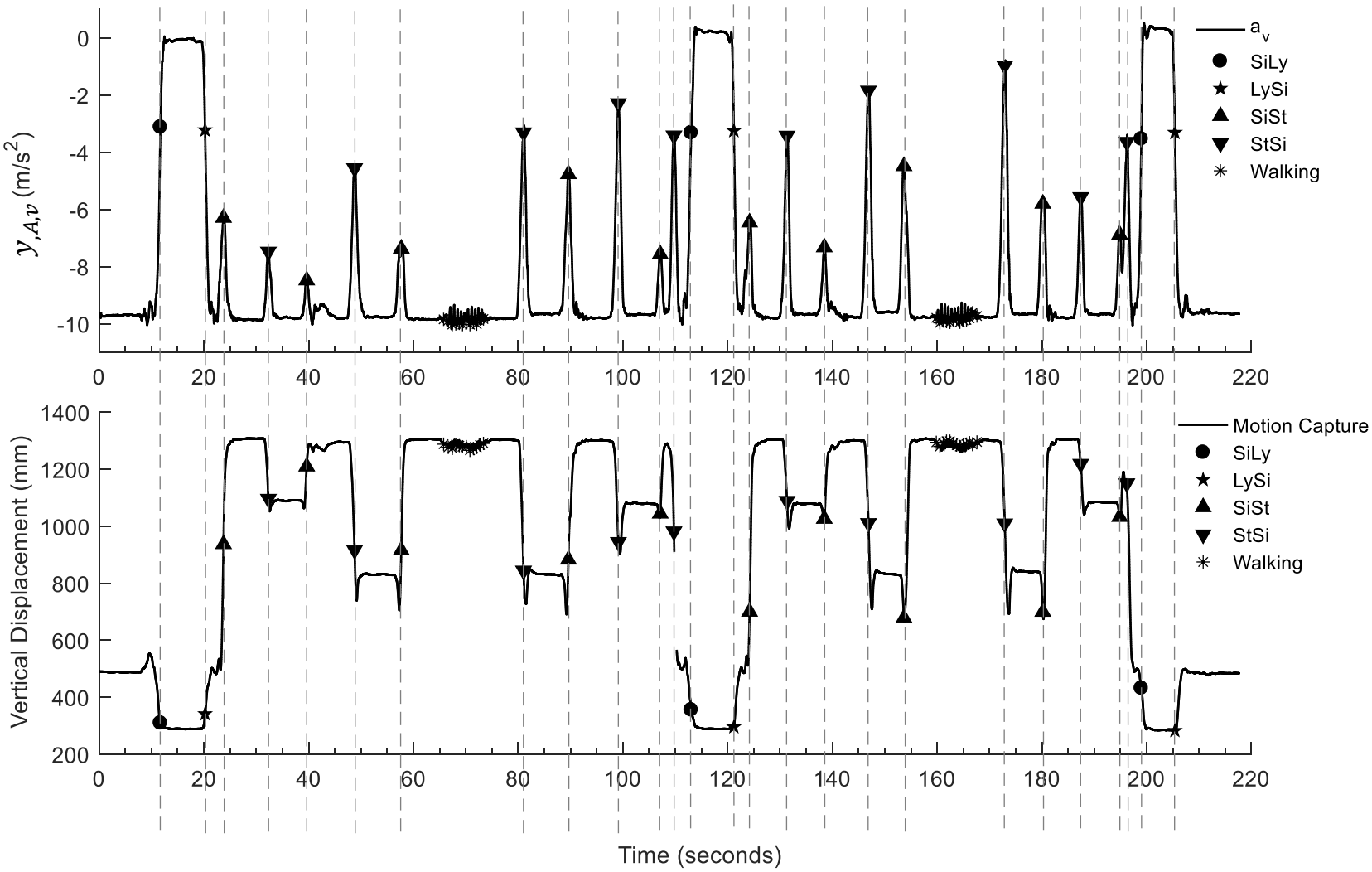

Figure 30 A representative acceleration pattern obtained with the accelerometer and associated vertical displacement of the trunk obtained with the MCS. The data were collected from a young, healthy participant in the laboratory. The detected and classified postural transitions, sit-lie (SiLy), lie-sit (LySi), stand-sit (StSi), and sit-stand (SiSt) are shown with circles, pentagons, downward triangles, and upward triangles, respectively. Steps during level walking periods are presented with stars. The vertical dashed lines represent the detected postural transitions using the proposed method.

Table 16(b) shows that the accuracy of our proposed method for level walking detection was the highest (96±3%) when a low threshold value was chosen and the trunk inclination angle was used to reject false detections (compared to the simple method without rejection phase using low/high threshold value). The application of this technique led to better accuracy even for the walking detection methods proposed in [389], [390] (Table 16(b)).

7.3.2 Study II: Experiments in Free-living Environment

The completion time for data collection for each participant was 18±2.5 minutes. The accuracy and specificity of SiSt detection were 99±2% and 97±5%, respectively. Detection and classification of other transitions (StSi, SiLy, and LySi) had accuracy, sensitivity, and specificity of 100%, for various movement habits. Both slow and normal pace level walkings were detected with an accuracy of 99±1%. Detection of fast walking was less accurate than slow and normal pace walking. Table 17 shows that the number of steps was counted with an accuracy of 97% and 96% during walking upstairs and downstairs, respectively. The second study also showed the ability of the proposed method to analyze the physical activities of both male and female participants.

Table 17 Performance of the proposed method for (a) detection and classification of postural transitions (StSi, SiSt, SiLy, LySi), and (b) level/non-level walking detection and step counting, outdoor (study II). The results are presented as mean±standard deviation among all participants.

(a) Postural transition detection				
	Number of PTs	**Accuracy (%)**	**Sensitivity (%)**	**Specificity (%)**
StSi	123	100±0	100±0	100±0
SiSt	123	99±2	100±0	97±5
SiLy	80	100±0	100±0	100±0
LySi	80	100±0	100±0	100±0

(b) Walking detection and step counting		
	Number of steps	**Accuracy (%)**
Level walking, normal pace	3,630	99±1
Level walking, slow pace	1,787	99±1
Level walking, fast pace	2,009	95±15
Walking upstairs	301	97±3
Walking downstairs	323	96±2

7.4 Discussion

This study made a twofold contribution. First, we developed a novel method for accurate detection and classification of StSi, SiSt, SiLy, and LySi transitions for daily activity analysis using a single chest-mounted accelerometer. We validated the performance of the proposed method in two experimental conditions (study I: in-lab and study II: outdoor), and showed its higher accuracy, sensitivity, and specificity, for several PTs, compared to other methods in the literature applied on our dataset. Second, we developed a novel method for the detection and classification of level walking with various speeds, walking upstairs and downstairs using the same single chest-mounted accelerometer. Higher accuracy, sensitivity, and specificity were observed in study II compared to study I, which could be due to fewer false detected or undetected events relative to the overall number of events in study II.

7.4.1 Postural Transition Detection and Classification

In our proposed method for computing trunk inclination angle and then comparing its value with thresholds to detect PTs eliminated the need for (1) recording a static period at the start of the experiment [389]; or (2) the use of a gyroscope [390] that would increase the power consumption considerably. Traditionally, StSi/SiSt detection and classification based on direct determination of postures have faced two challenges [391], [396]: (1) differentiating between standing and sitting postures using a single chest-mounted inertial sensor may not obtain high sensitivity and specificity [391]; and (2) slow-paced activities or transitions are hard to identify based on metrics such as signal magnitude area [396]. To tackle these two challenges, our proposed method involved three steps: (1) we detected all potential StSi/SiSt transitions based on a low threshold on the trunk inclination angle (20 degrees); (2) we identified and rejected the false detections using a threshold (individual's thigh length) on the chest height change (ΔY) during the transition; and (3) we distinguished StSi from SiSt using the pattern of the cumulative integration of SVM. To this end, we used the GA components to compute the SVM instead of using acceleration signals directly, as suggested in [393], [394], [409]. This method eliminates the need for time-consuming SVM modification based on discrete wavelet transform.

Our proposed method obtained higher accuracy, sensitivity, and specificity for SiSt/StSi transition classification compared to those presented in [389], [393], [399] and implemented on

our dataset. The large correlation coefficients between ΔY obtained with the accelerometer and cameras indicated accurate estimations obtained with the former during StSi/SiSt transitions. Nevertheless, estimation errors because of the double integration of the noisy acceleration signal were inevitable. Therefore, the application of ΔY for StSi/ SiSt classification inherently resulted in lower accuracy, sensitivity, and specificity, compared to our proposed method (Table 16(a)).

7.4.2 Detection of Level, Upstairs, and Downstairs Walking

Walking detection based on SVM peak detection faces two challenges: (1) several false peaks are detected when the threshold is set low (low specificity); (2) some true peaks are not detected when the threshold is set too large (low sensitivity). To investigate the effect of the threshold value on walking detection algorithms, we detected walking periods based on low and high threshold values using our proposed method and the methods proposed in [389], [390]. In addition, we implemented an extra step to reject false detections based on trunk inclination measurement when a low threshold value was chosen. According to Table 16(b), applying a low threshold value and rejection of false detections resulted in the highest accuracy during the study I for all methods.

Our method was also able to detect low and normal speed walking with an average accuracy of 99% during study II (Table 17). During fast walking, the walking pattern becomes more irregular compared to slow and normal walking. Although discriminating between non-level and fast level walking using the variance of the $GA_{y_{A,v}}$ can be challenging our method classified only one of the fast walking periods incorrectly as walking upstairs.

Detection and classification of walking upstairs/downstairs are more challenging than level walking. To the best of our knowledge, all the proposed methods for analyzing walking upstairs/downstairs detection were focused only on locomotion analysis [404]–[406], [410] and were unable to measure the number of steps [404]–[406]. Our method used $GA_{y_{A,v}}$ and $GA_{y_{A,f}}$ time-series to differentiate between level and non-level walking periods and to classify the type of non-level walking, respectively. As a result, walking upstairs and downstairs periods were classified correctly using the numerical integration of $GA_{y_{A,f}}$ and counted the number of steps with an accuracy of 97% and 96%, respectively.

7.5 Conclusions

This chapter proposed a novel algorithm for daily activity monitoring using the kinematic features of the postural transitions or the repetitive morphological features in the SVM time-series. As a result, SiLy and LySi were detected with an accuracy of 100% in both validation studies, and StSi and SiSt transitions were detected with the accuracy of 97% and 96%, respectively, in study I, and 100% and 99% in study II. Also, in addition to differentiating between different walking modalities, our algorithm counted the number of steps with an accuracy of 99%, 97%, and 96% during level walking (slow and normal pace), walking upstairs and walking downstairs, respectively. Thus, our proposed algorithm can be used to monitor the daily activities of the patients before/during/after therapeutic gait training to reveal the efficacy of the training. Also, while we tried to make a fair comparison with the literature by tuning the thresholds of the implemented algorithm, further investigation with clinical data is required to confirm the current finding. This is particularly important for daily activity monitoring, where the sensitivity and specificity of the algorithms can be influenced by jerkiness and slowness of movements observed in older adults and patients.

Chapter 8

Wearable Technology for Therapeutic Gait Training

This chapter describes how the previous chapters' technical contributions can be combined with one another to create a wearable system for therapeutic gait training. In particular, this chapter provides a step-by-step procedure for performing clinical lower limb motion analysis with the proposed technologies. Also, this chapter provides a brief description of the biofeedback system, the parameters that can be provided during rehabilitation, and the experimental protocol for therapeutic gait training with the proposed technology.

Using the developed techniques in Chapter 3 to Chapter 7, we can create a wearable system for therapeutic gait training to measure the lower-limb joint angles and gait temporal parameters in real-time. Then, a biofeedback control system (Figure 31) must be designed to translate the measured quantities to meaningful biofeedback for the patient.

However, as the integration of these technical contributions might seem difficult in the first step, we briefly describe how to integrate the technical contributions in Chapter 3 to Chapter 7 to calculate lower-limb joint angles and temporal gait events. These steps are presented in a separate chapter from Chapter 9: Conclusions & Future Perspectives, as the goal was to clarify the usage of the current system.

1. Seven IMUs are required to track the motion of both feet, shanks, thighs and pelvis. IMUs can be attached to the segments using double-sided tape or Velcro straps. It is important to ensure

that (1) IMUs are attached over the bony surface of the segments or at least far from the muscles belly to minimize the soft tissue artifacts; and (2) IMUs' attachments are secure to minimize the errors caused by IMU wobbling during the user's motion.

2. Before the main trials, a calibration trial is needed to find the sensor-to-segment transformation required for clinical joint angle measurement. As detailed in Chapter 3, a calibration trial must contain a period of quiet standing and repetitions of a single-axis rotation of the body segments (hip FE or walking on a straight line). For able-bodied individuals, we suggest the calibration using walking on a straight line (whether in a separate calibration trial or as a part of the main trial). We recommend the calibration using hip FE for patients with an impaired gait to ensure that a proper single-axis rotation is performed.
3. An SFA for IMU orientation tracking (Chapter 5) is required to calculate joint angles and detect temporal gait events. Adaptive gain tuning (Chapter 4) and offline calibration (Section 2.3.7 and Section 5.3.1) should be performed to ensure high accuracy and repeatability in orientation tracking.
4. At the beginning of the main trial, a few seconds of quiet standing is required to remove the bias in the measured joint angles due to attachment inaccuracies and sensor-to-segment calibration errors. Then, at each time instant, the orientation of the proximal and distal segments must be calculated using the SFA. Next, the orientation of the anatomical local coordinate system of a segment can be calculated by multiplying the IMU orientation and the sensor-to-segment transformation. Finally, the joint coordinate system defined in [309] can be utilized to measure clinically meaningful 3D joint angles, as recommended by the ISB [299]. Joint angles can be presented as biofeedback during therapeutic gait training.
5. Using the foot orientation tracked with the foot-worn IMU, temporal gait events (IC and TC) can be detected in real-time, as described in Chapter 6. Temporal gait events can be presented as biofeedback during therapeutic gait training.
6. A chest-mounted IMU, along with the heuristic algorithm described in Chapter 7, can track the patient's daily activities outside of the laboratory setting. This can reveal the efficacy of therapeutic gait training in increasing the mobility of patients.

Steps 1 to 5 described above will produce joint angles and temporal gait parameters in real-time. Then, a biofeedback display system is required (future work, see Section 9.2.5) to provide the patient and therapist with a visual or auditory biofeedback display during gait training.

In the simplest form, a display reports the measured biofeedback parameters to the patient and therapist in real-time. We have created a minimum viable display that presented the motion of the lower limb as a stick figure. Also, our display presented the joint angles in real-time to the patient and therapist as graphs to enable them to monitor the pattern of motion. Our system used seven Xsens IMUs (MTws, Xsens Technologies, The Netherlands), which transferred data to a computer via a proprietary wireless connection. All calculations were performed in MATLAB (MathWorks, USA).

On the other hand, a prescriptive biofeedback system requires a knowledge base to compare the pathological movement patterns with the targeted normal ones and present a proper visual or auditory display to help the therapist personalize the therapy based on the type and severity of the gait impairment and pathology. For such a system, a visual display that presents the error between the measured impaired movement and the targeted normal one can be produced. Also, audio cues synchronized with errors (e.g., a beeping sound with a frequency or amplitude proportional to the error) can be generated in real-time.

To perform therapeutic gait training, our wearable technology should be applied during training sessions of ambulatory stroke survivors. For example, there can be six weeks of training, three sessions per week, with one week of assessment/rest in the middle [411]. To examine the enhancement in motor function, a walking assessment should be performed one week before the beginning of training, during week 4 (assessment/rest week), one and six weeks after the training. The outcome measures obtained in pre-, during-, and post-training should be compared to evaluate the enhancement in motor function of patients.

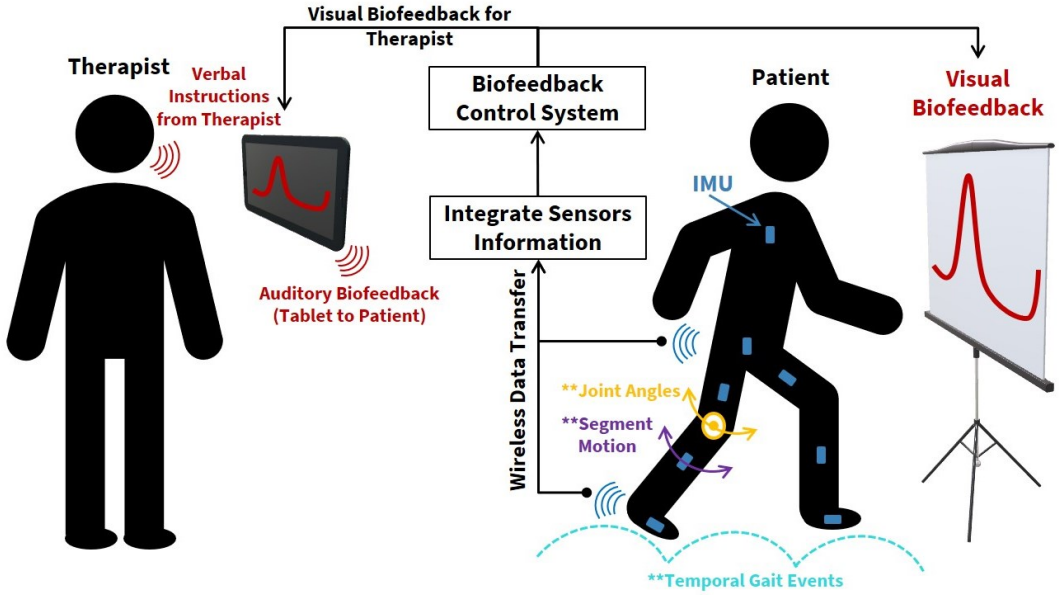

Figure 31 Wearable technology for gait rehabilitation. The blue rectangles show the IMUs. Seven IMUs attached to the lower limb will be used to track segments' orientation (and thus, joint angles) and gait temporal parameters. The chest-mounted IMU will track the daily activities of the patients in their natural living environment. IMU data will be transferred to a computer/tablet in real-time to perform the calculations and compute the measured biofeedback parameters. Then, a biofeedback control system must be designed to report the biofeedback parameters via a visual or auditory display.

Chapter 9

Conclusions & Future Perspectives

This chapter provides a summary of the results and presents the future directions for this research.

9.1 Conclusions

Using the technical contributions in this thesis, we can create a wearable sensor technology to measure clinically meaningful lower limb joint angles and detect temporal gait events. Then, these quantities can be presented as biofeedback to the patient and the therapist during therapeutic gait training.

9.1.1 Sensor-to-Segment Calibration

A survey of the literature showed that a reliable sensor-to-segment calibration procedure is required to transform the measured quantities from the IMU sensor frame to the anatomical frame of the segment. We, for the first time, showed that twenty consecutive hip FE movements or eight steps of straight walking, together with three to five seconds of quiet standing, can be used as an effortless yet accurate and repeatable sensor-to-segment calibration to obtain clinically meaningful lower limb joint angles using IMUs. The accuracy and repeatability of the proposed procedures were better than or comparable with the calibration-specific movements/postures in the literature. However, our calibration procedures will maximize the ambulatory measurement capability of IMUs in free-living environments.

9.1.2 Adaptive Gain Regulation of SFAs

A survey of the literature showed that the performance of SFAs highly depends on the selection of SFA gains, regardless of the SFA structure or complexity. Thus, we presented a general

framework for designing an optimal adaptive gain regulation scheme applicable to both families of SFAs: CFs and KFs. We showed that regulating the SFA's gains using IMU signal intensity resulted in significantly more accurate and repeatable estimates of body segment orientation during gait. Also, we showed that an optimized simple gain regulation scheme such as switching gains between two or three levels was sufficient, and there was no need for a more complex scheme such as a Mamdani fuzzy inference system.

9.1.3 IMU Orientation Tracking with Sensor Fusion

A survey of the literature revealed that most SFA's performance degrades during long-duration tasks. Thus, we proposed two new SFAs by estimating the error sources of sensors embedded in an IMU and correcting the IMU recordings before orientation estimation. Also, to fill the main gap in the literature, i.e., lack of comprehensive benchmarking studies, we compared the estimated orientation with 37 SFAs from CF, LKF, EKF, CKF, SRUKF and SRCKF families and shared the codes and sample data on our laboratory website. Our results identified the best SFAs for each family in terms of accuracy, robustness, and execution time.

9.1.4 Gait Event Detection

Detecting gait events with high reliability is a must for providing real-time biofeedback during therapeutic gait training or controlling a system such as Functional Electrical Stimulation. Therefore, to achieve high sensitivity and precision, i.e., detecting all and only true gait events, we proposed a novel approach based on the measurement of the foot orientation. Foot orientation, despite foot/shank angular velocity and acceleration, provides physiologically meaningful kinematic features corresponding to our observational recognition of IC and TC, regardless of the walking modality. Thus, we could use the tracked orientation of the foot (with one of the proposed SFAs in this thesis) to detect IC and TC and provide biofeedback in real-time.

9.1.5 Daily Activity Monitoring

To reveal the efficacy of the therapeutic gait training, we proposed a method to (1) detect and classify several types of postural transitions and walking modalities (level/non-level walking); and (2) count the number of steps during each walking modality with high accuracy, using only one chest-mounted accelerometer. Our proposed method can be an ideal choice for long-term

ambulatory monitoring of daily activities in the free-living environment to quantify the activity level and lifestyle of patients.

9.2 Future Perspectives

9.2.1 IMU Orientation Tracking with Sensor Fusion

While we performed a comprehensive experimental comparison survey of SFAs, there is still an urgent need for more studies with the following features:

1. Various test scenarios should be recorded. Especially, long-duration trials (longer than 6 minutes) are required to evaluate the effect of b_G.
2. Data from multiple IMUs, preferably with different manufacturing qualities, should be recorded. Such experimental trials can demonstrate the effectiveness of the SFA correction strategy using the accelerometer and magnetometer, specifically in the long-duration trials where strap-down integration faces a significant drift.

Using benchmarking studies with these features, the following should be evaluated.

1. Various adaptive gain tuning strategies must be assessed.
2. Various stochastic and heuristic models for estimating the unmeasurable time-varying terms in the IMU readouts must be investigated.
3. Less common modeling techniques, such as two-layer filters or variable state KF, must be further evaluated.

9.2.2 Gait Event Detection

In the future, the accuracy and robustness of our proposed gait event detection algorithm must be evaluated for the severely impaired gait of patients with neurological or orthopedic conditions. Also, in the future, the applicability of our proposed algorithm for gait event detection must be investigated in closed-loop control of a neural prosthesis during walking.

9.2.3 Lower Limb Position Tracking

An immediate next step for this thesis is to implement accurate and robust algorithms for body segment position tracking with IMUs. In the simplest form, first, the motion-induced acceleration must be obtained by removing the gravitational acceleration from the accelerometer readout.

Second, the motion-induced acceleration must be integrated twice to compute the position. Nevertheless, this simple approach will result in an ever-increasing drift in the estimated position because of the numerical integration drift. To address this challenge, corrective methods such as zero-velocity-update [412], [413] or more complex constrained estimation schemes such as a KF [414], [415] can be used.

9.2.4 Technical Validation with Clinical Population

The ultimate goal of this thesis was to develop a technology for gait rehabilitation of a clinical population. Therefore, a critical next step includes technical validation of the developed techniques in terms of accuracy and reliability for this clinical population. The results, including joint angles and temporal gait events, obtained by the proposed wearable technology must be compared to those obtained simultaneously by a stationary MCS to validate its accuracy and reliability.

9.2.5 Biofeedback Display System

The primary application of the outcome of this research is to develop a technology for real-time lower limb motion monitoring and providing biofeedback for therapeutic gait training. Thus, a graphical user interface should be developed to report the measured joint angles and gait events as visual and/or auditory biofeedback during gait training. Also, a knowledge-based system can be created to convert the error between pathological and targeted normal movement patterns to visual and/or auditory demonstrations or instructions.

9.2.6 Clinical Validation with Clinical Population

After validating the developed technology for the clinical population and developing the biofeedback system, the developed technology should be validated in terms of its efficacy for gait rehabilitation. To this end, our developed wearable sensor technology should be applied during training sessions of ambulatory stroke survivors to assess its efficacy in enhancing the motor function of these patients. Finally, the users' compliance will be investigated, and the technology will be fine-tuned to maximize its user-friendliness.

References

[1] H. Krueger, J. Koot, R. E. Hall, C. O'Callaghan, M. Bayley, and D. Corbett, "Prevalence of individuals experiencing the effects of stroke in Canada: trends and projections," *Stroke.*, vol. 46, no. 8, pp. 2226–2231, 2015.

[2] N. Mayo *et al.*, "Disablement following stroke," *Disabil. Rehabil.*, vol. 21, pp. 258–268, 1999.

[3] A. Pollock, B. St. George, M. Fenton, and L. Firkins, "Top 10 research priorities relating to life after stroke – consensus from stroke survivors, caregivers, and health professionals," *Int. J. Stroke*, vol. 9, pp. 313–320, 2014.

[4] M. A. Dimyan and L. G. Cohen, "Neuroplasticity in the context of motor rehabilitation after stroke," *Nat. Rev. Neurol.*, vol. 7, no. 2, pp. 76–85, 2011.

[5] D. Schliessmann *et al.*, "Feasibility of visual instrumented movement feedback therapy in individuals with motor incomplete spinal cord injury walking on a treadmill," *Front. Hum. Neurosci.*, vol. 8, p. 416, 2014.

[6] A. Kimura *et al.*, "Effects of neurofeedback training with an electroencephalogram-based Brain Computer Interface for hand paralysis in patients with chronic stroke: A preliminary case series study," *J. Rehabil. Med.*, vol. 43, no. 10, pp. 951–957, 2016.

[7] P. B. Shull, W. Jirattigalachote, M. A. Hunt, M. R. Cutkosky, and S. L. Delp, "Quantified self and human movement: A review on the clinical impact of wearable sensing and feedback for gait analysis and intervention," *Gait Posture*, vol. 40, pp. 11–19, 2014.

[8] Peter H. Veltink ; Danilo De Rossi, "Wearable technology for biomechanics: e-textile or micromechanical sensors? [Conversations in BME]," *IEEE Eng. Med. Biol. Mag.*, vol. 29, no. 3, pp. 37–43, 2010.

[9] W. Zijlstra and K. Aminian, "Mobility assessment in older people: New possibilities and challenges," *Eur. J. Ageing*, vol. 4, pp. 3–12, 2007.

[10] K. Aminian, S. Chopra, H. Rouhani, M. Assal, and X. Crevoisier, "Outcome of unilateral ankle arthrodesis and total ankle replacement in terms of bilateral gait mechanics," *J. Orthop. Res.*, vol. 32, no. 3, pp. 377–384, 2013.

[11] H. Rouhani, J. Favre, K. Aminian, and X. Crevoisier, "Multi-segment foot kinematics after total ankle replacement and ankle arthrodesis during relatively long-distance gait," *Gait Posture*, vol. 36, no. 3, pp. 561–566, 2012.

[12] F. B. Horak and M. Mancini, "Objective biomarkers of balance and gait for Parkinson's disease using body-worn sensors," *Mov. Disord.*, vol. 28, no. 11, pp. 1544–1551, 2013.

[13] A. Noamani, M. Nazarahari, J. Lewicke, A. H. Vette, and H. Rouhani, "Validity of using wearable inertial sensors for assessing the dynamics of standing balance," *Med. Eng. Phys.*, vol. 77, pp. 53–59, 2020.

[14] M. Nazarahari, K. M. Chan, and H. Rouhani, "A Novel Instrumented Shoulder Functional Test Using Wearable Sensors in Patients with Brachial Plexus Injury," *J. Shoulder Elb. Surg.*, 2020.

[15] N. Ahmadian, M. Nazarahari, J. L. Whittaker, and H. Rouhani, "Quantification of triple single-leg hop test temporospatial parameters: A validated method using body-worn sensors for functional evaluation after knee injury," *Sensors (Switzerland)*, vol. 20, no. 12, pp. 1–15, 2020.

[16] N. Ahmadian, M. Nazarahari, J. L. Whittaker, and H. Rouhani, "Instrumented triple single-leg hop test: A validated method for ambulatory measurement of ankle and knee angles using inertial sensors," *Clin. Biomech.*, vol. 80, p. 105134, 2020.

[17] A. K. Bourke *et al.*, "Evaluation of waist-mounted tri-axial accelerometer based fall-detection algorithms during scripted and continuous unscripted activities," *J. Biomech.*, vol. 43, no. 15, pp. 3051–3057, 2010.

[18] J. Liu and T. E. Lockhart, "Development and evaluation of a prior-to-impact fall event detection algorithm," *IEEE Trans. Biomed. Eng.*, vol. 61, no. 7, pp. 2135–2140, 2014.

[19] M. Schwenk, G. S. Grewal, D. Holloway, A. Muchna, L. Garland, and B. Najafi, "Interactive sensor-based balance training in older cancer patients with chemotherapy-induced peripheral neuropathy: A randomized controlled trial," *Gerontology*, vol. 62, no. 5, pp. 553–563, 2016.

[20] S. Patel, H. Park, P. Bonato, L. Chan, and M. Rodgers, "A review of wearable sensors and systems with application in rehabilitation," *J. Neuroeng. Rehabil.*, vol. 9, 2012.

[21] M. D. Hill *et al.*, "Impact of disability status on ischemic stroke costs in Canada in the first year," *Can. J. Neurol. Sci.*, vol. 39, no. 06, pp. 793–800, 2014.

[22] M. Nazarahari and H. Rouhani, "40 Years of Sensor Fusion for Orientation Tracking via Magnetic and Inertial Measurement Units: Methods, Lessons Learned, and Future Challenges," *Inf. Fusion*, vol. 68, pp. 67–84, 2021.

[23] M. Nazarahari, A. Noamani, N. Ahmadian, and H. Rouhani, "Sensor-to-body calibration procedure for clinical motion analysis of lower limb using Magnetic and Inertial Measurement Units," *J. Biomech.*, vol. 85, pp. 224–229, 2019.

[24] M. Nazarahari and H. Rouhani, "Semi-automatic Sensor-to-Body Calibration of Inertial Sensors on Lower Limb Using Gait Recording," *IEEE Sens. J.*, vol. 19, no. 24, pp. 12465–12474, 2019.

[25] M. Nazarahari and H. Rouhani, "Adaptive Gain Regulation of Sensor Fusion Algorithms for Orientation Estimation with Magnetic and Inertial Measurement Units," *IEEE Trans. Instrum. Meas.*, vol. 70, 2020.

[26] M. Nazarahari and H. Rouhani, "Sensor Fusion Algorithms for Orientation Tracking via Magnetic and Inertial Measurement Units: An Experimental Comparison Survey," *Inf. Fusion*, 2021.

[27] M. Nazarahari and H. Rouhani, "A Full-State Robust Extended Kalman Filter for Orientation Tracking During Long-duration Dynamic Tasks Using Magnetic and Inertial Measurement Units," *IEEE Trans. Neural Syst. Rehabil. Eng.*, 2021.

[28] M. Nazarahari and H. Rouhani, "Detection of daily postures and walking modalities using a single chest-mounted tri-axial accelerometer," *Med. Eng. Phys.*, vol. 57, pp. 75–81, 2018.

[29] B. L. B. Riemann and S. M. S. Lephart, "The sensorimotor system, part II: the role of proprioception in motor control and functional joint stability," *J. Athl. Train.*, vol. 37, no. 1, pp. 71–79, 2002.

[30] J. N. Sanes, K.-H. Mauritz, E. V Evarts, M. C. Dalakast, and A. Chut, "Motor deficits in patients with large-fiber sensory neuropathy," *Proc. Natl. Acad. Sci.*, vol. 81, pp. 979–982, 1984.

[31] V. Dietz, "Proprioception and locomotor disorders," *Nat. Rev. Neurosci.*, vol. 3, no. 10, pp. 781–790, 2002.

[32] R. Labruyère, C. N. Gerber, K. Birrer-Brütsch, A. Meyer-Heim, and H. J. A. van Hedel, "Requirements for and impact of a serious game for neuro-pediatric robot-assisted gait training," *Res. Dev. Disabil.*, vol. 34, no. 11, pp. 3906–3915, 2013.

[33] D. Schliessmann *et al.*, "Trainer in a pocket - Proof-of-concept of mobile, real-time, foot kinematics feedback for gait pattern normalization in individuals after stroke, incomplete spinal cord injury and elderly patients," *J. Neuroeng. Rehabil.*, vol. 15, no. 1, pp. 1–15, 2018.

[34] A. V. Dowling, D. S. Fisher, and T. P. Andriacchi, "Gait modification via verbal instruction and an active feedback system to reduce peak knee adduction moment," *J. Biomech. Eng.*, vol. 132, no. 7, 2010.

[35] J. A. Barrios, K. M. Crossley, and I. S. Davis, "Gait retraining to reduce the knee adduction moment through real-time visual feedback of dynamic knee alignment," *J. Biomech.*, vol. 43, no. 11, pp. 2208–2213, 2010.

[36] J. W. Wheeler, P. B. Shull, and T. F. Besier, "Real-time knee adduction moment feedback for gait retraining through visual and tactile displays," *J. Biomech. Eng.*, vol. 133, no. 4, 2011.

[37] P. B. Shull, W. Jirattigalachote, M. A. Hunt, M. R. Cutkosky, and S. L. Delp, "Quantified self and human movement: A review on the clinical impact of wearable sensing and feedback for gait analysis and intervention," *Gait Posture*, vol. 40, no. 1, pp. 11–19, 2014.

[38] A. Godfrey, R. Conway, D. Meagher, and G. ÓLaighin, "Direct measurement of human movement by accelerometry," *Med. Eng. Phys.*, vol. 30, no. 10, pp. 1364–1386, 2008.

[39] K. Aminian and B. Najafi, "Capturing human motion using body-fixed sensors: Outdoor measurement and clinical applications," *Comput. Animat. Virtual Worlds*, vol. 15, no. 2, pp. 79–94, 2004.

[40] J. Nilsson and I. Skog, “Inertial Sensor Arrays – A Literature Review,” *2016 Eur. Navig. Conf.*, pp. 1–10, 2016.

[41] N. Ahmad, R. Ariffin, R. Ghazilla, and N. M. Khairi, “Reviews on Various Inertial Measurement Unit (IMU) Sensor Applications,” *Int. J. Signal Process. Syst.*, vol. 1, no. 2, pp. 256–262, 2013.

[42] M. Cornacchia, K. Ozcan, Y. Zheng, and S. Velipasalar, “Survey on Activity Detection and Classification Using Wearable Sensors,” *IEEE Sens. J.*, vol. 17, no. 2, pp. 386–403, 2017.

[43] R. Harle, “A survey of indoor inertial positioning systems for pedestrians,” *IEEE Commun. Surv. Tutorials*, vol. 15, pp. 1281–1293, 2013.

[44] R. Bhardwaj, N. Kumar, and V. Kumar, “Errors in micro-electro-mechanical systems inertial measurement and a review on present practices of error modelling,” *Trans. Inst. Meas. Control*, vol. 40, no. 9, pp. 2843–2854, 2018.

[45] N. Trawny and S. I. Roumeliotis, “Indirect Kalman Filter for 3D Attitude Estimation,” 2005.

[46] N. H. Q. Phuong, H.-J. Kang, Y.-S. Suh, and Y.-S. Ro, “A DCM Based Orientation Estimation Algorithm with an Inertial Measurement Unit and a Magnetic Compass,” *J. Univers. Comput. Sci.*, vol. 15, no. 4, pp. 859–876, 2009.

[47] H. Qi and J. B. Moore, “Direct Kalman filtering approach for GPS/INS integration,” *IEEE Trans. Aerosp. Electron. Syst.*, vol. 38, pp. 687–693, 2002.

[48] G. Schall *et al.*, “Global pose estimation using multi-sensor fusion for outdoor augmented reality,” in *2009 8th IEEE International Symposium on Mixed and Augmented Reality*, 2009, pp. 153–162.

[49] A. Filippeschi, N. Schmitz, M. Miezal, G. Bleser, E. Ruffaldi, and D. Stricker, “Survey of Motion Tracking Methods Based on Inertial Sensors: A Focus on Upper Limb Human Motion,” *Sensors*, vol. 17, no. 6, Jun. 2017.

[50] D. Choukroun, H. Weiss, I. Y. Bar-Itzhack, and Y. Oshman, “Direction Cosine Matrix Estimation from Vector Observations using a Matrix Kalman Filter,” *IEEE Trans. Aerosp. Electron. Syst.*, vol. 46, no. 1, pp. 61–79, 2010.

[51] M. D. Shuster, “Constraint in Attitude Estimation Part I: Constrained Estimation,” *J. Astronaut. Sci.*, vol. 51, no. 1, pp. 51–74, 2003.

[52] I. Y. Bar-Itzhack, J. Deutschmann, and F. L. Markley, “Quaternion normalization in additive EKF for spacecraft attitude determination,” in *Navigation and Control Conference*, 1991.

[53] J. Hu and K. Sun, “A Robust Orientation Estimation Algorithm Using MARG Sensors,” *IEEE Trans. Instrum. Meas.*, vol. 64, no. 3, pp. 815–822, 2015.

[54] H. Hyyti and A. Visala, “A DCM Based Attitude Estimation Algorithm for Low-Cost MEMS IMUs,” *Int. J. Navig. Obs. Hindawi*, 2015.

[55] S. Patel, H. Park, P. Bonato, L. Chan, and M. Rodgers, “A review of wearable sensors and systems with application in rehabilitation,” *J. Neuroeng. Rehabil.*, vol. 9, no. 21, pp. 1–17, 2012.

[56] R. Gravina, P. \Alinia, H. Ghasemzadeh, and G. Fortino, “Multi-sensor fusion in body sensor networks: State-of-the-art and research challenges,” *Inf. Fusion*, vol. 35, pp. 68–80, 2017.

[57] M. Iosa, P. Picerno, S. Paolucci, and G. Morone, “Wearable inertial sensors for human movement analysis,” *Expert Rev. Med. Devices*, vol. 13, no. 7, pp. 641–659, 2016.

[58] G. Vannozzi, E. Bergamini, S. Fantozzi, and G. Vannozzi, “Trends Supporting the In-Field Use of Wearable Inertial Sensors for Sport Performance Evaluation: A Systematic Review,” *Sensors*, vol. 18, 2018.

[59] X. Guo, N. Ansari, F. Hu, Y. Shao, N. R. Elikplim, and L. Li, “A Survey on Fusion-based Indoor Positioning,” *IEEE Commun. Surv. Tutorials*, vol. 22, no. 1, pp. 566–594, 2020.

[60] A. M. Hasan, K. Samsudin, A. R. Ramli, and R. S. Azmir, “A Review of Navigation Systems (Integration and Algorithms),” *Aust. J. Basic Appl. Sci.*, pp. 943–959, 2009.

[61] Z. Yang, C. Wu, Z. Zhou, X. Zhang, X. Wang, and Y. Liu, “Mobility increases localizability: A survey on wireless indoor localization using inertial sensors,” *ACM Comput. Surv.*, vol. 47, pp. 1–34, 2015.

[62] J. L. Crassidis, F. L. Markley, and Y. Cheng, “A Survey of Nonlinear Attitude Estimation Methods,” *J. Guid. Control. Dyn.*, vol. 30, no. 1, 2007.

[63] A. Cavallo *et al.*, *Experimental comparison of sensor fusion algorithms for attitude estimation*, vol. 19, no. 3.

IFAC, 2014.

[64] S. O. H. Madgwick, A. J. L. Harrison, and R. Vaidyanathan, "Estimation of IMU and MARG orientation using a gradient descent algorithm," in *2011 IEEE International Conference on Rehabilitation Robotics*, 2011, pp. 1–7.

[65] R. Mahony, T. Hamel, and J.-M. Pflimlin, "Non-linear Complementary Filters on the Special Orthogonal Group," *IEEE Trans. Automat. Contr.*, vol. 53, no. 5, pp. 1203–1218, 2008.

[66] M. Gietzelt, K. H. Wolf, M. Marschollek, and R. Haux, "Performance comparison of accelerometer calibration algorithms based on 3D-ellipsoid fitting methods," *Comput. Methods Programs Biomed.*, vol. 111, no. 1, pp. 62–71, 2013.

[67] R. Zhu and Z. Zhou, "A real-time articulated human motion tracking using tri-axis inertial/magnetic sensors package," *IEEE Trans. Neural Syst. Rehabil.*, vol. 12, no. 2, pp. 295–302, 2004.

[68] X. Yun and E. R. Bachmann, "Design, implementation and experimental results of a quaternion-based Kalman filter for human body motion tracking," *IEEE Trans. Robot.*, vol. 22, no. 6, pp. 1216–1227, 2006.

[69] A. D. Young, "Use of body model constraints to improve accuracy of inertial motion capture," *2010 Int. Conf. Body Sens. Networks, BSN 2010*, pp. 180–186, 2010.

[70] G. Bleser, G. Hendeby, and M. Miezal, "Using egocentric vision to achieve robust inertial body tracking under magnetic disturbances," in *Proceedings of the 2011 10th IEEE International Symposium on Mixed and Augmented Reality (ISMAR)*, 2011, pp. 103–109.

[71] L. Peppoloni, A. Filippeschi, E. Ruffaldi, and C. A. Avizzano, "A novel 7 degrees of freedom model for upper limb kinematic reconstruction based on wearable sensors," in *Proceedings of the 2013 IEEE 11th International Symposium on Intelligent Systems and Informatics (SISY)*, 2013, pp. 105–110.

[72] R. Bischoff, U. Huggenberger, and E. Prassler, "KUKA youBot - A mobile manipulator for research and education," *Proc. - IEEE Int. Conf. Robot. Autom.*, pp. 1–4, 2011.

[73] A. D. Young, "Comparison of orientation filter algorithms for realtime wireless inertial posture tracking," *Proc. - 2009 6th Int. Work. Wearable Implant. Body Sens. Networks, BSN 2009*, pp. 59–64, 2009.

[74] X. Yun, E. Bachmann, and R. McGhee, "A simplified quaternion based algorithm for orientation estimation from Earth gravity and magnetic field measurements," *IEEE Trans. Instrum. Meas.*, vol. 57, no. 3, pp. 638–650, 2008.

[75] G. Lerner, "Spacecraft Attitude Determination and Control," in *Spacecraft Attitude Determination and Control*, Kluwer Academic, 1978, pp. 420–428.

[76] M. D. Shuster and S. D. Oh, "Three-axis attitude determination from vector observations," *J. Guid. Control. Dyn.*, vol. 4, pp. 70–77, 1981.

[77] A. M. Sabatini, "Estimating three-dimensional orientation of human body parts by inertial/magnetic sensing," *Sensors*, vol. 11, no. 2, pp. 1489–1525, 2011.

[78] B. Fan, Q. Li, and T. Liu, "How magnetic disturbance influences the attitude and heading in magnetic and inertial sensor-based orientation estimation," *Sensors (Switzerland)*, vol. 18, 2018.

[79] G. Ligorio and A. M. Sabatini, "Dealing with magnetic disturbances in human motion capture: A survey of techniques," *Micromachines*, vol. 7, no. 3, 2016.

[80] K. Feng *et al.*, "A new quaternion-based kalman filter for real-time attitude estimation using the two-step geometrically-intuitive correction algorithm," *Sensors*, vol. 17, no. 9, 2017.

[81] S. Madgwick, "AHRS Algorithms and Calibration Solutions to Facilitate New Applications Using Low-Cost MEMS," University of Bristol, 2014.

[82] E. Bergamini, G. Ligorio, A. Summa, G. Vannozzi, A. Cappozzo, and A. M. Sabatini, "Estimating Orientation Using Magnetic and Inertial Sensors and Different Sensor Fusion Approaches: Accuracy Assessment in Manual and Locomotion Tasks," *Sensors*, pp. 18625–18649, 2014.

[83] F. Alam, Z. Zhaihe, and H. Jiajia, "A Comparative Analysis of Orientation Estimation Filters using MEMS based IMU," in *2nd International Conference on Research in Science, Engineering and Technology (ICRSET'2014)*, 2014.

[84] T. Hamel and R. Mahony, "Attitude estimation on SO(3) based on direct inertial measurements," in *Proceedings of 2006 IEEE International Conference on Robotics and Automation, ICRA 2006*, 2006.

[85] G. Ligorio and A. M. Sabatini, “A Linear Kalman Filtering-based Approach for 3D Orientation Estimation from Magnetic/Inertial Sensors,” in *Proceedings of 2015 IEEE International Conference on Multisensor Fusion and Integration for Intelligent Systems (MFI)*, 2015, pp. 77–82.

[86] J. K. Lee and E. J. Park, “Minimum-Order Kalman Filter With Vector Selector for Accurate Estimation of Human Body Orientation,” *IEEE Trans. Robot.*, vol. 25, no. 5, pp. 1196–1201, 2009.

[87] M. Caruso, A. M. Sabatini, M. Knaflitz, M. Gazzoni, U. Della Croce, and A. Cereatti, “Accuracy of the Orientation Estimate Obtained Using Four Sensor Fusion Filters Applied to Recordings of Magneto-Inertial Sensors Moving at Three Rotation Rates,” in *2019 41st Annual International Conference of the IEEE Engineering in Medicine and Biology Society (EMBC)*, 2019.

[88] “Open Source Sensor Fusion.” [Online]. Available: https://github.com/memsindustrygroup/Open-Source-Sensor-Fusion/tree/master/docs.

[89] S. A. Ludwig and K. D. Burnham, “Comparison of Euler Estimate using Extended Kalman Filter, Madgwick and Mahony on Quadcopter Flight Data,” in *2018 International Conference on Unmanned Aircraft Systems (ICUAS)*, 2018, pp. 1236–1241.

[90] J. L. Marins, X. Yun, E. R. Bachmann, R. B. Mcghee, and M. J. Zyda, “An Extended Kalman Filter for Quaternion-Based Orientation Estimation Using,” in *Proceeding of the 2001 IEEE/RSJ International Conference on Intelligent Robots and Systems*, 2001, pp. 2003–2011.

[91] G. H. Lee, M. Achtelik, F. Fraundorfer, M. Pollefeys, and R. Siegwart, “A benchmarking tool for MAV visual pose estimation,” in *2010 11th International Conference on Control Automation Robotics & Vision*, 2010.

[92] T. Michel, H. Fourati, P. Genev, and N. Laya, “A Comparative Analysis of Attitude Estimation for Pedestrian Navigation with Smartphones,” in *nternational Conference on Indoor Positioning and Indoor Navigation*, 2015.

[93] V. Renaudin and C. Combettes, “Magnetic, Acceleration Fields and Gyroscope Quaternion (MAGYQ)-Based Attitude Estimation with Smartphone Sensors for Indoor Pedestrian Navigation,” *Sensors*, vol. 14, no. 12, pp. 22864–22890, 2014.

[94] D. Choukroun, I. Y. Bar-Itzhack, and Y. Oshman, “Novel quaternion Kalman filter,” *EEE Trans. Aerosp. Electron. Syst.*, vol. 14, no. 11, pp. 20008–20024, 2004.

[95] H. Fourati, “Heterogeneous Data Fusion Algorithm for Pedestrian Navigation via Foot-Mounted Inertial Measurement Unit and Complementary Filter,” *IEEE Trans. Instrum. Meas.*, vol. 64, no. 1, pp. 221–229, 2015.

[96] P. Martin and E. Salaun, “Design and implementation of a low-cost observer-based attitude and heading reference system,” *Control Eng. Pract.*, vol. 18, no. 7, pp. 712–722, 2010.

[97] X. Li and Y. Wang, “Evaluation of AHRS algorithms for Foot-Mounted Inertial-based Indoor Navigation Systems,” *GeoScape*, vol. 11, pp. 48–63, 2019.

[98] M. Angermann, P. Robertson, T. Kemptner, and M. Khider, “A high precision reference data set for pedestrian navigation using foot-mounted inertial sensors,” in *International Conference on Indoor Positioning and Indoor Navigation*, 2010, pp. 1–6.

[99] J. Tosi, F. Taffoni, A. Hussain, D. Campolo, and D. Formica, “Methodology for the Evaluation of Magneto-Inertial Orientation Filters in SO(3),” in *2019 II Workshop on Metrology for Industry 4.0 and IoT (MetroInd4.0&IoT)*, 2019, pp. 323–328.

[100] D. Campolo, L. Schenato, L. Pi, X. Deng, and E. Guglielmelli, “Attitude estimation of a biologically inspired robotic housefly via multimodal sensor fusion,” *Adv. Robot.*, vol. 23, pp. 955–977, 2009.

[101] Y. Tian, H. X. Wei, and J. D. Tan, “An adaptive-gain Complementary Filter for real-time human motion tracking with MARG sensors in free-living environments,” *IEEE Trans. Neural Syst. Rehabil. Eng.*, vol. 21, no. 2, pp. 254–264, 2013.

[102] H. Chen, M. C. Schall, and N. B. Fethke, “Measuring upper arm elevation using an inertial measurement unit: An exploration of sensor fusion algorithms and gyroscope models,” *Appl. Ergon.*, vol. 89, p. 103187, 2020.

[103] H. Chen, M. C. Schall, and N. Fethke, “Accuracy of angular displacements and velocities from inertial-based inclinometers,” *Appl. Ergon.*, vol. 67, pp. 151–161, 2018.

[104] G. Ligorio and A. M. Sabatini, “A novel kalman filter for human motion tracking with an inertial-based dynamic inclinometer,” *IEEE Trans. Biomed. Eng.*, vol. 62, no. 8, pp. 2033–2043, 2015.

[105] M. Carratu, S. Dello Iacono, M. Long Hoang, and A. Pietrosanto, "Energy characterization of attitude algorithms," in *IEEE International Conference on Industrial Informatics (INDIN)*, 2019, pp. 1585–1590.

[106] Angelo M. Sabatini, "Quaternion-based extended Kalman filter for determining orientation by inertial and magnetic sensing," *IEEE Trans. Biomed. Eng.*, vol. 53, no. 7, pp. 1346–1356, 2006.

[107] D. Roetenberg, H. J. Luinge, C. T. M. Baten, and P. H. Veltink, "Compensation of magnetic disturbances improves inertial and magnetic sensing of human body segment orientation," *IEEE Trans. Neural Syst. Rehabil. Eng.*, vol. 13, no. 3, pp. 395–405, 2005.

[108] F. Ferraris, U. Grimaldi, and M. Parvis, "Procedure for effortless in-field calibration of three-axis rate gyros and accelerometers," *Sensors Mater.*, vol. 7, pp. 311–330, 1995.

[109] H. J. Luinge and P. H. Veltink, "Inclination Measurement of Human Movement Using a 3-D Accelerometer with Autocalibration," *IEEE Trans. Neural Syst. Rehabil. Eng.*, vol. 12, no. 1, pp. 112–121, 2004.

[110] Y. S. Suh, "Orientation Estimation Using a Quaternion-Based Indirect Kalman Filter With Adaptive Estimation of External Acceleration," *IEEE Trans. Instrum. Meas.*, vol. 59, no. 12, pp. 3296–3305, 2010.

[111] J. C. K. Chou, "Quaternion Kinematic and Dynamic Differential Equations," *IEEE Trans. Robot. Autom.*, vol. 8, no. 1, pp. 53–64, 1992.

[112] J. K. Lee and M. J. Choi, "Effect of strapdown integration order and sampling rate on IMU-Based attitude estimation accuracy," *Sensors (Switzerland)*, vol. 18, no. 9, 2018.

[113] Y. Hao, Z. Xiong, W. Gao, and L. Li, "Study of strapdown inertial navigation integration algorithms," in *Proceedings of the 2004 International Conference on Intelligent Mechatronics and Automation*, 2004, pp. 751–754.

[114] H. J. Luinge and P. H. Veltink, "Measuring orientation of human body segments using miniature gyroscopes and accelerometers," *Med. Biol. Eng. Comput.*, vol. 43, no. 2, pp. 273–282, 2005.

[115] I. Pasciuto, G. Ligorio, E. Bergamini, G. Vannozzi, A. M. Sabatini, and A. Cappozzo, "How angular velocity features and different gyroscope noise types interact and determine orientation estimation accuracy," *Sensors (Switzerland)*, vol. 15, no. 9, pp. 23983–24001, 2015.

[116] G. Wahba, "A Least Squares Estimate of Spacecraft Attitude," *SIAM Rev.*, vol. 7, no. 3, p. 409, 1965.

[117] F. L. Markley and D. Mortari, "How to estimate attitude from vector observations," 1999.

[118] I. Y. Bar-Itzhack and R. R. Harman, "Optimized TRIAD Algorithm for Attitude Determination," *J. Guid. Control. Dyn.*, vol. 20, no. 1, pp. 208–211, 1997.

[119] M. D. Shuster and S. D. Oh, "Three-axis attitude determination from vector observations," *J. Guid. Control. Dyn.*, vol. 4, no. 1, pp. 70–77, 1981.

[120] P. B. Davenport, "A vector approach to the algebra of rotations with applications," *NASA, Tech. Rep.*, 1968.

[121] F. L. Markley, "Attitude determination from vector observations: A fast optimal matrix algorithm," *J. Astronaut. Sci.*, vol. 41, no. 2, pp. 261–280, 1993.

[122] F. L. Markley, "Attitude determination using vector observations and the singular value decomposition," *J. Astronaut. Sci.*, vol. 36, pp. 245–258, 1988.

[123] M. D. Shuster, "Filter QUEST or REQUEST," *J. Guid. Control. Dyn.*, vol. 32, no. 2, pp. 643–645, 2009.

[124] I. Y. Bar-Itzhack, "REQUEST—A recursive QUEST algorithm for sequential attitude determination," *J. Guid. Control. Dyn.*, vol. 19, no. 5, pp. 1034–1038, 1996.

[125] J. Wu, Z. Zhou, B. Gao, R. Li, Y. Cheng, and H. Fourati, "Fast Linear Quaternion Attitude Estimator Using Vector Observations," *IEEE Trans. Autom. Sci. Eng.*, vol. 15, no. 1, pp. 307–319, 2018.

[126] J. Wu, Z. Zhou, H. Fourati, and M. Liu, "Recursive linear continuous quaternion attitude estimator from vector observations," *IET Radar, Sonar Navig.*, vol. 12, no. 11, pp. 1196–1207, 2018.

[127] D. Gebre-Egziabher, G. H. Elkaim, J. Powell, and B. W. Parkinson, "A gyro-free quaternion-based attitude determination system suitable for implementation using low cost sensors," in *2000 IEEE Position Location and Navigation Symposium*, 2000, pp. 185–192.

[128] R. G. Valenti, I. Dryanovski, and J. Xiao, "Keeping a good attitude: A quaternion-based orientation filter for IMUs and MARGs," *Sensors*, vol. 15, no. 8, pp. 19302–19330, 2015.

[129] R. G. Valenti, I. Dryanovski, and J. Xiao, "A linear Kalman filter for MARG orientation estimation using the algebraic quaternion algorithm," *IEEE Trans. Instrum. Meas.*, vol. 65, no. 2, pp. 467–481, 2016.

[130] J. Calusdian, X. Yun, and E. Bachmann, "Adaptive-gain complementary filter of inertial and magnetic data for orientation estimation," *Proc. - IEEE Int. Conf. Robot. Autom.*, pp. 1916–1922, 2011.

[131] E. R. Bachmann, I. Duman, U. Y. Usta, R. B. McGhee, X. P. Yun, and M. J. Zyda, "Orientation tracking for humans and robots using inertial sensors," in *Proceedings 1999 IEEE International Symposium on Computational Intelligence in Robotics and Automation. CIRA'99 (Cat. No.99EX375)*, 1999, pp. 187–194.

[132] J. K. Lee and E. J. Park, "A fast quaternion-based orientation optimizer via virtual rotation for human motion tracking," *IEEE Trans. Biomed. Eng.*, vol. 56, no. 5, pp. 1574–1582, 2009.

[133] H. Fourati, N. Manamanni, L. Afilal, and Y. Handrich, "A Nonlinear Filtering Approach for the Attitude and Dynamic Body Acceleration Estimation Based on Inertial and Magnetic Sensors: Bio-Logging Application," *IEEE Sens. J.*, vol. 11, no. 1, pp. 233–244, 2011.

[134] H. Fourati, N. Manamanni, L. Afilal, and Y. Handrich, "Complementary observer for body segments motion capturing by inertial and magnetic sensors," *IEEE/ASME Trans. Mechatronics*, vol. 19, no. 1, pp. 149–157, 2014.

[135] M. B. Del Rosario, N. H. Lovell, and S. J. Redmond, "Quaternion-Based Complementary Filter for Attitude Determination of a Smartphone," *IEEE Sens. J.*, vol. 16, no. 15, pp. 6008–6017, 2016.

[136] B. Fan, Q. Li, C. Wang, and T. Liu, "An adaptive orientation estimation method for magnetic and inertial sensors in the presence of magnetic disturbances," *Sensors (Switzerland)*, vol. 17, no. 5, 2017.

[137] J. Wu, Z. Zhou, H. Fourati, R. Li, and M. Liu, "Generalized Linear Quaternion Complementary Filter for Attitude Estimation From Multisensor Observations: An Optimization Approach," *IEEE Trans. Autom. Sci. Eng.*, vol. 16, no. 3, pp. 1330–1343, 2019.

[138] S. Ghasemi-Moghadam and M. R. Homaeinezhad, "Attitude determination by combining arrays of MEMS accelerometers, gyros, and magnetometers via quaternion-based complementary filter," *Int. J. Numer. Model. Electron. Networks, Devices Fields*, vol. 31, no. 3, pp. 1–24, 2018.

[139] C. Yi *et al.*, "Estimating three-dimensional body orientation based on an improved complementary filter for human motion tracking," *Sensors*, vol. 18, no. 11, pp. 1–19, 2018.

[140] Y. Guan and X. Song, "Sensor Fusion of Gyroscope and Accelerometer for Low-Cost Attitude Determination System," in *Proceedings 2018 Chinese Automation Congress, CAC 2018*, 2018, pp. 1068–1072.

[141] R. Zhu and Z. Zhou, "A small low-cost hybrid orientation system and its error analysis," *IEEE Sens. J.*, vol. 9, no. 3, pp. 223–230, 2009.

[142] P. Daponte, L. De Vito, S. Rapuano, M. Riccio, and F. Picariello, "Compensating magnetic disturbances on MARG units by means of a low complexity data fusion algorithm," in *Proceedings of 2015 IEEE International Symposium on Medical Measurements and Applications, MeMeA 2015*, 2015, pp. 157–162.

[143] J. Cockcroft, J. H. Muller, and C. Scheffer, "A complementary filter for tracking bicycle crank angles using inertial sensors, kinematic constraints, and vertical acceleration updates," *IEEE Sens. J.*, vol. 15, no. 8, pp. 4218–4225, 2015.

[144] M. Kok and T. B. Schön, "A Fast and Robust Algorithm for Orientation Estimation Using Inertial Sensors," *IEEE Signal Process. Lett.*, vol. 26, no. 11, pp. 1673–1677, 2019.

[145] Y. C. Lai, S. S. Jan, and F. Bin Hsiao, "Development of a low-cost attitude and heading reference system using a three-axis rotating platform," *Sensors*, vol. 10, no. 4, pp. 2472–2491, 2010.

[146] R. Chang, X. Mu, and X. Shen, "Attitude estimation with complementary filter," *Appl. Mech. Mater.*, vol. 44–47, pp. 3781–3784, 2011.

[147] T. S. Yoo, S. K. Hong, H. M. Yoon, and S. Park, "Gain-scheduled complementary filter design for a MEMS based attitude and heading reference system," *Sensors*, vol. 11, no. 4, pp. 3816–3830, 2011.

[148] M. Euston, P. Coote, R. Mahony, J. Kim, and T. Hamel, "A complementary filter for attitude estimation of a fixed-wing UAV," in *Proceeding of 2008 IEEE International Conference on Intelligent Robots and Systems*, 2008, pp. 340–345.

[149] X. Wen *et al.*, "A first-order differential data processing method for accuracy improvement of complementary filtering in micro-UAV attitude estimation," *Sensors (Switzerland)*, vol. 19, no. 6, 2019.

[150] A. Khosravian and M. Namvar, "Rigid body attitude control using a single vector measurement and gyro," *IEEE Trans. Automat. Contr.*, vol. 57, no. 5, pp. 1273–1279, 2012.

[151] Y. Wang, E. Chang-Siu, M. Brown, M. Tomizuka, M. I. Almajed, and B. N. Alsuwaidan, "Three dimensional attitude estimation via the triad algorithm and a time-varying complementary filter," in *5th Annual Dynamic Systems and Control Conference Joint with the JSME 2012 11th Motion and Vibration Conference*, 2012, pp. 157–165.

[152] R. B. Widodo, H. Edayoshi, and C. Wada, "Complementary filter for orientation estimation: Adaptive gain based on dynamic acceleration and its change," in *2014 Joint 7th International Conference on Soft Computing and Intelligent Systems, SCIS 2014 and 15th International Symposium on Advanced Intelligent Systems, ISIS 2014*, 2014, pp. 906–909.

[153] H. F. Grip, T. I. Fossen, T. A. Johansen, and A. Saberi, "Attitude estimation based on time-varying reference vectors with biased gyro and vector measurements," *IEEE Trans. Automat. Contr.*, vol. 44, no. 1 PART 1, pp. 8497–8502, 2011.

[154] K. J. Jensen, "Generalized nonlinear complementary attitude filter," *J. Guid. Control. Dyn.*, vol. 34, no. 5, pp. 1588–1592, 2011.

[155] O. De Silva, G. K. I. Mann, and R. G. Gosine, "The Right Invariant Nonlinear Complementary Filter for Low Cost Attitude and Heading Estimation of Platforms," *J. Dyn. Syst. Meas. Control. Trans. ASME*, vol. 140, no. 1, 2018.

[156] M. D. Hua, G. Ducard, T. Hamel, R. Mahony, and K. Rudin, "Implementation of a nonlinear attitude estimator for aerial robotic vehicles," *IEEE Trans. Control Syst. Technol.*, vol. 22, no. 1, pp. 201–213, 2014.

[157] B. Fan, Q. Li, and T. Liu, "Improving the accuracy of wearable sensor orientation using a two-step complementary filter with state machine-based adaptive strategy," *Meas. Sci. Technol.*, vol. 29, no. 11, 2018.

[158] J. Wu, Z. Zhou, J. Chen, H. Fourati, and R. Li, "Fast Complementary Filter for Attitude Estimation Using Low-Cost MARG Sensors," *IEEE Sens. J.*, vol. 16, no. 18, pp. 6997–7007, 2016.

[159] P. Marantos, Y. Koveos, and K. J. Kyriakopoulos, "UAV State Estimation Using Adaptive Complementary Filters," *IEEE Trans. Control Syst. Technol.*, vol. 24, no. 4, pp. 1214–1226, 2016.

[160] Q. Q. Yang, L. L. Sun, and L. Yang, "A Fast Adaptive-Gain Complementary Filter Algorithm for Attitude Estimation of an Unmanned Aerial Vehicle," *J. Navig.*, vol. 71, no. 6, pp. 1478–1491, 2018.

[161] J. Chang, J. Cieslak, A. Zolghadri, J. Dávila, and J. Zhou, "Design of sliding mode observers for quadrotor pitch/roll angle estimation via IMU measurements," in *2015 Workshop on Research, Education and Development of Unmanned Aerial Systems, RED-UAS 2015*, 2016, pp. 393–400.

[162] J. Chang, J. Cieslak, J. Dávila, J. Zhou, A. Zolghadri, and Z. Guo, "A Two-Step Approach for an Enhanced Quadrotor Attitude Estimation via IMU Data," *IEEE Trans. Control Syst. Technol.*, vol. 26, no. 3, pp. 1140–1148, 2018.

[163] A. El Hadri and A. Benallegue, "Sliding mode observer to estimate both the attitude and the gyro-bias by using low-cost sensors," in *The 2009 IEEE/RSJ International Conference on Intelligent Robots and Systems*, 2009.

[164] J. F. Vasconcelos, B. Cardeira, C. Silvestre, P. Oliveira, and P. Batista, "Discrete-Time Complementary Filters for Attitude and Position Estimation: Design, Analysis and Experimental Validation," *IEEE Trans. Control Syst. Technol.*, vol. 19, no. 1, pp. 181–198, 2011, doi: 10.1016/j.ifacol.2019.11.274.

[165] A. Tayebi, S. McGilvray, A. Roberts, and M. Moallem, "Attitude estimation and stabilization of a rigid body using low-cost sensors," in *Proceedings of the IEEE Conference on Decision and Control*, 2007, pp. 6424–6429.

[166] H. Sheng and T. Zhang, "MEMS-based low-cost strap-down AHRS research," *Meas. J. Int. Meas. Confed.*, vol. 59, pp. 63–72, 2015.

[167] Z. Wu, Z. Sun, W. Zhang, and Q. Chen, "A Novel Approach for Attitude Estimation Based on MEMS Inertial Sensors Using Nonlinear Complementary Filters," *IEEE Sens. J.*, vol. 16, no. 10, pp. 3856–3864, 2016.

[168] A. A. Neto, D. G. Macharet, V. C. da Silva Campos, and M. F. M. Campos, "Adaptive complementary filtering algorithm for mobile robot localization," *J. Brazilian Comput. Soc.*, vol. 15, no. 3, pp. 19–31, 2009.

[169] R. Kottath, P. Narkhede, V. Kumar, V. Karar, and S. Poddar, "Multiple Model Adaptive Complementary Filter for Attitude Estimation," *Aerosp. Sci. Technol.*, vol. 69, pp. 574–581, 2017.

[170] S. Poddar, P. Narkhede, V. Kumar, and A. Kumar, "PSO Aided Adaptive Complementary Filter for Attitude Estimation," *J. Intell. Robot. Syst. Theory Appl.*, vol. 87, no. 3–4, pp. 531–543, 2017.

[171] J. Thienel and R. M. Sanner, "A Coupled Nonlinear Spacecraft Attitude Controller and Observer With an Unknown Constant Gyro Bias and Gyro Noise," *IEEE Trans. Automat. Contr.*, vol. 48, no. 11, pp. 2011–2015, 2003.

[172] K. Masuya, T. Sugihara, and M. Yamamoto, "Design of complementary filter for high-fidelity attitude estimation based on sensor dynamics compensation with decoupled properties," *Proc. IEEE Int. Conf. Robot. Autom.*, pp. 606–611, 2012.

[173] L. Benziane, A. Benallegue, and A. E. Hadri, "A globally asymptotic attitude estimation using complementary filtering," in *2012 IEEE International Conference on Robotics and Biomimetics, ROBIO 2012*, 2012, no. 3, pp. 878–883.

[174] M. Cheguini and F. Ruiz, "Real-time attitude estimation based on Gradient Descent algorithm," in *2012 IEEE 4th Colombian Workshop on Circuits and Systems (CWCAS)*, 2012.

[175] M. S. Karunarathne, S. W. Ekanayake, and P. N. Pathirana, "An adaptive complementary filter for inertial sensor based data fusion to track upper body motion," *7th Int. Conf. Inf. Autom. Sustain. ICIAfS 2014*, 2014.

[176] V. Kubelka and M. Reinstein, "Complementary filtering approach to orientation estimation using inertial sensors only," in *Proceedings of IEEE International Conference on Robotics and Automation*, 2012, pp. 599–605.

[177] M. Blachuta, R. Grygiel, R. Czyba, and G. Szafranski, "Attitude and heading reference system based on 3D complementary filter," in *19th International Conference on Methods and Models in Automation and Robotics, MMAR 2014*, 2014, pp. 851–856.

[178] R. S. McGinnis, S. M. Cain, S. P. Davidson, R. V. Vitali, S. G. McLean, and N. C. Perkins, "Validation of Complementary Filter Based IMU Data Fusion for Tracking Torso Angle and Rifle Orientation," in *International Mechanical Engineering Congress and Exposition 2014*, 2014.

[179] X. Li, C. He, Y. Wang, and Z. Li, "Generalized complementary filter for attitude estimation based on vector observations and cross products," in *2015 IEEE International Conference on Information and Automation*, 2015, pp. 1733–1737.

[180] S. Q. Liu and R. Zhu, "A Complementary Filter Based on Multi-Sample Rotation Vector for Attitude Estimation," *IEEE Sens. J.*, vol. 18, no. 16, pp. 6686–6692, 2018.

[181] S. Wilson *et al.*, "Formulation of a new gradient descent MARG orientation algorithm: Case study on robot teleoperation," *Mech. Syst. Signal Process.*, vol. 130, pp. 183–200, 2019.

[182] L. Wöhle and M. Gebhard, "SteadEye-Head—Improving MARG-Sensor Based Head Orientation Measurements Through Eye Tracking Data," *Sensors*, 2020.

[183] M. L. Hoang, A. Pietrosanto, S. Dello Iacono, and V. Paciello, "Pre-processing technique for compass-less madgwick in heading estimation for industry 4.0," in *IEEE International Instrumentation and Measurement Technology Conference (I2MTC)*, 2020.

[184] J. A. Barraza Madrigal, J. Cantillo Negrete, R. Muñoz Guerrero, L. A. Contreras Rodríguez, and H. Sossa, "3D Motion Tracking of the Shoulder Joint with Respect to the Thorax Using MARG Sensors and Data Fusion Algorithm," *Biocybern. Biomed. Eng.*, vol. 40, no. 3, pp. 1205–1224, 2020.

[185] J. Justa, V. Šmídl, and A. Hamáček, "Fast AHRS filter for accelerometer, magnetometer, and gyroscope combination with separated sensor corrections," *Sensors (Switzerland)*, vol. 20, no. 14, 2020.

[186] Z. Peng, L. Guan, X. Xu, J. Zeng, Y. Gao, and J. Yang, "Real-Time Attitude Estimation for High-Speed UAV in High-Frequency Environmental Dithering Based on AMCF," in *China Satellite Navigation Conference (CSNC) 2020*, 2020, pp. 89–98.

[187] S. O. H. Madgwick, S. Wilson, R. Turk, J. Burridge, C. Kapatos, and R. Vaidyanathan, "An Extended Complementary Filter for Full-Body MARG Orientation Estimation," *IEEE/ASME Trans. Mechatronics*, vol. 25, no. 4, pp. 2054–2064, 2020.

[188] Dan Simon, *Optimal State Estimation, Kalman, H-infinity, and Nonlinear Approaches*. John Wiley & Sons, Inc., 2006.

[189] B. Barshan and H. F. Durrant-whyte, "Evaluation of a Solid-state Gyroscope for Robotics Applications," *IEEE Trans. Instrum. Meas.*, vol. 44, no. 1, pp. 61–67, 1995.

[190] X. Yun, M. Lizarraga, E. R. Bachmann, and R. B. McGhee, "An Improved Quaternion-Based Kalman Filter for Real-Time Tracking of Rigid Body Orientation," in *Proceedings of the 2003 IEEWRSJ Inll. Conference*

on Intelligent Robots and Systems, 2003, pp. 1074–1079.

[191] S. Yean, B. S. Lee, C. K. Yeo, C. H. Vun, and H. L. Oh, "Smartphone Orientation Estimation Algorithm Combining Kalman Filter With Gradient Descent," *IEEE J. Biomed. Heal. Informatics*, vol. 22, no. 5, pp. 1421–1433, 2018.

[192] L. Wöhle and M. Gebhard, "A Robust Quaternion based Kalman Filter Using a Gradient Descent Algorithm for Orientation Measurement," in *Proceedings of 2018 IEEE International Instrumentation and Measurement Technology Conference (I2MTC)*, 2018.

[193] F. L. Markley, "Fast quaternion attitude estimation from two vector measurements," *J. Guid. Control. Dyn.*, vol. 25, no. 2, pp. 411–414, 2002.

[194] E. Seo, C. Park, D. Kim, and J. Song, "Quaternion-Based Orientation Estimation with Static Error Reduction," in *Proceedings of the 2011 IEEE International Conference on Mechatronics and Automation*, 2011, pp. 1624–1629.

[195] S. Guo, J. Wu, Z. Wang, and J. Qian, "Novel MARG-sensor orientation estimation algorithm using Fast Kalman Filter," *J. Sensors*, pp. 1–12, 2017.

[196] A. Kim and M. F. Golnaraghi, "A quaternion-based orientation estimation algorithm using an inertial measurement unit," in *Record - IEEE PLANS, Position Location and Navigation Symposium*, 2004, pp. 268–272.

[197] J. K. Lee, "A Parallel Attitude-Heading Kalman Filter Without State-Augmentation of Model-Based Disturbance Components," *IEEE Trans. Instrum. Meas.*, vol. 68, no. 7, pp. 2668–2670, 2019.

[198] J. K. Lee and M. J. Choi, "A Sequential Orientation Kalman Filter for AHRS Limiting Effects of Magnetic Disturbance to Heading Estimation," *J. Electr. Eng. Technol.*, vol. 12, no. 4, pp. 1921–1928, 2017.

[199] R. Zhu, D. Sun, Z. Zhou, and D. Wang, "A linear fusion algorithm for attitude determination using low cost MEMS-based sensors," *Measurement*, vol. 40, pp. 322–328, 2007.

[200] P. Batista, C. Silvestre, and P. Oliveira, "Sensor-based Complementary Globally Asymptotically Stable Filters for Attitude Estimation," in *Joint 48th IEEE Conference on Decision and Control and 28th Chinese Control Conference*, 2009, pp. 7563–7568.

[201] P. Batista, C. Silvestre, P. Oliveira, and S. Member, "Sensor-Based Globally Asymptotically Stable Filters for Attitude Estimation: Analysis, Design, and Performance Evaluation," *IEEE Trans. Automat. Contr.*, vol. 57, no. 8, pp. 2095–2100, 2012.

[202] D. Jurman, M. Jankovec, R. Kamnik, and M. Topic, "Calibration and data fusion solution for the miniature attitude and heading reference system," *Sensors Actuators A*, vol. 138, pp. 411–420, 2007.

[203] S. Sun, X. Meng, L. Ji, Z. Huang, and J. Wu, "Adaptive Kalman Filter for Orientation Estimation in Micro-sensor Motion Capture," in *Proceeding of 14th International Conference on Information Fusion*, 2011.

[204] A. Makni, H. Fourati, and A. Y. Kibangou, "Adaptive Kalman Filter for MEMS-IMU based Attitude Estimation under External Acceleration and Parsimonious use of Gyroscopes," in *Proceedings of 2014 European Control Conference (ECC)*, 2014, pp. 1379–1384.

[205] A. Makni *et al.*, "Energy-aware Adaptive Attitude Estimation Under External Acceleration for Pedestrian Navigation," *IEEE Trans. Instrum. Meas.*, vol. 21, no. 3, pp. 1366–1375, 2016.

[206] H. Rehbinder and X. Hu, "Drift-free attitude estimation for accelerated rigid bodies," *Automatica*, vol. 40, no. 4, pp. 653–659, 2004.

[207] H. Rehbinder and X. Hu, "Nonlinear pitch and roll estimation for walking robots," in *Proceedings of IEEE International Conference on Robotics and Automation*, 2000, vol. 3, pp. 2617–2622.

[208] E. J. Lefferts, F. L. Markley, and M. D. Shuster, "Kalman filtering for spacecraft attitude estimation," *J. Guid. Control. Dyn.*, vol. 4, pp. 417–429, 1982.

[209] M. Koifman and S. J. Merhav, "Autonomously aided strapdown attitude reference system," *J. Guid. Control. Dyn.*, vol. 14, no. 6, pp. 1164–1172, 1991.

[210] J. Vaganay and M. J. Aldon, "Attitude estimation for a vehicle using inertial sensors," *Control Eng. Pract.*, vol. 2, no. 2, pp. 281–287, 1994.

[211] X. Yun, C. Aparicio, E. R. Bachmann, and R. B. McGhee, "Implementation and Experimental Results of a Quaternion-Based Kalman Filter for Human Body Motion Tracking," in *Proceedings of the 2005 IEEE*

International Conference on Robotics and Automation, 2005, pp. 317–322.

[212] C. Mazzà, M. Donati, J. McCamley, P. Picerno, and A. Cappozzo, "An optimized Kalman filter for the estimate of trunk orientation from inertial sensors data during treadmill walking," *Gait Posture*, vol. 35, pp. 138–142, Jan. 2012.

[213] S. Zhang, K. Xiao, Q. Zhang, H. Zhang, and Y. Liu, "Improved Extended Kalman Fusion Method For Upper Limb Motion Estimation With Inertial Sensors," in *Proceedings of Fourth International Conference on Intelligent Control and Information Processing (ICICIP)*, 2013, pp. 587–593.

[214] A. M. Sabatini, "Kalman-filter-based orientation determination using inertial/magnetic sensors: Observability analysis and performance evaluation," *Sensors*, vol. 11, no. 10, pp. 9182–9206, 2011.

[215] A. M. Sabatini, "Variable-state-dimension Kalman-based filter for orientation determination using inertial and magnetic sensors," *Sensors*, vol. 12, no. 7, pp. 8491–8506, 2012.

[216] Y. Xu, J. Guo, and Y. Guan, "EKF based Multiple-Mode Attitude Estimator for Quadrotor Using Inertial Measurement Unit," in *Proceedings of the 36th Chinese Control Conference*, 2017, pp. 6191–6198.

[217] S. I. Roumeliotis, G. S. Sukhatme, and G. A. Bekey, "Smoother based 3D attitude estimation for mobile robot localization," *Proc. IEEE Int. Conf. Robot. Autom.*, vol. 3, pp. 1979–1986, 1999.

[218] M. Ahmadi, A. Khayatian, and P. Karimaghaee, "Orientation Estimation by Error-State Extended Kalman Filter in Quaternion Vector Space," in *SICE Annual Conference 2007*, 2007, pp. 60–67.

[219] R. G. Brown and P. Y. C. Hwang, *Introduction to Random Signals and Applied Kalman Filtering*, 2nd Editio. New York: John Wiley & Sons, Inc., 1992.

[220] E. Foxlin, "Inertial head-tracker sensor fusion by a complementary separate-bias Kalman filter," in *Proceedings of the IEEE 1996 Virtual Reality Annual International Symposium*, 1996, pp. 185–194.

[221] P. Setoodeh, A. Khayatian, and E. Farjah, "Attitude Estimation By Separate-Bias Kalman Filter-Based Data Fusion," *J. Navig.*, vol. 57, pp. 261–273, 2004.

[222] D. Gebre-egziabher, R. C. Hayward, and J. D. Powell, "Design of Multi-Sensor Attitude Determination Systems," *IEEE Trans. Aerosp. Electron. Syst.*, vol. 40, no. 2, pp. 627–649, 2004.

[223] R. Zhang and L. M. Reindl, "Pedestrian Motion based Inertial Sensor Fusion by a Modified Complementary Separate-bias Kalman Filter," in *Proceedings of 2011 IEEE Sensors Applications Symposium*, 2011.

[224] Y. Fuke and E. Krotkov, "Dead Reckoning for a Lunar Rover on Uneven Terrain," in *Proceedings of 1996 IEEE Inertnational Conference on Robotics and Automation*, 1996, pp. 411–416.

[225] J. K. Hall, N. B. Knoebel, and T. W. McLain, "Quaternion Attitude Estimation for Miniature Air Vehicles Using a Multiplicative Extended Kalman Filter," in *2008 IEEE/ION Position, Location and Navigation Symposium*, 2008, pp. 1230–1237.

[226] G. F. Welch, "SCAAT: Incremental Tracking with Incomplete Information," University of North Carolina at Chapel Hill, 1996.

[227] C. H. Kang, C. G. Park, and J. W. Song, "An Adaptive Complementary Kalman Filter Using Fuzzy Logic for a Hybrid Head Tracker System," *IEEE Trans. Instrum. Meas.*, vol. 65, no. 9, pp. 2163–2173, 2016.

[228] R. Kannan, "Orientation Estimation Based on LKF Using Differential State Equation," *IEEE Sens. J.*, vol. 15, no. 11, pp. 6156–6163, 2015.

[229] M. Haid and J. Breitenbach, "Low cost inertial orientation tracking with Kalman filter," *Appl. Math. Comput.*, vol. 153, pp. 567–575, 2004.

[230] Y.-S. Shu, S.-K. Park, H.-J. Kank, and Y.-S. Ro, "Attitude Estimation Adaptively Compensating External Acceleration," *JSME Int. J. Ser. C Mech. Syst. Mach. Elem. Manuf.*, vol. 49, no. 1, pp. 172–179, 2006.

[231] J. Bijker and W. Steyn, "Control Engineering Practice Kalman filter configurations for a low-cost loosely integrated inertial navigation system on an airship," *Control Eng. Pract.*, vol. 16, pp. 1509–1518, 2008.

[232] P. Tome and O. Yalak, "Improvement of Orientation Estimation in Pedestrian Navigation by Compensation of Magnetic Disturbances," *Navigation*, vol. 55, pp. 179–190, 2008.

[233] H. Ren and P. Kazanzides, "Hybrid Attitude Estimation for Laparoscopic Surgical Tools: A Preliminary Study," in *31st Annual International Conference of the IEEE EMBS*, 2009, pp. 5583–5586.

[234] G. Cooper *et al.*, "Inertial sensor-based knee flexion/extension angle estimation," *J. Biomech.*, vol. 42, no. 16, pp. 2678–2685, 2009.

[235] J. Musić, M. Cecić, and V. Zanchi, "Real-Time Body Orientation Estimation Based on Two-Layer Stochastic Filter Architecture," *Automatika*, vol. 51, no. 3, pp. 264–274, 2010.

[236] S. Sun, X. Meng, L. Ji, J. Wu, and W.-C. Wong, "Adaptive Sensor Data Fusion in Motion Capture," in *Proceedings of 13th International Conference on Information Fusion*, 2010.

[237] F. Jiancheng and Y. Sheng, "Study on Innovation Adaptive EKF for In-Flight Alignment of Airborne POS," *IEEE Trans. Instrum. Meas.*, vol. 60, no. 4, pp. 1378–1388, 2011.

[238] C. M. N. Brigante, N. Abbate, A. Basile, A. C. Faulisi, and S. Sessa, "Towards Miniaturization of a MEMS-Based Wearable Motion Capture System," *IEEE Trans. Ind. Electron.*, vol. 58, no. 8, pp. 3234–3241, 2011.

[239] A. R. Jiménez, F. Seco, J. C. Prieto, and J. Guevara, "Indoor Pedestrian Navigation using an INS/EKF framework for Yaw Drift Reduction and a foot-mounted IMU," in *Proceedings of 7th Workshop on Positioning, Navigation and Communication*, 2010.

[240] J. Borestein, L. Ojeda, and S. Kwanmuang, "Heuristic reduction of gyro drift in IMU-based personnel tracking system," in *Procedding of SPIE Defense, Security and Sensing Conference*, 2009.

[241] S. Sabatelli, F. Sechi, L. Fanucci, and A. Rocchi, "A sensor fusion algorithm for an integrated angular position estimation with inertial measurement units," in *Proceeding of 2011 Design, Automation & Test in Europe*, 2011.

[242] S. Han and J. Wang, "A Novel Method to Integrate IMU and Magnetometers in Attitude and Heading Reference Systems," *J. Navig.*, vol. 64, pp. 727–738, 2011.

[243] R. Munguia and A. Grau, "Attitude and Heading System based on EKF Total State Configuration," in *Proceeding of 2011 IEEE International Symposium on Industrial Electronics*, 2011, pp. 2147–2152.

[244] E. Edwan, J. Zhang, J. Zhou, and O. Loffeld, "Reduced DCM Based Attitude Estimation Using Low-cost IMU and Magnetometer Triad," in *Proceedings of 2011 8th Workshop on Positioning, Navigation and Communication*, 2011.

[245] M. H. Afzal, V. Renaudin, and G. Lachapelle, "Use of Earth's Magnetic Field for Mitigating Gyroscope Errors Regardless of Magnetic Perturbation," *Sensors*, vol. 11, pp. 11390–11414, 2011.

[246] H. Ren and P. Kazanzides, "Investigation of Attitude Tracking Using an Integrated Inertial and Magnetic Navigation System for Hand-Held Surgical Instruments," *IEEE Trans. Mechatronics*, vol. 17, no. 2, pp. 210–217, 2012.

[247] J. K. Lee, E. J. Park, and S. N. Robinovitch, "Estimation of attitude and external acceleration using inertial sensor measurement during various dynamic conditions," *IEEE Trans. Instrum. Meas.*, vol. 61, no. 8, pp. 2262–2273, 2012.

[248] M. Carminati, G. Ferrari, R. Grassetti, and M. Sampietro, "Real-Time Data Fusion and MEMS Sensors Fault Detection in an Aircraft Emergency Attitude Unit Based on Kalman Filtering," *IEEE Sens. J.*, vol. 12, no. 10, pp. 2984–2992, 2012.

[249] Z. Zhang, X. Meng, and J. Wu, "Quaternion-Based Kalman Filter With Vector Selection for Accurate Orientation Tracking," *IEEE Trans. Instrum. Meas.*, vol. 61, no. 10, pp. 2817–2824, 2012.

[250] W. Li and J. Wang, "Effective Adaptive Kalman Filter for MEMS-IMU/Magnetometers Integrated Attitude and Heading Reference Systems," *J. Navig.*, vol. 66, pp. 99–113, 2013.

[251] A. Dang and V. Nguyen, "DCM-based orientation estimation using cascade of two adaptive extended Kalman filters," in *Proceeding of 2013 International Conference on Control, Automation and Information Sciences (ICCAIS)*, 2013, pp. 152–157.

[252] Q. Zhang, X. Niu, H. Zhang, and C. Shi, "Algorithm Improvement of the Low-End GNSS/INS Systems for Land Vehicles Navigation," *Hindawi Publ. Corp. Math. Probl. Eng.*, 2013.

[253] S. Sabatelli, M. Galgani, L. Fanucci, and A. Rocchi, "A Double-Stage Kalman Filter for Orientation Tracking With an Integrated Processor in 9-D IMU," *IEEE Trans. Instrum. Meas.*, vol. 62, no. 3, pp. 590–598, 2013.

[254] M. Jin, J. Zhao, J. Jin, G. Yu, and W. Li, "The adaptive Kalman filter based on fuzzy logic for inertial motion capture system," *Measurement*, vol. 49, pp. 196–204, 2014.

[255] R. Munguía and A. Grau, "A Practical Method for Implementing an Attitude and Heading Reference System," *Int. J. Adv. Robot. Syst.*, vol. 11, no. 62, 2014.

[256] S. Zihajehzadeh, D. Loh, M. Lee, R. Hoskinson, and E. J. Park, "A Cascaded Two-Step Kalman Filter for

Estimation of Human Body Segment Orientation Using MEMS-IMU," in *Proceedings of 36th Annual International Conference of the IEEE Engineering in Medicine and Biology Society*, 2014, pp. 6270–6273.

[257] C. Miao, Q. Zhang, and J. Fang, "Design of orientation estimation system by inertial and magnetic sensors," *Proc. Inst. Mech. Eng. Part G J. Aerosp. Eng.*, vol. 228, no. 7, pp. 1105–1113, 2014.

[258] Y. Wang, A. Hussain, and M. Soltani, "A MEMS-based Adaptive AHRS for Marine Satellite Tracking Antenna," *IFAC-PapersOnLine*, vol. 48, no. 16, pp. 121–126, 2015.

[259] L. Wang, Z. Zhang, and P. Sun, "Quaternion-based Kalman Filter for AHRS Using an Adaptive-step Gradient Descent Algorithm," *Int. J. Adv. Robot. Syst.*, vol. 12, no. 131, 2015.

[260] Z. Deng, G. Wang, Y. Hu, and D. Wu, "Heading Estimation for Indoor Pedestrian Navigation Using a Smartphone in the Pocket," *Sensors*, vol. 15, pp. 21518–21536, 2015.

[261] P. Neto, N. Mendes, and A. P. Moreira, "Kalman filter-based yaw angle estimation by fusing inertial and magnetic sensing: a case study using low cost sensors," *Sens. Rev.*, vol. 35, no. 3, pp. 244–250, 2015.

[262] L. R. Lustosa, S. Pizziol, F. Defay, and J.-M. Moschetta, "An Error Model of a Complementary Filter for use in Bayesian Estimation - The CF-EKF Filter," *IFAC-PapersOnLine*, vol. 49, no. 17, pp. 444–449, 2016.

[263] S. Zhang, S. Yu, C. Liu, X. Yuan, and S. Liu, "A Dual-Linear Kalman Filter for Real-Time Orientation Determination System Using Low-Cost MEMS Sensors," *Sensors*, vol. 16, 2016.

[264] R. B. Widodo and C. Wada, "Attitude Estimation Using Kalman Filtering: External Acceleration Compensation Considerations," *J. Sensors, Hindawi*, 2016.

[265] C. W. Kang, H. J. Kim, and C. G. Park, "A Human Motion Tracking Algorithm Using Adaptive EKF Based on Markov Chain," *IEEE Sens. J.*, vol. 16, no. 24, pp. 8953–8962, 2016.

[266] L. Chang, F. Zha, and F. Qin, "Indirect Kalman Filtering Based Attitude Estimation for Low-Cost Attitude and Heading Reference Systems," *IEEE/ASME Trans. Mechatronics*, vol. 22, no. 4, pp. 1850–1858, 2017.

[267] T. Zhang and Y. Liao, "Attitude measure system based on extended Kalman filter for multi-rotors," *Comput. Electron. Agric.*, vol. 134, pp. 19–26, 2017.

[268] P. Bernal-Polo and H. Martinez-Barbera, "Orientation Estimation by Means of Extended Kalman Filter, Quaternions, and Charts," *J. Phys. Agents*, vol. 8, no. 1, pp. 11–24, 2017.

[269] Y. Wang, M. Soltani, and D. M. A. Hussain, "An Attitude Heading and Reference System for Marine Satellite Tracking Antenna," *IEEE Trans. Ind. Electron.*, vol. 64, no. 4, pp. 3095–3104, 2017.

[270] S. Šlajpah, R. Kamnik, and M. Munih, "Compensation for Magnetic Disturbances in Motion Estimation to Provide Feedback to Wearable Robotic Systems," *IEEE Trans. Neural Syst. Rehabil. Eng.*, vol. 25, no. 12, pp. 2398–2406, 2017.

[271] X. Tong *et al.*, "Adaptive EKF Based on HMM Recognizer for Attitude Estimation Using MEMS MARG Sensors," *IEEE Sens. J.*, vol. 18, no. 8, pp. 3299–3310, 2018.

[272] M. B. Del Rosario, H. Khamis, P. Ngo, N. H. Lovell, and S. J. Redmond, "Computationally Efficient Adaptive Error-State Kalman Filter for Attitude Estimation," *IEEE Sens. J.*, vol. 18, no. 22, pp. 9332–9342, 2018.

[273] P. J. Glavine *et al.*, "GPS Integrated Inertial Navigation System Using Interactive Multiple Model Extended Kalman Filtering," in *Proceedings of 2018 Moratuwa Engineering Research Conference (MERCon)*, 2018, pp. 414–419.

[274] G. Shi, X. Li, and Z. Jiang, "An improved yaw estimation algorithm for land vehicles using MARG sensors," *Sensors*, vol. 18, no. 10, 2018.

[275] Q. Yuan, E. Asadi, Q. Lu, G. Yang, and I. Chen, "Uncertainty-Based IMU Orientation Tracking Algorithm for Dynamic Motions," *IEEE/ASME Trans. Mechatronics*, vol. 24, no. 2, pp. 872–882, 2019.

[276] H. Ahmed *et al.*, "Adaptive filtering on gps-aided mems-imu for optimal estimation of ground vehicle trajectory," *Sensors (Switzerland)*, vol. 19, no. 24, pp. 1–18, 2019.

[277] A. P. Sage and G. W. Husa, "Adaptive filtering with unknown prior statistics," *IEEE Trans. Autom. Control*, vol. 7, pp. 760–769, 1969.

[278] Q. Ge, T. Shao, C. Wen, and R. Sun, "Analysis on strong tracking filtering for linear dynamic systems," *Math. Probl. Eng.*, vol. 2015, 2015.

[279] H. T. Butt, M. Pancholi, M. Musahl, P. Murthy, M. A. Sanchez, and D. Stricker, "Inertial Motion Capture Using Adaptive Sensor Fusion and Joint Angle Drift Correction," in *22nd International Conference on*

Information Fusion, 2019.

[280] Q. Fan *et al.*, "Improved pedestrian dead reckoning based on a robust adaptive Kalman filter for indoor inertial location system," *Sensors (Switzerland)*, vol. 19, no. 2, 2019.

[281] Á. Odry, I. Kecskes, P. Sarcevic, Z. Vizvari, A. Toth, and P. Odry, "A Novel Fuzzy-Adaptive Extended Kalman Filter for Real-Time Attitude Estimation of Mobile Robots," *Sensors*, 2020.

[282] K. Wen, K. Yu, Y. Li, S. Zhang, and W. Zhang, "A New Quaternion Kalman Filter Based Foot-Mounted IMU and UWB Tightly-Coupled Method for Indoor Pedestrian Navigation," *IEEE Trans. Veh. Technol.*, vol. 69, no. 4, pp. 4340–4352, 2020.

[283] M. A. Javed, M. Tahir, and K. Ali, "Cascaded Kalman Filtering-Based Attitude and Gyro Bias Estimation With Efficient Compensation of External Accelerations," *IEEE Access*, vol. 8, pp. 50022–50035, 2020.

[284] M. Ji, J. Liu, X. Xu, Y. Guo, and Z. Lu, "Improved Pedestrian Positioning with Inertial Sensor Based on Adaptive Gradient Descent and Double-Constrained Extended Kalman Filter," *Complexity, Hindawi*, 2020.

[285] F. Farhangian and R. Landry Jr., "Accuracy Improvement of Attitude Determination Systems Using EKF-Based Error Prediction Filter and PI Controller," *Sensors (Switzerland)*, vol. 20, p. 4055, 2020.

[286] H. Du, W. Wang, C. Xu, R. Xiao, and C. Sun, "Real-time onboard 3D state estimation of an unmanned aerial vehicle in multi-environments using multi-sensor data fusion," *Sensors (Switzerland)*, vol. 20, 2020.

[287] S. Park, J. Park, and C. G. Park, "Adaptive Attitude Estimation for Low-Cost MEMS IMU Using Ellipsoidal Method," *IEEE Trans. Instrum. Meas.*, vol. 69, no. 9, pp. 7082–7091, 2020.

[288] C. Hide, T. Moore, and M. Smith, "Adaptive Kalman Filtering for Low-cost INS/GPS," *J. Navig.*, vol. 56, pp. 143–152, 2003.

[289] C. Hu, Y. Chen, and W. Chen, "Adaptive Kalman filtering for DGPS positioning," in *International Symposium on Kinematic Systems in Geodesy, Geomatics and Navigation*, 2001.

[290] M. E. Johnson and T. Sathyan, "Improved Orientation Estimation in Complex Environments Using Low-Cost Inertial Sensors," in *14th International Conference on Information Fusion*, 2011.

[291] F. Jamil, N. Iqbal, S. Ahmad, and D. H. Kim, "Toward accurate position estimation using learning to prediction algorithm in indoor navigation," *Sensors (Switzerland)*, vol. 20, no. 16, pp. 1–27, 2020.

[292] R. Mehra, "Approaches to adaptive filtering," *IEEE Trans. Automat. Contr.*, vol. 17, no. 5, pp. 693–698, 1972.

[293] P. D. Hanlon and P. S. Maybeck, "Multiple-model adaptive estimation using a residual correlation Kalman filter bank," *IEEE Trans. Aerosp. Electron. Syst.*, vol. 36, no. 2, pp. 393–406, 2000.

[294] J. Li, K. Shu, and H. Zhang, "An efficient method for tri-axis magnetometer calibration," in *IEEE SmartWorld, Ubiquitous Intelligence and Computing, Advanced and Trusted Computing, Scalable Computing and Communications, Internet of People and Smart City Innovation, SmartWorld/UIC/ATC/SCALCOM/IOP/SCI 2019*, 2019, pp. 654–660.

[295] D. Gebre-Egziabher, G. Elkaim, J. Powell, and B. Parkinson, "A non-linear, two-step estimation algorithm for calibrating solid-state strapdown magnetometers.," in *8th International Conference on Integrated Navigation Systems*, 2001, pp. 290–297.

[296] M. Nazarahari and H. Rouhani, "Detection of daily postures and walking modalities using a single chest-mounted tri-axial accelerometer," *Med. Eng. Phys.*, vol. 57, pp. 75–81, 2018.

[297] H. Rouhani, J. Favre, X. Crevoisier, and K. Aminian, "A wearable system for multi-segment foot kinetics measurement," *J. Biomech.*, vol. 47, no. 7, pp. 1704–1711, 2014.

[298] J. R. Rebula, L. V. Ojeda, P. G. Adamczyk, and A. D. Kuo, "Measurement of foot placement and its variability with inertial sensors," *Gait Posture*, vol. 38, no. 4, pp. 974–980, 2013.

[299] G. Wu and P. R. Cavanagh, "ISB recommendations for standardization in the reporting of kinematic data," *J. Biomech.*, vol. 28, no. 10, pp. 1257–1261, 1995.

[300] E. Palermo, S. Rossi, F. Marini, F. Patanè, and P. Cappa, "Experimental evaluation of accuracy and repeatability of a novel body-to-sensor calibration procedure for inertial sensor-based gait analysis," *Meas. J. Int. Meas. Confed.*, vol. 52, no. 1, pp. 145–155, 2014.

[301] J. Favre, R. Aissaoui, B. M. Jolles, J. A. de Guise, and K. Aminian, "Functional calibration procedure for 3D knee joint angle description using inertial sensors," *J. Biomech.*, vol. 42, no. 14, pp. 2330–2335, 2009.

[302] A. G. Cutti, A. Ferrari, P. Garofalo, M. Raggi, A. Cappello, and A. Ferrari, "'Outwalk': A protocol for clinical

gait analysis based on inertial and magnetic sensors," *Med. Biol. Eng. Comput.*, vol. 48, pp. 17–25, 2010.

[303] T. Seel, J. Raisch, and T. Schauer, "IMU-Based Joint Angle Measurement for Gait Analysis," *Sensors*, vol. 14, no. 4, pp. 6891–6909, 2014.

[304] D. Roetenberg, H. Luinge, and P. Slycke, "Xsens MVN : Full 6DOF Human Motion Tracking Using Miniature Inertial Sensors," 2013.

[305] X. Robert-Lachaine, H. Mecheri, C. Larue, and A. Plamondon, "Validation of inertial measurement units with an optoelectronic system for whole-body motion analysis," *Med. Biol. Eng. Comput.*, vol. 55, no. 4, pp. 609–619, 2017.

[306] K. J. O'Donovan, R. Kamnik, D. T. O'Keeffe, and G. M. Lyons, "An inertial and magnetic sensor based technique for joint angle measurement," *J. Biomech.*, vol. 40, no. 12, pp. 2604–2611, 2007.

[307] P. Picerno, A. Cereatti, and A. Cappozzo, "Joint kinematics estimate using wearable inertial and magnetic sensing modules," *Gait Posture*, vol. 28, no. 4, pp. 588–595, 2008.

[308] A. Cappozzo, F. Catani, U. Della Croce, and A. Leardini, "Position and orietnation in space of bones during movement: anatomical frame definition and determination," *Clin. Biomech.*, vol. 10, no. 4, pp. 171–178, 1995.

[309] S. Grood and W. Suntay, "A joint coordinate system for the clinical description of three-dimentional motions: application to the knee," *J. Biomech. Eng.*, vol. 105, no. 2, pp. 136–144, 1983.

[310] R. Moe-nilssen and J. L. Helbostad, "Trunk accelerometry as a measure of balance control during quiet standing," *Gait Posture*, vol. 16, no. 1, pp. 60–68, 2002.

[311] R. Moe-Nilssen, "A new method for evaluating motor control in gait under real-life environmental conditions. Part 1: The instrument," *Clin. Biomech.*, vol. 13, pp. 320–327, 1998.

[312] H. Xing, B. Hou, Z. Lin, and M. Guo, "Modeling and Compensation of Random Drift of MEMS Gyroscopes Based on Least Squares Support Vector Machine Optimized by Chaotic Particle," *Sensors*, vol. 17, no. 10, p. 2335, 2017.

[313] H. Mecheri, X. Robert-Lachaine, C. Larue, and A. Plamondon, "Evaluation of eight methods for aligning orientation of two coordinate systems," *J. Biomech. Eng.*, vol. 138, no. 8, 2016.

[314] J. Favre, B. M. Jolles, R. Aissaoui, and K. Aminian, "Ambulatory measurement of 3D knee joint angle," *J. Biomech.*, vol. 41, no. 5, pp. 1029–1035, 2008.

[315] C. M. Jarque and A. K. Bera, "A Test for Normality of Observations and Regression Residuals," *Int. Stat. Rev.*, vol. 55, no. 2, pp. 163–172, 1987.

[316] B. Fasel, J. Spörri, P. Schütz, S. Lorenzetti, and K. Aminian, "Validation of functional calibration and strap-down joint drift correction for computing 3D joint angles of knee, hip, and trunk in alpine skiing," *PLoS One*, vol. 12, no. 7, pp. 1–17, 2017.

[317] G. Ligorio, D. Zanotto, A. M. Sabatini, and S. K. Agrawal, "A novel functional calibration method for real-time elbow joint angles estimation with magnetic-inertial sensors," *J. Biomech.*, vol. 54, pp. 106–110, 2017.

[318] A. Noamani, A. H. Vette, R. Preuss, M. R. Popovic, and H. Rouhani, "Optimal Estimation of Anthropometric Parameters for Quantifying Multi-Segment Trunk Kinetics," *J. Biomech. Eng.*, vol. 140, no. 10, 2018.

[319] A. Noamani, A. H. Vette, R. Preuss, M. R. Popovic, and H. Rouhani, "Quantification of multi-segment trunk kinetics during multi-directional trunk bending," *Gait Posture*, vol. 64, pp. 205–212, 2018.

[320] T. Zimmermann, B. Taetz, and G. Bleser, *IMU-to-Segment Assignment and Orientation Alignment for the Lower Body Using Deep Learning*. 2018.

[321] M. Nazarahari, S. Ghorbanpour Namin, A. H. Davaie Markazi, and A. Kabir Anaraki, "A multi-wavelet optimization approach using similarity measures for electrocardiogram signal classification," *Biomed. Signal Process. Control*, vol. 20, pp. 142–151, 2015.

[322] S. Doostie, A. K. Hoshiar, M. Nazarahari, S. Lee, and H. Choi, "Optimal path planning of multiple nanoparticles in continuous environment using a novel Adaptive Genetic Algorithm," *Precis. Eng.*, vol. 53, pp. 65–78, 2018.

[323] M. Nazarahari, E. Khanmirza, and S. Doostie, "Multi-objective multi-robot path planning in continuous environment using an enhanced genetic algorithm," *Expert Syst. Appl.*, vol. 115, pp. 106–120, 2019.

[324] W. Kong, S. Sessa, M. Zecca, and A. Takanishi, "Anatomical Calibration through Post-Processing of Standard Motion Tests Data," *Sensors (Switzerland)*, 2016.

[325] A. Nez, L. Fradet, F. Marin, T. Monnet, and P. Lacouture, “Identification of noise covariance matrices to improve orientation estimation by kalman filter,” *Sensors (Switzerland)*, vol. 18, no. 10, pp. 1–20, 2018.

[326] Y. Teruyama and T. Watanabe, “Effectiveness of Variable-Gain Kalman Filter Based on Angle Error Calculated from Acceleration Signals in Lower Limb Angle Measurement with Inertial Sensors,” *Comput. Math. Methods Med.*, 2013.

[327] R. K. Mehra, “On the Identification of Variances and Adaptive Kalman Filtering,” *IEEE Trans. Automat. Contr.*, vol. 15, no. 2, pp. 175–184, 1970.

[328] D. Loebis, R. Sutton, J. Chudley, and W. Naeem, “Adaptive tuning of a Kalman filter via fuzzy logic for an intelligent AUV navigation system,” *Control Eng. Pract.*, vol. 12, pp. 1531–1539, 2004.

[329] A. Chatterjee and F. Matsuno, “A neuro-fuzzy assisted extended kalman filter-based approach for simultaneous localization and mapping (SLAM) problems,” *IEEE Trans. Fuzzy Syst.*, vol. 15, no. 5, pp. 984–997, 2007.

[330] J. Kennedy and R. Eberhart, “Particle Swarm Optimization,” in *Proceedings of IEEE International Conference on Neural Networks. IV.*, 1995, pp. 1942–1948.

[331] J. A. de la O Serna and J. Rodriguez-Maldonado, “Instantaneous oscillating phasor estimates with taylor-kalman filters,” *IEEE Trans. Power Syst.*, vol. 26, no. 4, pp. 2336–2344, 2011.

[332] J. H. Park, C. H. Shea, and D. L. Wright, “Reduced-frequency concurrent and terminal feedback: A test of the guidance hypothesis,” *J. Mot. Behav.*, vol. 32, no. 3, pp. 287–296, 2000.

[333] E. H. and S. A. Mamdani, “An experiment in linguistic synthesis with a fuzzy logic controller,” *Int. J. Man. Mach. Stud.*, vol. 7, no. 1, pp. 1–13, 1975.

[334] D. Dubois and H. Prade, *Fuzzy Sets and Systems: Theory and Applications*. New York: Academic Press, 1980.

[335] P. J. Escamilla-Ambrosio and N. Mort, “Hybrid Kalman Filter-Fuzzy Logic Adaptive Multisensor Data Fusion Architectures,” *Proc. IEEE Conf. Decis. Control*, pp. 5215–5220, 2003.

[336] P. J. Escamilla-Ambrosio and N. Mort, “Development of a fuzzy logic-based adaptive Kalman filter,” *2001 Eur. Control Conf. ECC 2001*, pp. 1768–1773, 2001.

[337] Y. O. Markley, F. Landis, Yang Cheng, John Lucas Crassidis, “Averaging Quaternions,” *J. Guid. Control. Dyn.*, vol. 30, no. 4, pp. 1193–1197, 2007.

[338] M. Zamani-Gargari, M. Nazari-Heris, and B. Mohammadi-Ivatloo, “Application of Particle Swarm Optimization Algorithm in Power System Problems,” in *Handbook of Neural Computation*, Academic Press, 2017, pp. 571–579.

[339] D. W. Allan, “Statistics of Atomic Frequency Standards,” *Proc. IEEE*, vol. 54, no. 2, pp. 221–230, 1966.

[340] J. Wang, C.-Y. Su, and M. Oya, “Robust motion tracking control of partially nonholonomic mechanical systems,” *Proc. IEEE Int. Conf. Robot. Autom. (ICRA ’04)*, vol. 5, pp. 4608–4613, 2004.

[341] A. Makni, H. Fourati, and A. Y. Kibangou, “Energy-Aware Adaptive Attitude Estimation Under External Acceleration for Pedestrian Navigation,” *IEEE/ASME Trans. Mechatronics*, vol. 21, no. 3, pp. 1366–1375, 2016.

[342] F. Edrisi and V. J. Majd, “Attitude estimation of an accelerated rigid body with sensor fusion based-on switching extended Kalman filter,” in *2015 AI & Robotics (IRANOPEN)*, 2015, pp. 1–6.

[343] W. H. K. De Vries, H. E. J. Veeger, C. T. M. Baten, and F. C. T. Van Der Helm, “Magnetic distortion in motion labs, implications for validating inertial magnetic sensors,” *Gait Posture*, vol. 29, pp. 535–541, 2009.

[344] D. A. Winter, *Biomechanics and Motor Control of Human Movement*, Fourth Edi. John Wiley & Sons, Inc., 2009.

[345] H. M. T. Menegaz, J. Y. Ishihara, G. A. Borges, and A. N. Vargas, “A Systematization of the Unscented Kalman Filter Theory,” *IEEE Trans. Automat. Contr.*, vol. 60, no. 10, pp. 2583–2598, 2014.

[346] K. P. B. Chandra, D.-W. Gu, and I. Postlethwaite, “Square Root Cubature Information Filter,” *Kumar Pakki Bharani Chandra; Da-Wei Gu; Ian Postlethwaite*, vol. 12, no. 2, pp. 750–758, 203AD.

[347] I. Arasaratnam and S. Haykin, “Cubature Kalman Filters,” *IEEE Trans. Automat. Contr.*, vol. 54, no. 6, pp. 1254–1269, 2009.

[348] H. Chen, M. C. Schall, and N. Fethke, “Effects of Movement Speed and Magnetic Disturbance on the Accuracy of Inertial Measurement Units,” in *Proceedings of the Human Factors and Ergonomics Society*

Annual Meeting, 2017, vol. 61, no. 1, pp. 1046–1050.

[349] R. Van der Merwe and E. A. Wan, "The square-root unscented Kalman filter for state and parameter-estimation," in *2001 IEEE International Conference on Acoustics, Speech, and Signal Processing*, 2001, pp. 3461–3464.

[350] C. Moler and C. Van Loan, "Nineteen dubious ways to compute the exponential of a matrix, twenty-five years later," *SIAM Rev.*, vol. 45, no. 1, pp. 3–49, 2003.

[351] R. G. Valenti, I. Dryanovski, and J. Xiao, "A linear Kalman Filter for MARG orientation estimation using an algebraic quaternion algorithm," *IEEE Trans. Instrum. Meas.*, vol. 65, no. 2, pp. 467–481, 2015.

[352] W. Li and Y. Jia, "H-infinity filtering for a class of nonlinear discrete-time systems based on unscented transform," *Signal Processing*, vol. 90, no. 12, pp. 3301–3307, 2010.

[353] B. Hassibi, A. H. Sayed, and T. Kailath, *Indefinite-quadratic estimation and control: a unified approach to H2 and H∞ theories*. SIAM, Philadelphia, 1999.

[354] G. A. Einicke and L. B. White, "Robust Extended Kalman Filtering," *IEEE Trans. SIGNAL Process.*, vol. 47, no. 9, pp. 2596–2599, 1999.

[355] L. Markley, "Attitude Error Representations for Kalman Filtering," *J. Guid. Control. Dyn.*, vol. 26, no. 2, pp. 311–317, 2003.

[356] D. Choukroun, Y. Bar-Itzhack, and Y. Oshman, "Novel Quaternion Kalman Filter," *IEEE Trans. Aerosp. Electron. Syst.*, vol. 42, no. 1, pp. 174–190, 2006.

[357] T. Michel, P. Genevès, H. Fourati, and N. Layaïda, "On Attitude Estimation with Smartphones," in *IEEE International Conference on Pervasive Computing and Communications*, 2017.

[358] Y. S. O. O. Suh, "Simple-Structured Quaternion Estimator Separating Inertial and Magnetic Sensor Effects," *IEEE Trans. Aerosp. Electron. Syst.*, vol. 55, no. 6, pp. 2698–2706, 2019.

[359] J. Wu, "MARG Attitude Estimation Using Gradient-Descent Linear Kalman Filter," *IEEE Trans. Autom. Sci. Eng.*, vol. 17, no. 4, pp. 1777–1790, 2020.

[360] V. Maximov, "GyroLib - AHRS Library," *MATLAB Central File Exchange*, 2020. [Online]. Available: https://www.mathworks.com/matlabcentral/fileexchange/63250-gyrolib-ahrs-library.

[361] S. Julier and J. K. Uhlmann, "A New Approach for Filtering Nonlinear Systems," in *Proceedings of the American Control Conference*, 1995, pp. 1628–1632.

[362] S. J. Julier, "The spherical simplex unscented transformation," in *Proceedings of the 2003 American Control Conference*, 2003, pp. 2430–2434.

[363] H. M. Menegaz, J. Y. Ishihara, and G. A. Borges, "A new smallest sigma set for the Unscented Transform and its applications on SLAM," in *50th IEEE Conference on Decision and Control and European Control Conference (CDC-ECC)*, 2011, pp. 3172–3177.

[364] H. Wang, Z. Deng, B. Feng, H. Ma, and Y. Xia, "An adaptive Kalman filter estimating process noise covariance," *Neurocomputing*, vol. 223, pp. 12–17, 2017.

[365] J. H. Challis, "An examination of procedures for determining body segment attitude and position from noisy biomechanical data," *Med. Eng. Phys.*, vol. 17, no. 2, pp. 83–90, 1995.

[366] F. E. Veldpaus, H. J. Woltring, and L. J. M. G. Dortmans, "A least-squares algorithm for the equiform transformation from spatial marker co-ordinates," *J. Biomech.*, vol. 21, no. 1, pp. 45–54, 1988.

[367] D. Q. Huynh, "Metrics for 3D Rotations: Comparison and Analysis," *J. Math. Imaging Vis.*, vol. 35, pp. 155–164, 2009.

[368] G. Ligorio, E. Bergamini, I. Pasciuto, G. Vannozzi, A. Cappozzo, and A. M. Sabatini, "Assessing the Performance of Sensor Fusion Methods: Application to Magnetic-Inertial-Based Human Body Tracking," *Sensors (Switzerland)*, vol. 16, no. 153, 2016.

[369] B. Mariani, H. Rouhani, X. Crevoisier, and K. Aminian, "Quantitative estimation of foot-flat and stance phase of gait using foot-worn inertial sensors," *Gait Posture*, vol. 37, no. 2, pp. 229–234, 2013.

[370] N. C. Bejarano, E. Ambrosini, A. Pedrocchi, G. Ferrigno, M. Monticone, and S. Ferrante, "A novel adaptive, real-time algorithm to detect gait events from wearable sensors," *IEEE Trans. Neural Syst. Rehabil. Eng.*, vol. 23, no. 3, pp. 413–422, 2015.

[371] D. Gouwanda and A. A. Gopalai, "A robust real-time gait event detection using wireless gyroscope and its

application on normal and altered gaits," *Med. Eng. Phys.*, vol. 37, no. 2, pp. 219–225, 2015.

[372] P. Catalfamo, S. Ghoussayni, and D. Ewins, "Gait event detection on level ground and incline walking using a rate gyroscope," *Sensors (Switzerland)*, vol. 10, no. 6, pp. 5683–5702, 2010.

[373] J. C. Perez-Ibarra, A. A. G. Siqueira, and H. I. Krebs, "Real-Time Identification of Gait Events in Impaired Subjects Using a Single-IMU Foot-Mounted Device," *IEEE Sens. J.*, vol. 20, no. 5, pp. 2616–2624, 2020.

[374] S. Barnett, J. L. Cunningham, and S. West, "A comparison of vertical force and temporal parameters produced by an in-shoe pressure measuring system and a force platform," *Clin. Biomech.*, vol. 16, pp. 353–357, 2001.

[375] H. Rouhani, J. Favre, X. Crevoisier, B. M. Jolles, and K. Aminian, "A comparison between joint coordinate system and attitude vector for multi-segment foot kinematics," *J. Biomech.*, vol. 45, no. 11, pp. 2041–2045, 2012.

[376] J. A. Zeni, J. G. Richards, and J. S. Higginson, "Two simple methods for determining gait events during treadmill and overground walking using kinematic data," *Gait Posture*, vol. 27, no. 4, pp. 710–714, 2008.

[377] L. Smith, S. Preece, D. Mason, and C. Bramah, "A comparison of kinematic algorithms to estimate gait events during overground running," *Gait Posture*, vol. 41, pp. 39–43, 2015.

[378] H. F. Maqbool, M. A. B. Husman, M. I. Awad, A. Abouhossein, N. Iqbal, and A. A. Dehghani-Sanij, "A Real-Time Gait Event Detection for Lower Limb Prosthesis Control and Evaluation," *IEEE Trans. Neural Syst. Rehabil. Eng.*, vol. 25, no. 9, pp. 1500–1509, 2017.

[379] J. K. Lee and E. J. Park, "Quasi real-time gait event detection using shank-attached gyroscopes," *Med. Biol. Eng. Comput.*, vol. 49, no. 6, pp. 707–712, 2011.

[380] E. Allseits, J. Lučarević, R. Gailey, V. Agrawal, I. Gaunaurd, and C. Bennett, "The development and concurrent validity of a real-time algorithm for temporal gait analysis using inertial measurement units," *J. Biomech.*, vol. 55, pp. 27–33, 2017.

[381] J. M. Jasiewicz *et al.*, "Gait event detection using linear accelerometers or angular velocity transducers in able-bodied and spinal-cord injured individuals," *Gait Posture*, vol. 24, no. 4, pp. 502–509, 2006.

[382] D. Kotiadis, H. J. Hermens, and P. H. Veltink, "Inertial Gait Phase Detection for control of a drop foot stimulator, Inertial sensing for gait phase detection.," *Med. Eng. Phys.*, vol. 32, no. 4, pp. 287–297, 2010.

[383] J. M. Bland and D. G. Altman, "Measuring agreement in method comparison studies," *Stat. Methods Med. Res.*, vol. 8, no. 2, pp. 135–160, 1999.

[384] S. Sahoo, M. Saboo, D. K. Pratihar, and S. Mukhopadhyay, "Real-Time Detection of Actual and Early Gait Events during Level-Ground and Ramp Walking," *IEEE Sens. J.*, vol. 20, no. 14, pp. 8128–8136, 2020.

[385] J. Leitch, J. Stebbins, G. Paolini, and A. B. Zavatsky, "Identifying gait events without a force plate during running: A comparison of methods," *Gait Posture*, vol. 33, no. 1, pp. 130–132, 2011.

[386] N. Ahmadian, M. Nazarahari, J. L. Whittaker, and H. Rouhani, "Quantification of triple dingle-leg hop test temporospatial parameters: a validated method using body-worn sensors for functional evaluation after knee injury," *Sensors*, vol. 20, no. 12, p. 3464, 2020.

[387] K. J. Coleman, B. E. Saelens, M. D. Wiedrich-Smith, J. D. Finn, and L. H. Epstein, "Relationships between TriTrac-R3D vectors, heart rate, and self-report in obese children," *Med. Sci. Sport. Exerc.*, vol. 29, no. 11, pp. 1535–1542, 1997.

[388] A. K. Bourke, K. J. O'Donovan, and G. ÓLaighin, "The identification of vertical velocity profiles using an inertial sensor to investigate pre-impact detection of falls," *Med. Eng. Phys.*, vol. 30, no. 7, pp. 937–946, 2008.

[389] A. Godfrey *et al.*, "Activity classification using a single chest mounted tri-axial accelerometer," *Med. Eng. Phys.*, vol. 33, no. 9, pp. 1127–1135, 2011.

[390] B. Najafi, K. Aminian, A. Paraschiv-Ionescu, F. Loew, C. J. Büla, and P. Robert, "Ambulatory system for human motion analysis using a kinematic sensor: monitoring of daily physical activity in the elderly," *Biomed. Eng. IEEE Trans.*, vol. 50, no. 6, pp. 711–723, 2004.

[391] D. M. Karantonis, M. R. Narayanan, M. Mathie, N. H. Lovell, and B. G. Celler, "Implementation of a real-time human movement classifier using a triaxial accelerometer for ambulatory monitoring," *Inf. Technol. Biomed. IEEE Trans.*, vol. 10, no. 1, pp. 156–167, 2006.

[392] B. Najafi, K. Aminian, F. Loew, Y. Blanc, P. a Robert, and S. Member, "Measurement of stand–sit and sit–stand transitions using a miniature gyroscope and its application in fall risk evaluation in the elderly," *IEEE*

Trans. Biomed. Eng., vol. 49, no. 8, pp. 843–851, 2002.

[393] N. Bidargaddi *et al.*, "Wavelet based approach for posture transition estimation using a waist worn accelerometer," *Annu. Int. Conf. IEEE Eng. Med. Biol. - Proc.*, pp. 1884–1887, 2007.

[394] A. Hickey, B. Galna, J. C. Mathers, L. Rochester, and A. Godfrey, "A multi-resolution investigation for postural transition detection and quantification using a single wearable," *Gait Posture*, vol. 49, pp. 411–417, 2016.

[395] M. J. Mathie, A. C. Coster, N. H. Lovell, and B. G. Celler, "Detection of daily physical activities using a triaxial accelerometer," *Med Biol Eng Comput*, vol. 41, no. 3, pp. 296–301, 2003.

[396] V. Lugade, E. Fortune, M. Morrow, and K. Kaufman, "Validity of using tri-axial accelerometers to measure human movement-Part I: Posture and movement detection," *Med. Eng. Phys.*, vol. 36, no. 2, pp. 169–176, 2014.

[397] M. J. Mathie, A. C. F. Coster, N. H. Lovell, B. G. Celler, S. R. Lord, and A. Tiedemann, "A pilot study of long-term monitoring of human movements in the home using accelerometry," *J. Telemed. Telecare*, vol. 10, no. 3, pp. 144–151, 2004.

[398] G. M. Lyons, K. M. Culhane, D. Hilton, P. A. Grace, and D. Lyons, "A description of an accelerometer-based mobility monitoring technique," *Med. Eng. Phys.*, vol. 27, no. 6, pp. 497–504, 2005.

[399] A. Paraschiv-Ionescu, E. E. Buchser, B. Rutschmann, B. Najafi, and K. Aminian, "Ambulatory system for the quantitative and qualitative analysis of gait and posture in chronic pain patients treated with spinal cord stimulation," *Gait Posture*, vol. 20, no. 2, pp. 113–125, 2004.

[400] C. A. Ronao and S. Cho, "Human activity recognition with smartphone sensors using deep learning neural networks," *Expert Syst. Appl.*, vol. 59, pp. 235–244, 2016.

[401] C. Catal, S. Tufekci, E. Pirmit, and G. Kocabag, "On the use of ensemble of classifiers for accelerometer-based activity recognition," *Appl. Soft Comput. J.*, vol. 37, pp. 1018–1022, 2015.

[402] F. Massé, A. K. Bourke, J. Chardonnens, A. Paraschiv-Ionescu, and K. Aminian, "Suitability of commercial barometric pressure sensors to distinguish sitting and standing activities for wearable monitoring," *Med. Eng. Phys.*, vol. 36, no. 6, pp. 739–744, 2014.

[403] F. Massé, R. R. Gonzenbach, A. Arami, A. Paraschiv-Ionescu, A. R. Luft, and K. Aminian, "Improving activity recognition using a wearable barometric pressure sensor in mobility-impaired stroke patients.," *J. Neuroeng. Rehabil.*, vol. 12, 2015.

[404] M. Sekine, T. Tamura, T. Fujimoto, and Y. Fukui, "Classification of walking pattern using acceleration waveform in elderly people," *Proc. Int. Conf. Eng. Med. Biol. Soc.*, vol. 2, pp. 1356–1359, 2000.

[405] M. Sekine, T. Tamura, M. Akay, T. Fujimoto, T. Togawa, and Y. Fukui, "Discrimination of walking patterns using wavelet-based fractal analysis," *IEEE Trans. Neural Syst. Rehabil. Eng.*, vol. 10, no. 3, pp. 188–196, 2002.

[406] M. N. Nyan, F. E. H. Tay, K. H. W. Seah, and Y. Y. Sitoh, "Classification of gait patterns in the time-frequency domain," *J. Biomech.*, vol. 39, no. 14, pp. 2647–2656, 2006.

[407] Y. C. Pai and J. Patton, "Center of mass velocity-position predictions for balance control," *J. Biomech.*, vol. 30, no. 4, pp. 347–354, 1997.

[408] V. Lugade, V. Lin, and L. S. Chou, "Center of mass and base of support interaction during gait," *Gait Posture*, vol. 33, no. 3, pp. 406–411, 2011.

[409] A. Godfrey, G. Barry, J. C. Mathers, and L. Rochester, "A comparison of methods to detect postural transitions using a single tri-axial accelerometer," *Annu. Int. Conf. IEEE Eng. Med. Biol. Soc.*, vol. 2014, pp. 6234–6237, 2014.

[410] B. Coley, B. Najafi, A. Paraschiv-Ionescu, and K. Aminian, "Stair climbing detection during daily physical activity using a miniature gyroscope," *Gait Posture*, vol. 22, no. 4, pp. 287–294, 2005.

[411] I. Carpinella *et al.*, "Wearable sensor-based biofeedback training for balance and gait in Parkinson Disease: a pilot randomized controlled trial," *Arch. Phys. Med. Rehabil.*, vol. 98, no. 4, pp. 622–630, 2017.

[412] I. Skog, P. Händel, J. O. Nilsson, and J. Rantakokko, "Zero-velocity detection-An algorithm evaluation," *IEEE Trans. Biomed. Eng.*, vol. 57, no. 11, pp. 2657–2666, 2010.

[413] X. Tian, J. Chen, Y. Han, J. Shang, and N. Li, "A novel zero velocity interval detection algorithm for self-

contained pedestrian navigation system with inertial sensors," *Sensors (Switzerland)*, vol. 16, no. 10, 2016.

[414] X. Meng, Z. Q. Zhang, J. K. Wu, and W. C. Wong, "Hierarchical information fusion for global displacement estimation in microsensor motion capture," *IEEE Trans. Biomed. Eng.*, vol. 60, no. 7, pp. 2052–2063, 2013.

[415] X. L. Meng, Z. Q. Zhang, S. Y. Sun, J. K. Wu, and W. C. Wong, "Biomechanical model-based displacement estimation in micro-sensor motion capture," *Meas. Sci. Technol.*, vol. 23, no. 5, 2012.